UNIVERSIDADE DE SANTIAGO DE COMPOSTELA

FACULTAD DE FÍSICA

Departamento de Física de Partículas

Neutron-induced fission fragment angular distribution and cross section of uranium targets at CERN-n_TOF.

Esther Leal Cidoncha

Marzo 2017

UNIVERSIDADE DE SANTIAGO DE COMPOSTELA

FACULTAD DE FÍSICA

Departamento de Física de Partículas

Neutron-induced fission fragment angular distribution and cross section of uranium targets at CERN-n_TOF.

Memoria presentada por:
Esther Leal Cidoncha
como disertación para optar al
Grado de Doctora en Física
Marzo 2017

UNIVERSIDADE DE SANTIAGO DE COMPOSTELA

Ignacio Durán Escribano, Catedrático de Física Atómica, Molecular y Nuclear de la Universidad de Santiago de Compostela y **Carlos Paradela Dobarro**, Contract Researcher Group IV de la Comisión Europea,

CERTIFICAN:

que la memoria titulada **Neutron-induced fission fragment angular distribution and cross section of uranium targets at CERN-n_TOF** ha sido realizada por **Esther Leal Cidoncha** en el **Departamento de Física de Partículas** bajo su dirección y constituye el **Trabajo de tesis** que presenta para optar al grado de **Doctora en Física**.

Santiago de Compostela, a 16 de Marzo de 2017.

Fdo. Ignacio Durán Escribano

Fdo. Carlos Paradela Dobarro

Fdo. Esther Leal Cidoncha

Contents

Introduction

This thesis work focuses on the new results obtained for the fission fragment angular distribution (FFAD) and neutron-induced fission cross section on ^{234}U and ^{235}U targets, measured at the n_TOF facility at CERN, using Parallel Plate Avalanche Counter (PPAC) detectors.

The need of accurate data on heavy nuclei fission has existed for a long time, being of interest for both fundamental and applied nuclear physics. However, despite considerable experimental and theoretical efforts aimed at the understanding of the fission process, many details of its mechanism are still unclear. It is worth to note that, after the many years since the discovery of binary fission, there is not an adequate theory to describe the characteristics of the fission process for a broad range of fissioning nuclei along a wide projectile energy region. Measurements of the energy dependence of neutron-induced fission cross sections for uranium isotopes, as well as its fission fragment angular distributions, would help to get new insights into both the fission process and the mechanism of the projectile interaction with the nucleus. The measurement of accurate neutron-induced cross sections is also required for new reactors designs. This thesis deals with two of the relevant nuclides in the fuel dynamics of a reactor, the ^{234}U and ^{235}U, whose importance will be detailed in the following sections.

The ^{234}U(n,f) cross section has been obtained in this work in the whole energy range from a few eV up to 1 GeV using the ^{235}U(n,f) cross section as reference. The ^{235}U(n,f) cross section has been calculated up to 100 keV using the n_TOF flux shape based on the measurement of the ^{10}B(n,α) reaction with MGAS. The ^{234}U(n,f) cross section has been calculated below 100 keV using the neutron flux shape obtained through two different reactions (^{10}B(n,α) and ^{235}U(n,f)) obtaining results in quite good agreement between them.

At neutron energies above hundreds of keV, the fission fragments (FFs) are anisotropically emitted and their angular distribution has to be considered in the detection efficiency calculation because the setup efficiency is reduced. Therefore, taking advantage of the possibility to measure the detec-

tion position of the FFs with the PPAC detectors at all the emission angles, the fission fragment angular distributions (FFADs) have been also measured. Two different setup configurations have been used in the n_TOF measurements with PPAC: the configuration of targets and detectors perpendicular to the beam, that only allowed to measure the FFAD up to 60°, and the more recent, tilted configuration, also used in this thesis, that was suitably utilised to calculate the FFAD of the ^{232}Th target [37,31]. It allowed to cover the full angular range from 0° to 90°, improving the accuracy in the detection efficiency calculation.

Successful and precise results were obtained from previous experiments using the present setup concerning the fission cross sections of the isotopes ^{234}U and ^{237}Np [1], ^{nat}Pb and ^{209}Bi [2], and ^{232}Th [3] in the entire energy range up to 1 GeV.

Even though several previous experimental measurements of the ^{234}U(n,f) cross section can be retrieved from the EXFOR library [4], the only experimental data set provided up to 1 GeV is the one measured by Paradela [1] at the CERN-n_TOF facility, but the experiment was performed using the PPACs setup with its perpendicular configuration of targets and detectors. The new measurement presented in this thesis has been performed using the PPACs tilted setup improving the accuracy in the detection efficiency calculation.

Neutron sources

The neutron is not a stable particle, having a well-known half-life of 10.24(2) min. It decays to a proton by emitting a β particle and an antineutrino, and so free neutrons can only be found after being produced through nuclear reactions. These neutrons are usually generated at energies of several MeV or higher, and they can be moderated to cover energies till below eV by undertaking elastic collisions in moderators containing light nuclides (for instance H, D, Be, C). Typical spectra of some neutron sources are shown in Fig. 1.

Being an uncharged particle, a neutron with an arbitrarily low kinetic energy can approach a nucleus without being affected by the Coulomb barrier and can eventually be captured by the nuclear forces and an excited compound nucleus is formed, which, depending on the excitation energy, decays emitting a neutron (elastic/inelastic scattering), gamma radiation (radiative capture), a charge particle (for instance an alpha) or, for certain nuclei fission.

According to their energies, neutrons are customary classified in different groups. Slow neutrons are those produced during the so-called thermalisation

in moderators at approximately room-temperature adopting an energy distribution that depends on the temperature of the moderator according to the Maxwellian distribution model, as it was originally introduced for the ideal-gas thermal motion distribution. By convention, cold neutrons are those having energies smaller than the so-called thermal-point, stablished at 0.025 eV; thermal neutrons range from the thermal point up to about 100 meV, and the neutrons having energies of about 0.1-1 eV are called epithermal. Above around 1 eV the resonances show up in the cross-section of different reactions and two regions can be distinguished: the Resolved Resonance Region (RRR) and the Unresolved Resonance Region (URR), typically ranging up to a few keV, and to some tens of keV, respectively.

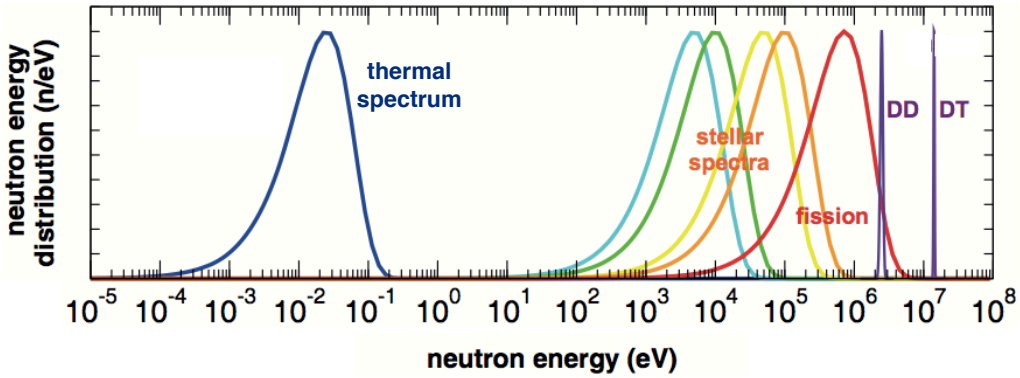

Figure 1: Common spectra from different neutron sources; namely, the thermal Maxwellian after water moderation, a few stellar scenarios, a fission reactor, deuterium-deuterium, and deuterium-tritium. Figure from [7].

Fast neutron energies are generally regarded above 100 keV, even though the transitional range between the URR and fast neutrons is not well defined. This range acquired renewed interest because the new designs of fast reactors, which required to burn up the transuranic isotopes generated in the nuclear reactors of thermal-neutron spectrum.

Around 200 MeV, starts what it is called the Intermediate energy region, even though this term is not unambiguous (in nuclear literature the sub-threshold region has been often termed Intermediate as well). This region spans up to around 1 GeV, where hadronic reactions dominate.

Nuclear power production

A nucleus capable of undergoing fission after capturing a neutron is referred as *fissionable*. The term *fissile* is customary used to refer a fission-

able nuclide that can be induced to fission by low-energy neutrons with a high probability, because the energy gained in the absorption of a neutron is greater than the critical energy required for fission. ^{235}U is a fissile isotope; conversely, the binding energy gained by ^{238}U or ^{234}U after absorbing a thermal neutron is less than the critical energy so the neutron must possess additional energy for fission to be possible. Consequently, ^{238}U or ^{234}U are fissionable but can not be termed fissile.

The practical importance of neutron-induced fission rests upon the fact that additional neutrons are produced in the fission process, and hence, a chain reaction becomes possible. This chain reaction is the operational principle of a nuclear reactors that provide a substantial fraction of the energy supply in many countries. However, this form of power production has a delicate issue in the handling of the long-lived radiotoxic nuclear waste generated.

This radioactive waste consists of fission products and also of actinides from nuclear fuel nuclei that capture neutrons but fail to fission. After the useful fuel is removed from reactors, its radioactivity is mostly due to the fission products that are commonly short-lived. Therefore, after a few tens of years, the bulk of remaining radioactivity comes from actinides, notably ^{239}Pu, ^{240}Pu, ^{241}Am, ^{243}Am, ^{245}Cu and ^{246}Cu. Even though these isotopes can be recovered by nuclear reprocessing, it creates a major problem for the nuclear waste managing and so the reduction of the radioactive waste is one of the main objectives of current reactors studies.

In nuclear reactors, the most common used fuel consists of enriched uranium (^{238}U with a percentage of ^{235}U). The ^{235}U fission cross section is higher at low neutron energies . Also, the ^{238}U is called a fertile isotope because it may capture neutrons of any energy and, after a β decay chain, the fissile compound nucleus ^{239}Pu is formed through the reaction:

$$n + {}^{238}_{92}U \rightarrow {}^{239}_{92}U \xrightarrow{\beta-} {}^{239}_{93}Np \xrightarrow{\beta-} {}^{239}_{94}Pu \tag{1}$$

Thermal reactors operate in the thermal energy regime, using a moderator to slow the neutrons produced in the chain reaction, which are of the order of 1-2 MeV. Fast neutron-induced fission on ^{239}Pu produces a high enough rate of emitted neutrons allowing to maintain the chain reaction. This is known as the *uranium − plutonium fuel cycle*. One of the advantages of operating in this fast energy region is that the moderator can be removed from the reactor, reducing its size, which is suitable for space reduced requirements like in submarines. Mostly based on the uranium-plutonium fuel cycle are the so-called fast reactors and fast breeder reactors, those last receive their name because neutrons generated on the ^{239}Pu fission may react with the ^{238}U to

produce additional ^{239}Pu. The uranium and plutonium may be collected and later re-used as fuel.

One of the advantages of fast reactors is the reduction of the radiotoxicity in the nuclear waste through the transmutation of the actinides content. The isotopes transmuted into even-odd nuclei are fissile and its fission products are less radiotoxic and have reduced lifetimes than the initial isotopes, specially than the transuranic. The half-life of the fission products, of less than a few hundreds of years, is highly reduced with respect to the transuranic isotopes, with lifetimes of millions of years.

^{232}Th is more abundant in nature than uranium and it can be also used as combustible. The fuel cycle based on this isotope is called the *thorium fuel cycle* (see Fig. 2), where the ^{232}Th, which is fertile, decays into the fissile isotope ^{233}U through the reaction:

$$n + {}^{232}_{90}Th \rightarrow {}^{233}_{90}Th \xrightarrow{\beta-} {}^{233}_{91}Pa \xrightarrow{\beta-} {}^{233}_{92}U \tag{2}$$

Neutron-induced fission on ^{233}U produces a large rate of emitted neutrons, even for low energetic incident neutrons, enough to maintain the chain reaction. For this reason, the thorium fuel cycle may be the basis of thermal breeder reactors, being also suitable to use in fast reactors. In addition, this isotope presents chemical advantages with respect to the uranium such as its higher melting point and thermal conductivity.

The ^{234}U isotope, which is studied in this work, is formed in natural uranium ore, as an indirect decay product of ^{238}U, but it makes up only 0.005% of the raw uranium because its half-life of just $2.455{\cdot}10^5$ years is only about 1/18000 as long as that of ^{238}U. The primary path of production of ^{234}U via nuclear decay is as follows: ^{238}U nuclei emit an α particle to become ^{234}Th. Next, with a short half-life, a β particle is emitted from the ^{234}Th nuclei to become ^{234}Pa. Finally ^{234}Pa nuclei emit another β particle to become ^{234}U. Apart of its natural occurrence, it is formed in the thermonuclear reactions based on the thorium fuel cycle, where it can be formed in the production of the fissile ^{233}U isotope by neutron absorption.

The data used to study the fuel cycles and reactor concepts are obtained from the evaluated nuclear data libraries. Therefore, an improvement in the accuracy of the available experimental information will redound in the quality of the reactor simulations.

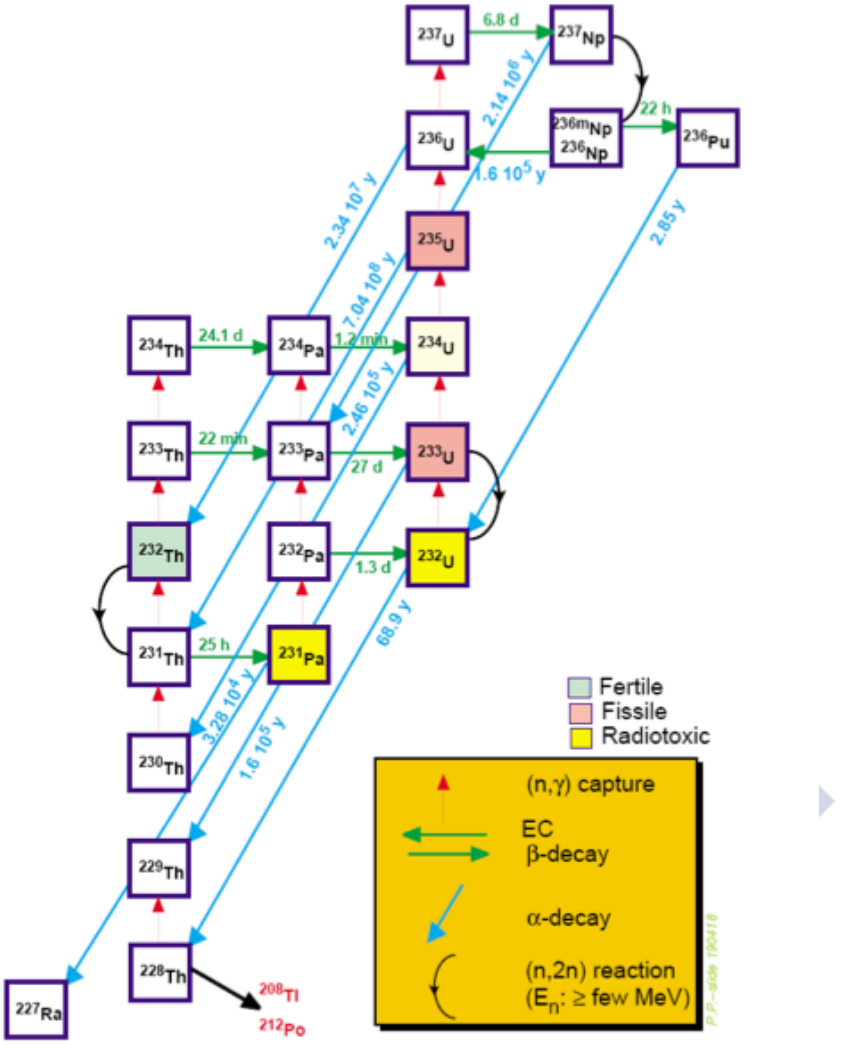

Figure 2: Illustration of the thorium cycle.

Nuclear databases

Nuclear data refers to the collection of relevant information relative to the nuclear reactions. They are available in two kinds of international databases: the Experimental nuclear reaction data (EXFOR) [4], which provides experimental results from absolute or relative measurements; and the evaluated nuclear data file libraries [5]. EXFOR is coordinated by NEA (Nuclear Energy Agency) and contains information from more than 21000 experiments

from the whole nuclear community around the world. The main evaluated data libraries comes from different national agencies, namely: ENDF (USA), JENDL (Japan), CENDL (China) and ROSFOND (Russia). More recently the NEA created a working group to develop a Joint Evaluated Fission and Fusion File library (JEFF) and there is a pilot project called CIELO [70] (Collaborative International Evaluated Library Organisation) with the goal of improving the understanding of neutron reactions on key isotopes in nuclear applications.

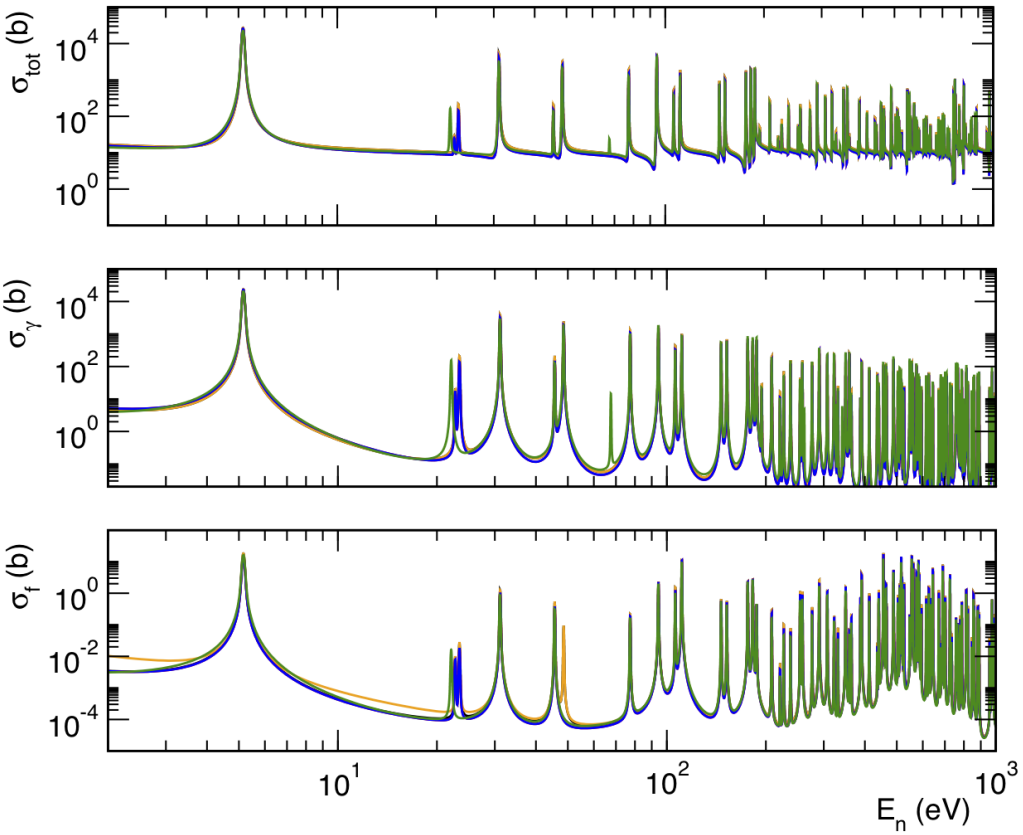

Figure 3: Evaluated cross section of some neutron-induced reactions in ^{234}U from ROSFOND-2010 (black line), CENDL-3.1 (yellow line), ENDF/B-VII.1 (red line), JEFF-3.2 (blue line) and JENDL-4.0 (green line).

The ^{234}U(n,f) cross section data given in the last version of the mentioned evaluations is shown in Fig. 3. Discrepancies can be found when comparing the ^{234}U(n,f) experimental cross sections in EXFOR and also between the last versions of the evaluated cross sections. An example of the evaluations are ENDF/B-VII.1 and JENDL-4.0, which are shifted in energy

and show differences in the evaluated number of resonances. In the Resolved Resonance Region (RRR), both evaluations are based on the ORELA[1] experimental data of James et al. [7], but JENDL-4.0 includes also the resonance parameters provided by Dridi [8] for the capture reaction, which were measured in n_TOF, and the fission cross section of Heyse et al. [9] for the 5.17 eV resonance, measured in GELINA[2]. In the Unresolved Resonance Region (URR), above 1.5 keV, the fission data of James et al. and the capture data of Pennington are used in ENDF/B-VII.1 whereas JENDL-4.0 uses the sets of experimental data mentioned in [4].

The recent n_TOF fission experimental data [1], which show discrepancies with the evaluations in the RR, are not included in the evaluations.

The nuclear fission

A general overview of the nuclear fission process is here introduced, being focused on the neutron-induced fission reactions on which this dissertation is centered.

After the discovery of the neutron by Chadwick (1932), Fermi et al. started to perform experiments irradiating nuclei with a neutron beam, leading to the discovery of the β radioactivity (1934) for which he obtained the Nobel Prize in 1938. This technique was then employed using a uranium target to synthesize transuranic elements and some new radioactive species were produced and identified using a chemical analysis. Some of them had chemical properties that were attributed to be radium or actinium. Hahn and Strassmann [10] repeated the experiments in 1939 using different techniques, leading to confirm these species as barium and lanthanum which were interpreted as fission fragments.

Lise Meitner and Otto Frisch (1939) [11] gave a qualitative explanation of the process based on the charged liquid drop model formerly proposed by George Gamow in 1928. They supposed that a uranium nucleus could vibrate induced by the capture of a neutron, and then divide into two daughter nuclei, this process was named *fission*.

In the same year, Bohr and Wheeler published the article *The Mechanism of Nuclear Fission* [12], which gives a comprehensive description of the process, based on the liquid-drop behaviour. The concept of fission barrier was included in this article. The authors make a detailed development of the neutron capture process, the fission induced by slow and fast neutrons, deuterons, and radiation. This constitutes the basis of the subsequent studies of fission.

[1] Oak Ridge Electron Linear Accelerator (USA).
[2] GEel LINear Accelerator (Belgium).

Frederic Joliot discovered that neutrons may produce a chain reaction and he explored, with Halban and Kowarski, the possibility to liberate energy from a neutron-induced fission reaction.

The fission barrier

The concept of fission barrier is explained in this section in order to better understand the behaviour of the fission cross section with the kinetic energy of the incident neutron.

The liquid drop model (LDM) proposed by G. Gamow in 1928, treats the nucleus macroscopically, in analogy to an homogeneous uniformly charged liquid drop. The nucleus shape in the drop model is related to the nuclear vibrations and rotations between the center of mass of the drop and an arbitrary point of its surface and its stability results in the equilibrium between the surface tension of the drop and the repulsive Coulomb force.

Bohr and Wheeler used this model to describe the fission process because it explained the variation of energy with the deformation. They defined the fissility parameter, which relates the Coulomb energy of a uniformly charged sphere with the deformation energy of the liquid drop. This parameter measures the probability of a nucleus to undergo fission: if the fissility parameter is high, then the Coulomb force dominates over the surface tension. The **fission barrier** concept appears when the deformation energy is calculated as a function of the elongation of the system along the axis defined by the final fission fragments.

When a neutron is captured by a nucleus becoming excited to an energy close to the height of the fission barrier, the compound nucleus may deform beyond the saddle-point, after which it undergoes fission. Also, when the excitation energy is lower than the maximum of the fission barrier, spontaneous fission may occur by tunneling through the barrier. This model could not offer an explanation for the deformation in the ground state, because it predicted spherical ground states for all stable nuclei, neither for the asymmetric fission, because a liquid drop is divided in two drops of equal masses. The shell structure of the nucleus had to be included in the model to correct the energy deformation. The nuclear shell model presents the excited energy levels of the nucleus by shells filled with nucleons. This is an independent particle model in which each single nucleon is governed by a nuclear potential generated by all the other nucleons. For the shake of simplicity, the nuclear potential was considered as a spherical central potential with a strong $spin - orbit$ contribution, the inclusion of which could give the proper separation of the subshells. It was observed that the nucleus with a specific numbers of protons and/or neutrons (magic numbers) (Z or N equal to 2, 8,

20, 28, 50, 82, 126, ...) were more bound than the neighbours. This fact was not predicted by the LDM but the shell model offered a suitable explanation as being attributed to closed shells of nucleons. The extension of the shell model to deformed nuclei was introduced by Nilsson, which proposed an elliptic central potential explaining why some nuclei adopt a deformed shape in the ground state. This model is a good approximation to treat independently the nucleons, but it is insufficient to describe the nucleus as a collective, for which the LDM was more suitable.

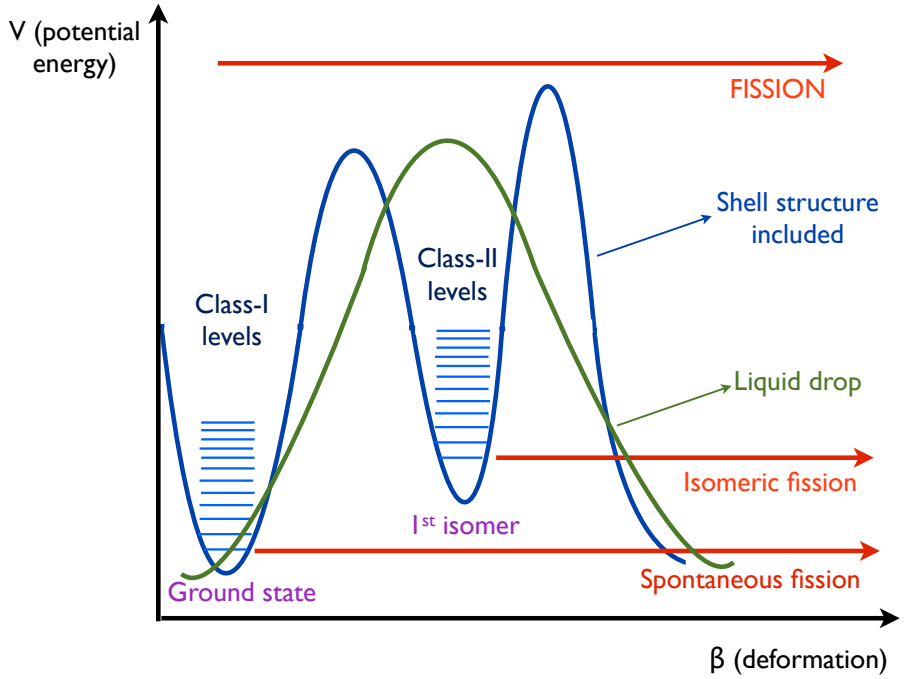

Figure 4: Schematic illustration of the LDM single-humped fission barrier and the double-humped fission barrier obtained by adding the shell structure to the LDM.

Strutinsky proposed a theory based on a procedure that combine the average energy of the liquid drop model with a realistic way of calculating fluctuations of the total energy due to single- particle effects. This theory was employed to correct the binding energy of the nucleus in its ground state. The shell correction was calculated for every deformed nuclear configuration which appear in the path to fission, this is in every point of the fission barrier obtained with the drop model, resulting in a corrected fission barrier that has into account the shell effects.

For the actinides, the inclusion of shell corrections leads to divide the

simple fission barrier from the LDM in two humps. This is known as the **double − humped fission barrier**. An example of the one-dimensional double-humped fission barrier of a typical actinide nucleus obtained with the Strutinsky procedure is shown in Fig. 4, and it is compared with the simple fission barrier obtained with the liquid drop model. The potential energy is usually plotted as a function of a parameter that should be understood as the elongation of the fissile system along the energetically most favorable path to fission.

The first minimum defines the energy levels of the deformed ground state and the second one corresponds to a more deformed state with higher energy defining a series of isomeric levels [3]. Therefore the fission barrier is populated by a number of energy levels, those above the maxima being called transition states, while those in the wells are called of Class I or II, indicating the well in which they are formed.

Most actinide nuclei are not spherical in their ground states, and obviously neither in their excited ones. In general, the excited nucleus decay to the ground state, via the (n,γ) reaction, or it pass through the first hump of the barrier to the second well. The population of states inside the second well offered a natural explanation for the fissioning isomers or shape isomers and the half-life of the states in the second well, being of the order of ns or μs for most actinides, have so a high probability of fissioning.

The existence of the second well is proved by the presence, in the fission cross section, of a structure of narrow resonances below the first-chance threshold, which was claimed to correspond to the Class-II levels. However it could not explain properly the structure of narrower resonances found in this threshold region for some thorium isotopes for instance in the compound nuclei ^{230}Th and ^{232}Th. If these resonances were produced in the second well, then it may be much above the first well than the theoretically predicted. In 1974, Möller and Nix [13] offered a more suitable explanation for these structures, splitting in two the second hump of the fission barrier, with a new narrow well populated by levels. This is the so-called **triple − humped fission barrier**. According to it, these resonances would be produced by the Class-III levels populating the third well (see Fig. 5).

[3]The term "isomer" refers to the property of those nuclei having excited levels with half-lives more than 100 to 1000 times the half-lives of the excited nuclear states that decay by a "prompt-gamma" cascade (ordinarily of the order of 10^{-12}s).

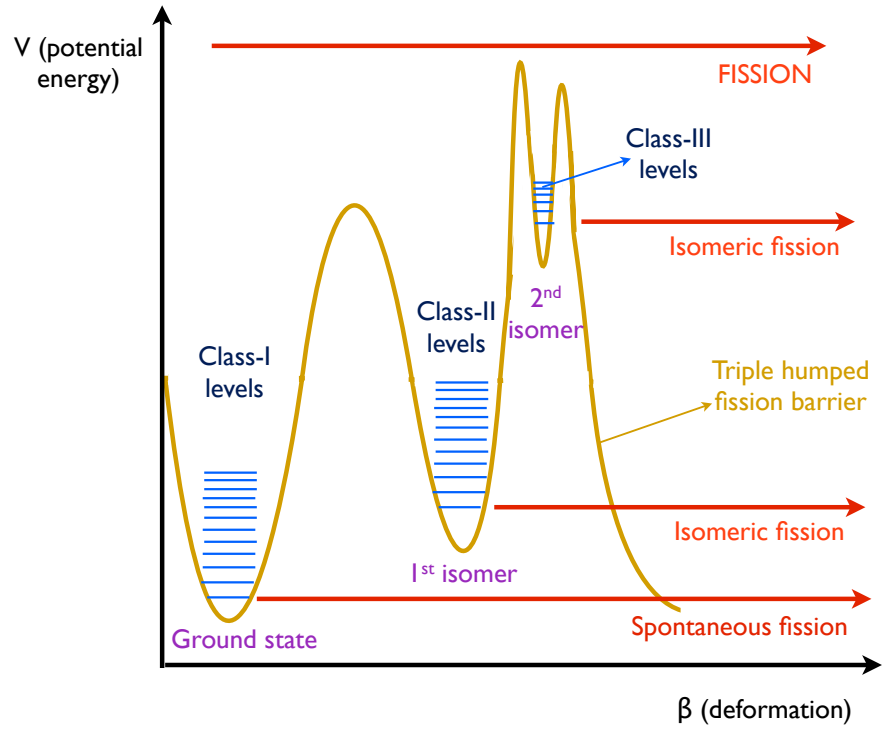

Figure 5: Schematic illustration of the triple-humped fission barrier.

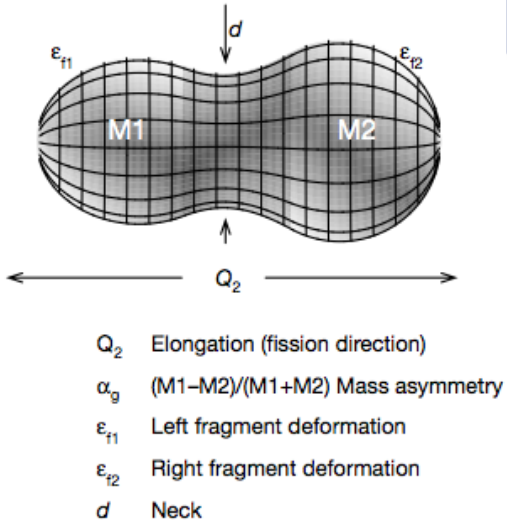

Figure 6: Five-dimensional shape parametrization used in [14]. The masses of the FF are denoted as M1 and M2. Figure from [14].

A more complete approach has been proposed in 2001 by Möller et al. [14], who performed a potential-energy model using five parameters to describe the nuclear deformation (see Fig. 6).

In this parametrization, the potential energy is described as a **multi − dimensional potential − energy surface**, and the transition of a nucleus from the ground state to the separated FF may occur through different paths in this landscape. These different paths are known as **fission modes**.

An example of the potential-energy surface for the compound nucleus ^{236}U is shown in Fig. 7 [15], where some saddle points are denoted by red crossed lines and the minima are indicated in dark blue. The final distribution of the FFs may be described at least through the presence of two fission modes, the first one corresponds to a symmetric mass distribution of the fission fragments (symmetric mode) and the second one to an asymmetric mass distribution (asymmetric mode) (see Fig. 8).

However, more fission modes are usually required to describe the nuclear deformation for actinides (see [16]). These are the superlong (SL) symmetric mode and the two standard asymmetric modes: the standard 1 (S1) and the standard 2 (S2). The superlong mode receives its name due to its large deformation. Another commonly used fission mode is the superasymmetric, although its contribution is lower.

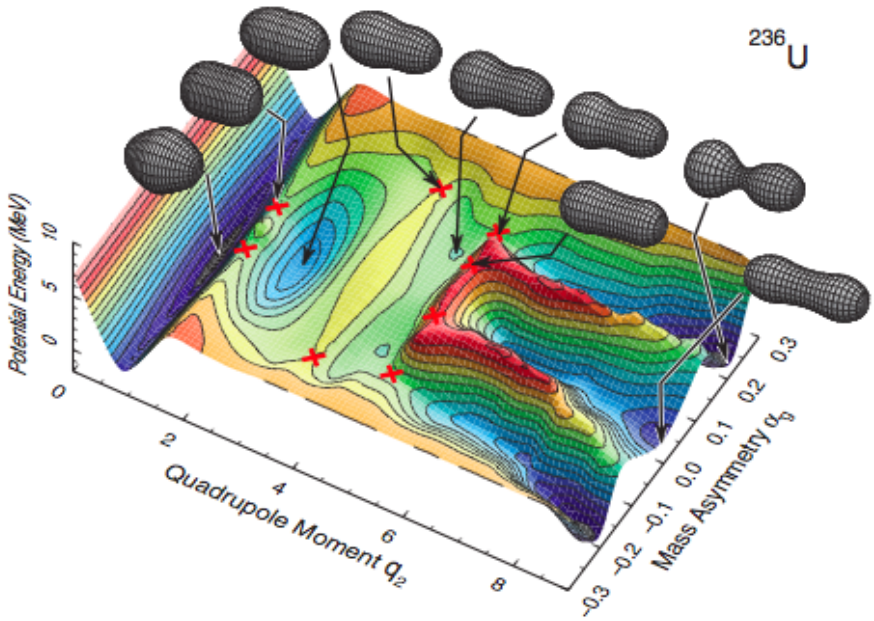

Figure 7: Two-dimensional potential energy surface for ^{236}U. Figure from [15].

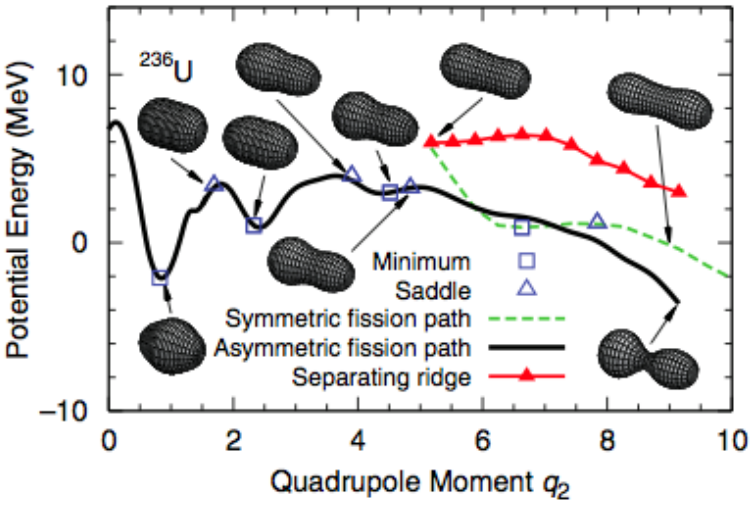

Figure 8: Potential energy along the two fission paths for ^{236}U [15]. The symmetric mode is indicated by the solid black line and the asymmetric mode by the dashed green line. Figure from [15].

Neutron-induced fission

When a neutron collides with a nucleus with a given mass number A, it may happen that it is captured, then a compound nucleus with a higher mass number, $A^* = A + 1$, is formed in an excited state, and there are several modes of decay that are independent of the formation mode of the compound nucleus. These modes of decay compete between them in terms of probability, which is related with their half-lives.

The probability for a given reaction to occur is measured through the cross section, whose unit is the barn ($1b = 10^{-24} cm^2$). It depends on the nature of both the target and the projectile and the kinetic energy of the incident particle. The time-of-flight technique, which will be explained in Chapter 1, offers the possibility to investigate the dependence of cross sections for neutron-induced reactions, expressed as a function of the incident neutron energy, that strongly depends on the relation between the fission barrier and the neutron binding energy.

When a neutron is absorbed by an **even − even** target, such as ^{234}U, an even-odd compound nucleus is formed in an excited state with a neutron binding energy usually lower than the fission barrier. Then, if the sum of the binding energy and the kinetic energy of the incident neutron is below the first maximum of the barrier, it is only possible to undergo fission by tunneling and, therefore, its fission cross section is low. If fission occurs in this region

by tunneling the barrier, some class-I, class-II or class-III resonances are observed in the cross section, depending on which well is placed the energy level through which the barrier is penetrated. The first well corresponds to the equilibrium shape of the nuclei containing the class-I or normal levels. The second well, or first isomer, contains the super-deformed states, also called class-II. The hyper-deformed states, or class-III, are accumulated in the third well, corresponding to the second isomer. As the height of the wells increases with the deformation, the class-I resonances are initially observed at lower energy, then the class-II start to appear and later the class-III. The fission cross section remains low up to certain energy that corresponds to the first maximum of the barrier, also known as the fission threshold, above which, fission becomes more probable, increasing rapidly its cross section.

Above a few hundred eV, for actinides, different fission processes open their thresholds, with increasing energy. The first-chance threshold is found near the MeV region for even-even target nuclei, corresponding to the first maximum of their fission barriers. One of the subjects of this thesis is dedicated to the study of the ^{234}U neutron-induced fission cross section, that is an even-even target nucleus. Along this thesis this energy region will be termed the first-chance region or, shortly, the threshold region. Several structures may appear below this first-chance fission threshold corresponding to vibrational resonances in the fission barrier wells.

When the target is **even – odd**, such as ^{235}U, the situation is normally the opposite and the neutron binding energy of the compound nucleus is, in general, higher than the fission barrier. Its fission cross section is high with an 1/v trend with resonances, being v the velocity of the neutron.

In both cases, at a certain energy corresponding to the sum of the height of the barrier and the neutron binding energy, a neutron may be emitted from the compound nucleus before fission. This is known as the second-chance, corresponding to the (n,nf) reaction, and opens its threshold around 6-7 MeV, that is to say, some 5 MeV above the first-chance threshold (the neutron binding energy is 5.267 MeV for ^{234}U and 6.545 MeV for ^{235}U [71]). After the second-chance a plateau is observed in the cross section where the (n,nf) channel compete with the (n,f) channel, decreasing slightly its fission cross section, it is followed by the third chance at tens of MeV, when the incident neutron energy is enough to remove two neutrons from the compound nucleus before fission, also followed by a plateau where the new opened channel (n,2nf) starts to compete with the (n,f) and (n,nf) channels, and so on. It is worth to mention that other fission chances may appear as the incident neutron energy increases, including the (n,pf), (n,αf) channels, and also other spallation processes, and therefore the step-like structure observed in the cross section disappears.

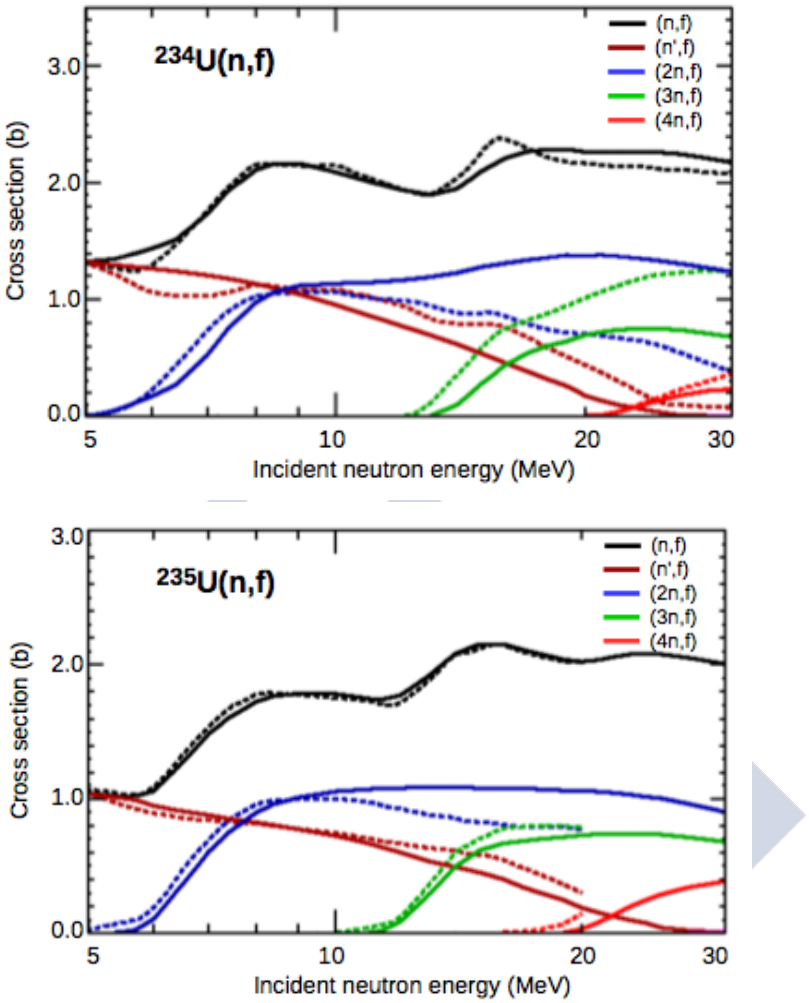

Figure 9: Total fission and partial fission chances cross sections obtained by Sin et al. (solid lines) compared with the ENDF/B-VII.1 evaluation (dashed lines). Figure from [17].

The most relevant information about the fission barrier is obtained from these resonant structures. Their positions provide the energies of the levels and the width of the deformed wells. Their magnitudes provide information of the energies of the transition states, the strengths of the potential and their spin and parity [17].

The fission barrier parameters for uranium isotopes were studied in numerous works, the most recent of which has been published in January of 2017 by Sin et al. [17]. The EMPIRE code with triple-humped fission barriers was used in this work to describe accurate and consistently the experimen-

tal fission cross sections, and the competition between the different reaction channels, for light uranium isotopes from ^{232}U to ^{237}U, in the energy range from 10 keV up to 30 MeV. The partial fission chances obtained by Sin et al. for the ^{234}U(n,f) and the ^{235}U(n,f) cross sections are shown in Fig. 9, from which the contributions of the fission chances to the total fission cross section were calculated.

In Table 1, the main barrier parameters are summarised for ^{234}U and ^{235}U target nuclei (^{235}U and ^{236}U compound nuclei).

In the work of Sin et al., the fission barrier parameters after the emission of a number of neutrons by the compound nucleus was derived from the analysis of the fissioning system cross section, for instance, the parameters of the ^{235}U(n,nf) reaction were derived from the analysis of the ^{234}U(n,f) experimental cross section.

Compound nucleus	V_{h_1}	ω_{h_1}	V_{h_2}	ω_{h_2}	V_{h_3}	ω_{h_3}	S_n
^{235}U	4.80	0.6	6.10	1.45	5.78	1.45	5.29
^{236}U	4.60	0.6	5.90	1.45	5.64	1.45	6.54

Table 1: Fission barrier parameters in MeV obtained by Sin et al. [17].

Fission Fragment Angular Distribution

Non isotropic angular distribution of fission fragments was observed for first time in 1952, when, studying the photofission of ^{232}Th (see [65,66]), fission fragments emitted preferentially at 90° with respect to the gamma beam direction were found. Later experiments found similar results in neutron-induced fission reactions [67,68,69].

The standard theory is developed in [20] being based on the model of axially symmetric transition states at the saddle point of the fissioning nucleus, that is supposed to be a symmetrical spinning top (for example a rigid body with two equal moments of inertia and different from the third one). Its fundamentals are summarised in Appendix C.

It must be noticed that, in the unresolved resonance energy region, the FFAD is isotropic, becoming anisotropic when the quantum numbers of the fissioning compound nucleus are well defined, fulfilling specific constraints, as explained in Appendix C. This is the case for the actinide isotopes at excitation energies close to its fission threshold, as it will be discussed in Chapter 2. It is worth to mention here that, for neutron energies above

the second chance threshold, several fission channels are open, having each channel its own fission modes, defined by the potential-energy surface as it was forementioned. Therefore, what one can observe in a (n,f) experiment at these energies is the addition of the different possible angular distributions.

Thesis structure:

Besides this Introduction, this memory is divided in four chapters, followed by the main conclusions drawn from this work.

- Chapter 1 is dedicated to the description of the time-of-flight technique, used in this work to calculate the neutron-induced fission cross section as a function of the incident neutron kinetic energy. The facility and the detectors used in this experiment will be introduced as well as the development of the experimental data analysis from the signals measured in the detectors to the final identification of the fission events and the position of the FFs in the detector.

- Chapter 2 presents the angular distributions of the FFs obtained in this work for the ^{234}U and ^{235}U targets. The results of the FFAD have been obtained for each energy interval, being compared with previous measurements in the energy regions of main interest. The anisotropy parameter has been calculated, completing the information available in EXFOR and extending the energy range up to 300 MeV, above the 15 MeV provided in previous measurements for the ^{234}U target and the 200 MeV provided for the ^{235}U. The calculation of the detection efficiency is included in this chapter, taking into account the FFAD results above 100 keV.

- Chapter 3 reports the methods used to calculate the ^{234}U(n,f) and ^{235}U(n,f) cross sections below 100 keV, where the angular distribution of the FFs is isotropic and, therefore, does not affect the detection efficiency calculation. The results obtained for both isotopes are compared with previous experimental measurements and with the main evaluations [5], being further discussed.

- Chapter 4 deals with the calculation of the ^{234}U(n,f) cross section above 100 keV up to 1 GeV. The detection efficiency, taking into account the

effect due to the anisotropic emission of the FFs, is used to correct the fission cross sections in this energy region. The obtained results are discussed and compared with the EXFOR data and with the evaluated libraries.

The conclusions are summarissed at the end of this document, being followed by the Appendices.

USC
UNIVERSIDADE
DE SANTIAGO
DE COMPOSTELA

Chapter 1

The Time-of-Flight technique

This chapter is dedicated to the description of the measurement technique used in this work: the neutron beam source, the long flight path to the experimental area, the detectors and the data acquisition system are described in the following sections.

1.1 The n_TOF facility at CERN

All around the world several facilities are dedicated to the cross sections measurements of neutron-induced reactions using the time-of-flight (ToF) technique in a wide energy spectrum. Besides n_TOF facility at CERN in Switzerland, GELINA at JRC-IRMM in Belgium, LANSCE at LANL in USA, nELBE at Helmholtz Zentrum Dresden Rossendorf in Germany, and MLF at J-PARC in Japan, have comparable performances, being the CERN-n_TOF outstanding due to the high energy resolution and to the extremely low background achieved. The n_TOF facility started in operation in 2001 producing an intense neutron flux by spallation reaction of a 20 GeV/c proton beam in a massive lead target. Two neutron beam lines are operating at present in n_TOF: the Experimental Area 1 (EAR1), which is an horizontal line of approximately 185 m long operative since 2001, and the Experimental Area 2 (EAR2), a vertical line of around 20 m long working since 2014. A larger path length produces a larger time of flight, improving the energy resolution, as it was explained in the previous section, at the cost of a lower neutron flux intensity. The higher energy resolution is obtained in the EAR1 whereas the higher neutron flux is achieved in the EAR2. The experiment of the ^{234}U(n,f) reaction leading to this thesis work has been performed at the neutron time-of-flight (n_TOF) facility at CERN using a setup based on parallel plate avalanche counters (PPACs) placed at the EAR1.

The n_TOF measurements are classified in three time frames: the Phase-I (2001-2004), the Phase-II (2009-2012) and the Phase-III (from 2014).

The spallation target was changed in the Phase-II by a cylindrical shaped of (l=60, r=20) cm with a new cooling circuit of water separated from a exchangeable moderator system which allows to choose between distilated water or borated water to moderate the neutrons. The Phase-III started after the construction of the EAR2 together with a new data acquisition (DAQ) system with a better amplitude resolution and a larger on-board memory.

The data presented in this work were taken in 2012 in the EAR1 during the Phase-II. In the following subsections the main parts of the CERN-n_TOF facility will be described in detail.

1.1.1 The neutron production principle

The short lifetime of neutrons does not allow to find them available free in the nature and they have to be produced by nuclear reactions. Several types of reactions can be used to produce monoenergetic neutrons. These neutrons are generated at energies of typically several MeV, an so, in order to have a wider spectrum, they must be slowed down, reaching energies below the eV level in moderators containing light nuclides. To have an even wider spectrum going above these MeV energies, one must turn to spallation reactions. Spallation is a nuclear reaction induced by a high energetic light particle, which collides on a heavy target, ejecting one or more nucleon clusters and leaving the residual nuclei in the target in an excited state. These excited nuclei decay to the ground state by particles evaporation. When the excitation energy is larger than the binding energy of the "last neutron" in the compound nucleus, a neutron may be emitted. The emitted particles are propagated inside the target and could induce other spallation reactions. A heavy nucleus target, with a rich amount of neutrons, is preferred for this purpose, this is the reason why the spallation target used in n_TOF is made of lead.

The spallation reaction produced in n_TOF is induced by an intense proton beam. The proton source used at CERN is a bottle of hydrogen gas which electrons are removed using an electric field being the protons injected in the linear accelerator Linac 2 where they are accelerated in bunches of 50 MeV.

Afterwards, the proton bunch pass through the proton synchrotron Booster (PSB) reaching a kinetic energy of 1.4 GeV and being then injected in the Proton Synchrotron (PS).

The proton beam coming from the PSB is accelerated on the PS up to 25

GeV. Afterwards, it is carried up through a transfer line to the lead spallation target, where neutrons are produced and directed to the experimental area through a second transfer line.

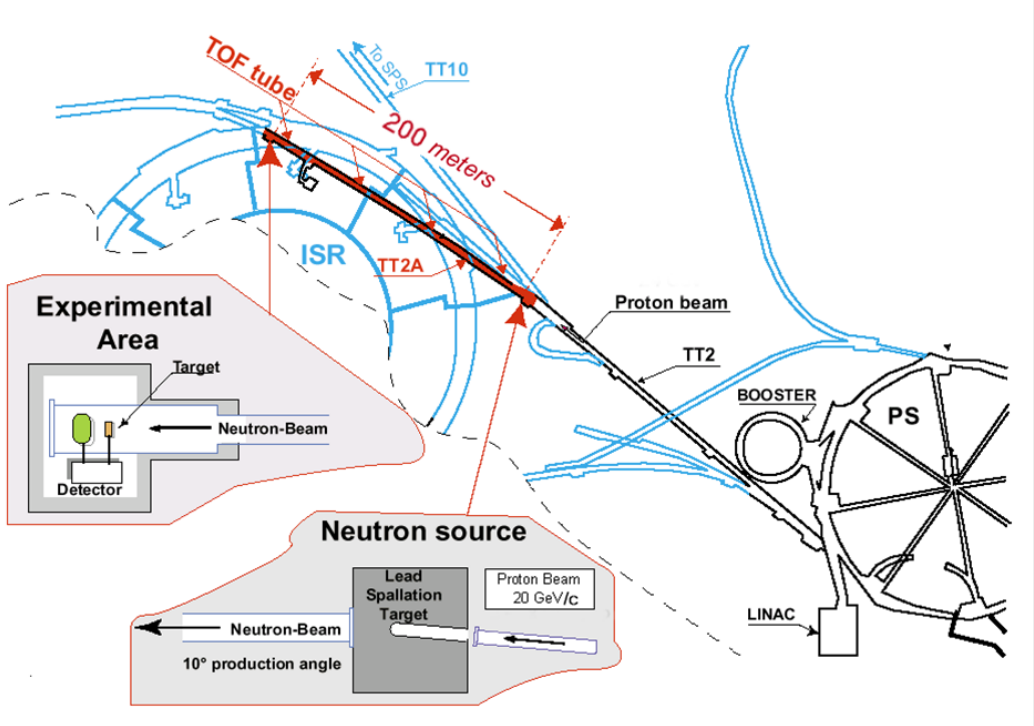

Figure 1.1: Schematic view of the n_TOF facility.

Depending on the proton bunch intensity, two operation modes are possible in n_TOF, the *dedicate* and the *parasitic* mode. At the *dedicate* mode it can reaches the highest bunch intensity, 7 x 10^{12} protons/bunch with a Gaussian shape of 7ns. At the *parasitic* mode, the bunch intensity is about 3 to 4 x 10^{12} protons/bunch with the same bunch length than the dedicated mode. In this last case, the n_TOF bunch is accelerated with a lower intensity bunch extracted to the East Hall experimental areas.

A maximum of 10 bunches per PS supercycle of the order of 30 s is allowed to avoid the lead target to overheat.

The proton beam impinges the spallation target with an incident angle of 10° in order to remove from the neutron beam the high number of secondary spallation products which are emitted in the direction of the incident proton beam, such as high-energetic charged particles and γ rays.

The n_TOF facility is illustrated in Fig. 1.1.

1.1.2 The lead spallation target

The natural lead has a high atomic mass, a large neutron elastic scattering and a high transparence of neutrons with lower energy than 1 MeV. That is the reason by which it produces a large spallation rate for a weak activation rate.

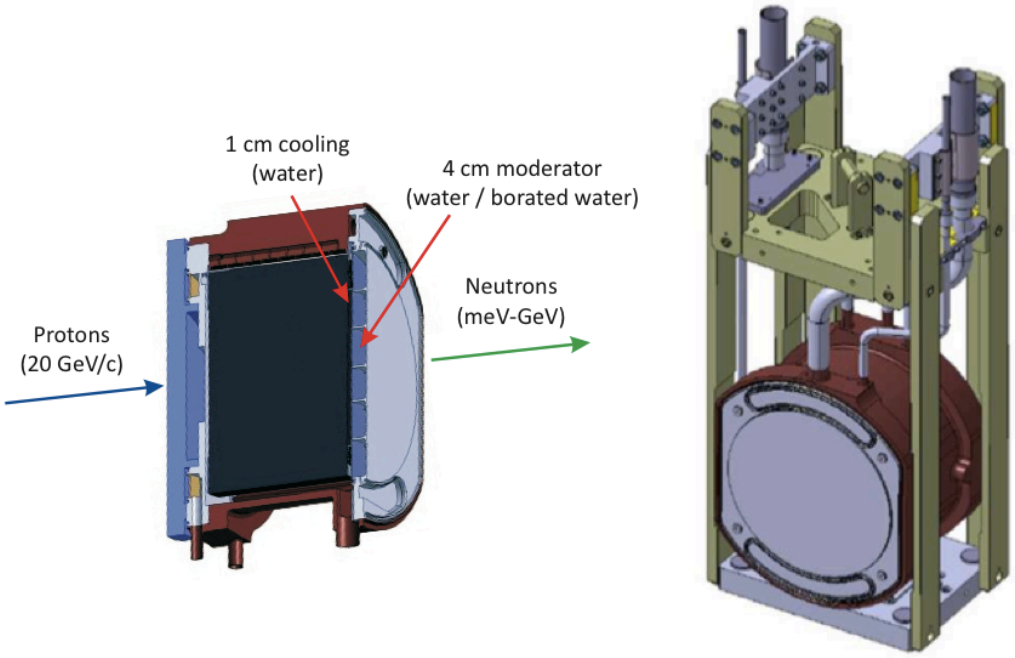

Figure 1.2: The lead target.

As it was mentioned before, the lead target used since the beginning of the n_TOF phase II consists of a cylindrical block of 60 cm in diameter and 40 cm in length, surrounded and cooled by a 1 cm thick water flow, it is represented in Fig. 1.2.

Its dimension and geometry were optimized to achieve a compromise between the neutron flux intensity and the neutron energy resolution.

The water serves as a cooling system by dissipating the heat generated in the spallation process. An additional 4 cm container filled with borated water acts as a moderator to produce a wide neutron spectrum from thermal to GeV. Before 2012, water was used as a moderator for fission measurements but it was changed to borated water to reduce the 2.2 MeV γ background produced by the radioactive capture on hydrogen through the ^{10}B(n,α) reaction in which most of the thermal neutrons are absorbed.

An aluminum window is located at the entrance of the neutron beam line.

1.1.3 n_TOF neutron line

The neutrons produced by spallation travel inside a stainless steel vacuum tube of 182.5 m divided in 3 sections with a progressively reduced diameter before arriving to the experimental area, as it is shown in Fig. 1.3.

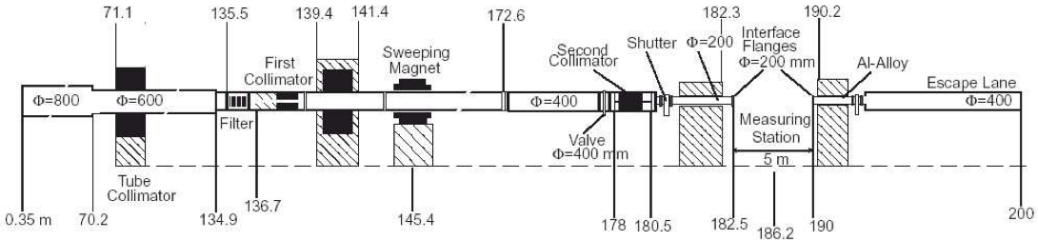

Figure 1.3: The TOF tube.

The first and the second section measure 70 m with Ø = 80 cm and 68.4 m with Ø = 60 cm respectively. Several optic systems are located in the third section, which measures 61.4 m and Ø = 40 cm.

The first collimator, called the *Source Screening Collimator* (*SSC*), is located at 136.7 m of the target and is made of 1 m of iron and 1 m of concrete. Then, at 145.4 m, a dipolar magnet with a length of 2 m is placed to sweep charged particles away from the neutron beam with an iron shielding downstream which used to reduce the muon background. The second collimator is called the *Beam Shaping Collimator* (*BSC*) and is placed at 178 m of the target. Its diameter can vary depending on the size of the sample: a Ø = 1.8 cm is used for capture measurements while a Ø = 8 cm is used for fission measurements. Being so close to the experimental area, it constitutes an important neutron background source. To minimize this background, it is divided in three sections made of 50 cm of 5 % borated polyethylene, 125 cm of iron and 75 cm of 5 % borated polyethylene. The borated polyethylene is used to absorb scattered neutrons.

1.1.4 The Experimental Area 1 (EAR1)

The EAR1 is separated from the second collimator by a concrete wall located at 182.5 m from the spallation target and it is extended up to 190 m. The neutron beam monitors and neutron-induced reaction detectors are placed in this zone.

The dimension of the experimental area allows to perform more than one measurements simultaneously in order to optimize the available beam time. The PPACs fission detector chamber was measuring in parallel with a Micromegas (MGAS) chamber.

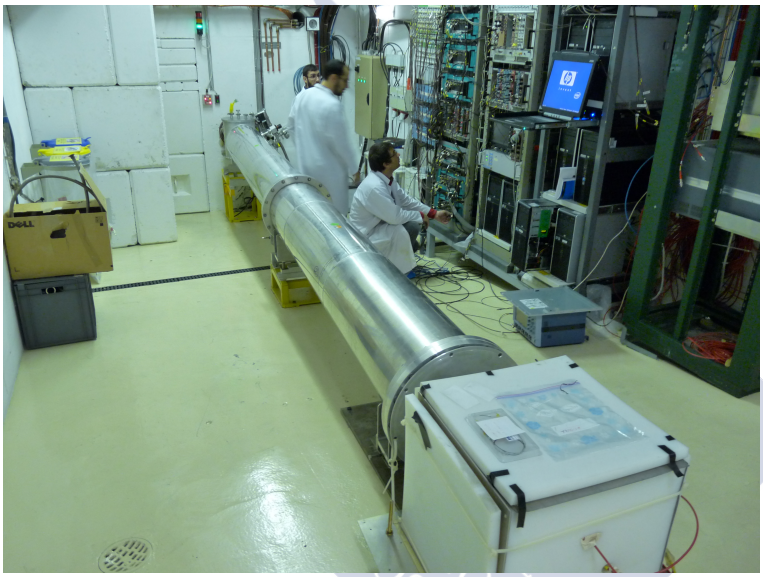

Figure 1.4: The TOF tube end and the poliethylene beam dump.

After the experimental area, the TOF tube continues along the escape line with a beam dump in the end which consists in a polyethylene block with a cadmium cover to reduce the neutron back-scattering to the experimental area (see Fig. 1.4). Three BF3 counters are placed inside the beam dump to monitor the neutron flux [26]. In this area the DAQ and the power supply are placed.

1.2 Neutron beam characterisation

The neutron beam is characterized by a white spectrum covering the energy range from thermal to 1 GeV. A detailed characterization of the neutron beam requires the study of the neutron flux, the beam profile and the energy resolution.

1.2.1 The neutron flux and the beam profile

The n_TOF **neutron flux** has been determined in [25] using three nuclear reactions which cross sections are classified as standards in some energy regions [24] (see Appendix A).

The detectors used to measure these reactions are: a thin-windowed silicon detectors (SiMon) used to measure the ^{6}Li(n,α)t, a MicroMegas (MGAS) detector used to measure the ^{10}B(n,α)^{7}Li and three detectors to measure the ^{235}U(n,f): a MicroMegas detector, an ionization chamber from Physikalisch-Technische Bundesanstalt (PTB) and the Parallel Plate Avalanche Counters (PPACs). The detectors used to obtain the neutron flux for each energy range are summarised in Table 1.1.

Detector	Reaction	Energy range
SiMon	^{6}Li(n,α)t	30 meV to 100 keV
MGAS	^{10}B(n,α)^{7}Li	30 meV to 100 keV
	^{235}U(n,f)	100 keV to 1 MeV
PTB	^{235}U(n,f)	30 meV to 10 MeV
PPAC	^{235}U(n,f)	10 MeV to 1 GeV

Table 1.1: Reactions used for the neutron flux characterization.

Although the ^{6}Li(n,α)t and the ^{10}B(n,α)^{7}Li reactions are considered as standards in the neutron energy range from 0.0253 eV to 1 MeV, both reactions were used to extract the neutron flux up to 100 keV because, above such energy it was not reliable due to angular anisotropy effects. In order to calculate the neutron flux in the whole energy range from thermal up to 1 GeV, the ^{235}U(n,f) had to be considered above 100 keV, because, although it is a standard at 0.0253 eV and from 150 keV to 200 MeV, it is well-known in the energy interval from 100 keV to 150 keV. Above 10 MeV

it was calculated using the JENDL/HE-2007 evaluation, which was the only one providing cross section values up to such energy.

Some discrepancies were found in [25] between the experimental result and the simulation of the neutron flux in the energy interval between 10 keV and 30 keV which have motivated a new measurement of the neutron flux, and, also above 10 MeV up to 1 GeV.

During the Phase-II some modifications in the moderator system between the different campaigns have dealt to differences between the corresponding measured flux. The moderator used in 2009 for all reactions was ordinary water. In 2010 and 2011, for fission measurements, the moderator continued being normal water but it was changed to borated water for the other measurements. In order to allow the change of moderator material which was required in each case, the circuit was modified through an exchangeable container.

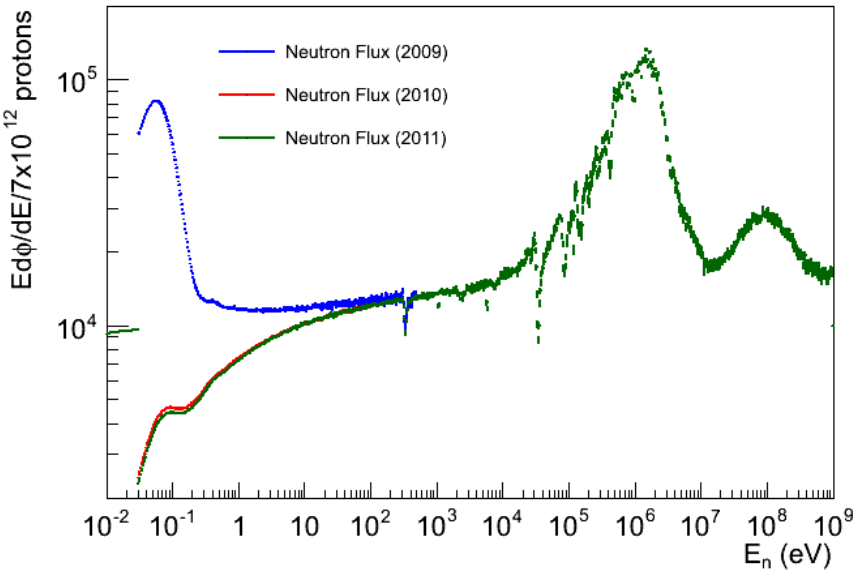

Figure 1.5: The n_TOF flux measured in [25] during the Phase-II campaigns.

In 2012 borated water was used as a moderator for all the reactions. The flux obtained using water (2009) or borated water (2010, 2011) is shown in Fig. 1.5. It is expressed as the total number of measured counts divided by the total number of incident protons and multiplied by the pulse intensity in the dedicated mode. The main difference in the flux obtained with borated water with respect to the one obtained using normal water is the reduction of the thermal peak. Above a few keV the flux is independent on the type

of moderator used. The differences observed below a few hundreds of eV between the flux measured with borated water for different campaigns are due to the ^{10}B concentration used in each case, which slightly changed when the water container was empty and refilled.

The **beam profile** was characterized in the Phase-II experiments with a X-Y MicroMegas (XYMG) detector. This offered the advantage in the direct measurement of the X-Y spatial position of the neutrons towards the Micromegas detector used in the Phase-I which provided only one-dimensional information being required different positions of the detector in order to have the 2D spatial information. The reactions measured in each case are the ^{6}Li(n,α)t in the Phase-I and the ^{10}B(n,α)^{7}Li in the Phase-II. The two-dimensional beam profile from [72] is shown in Fig. 1.6.

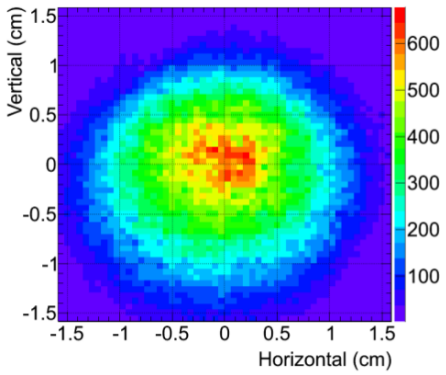

Figure 1.6: Two-dimensional plot of the n_TOF beam profile obtained for a dedicated pulse at thermal energy in the Phase-II (figure from [72]).

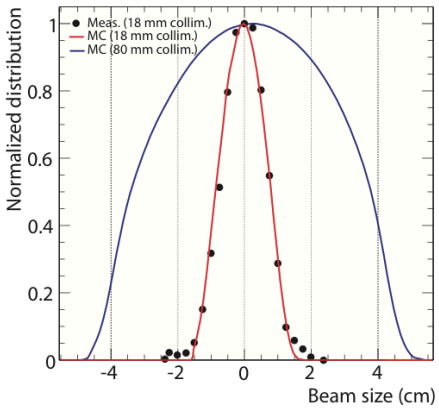

Figure 1.7: Beam profile for the two possible diameters of the *Beam Shaping Collimator* (*BSC*): Ø = 1.8 cm and Ø = 8 cm (figure from [27]).

The beam profile depends on the diameter of the collimator. As two sizes of collimator are used for capture and fission measurements, the beam profile obtained in both cases is different, as shown in Fig. 1.7.

1.2.2 The neutron kinetic energy of a white source

In a neutron source having a white spectrum, the relativistic kinetic energy, E_n, of neutrons can be expressed as:

$$E_n = m_n c^2(\gamma - 1) \tag{1.1}$$

where m_n is the mass of the neutron at rest, c is the velocity of light in vacuum and γ is the Lorentz factor given by:

$$\gamma = \frac{1}{\sqrt{1-(v/c)^2}} \tag{1.2}$$

As the velocity of light in vacuum is an universal constant ($c = 2.9979 \cdot 10^8$ m/s) and the neutron mass is well known ($m = 939.56$ MeV/c^2), the E_n precision relays on the determination of the Lorentz factor, where the neutron velocity, $v_n = L/t$, is determined by knowing both, t which is the time needed by the neutron to travel from the spallation target to the detector and L, which is the path length.

For E_n values below 1 MeV, as the Lorentz factor is close to one ($\gamma \approx 1$) one can take the Taylor expansion for the reciprocal square root, keeping only the first two terms, that leads to the more practical classical expression:

$$E_n = \frac{1}{2} m_n v^2 \tag{1.3}$$

Therefore, the relative energy resolution of a ToF facility is expressed as:

$$\frac{\Delta E_n}{E_n} = 2\sqrt{\left(\frac{\Delta t}{t}\right)^2 + \left(\frac{\Delta L}{L}\right)^2} \tag{1.4}$$

The energy resolution depends on the uncertainty on the measurement of the path length and on the time resolution of: the proton beam hitting the lead target (where the spallation reactions occur), the detector and electronics and, the transport of the neutrons in the spallation target and in the detector or target. From these components, the main contribution to the uncertainty in the determination of the effective path length has two components: one is the geometrical path length and the other the moderation distance ($\Delta\lambda$) of the neutrons inside the spallation target and the moderator, that is strongly dependent on the kinetic energy. The larger uncertainty

on time is due to the 7 ns width of the proton pulse, which becomes more significant above a few MeV (see Fig. 1.8).

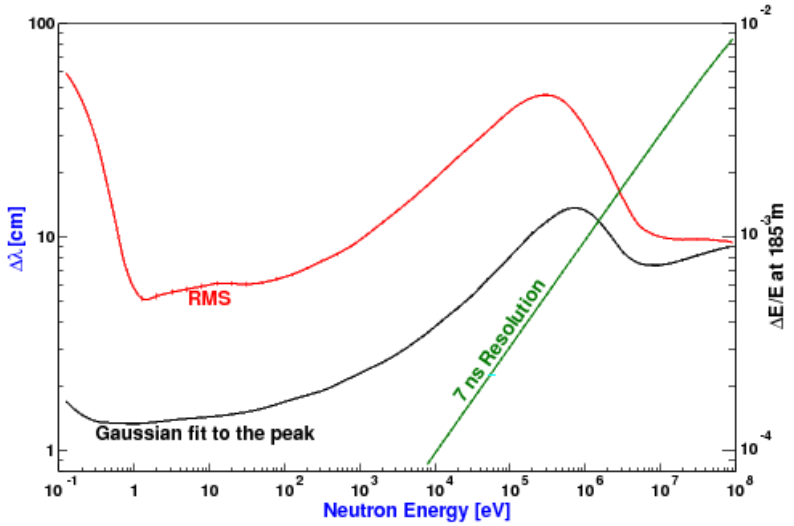

Figure 1.8: Resolution function obtained in [28] with a Monte Carlo simulation for a path length of 185 m for the Phase I lead target (figure from [28]). At low neutron energies the resolution function is dominated by the moderation length and above 1 MeV by the 7 ns proton pulse width.

1.3 Fission detection setup

Different types of gas detectors have been extensively used to measure fission cross sections in n_TOF. The Parallel Plate Avalanche Counters (PPACs) show the ability of detecting both FF in coincidence, with an intrinsic efficiency almost one. This coincidence detection and the signal amplitude permit a very good discrimination of FFs and alpha particles from spontaneous decays of radioactive samples. Besides this, their insensitivity to gammas and their very short dead time make them very well suited to efficiently detect fission events at neutron energies up to 1 GeV [29,3,2].

In this work the PPAC detectors have been used to measure both, the FFAD and the cross sections of the actinides: ^{234}U and ^{235}U.

PPAC detectors belong to the gaseous detectors type which operate after the application of an electric field between two parallel plates immersed in a gas enclosure at low pressure. The type of gas, its pressure and the electric

field in between the plate electrodes, play an important role when detecting the charged particles moving inside the detector active volume.

The highly ionising FF creates an specific number of electrons and positive ions first when passing through the electrode plates and also in flight by the gas. These electrons and ions are drifted to the anode and the cathode respectively by the electric field. During such drift, both, the electrons and ions, are accelerated becoming able to create new pairs of electrons and ions in what is called an avalanche. Therefore, creating a rising swarm of electrons that drifts to the anode, and an opposite swarm of ions, each with a characteristic velocity given by the type of gas, the pressure and the field. The electron drift is much faster than that of the ions, because the mobility of the ions in a gas is well below 1% of that of the electrons, and so the signal induced in the anode is faster and bigger than the one produced by the ion swarm. In proportional gas counters the avalanche is allowed to grow up to its maximum, but in PPAC detectors it is self-extinguished due to the short path and the well controlled electric field. This leads to restricted gain and proportionality but it produces a very fast signal and avoid self-sparking at its turn.

Parallel Plate Avalanche Counters are highly used for applications in which having a fast timing information and therefore a good time resolution is more important than obtaining a good resolution in energy. This detector has been designed to provide in addition two dimensional-information of the detection position through the use of segmented cathodes.

1.3.1 n_TOF detectors description

The PPACs used in this experiment were developed at the IPN[1] d'Orsay (France). They consist of three parallel electrodes made of foils, one central anode and two cathodes with area of 20 x 20 cm^2, separated by 3.2 mm gaps to obtain a fast timing response reducing the time that takes a particle passing perpendicularly through them.

The gaps have been filled with octafluoropropane (C_3F_8), which has a fast signal rise time and large ion energy loss, presenting the advantage of being a non-flammable gas, conversely to the commonly used isobutane (C_4H_10). The gas is maintained clean of any oxygen or water contamination by means of an external gas circulation of 50 l/h.

Low pressure conditions are needed to get the desired gain at a reduced electric field of 300 V/cm · mbar between the electrodes, hence the gas pressure has been regulated at 4 mbar. In order to have a compromise between

[1]Institut de Physique Nucléaire.

the signals amplification and the detector stability, voltages of around 500 V were applied to the anodes while the cathodes have been kept tied to ground. The electrons induce a big signal in the anode in a few ns while a feeble signal of the order of μs is induced by the ions. The signal shape has, therefore, two components, a fast-rising component due to the electrons collection and a slow component caused by the positive ions motion, but only the fast part is considered being the slow part suppressed by signal differentiation.

The detector scheme is represented in Fig. 1.9.

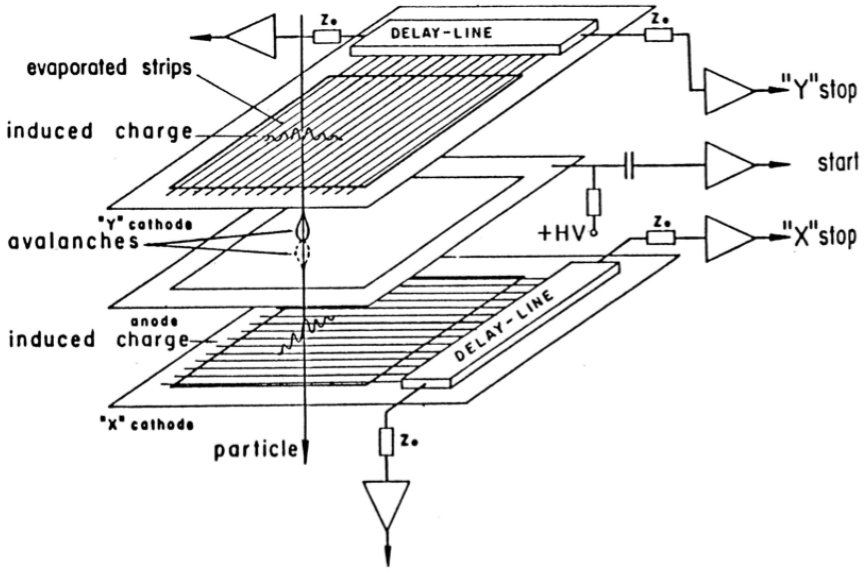

Figure 1.9: Scheme representing the principle of a particle detection in a PPAC.

The anode is composed by a 1.5 μm aluminized Mylar foil aluminized on both sides and glued onto a frame made of a type of epoxy resin covered with a thin copper layer to shield the detector against electromagnetic noise. In order to prevent copper oxidation, it is plated with gold. The good time resolution (∼500 ps) is achieved by the use of the signal generated in the anodes.

The cathodes are used to provide information of the fission fragment detection position. They are made of Mylar foils with parallel aluminum strips separated 2 mm between them and set on their full surface; every strip is connected to a delay line (DL) made of a copper wire rolled on a plastic stick which is read by two adapted preamplifiers placed at both ends. The aluminum strips are situated in perpendicular directions in a cathode respect

to the other in order to give a two dimensional position (X,Y) of the fission fragment hit. Some cathode pictures are shown in Fig. 1.10.

Figure 1.10: Photographs of one cathode with the delay line at the left side before (left top) and after the strips assembly (right top). Detailed view of the delay line connected to a preamplifier (left bottom) and picture of the location of detectors and targets inside the chamber (right bottom).

The reaction chamber

In order to maintain the detectors at low pressure conditions, all the system is contained in a fission chamber (see Fig. 1.11). The fission chamber consist in a stainless steel cylindrical container with dimensions of 1.63 m length and 600 mm diameter which base is placed facing the neutron beam. The 10 detectors and 9 targets interposed are hold onto a curved aluminium bottom on the opposite end of the chamber. It is connected to the beam pipes by two flanges made of kapton foils of 125 μm and 12 cm diameter. The foils are tightened between two metallic flanges.

Each PPAC has five preamplifiers, one for the anode and two for each cathode, plugged to the Acquiris flash analog-to-digital converters (FADCs) of the n_TOF data-acquisition system, which is described in the next section.

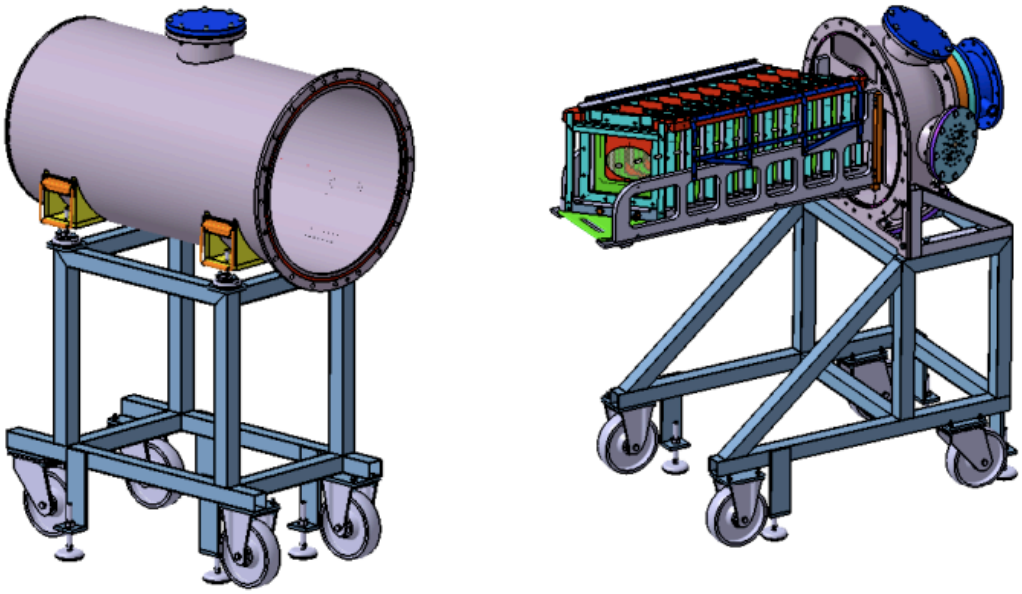

Figure 1.11: Pictures of the detection chamber containing the PPACs and the targets.

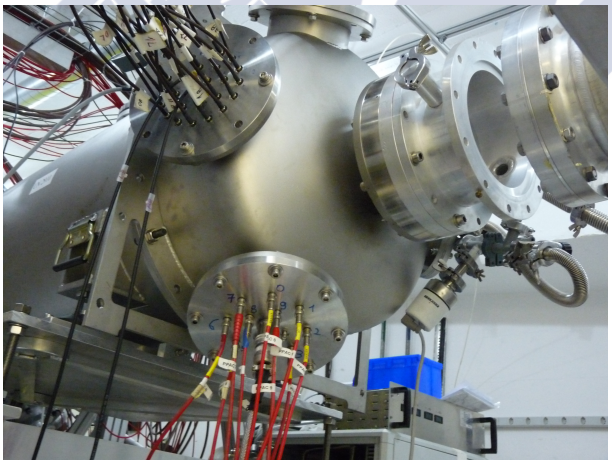

Figure 1.12: Photography of the connections to the detection chamber.

The targets

Different fissionable isotopic samples were measured simultaneously in this experiment using a total of nine targets: one of ^{237}Np, three of ^{234}U, two of ^{235}U and three of ^{238}U. Each sample is located between two PPACs at

2.5 cm from each anode in orthogonal direction. The detectors and targets disposition is shown in Fig. 1.13.

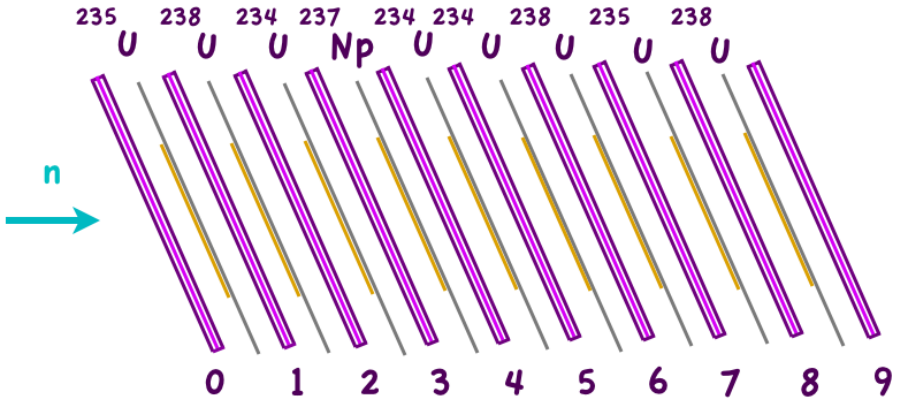

Figure 1.13: Schematic view of the setup.

The targets are made of a thin radioactive layer of 80 mm in diameter and between 200 and 300 μg/cm^2 electrodeposited in an aluminium layer with area of 10 x 10 cm^2. The foil is glued on the corners to a coppered epoxy frame with a central hole where the sample is placed, see Fig. 1.14. Foils of two different thickness have been used, the first six targets were deposited in an aluminium layer of 2 μm and the last three in a layer of 0.7 μm. The main features of the targets analysed in this work are given in Table 1.2. The masses of the three last targets shown in Fig. 1.13 have not been measured for the moment in the IPN laboratory.

The sample material was deposited in the aluminium foil by molecular plating, which is a chemical method commonly used to prepare targets and sources of actinides. It consists in dissolving a nitrate form of the element in isopropylique alcohol with a little quantity of water. Then, a 600 V potential is applied between the aluminium foil used as a backing and a platinum foil with the solution between them to fix the sample material to the backing by electrodeposition. Afterwards, the targets are introduced in an oven to remove the residual alcohol and water, resting the samples deposits in an oxide form. With this method the obtained samples are highly pure with minor impurities.

As the ^{235}U samples were made from the same material they have the same activity. Both targets contained a 6.28 % of ^{238}U, a 0.74 % of ^{234}U and a 0.27 % of ^{236}U. The ^{234}U samples included a presence of 0.077 % of ^{235}U.

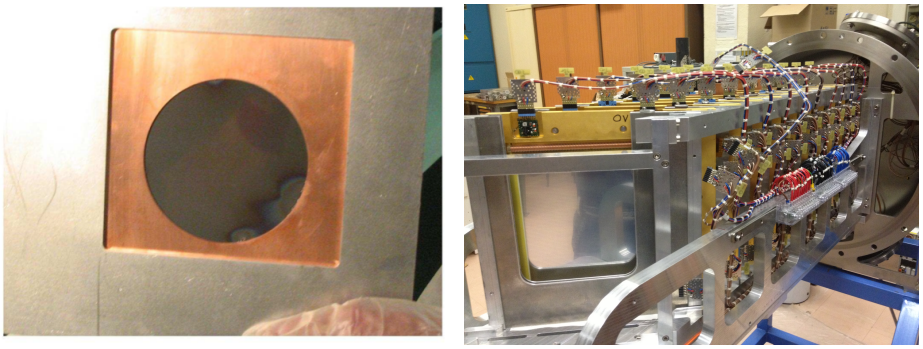

Figure 1.14: The picture on the left corresponds to one target. The picture on the right shows the distribution of the samples and PPACs inside the detection chamber.

Sample	Mass (mg)	Purity (%)	Activity
$^{235}U(0)$	14.00	92.71	25 kBq
$^{234}U(2)$	13.20	99.08	3.23 MBq
$^{234}U(4)$	13.39	99.08	3.23 MBq
$^{234}U(5)$	13.59	99.08	3.23 MBq
$^{235}U(7)$	–	92.71	25 kBq

Table 1.2: Table with the main features of the samples. The number in parentheses indicates the position of the target inside the chamber.

The analysis presented in this work correspond to the ^{234}U and ^{235}U targets, using this last as reference.

1.4 Data Acquisition System (DAQ)

The n_TOF Data Acquisition System (DAQ) was developed considering the beam repetition rates with a maximum of 2.4 s per burst, the expected number of event rates and the features of the detector signals [30]. It is composed by 60 Flash Analog to Digital Converters (FADCs) modules which avoid digital conversion to be blocked by data readout, 8-bit resolution channels, sampling rates up to 2 GHz and an internal buffer memory of 8 or 16 MB. The main feature of this DAQ is the possibility of recording the full ana-

logue waveform of the detector signals by the use of on-line-zero-suppression. This design allows the total reconstruction of the detector response in an off-line analysis which permits to solve events due to pile-up or background events.

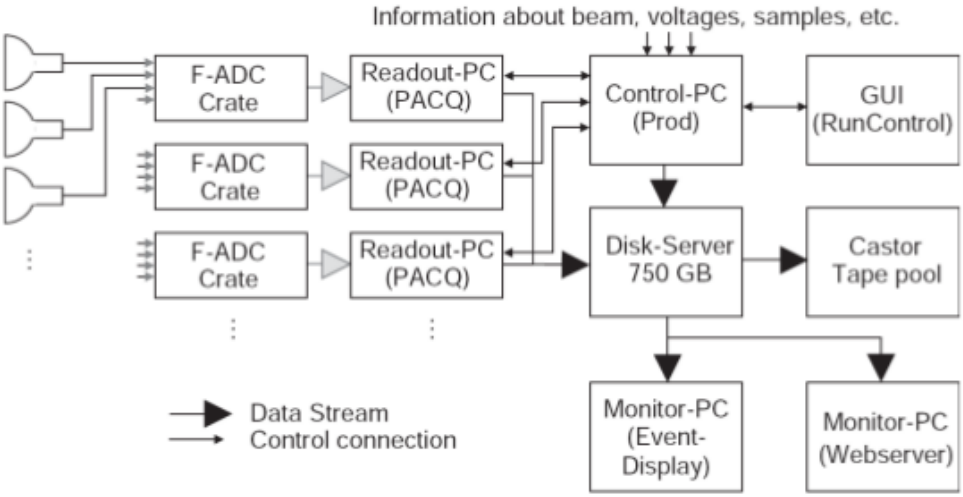

Figure 1.15: The n_TOF DAQ scheme.

The proton pulse from the PS generates the trigger when it impinges the spallation target opening a time window of 16 ms maximum size. This is the time required to full fill the buffer memory of 8 MB at 500 MHz sampling rate corresponding to a time resolution of 2 ns. A time of flight of 16 ms corresponds to an energy value of 0.7 eV which is therefore the lower neutron energy available. During this experiment a time window of 8 ms was used, corresponding to a minimum energy of ∼2.75 eV, to reduce the large amount of data generated due to the non-zero-suppression condition which was used to record all the information of the FADC movie.

The FADCs modules are placed in a Peripheral Component Interconnect (PCI) crate containing two or three modules with 2 or 4 channels each one. The data are transferred from the PCIs to the PCs at 80-100 MB/s, this rate limits the number of channels that can be transferred during the 1.2 s minimum time between two proton bunches to 8, this corresponds to a stream. A total of 7 streams and 50 channels have been required for this measurement, one channel per anode and 2 channels per cathode, which makes 5 channels per PPAC detector.

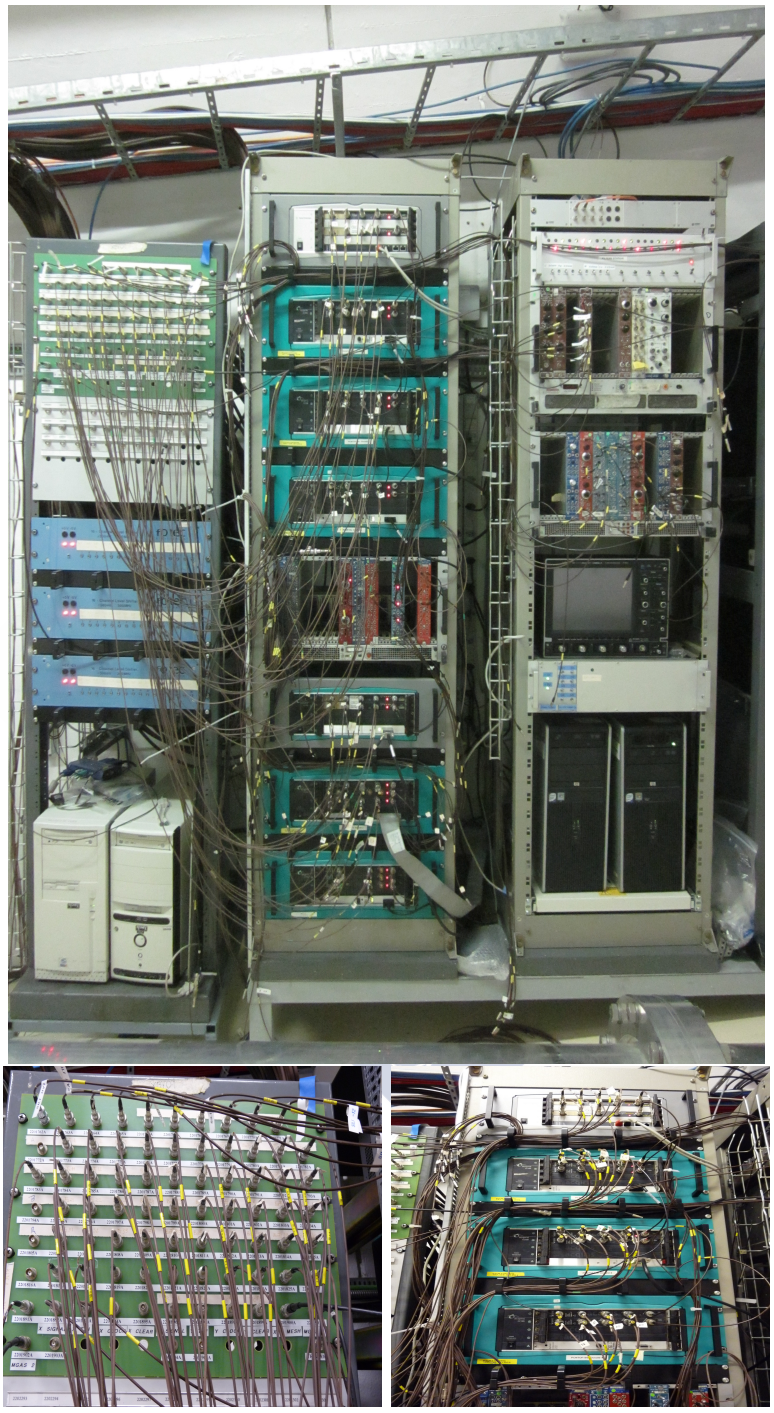

Figure 1.16: General view of the n_TOF DAQ on the top. The path panel with the detector signals connectors and the PCI crates with the FADC modules are shown in detail in the left and right down figures respectively.

The raw data are accessible from a PC monitor during the short period of time in which they are stored on the disk-server before they are transferred to the CASTOR (CERN Advanced STORage manager) storage system, this is when the raw data files exceed 2GB. This allows to monitor almost on-line the signals. Once the raw data are saved on tape the pulse shape analysis is performed using the appropriated algorithm depending on the detectors. As the raw data are very heavy, a lighter format containing only the relevant information of the signals (time, amplitude) is required to perform the data analysis, this is the Data Summary Tape (DST) which contains the pulse shape analysis output data. The DSTs are saved and stored on tape and disk, it is represented in Fig. 1.15.

1.5 Raw data processing

The raw data are converted into DSTs after the pulse shape analysis, as previously mentioned. The pulse shape analysis is performed using a software package developed by the n_TOF Collaboration which includes an specific routine for the analysis of PPAC signals.

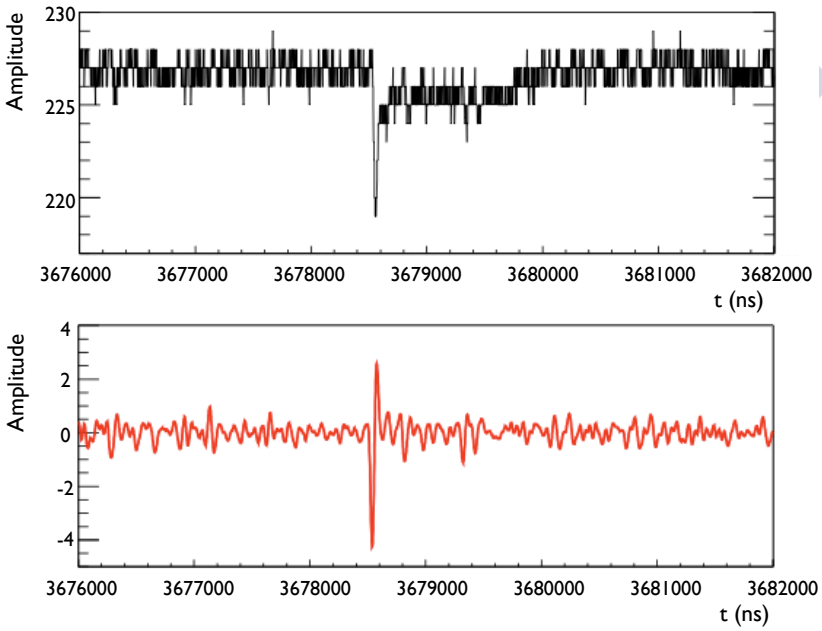

Figure 1.17: The signal obtained for the anode and the cathode before (upper panel) and after (down panel) applying the derivative filter.

The PPAC routine is based on a derivative filter which discriminates de-

tector signals from high-frequency oscillations. After the filter derivation signals acquire a bipolar shape as shown in Fig. 1.17. The peak discrimination is done through the application of some conditions to the derived signal. The signal polarity must be negative, hence the negative part has to arrive first. Two thresholds (positive and negative) are imposed to the bipolar signal. The time between both parts of the bipolar signal and the ratio between their amplitudes are restricted to a limit to be recognized as valid signals.

The parameters stored for each signal are the zero-crossing **time** and the peak-to-peak **amplitude** of the treated signal. The DSTs containing both parameters are saved in CASTOR.

1.6 The γ-flash signal

The gamma flash (γ-flash) signal is the first signal detected correlated with the neutron pulse. It is generated by the gamma rays and relativistic particles produced in the spallation reaction. This signal temporarily "blinds" the detectors limiting the maximum energy that can be reach for each type of detector. For detectors very sensitive to gammas this is an annoying effect, however, as the PPACs are mostly insensitive to gammas, this effect is less dramatic, allowing to reach neutron energies up to 1 GeV.

The γ-flash signal is present in every detector and takes ∼2 ns to travel from the first to the last PPAC being considered as instantaneous and a time reference for each proton pulse. Some background signals may be found preceding the γ-flash, mainly due to the alpha particles emitted by the radioactive targets or from fission products induced by non correlated neutrons. These signals are only present in one or a few detectors being discarded in the search of the γ-flash, which is conditioned to be found in all the detectors. The algorithm used to identify the γ-flash signals between the first signals found in each detector is based in the detection in coincidence of the signals present in all the detectors.

The γ-flash timing depends on the type of PS pulse, which may be dedicated or parasitic (see Section 1.1.1), because the trigger signal is different for each type of PS pulse. An example of the γ-flash time distribution obtained for the dedicated and parasitic PS pulses is shown in Fig. 1.18.

The γ-flash signal may be used to correct the time differences between two FADC channels, taking one as a reference, as it is explained in detail in the next section.

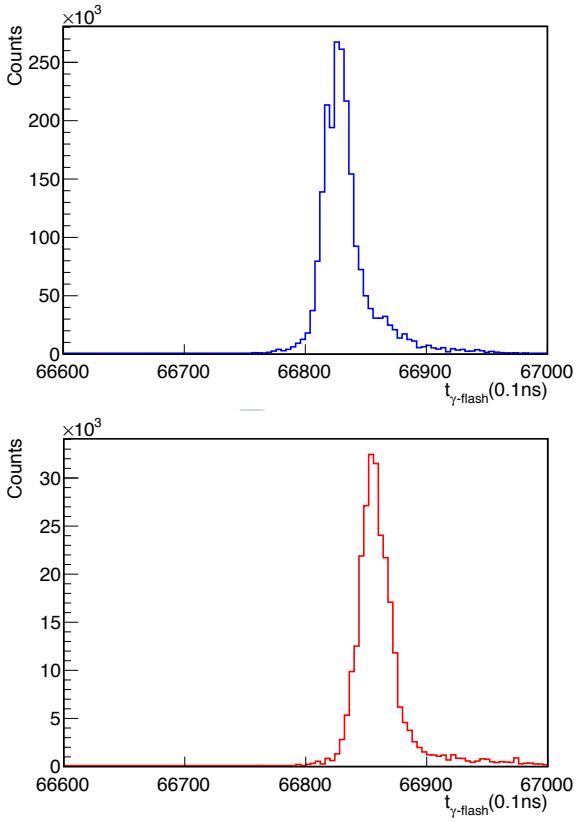

Figure 1.18: γ-flash time distribution for every PS pulse: dedicated (upper panel) and parasitic (lower panel).

1.7 Time calibration of the Digitizers

Each Acquiris digitizer is provided with an internal clock having a nominal accuracy of ± 2 ppm (parts per million) which may produce deviations up to tens of ns between FADC channels for the largest registered times. In addition, as it was observed in previous fission campaigns [29], a time deviation between channels is found due to the length of the electronic paths connecting the detectors to the digitizers (larger than 10 m) which are placed in different areas for security reasons. The fission events analysis is based on the search of signals in coincidence between detectors which requires time coincidences of only a few ns accuracy, hence the time differences between the Digitizers must be corrected. This time offset has been calibrated taking advantage of the presence of split PPAC anodes in the digitizers. The anode channels are placed in the modules following the scheme of Fig. 1.19. The channel 3 has been connected to the module 2 and the channel 6 to the

module 3 through the channels called 93 and 96 respectively. The channels 93 and 96 contain the information of the same FADC as the channels 3 and 6 with an additional offset corresponding to the Digitizer internal clock deviation between modules plus the 4 ns that takes the signal in traversing the wire which connects both modules.

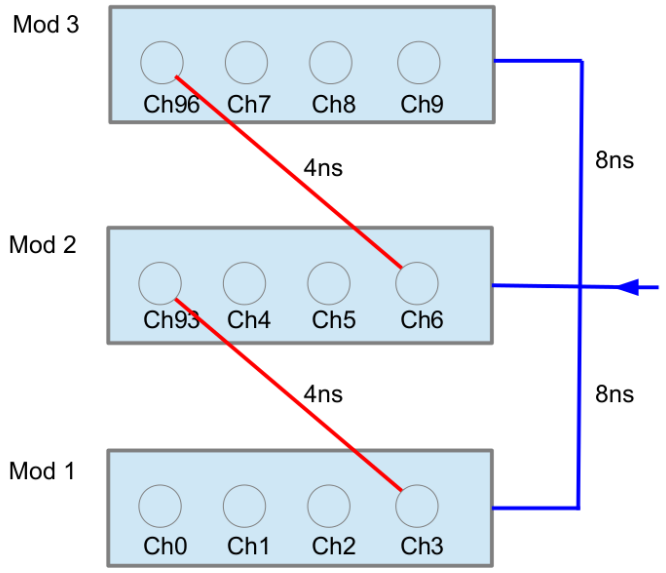

Figure 1.19: Connection scheme of the anode channels in the Digitizers.

There are two components in the time difference between two FADC modules, one is the constant offset between channels and the other is the time deviation inside a FADC channel. The offset between channels has been calibrated using the gamma flash (γ-flash) signal for the previously exposed reasons. The channel 6, which is in the module 2, has been taken as a reference and the rest of the channels have been calibrated correcting the γ-flash differences on time with respect to it, for instance, the distribution obtained with the channel 0 is given in Fig. 1.20 showing an offset of 8 ns between both channels. The exact value of the time difference between channels is calculated by fitting the distribution to a gaussian function.

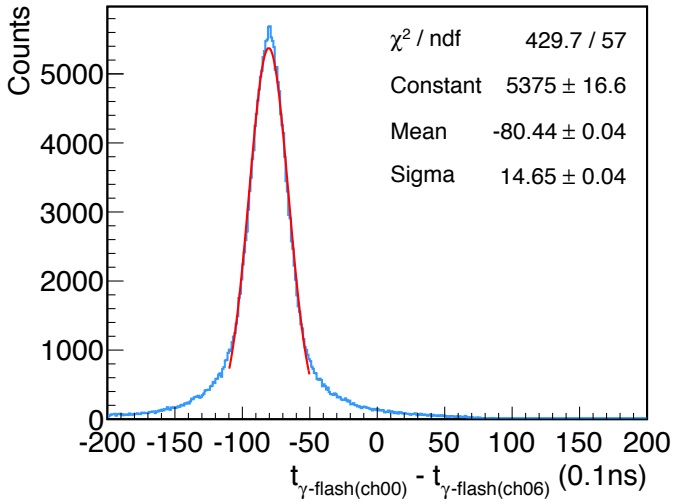

Figure 1.20: Time difference between the γ-flash in the anodes 0 and 6 (reference).

The time of the γ-flash signals for each anode are distributed as it is shown in Fig. 1.21 after being corrected by the time calibration between channels.

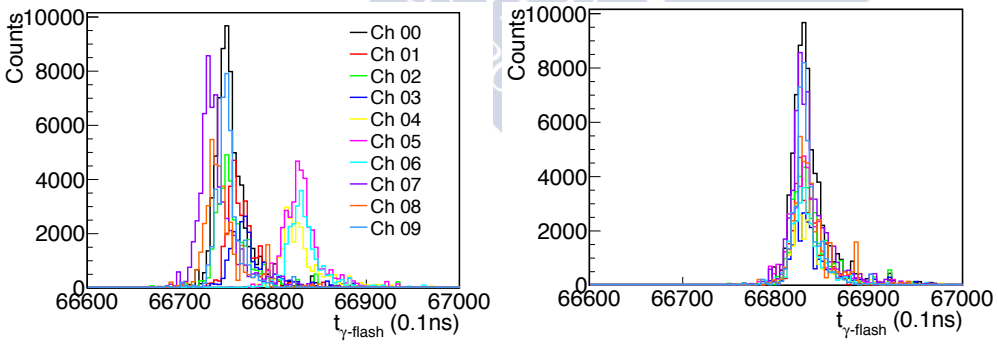

Figure 1.21: γ-flash time distribution for each PPAC anode before (left panel) and after (right panel) the channel calibration.

The different behaviour with the time of the FADC internal clocks has also been calibrated using the split anode signals. The time differences corresponding to the same anode in two different modules have been fitted to a linear function (see Fig. 1.22).

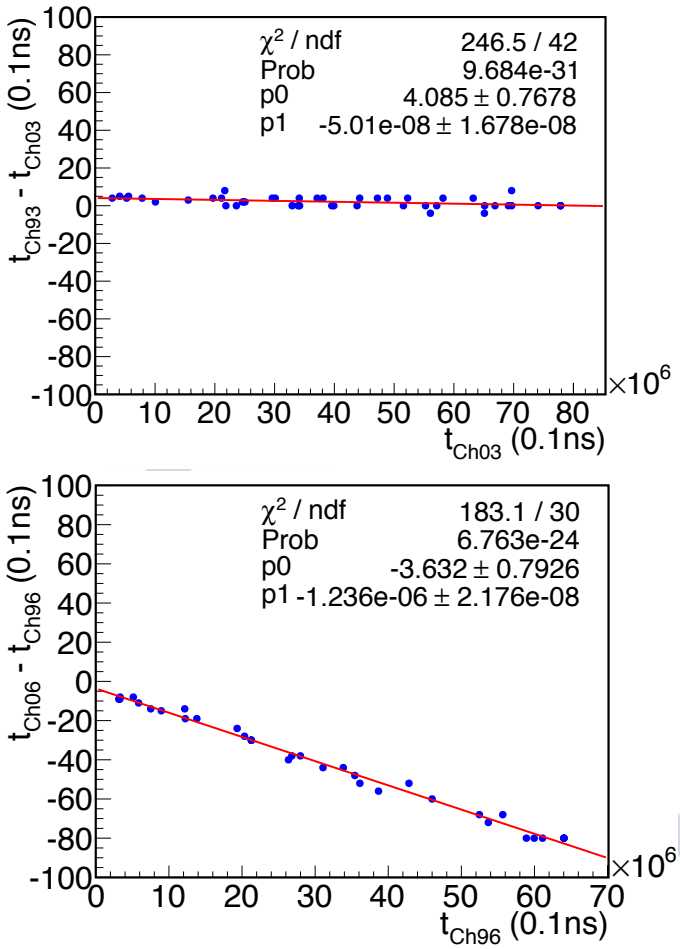

Figure 1.22: Time deviation of the double channels from the reference channels versus the time for one event. The slope of the fits represents the deviation of the internal time scale of the channel to the reference.

As it is shown in Fig. 1.22, the deviation with respect to the module 2 of the internal time scale of the module 1 is lower than 1 ns around 7 ms, while the one of the module 3 is about 9 ns.

These parameters are used to correct the deviations between the FADC modules. This correction increases the accuracy in the identification of fission events when it is based on the coincidence between signals from different channels, and is required when the neutron energy calibration of a target is performed using another as a reference.

1.8 Fission event building

As it was previously mentioned the relevant parameters obtained from the signals are the time and amplitude, hence the data treatment is based on such parameters. When a neutron collides with an atom in the target producing its fission, both fission fragments (FFs) are emitted in opposite directions being detected almost simultaneously in the two detectors flanking the target. The condition of two signals in coincidence allows to reject most of the background, mainly due to alphas and spallation reaction products.

The fission event detection is represented in Fig. 1.23.

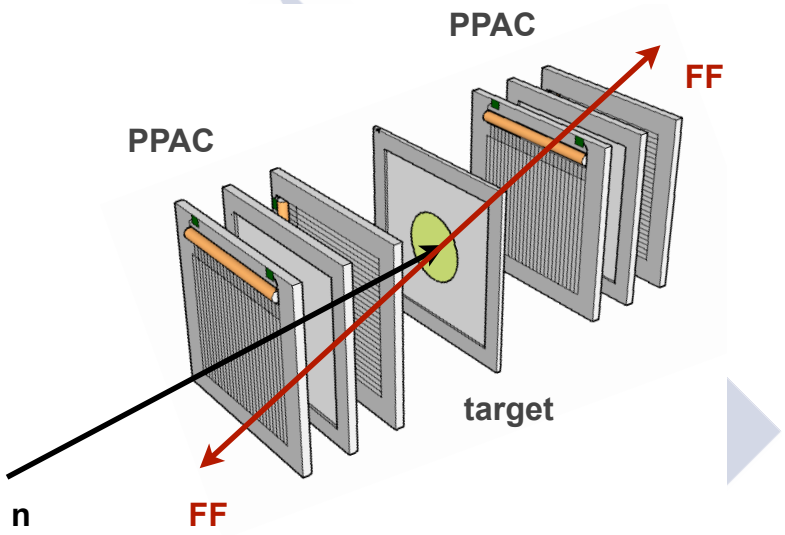

Figure 1.23: Fission event detection scheme.

Nine targets with ten detectors in between have been used in this experiment. So that each detector, except those placed at the extremes, has two targets at its sides and may detect FFs from both of them. In addition it may happen that one FF traverses several detectors, therefore one PPAC can detect FFs from more than two targets. This fact difficult the identification of the FFs when trying to know from which target they were emitted.

1.8.1 The anode signal

The coincidence method used in this experiment is similar to the algorithms previously used in PPAC measurements [29,3,31]. The anode signals, corrected from the time deviations between FADC modules, are used to identify the fission events due to its good time resolution, of the order of hundreds of picoseconds.

Multiple-type events

The search of coincidences starts with the first detector facing the beam, when a signal is found in the anode, a time window of 25 ns, which is enough large to contain the signals produced by the other FF in two consecutive detectors, is opened to look for signals in the next detector. If a signal is found, a new time window is opened from it to look for a signal in the following detector and, so on until no signal is found in the subsequent detector inside this time window. During this process the signals which were included in any previous configuration are excluded in the followings. An event is classified according to the number of PPACs with signals as type-2, type-3 and type-4 respectively. Coincidences involving more than four detectors may be also possible, although they are not completely produced by the same FF but for another particle detected in coincidence with the type-4. The detection scheme is represented in Fig. 1.24.

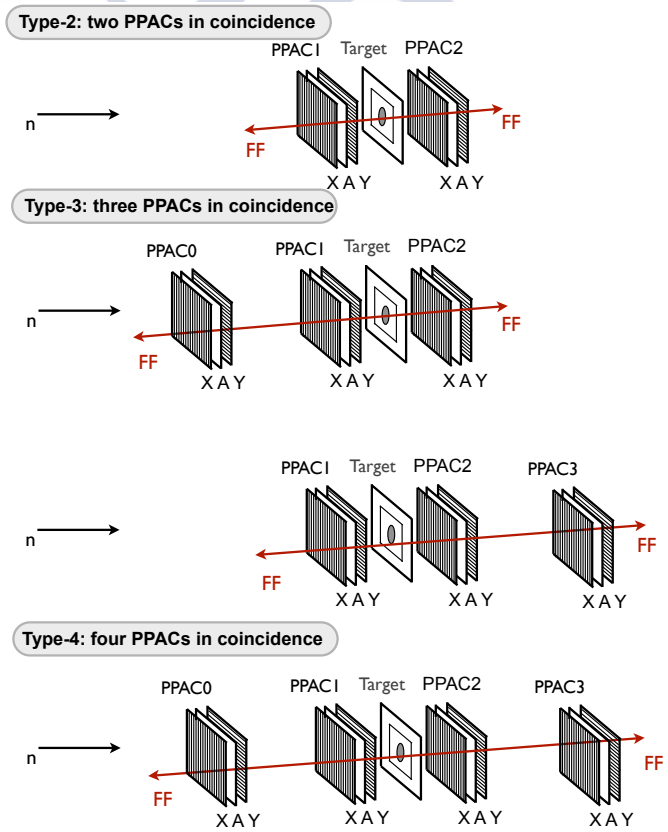

Figure 1.24: Fission event detection scheme.

Once a group of signals has been found in coincidence in a set of detectors,

the identification process starts searching of the signal with a maximum amplitude taking this as the reference signal, considering that it has been produced by a FF coming from one of the two targets flanking such detector.

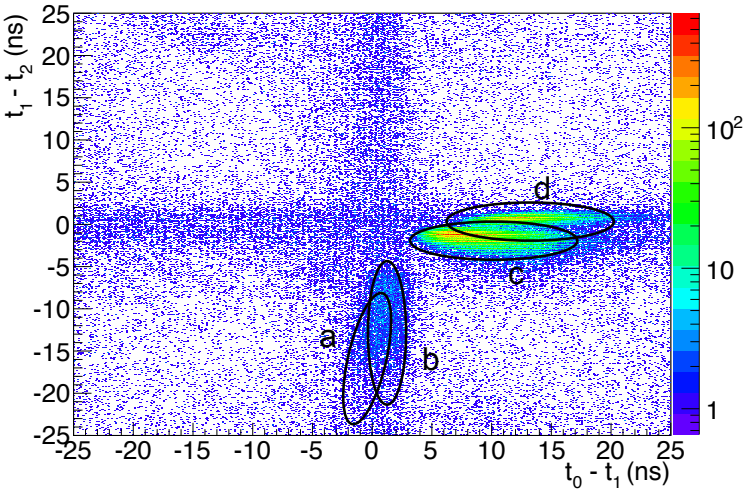

Figure 1.25: Two-dimensional plot of (t_0-t_1,t_1-t_2). The group of fission events produced in the target 0 are designated as "**a**" in the case in which the Heavy Fission Fragment (HFF) passes through the backing and as "**b**" when the Light Fission Fragment (LFF) passes through it. The fission events emitted from target 1 are named "**c**" if the LFF passes through the backing and "**d**" if the HFF goes through it.

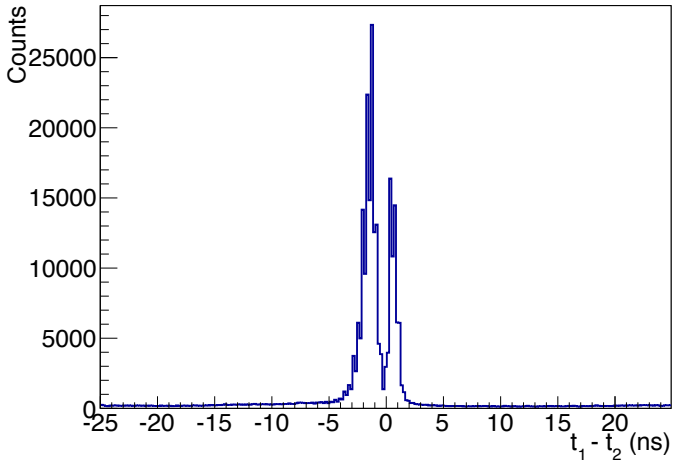

Figure 1.26: Projection in the Y axis of the two-dimensional plot of Fig. 1.25.

The multiple-type is therefore reduced to three signals in coincidence (type-3), those are the reference signal (detector 1) and the signals detected in the previous and following detectors (detectors 0 and 2 respectively). Comparing the time differences t_0-t_1 and t_1-t_2, it is possible to distinguish fission events coming from target 0 (placed between the detectors 0 and 1) or from target 1 (placed between the detectors 1 and 2), it is shown in the two-dimensional histogram of Fig. 1.25 where the group of events which appears in the figure with t_0-t_1 around zero corresponds to the target 0 and the group of events with t_1-t_2 around zero corresponds to the target 1. From these events, those with t_0-t_1 around zero and accumulated in a group are mostly FF coming from the target 0 which have been detected in the three detectors while those which are not confined in the group but have positive values of t_1-t_2 are mainly FF of the target 0 that have been detected in the 0 and 1 detectors when another particle like a FF produced in the target 1 is detected in the detector 2. For the target 1 an equivalent situation occurs.

The events represented in Fig. 1.25 correspond to a type-3 coincidence between the detectors 6, 7 and 8, therefore the target labeled as 0 is, in this case, the target 6 (^{238}U) and the target named 1 is the target 7 (^{235}U). As the fission cross section for the ^{235}U is larger than for the ^{238}U, the number of counts observed in the histogram for the target 0 is lower than for the target 1. The projection in the Y axis of the two-dimensional plot of Fig. 1.25 is given in Fig. 1.26 showing the time difference t_1-t_2.

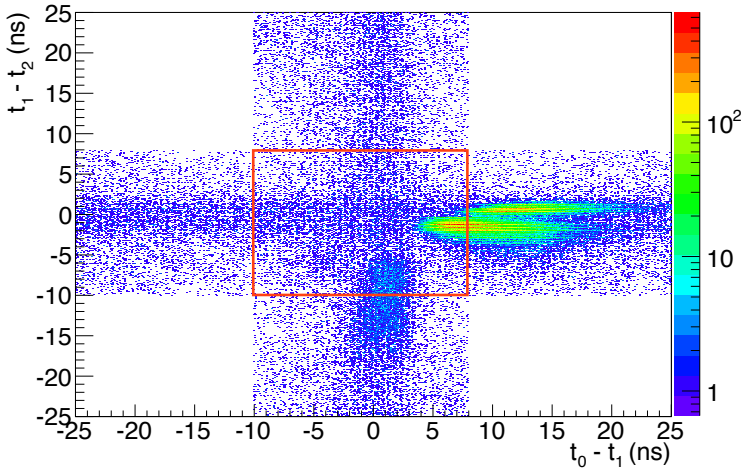

Figure 1.27: Two-dimensional histogram of (t_0-t_1,t_1-t_2) after the application of the time window to each couple of consecutive detectors. The red box contains the events which are inside both time windows.

In order to separate the events coming from each of the two targets, some

conditions in time and amplitude must be applied to the type-3 events. First a time window of 18 ns is defined between each two consecutive detectors as it is shown in Fig. 1.27 where the events inside the time window defined for t_0 - t_1 would belong to the target 0 and the events inside the time window defined for t_1 - t_2 would belong to the target 1. However, as it can be seen in Fig. 1.27, there are fission events coming from both targets which are inside both time windows (events confined inside the red box in the figure), hence this time condition is not enough to separate them.

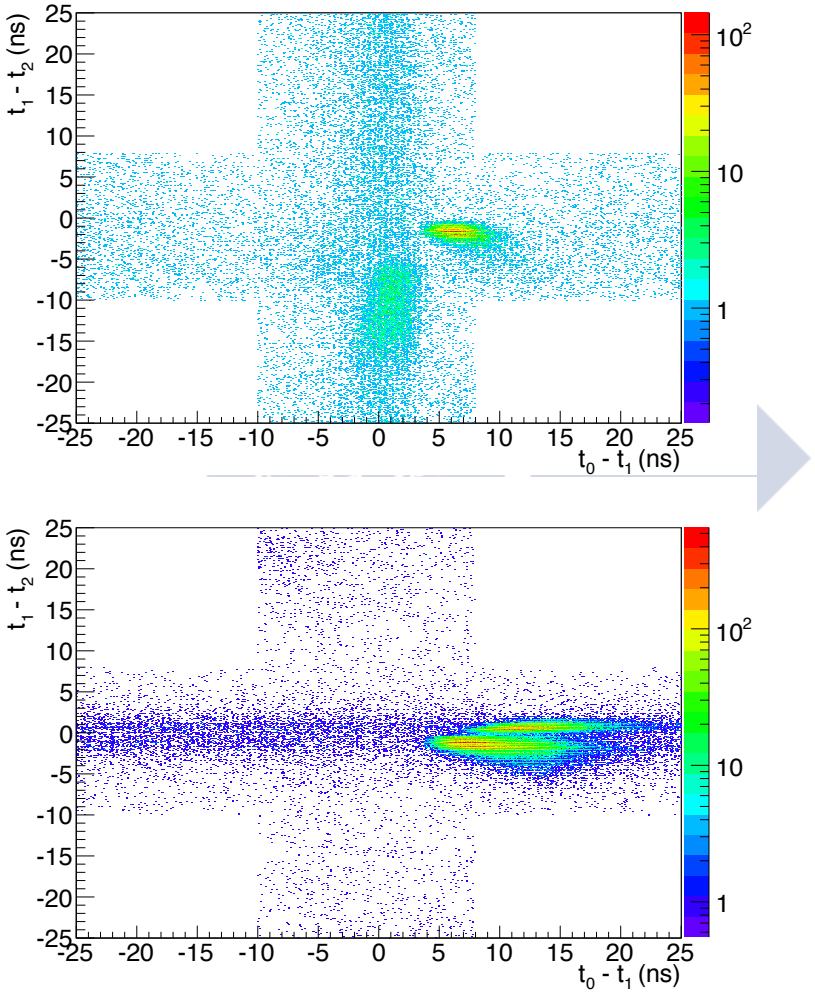

Figure 1.28: Histogram represented in Fig. 1.27 after the application of the condition $amp_0 > amp_2$ (upper panel) and the condition $amp_0 < amp_2$ (lower panel).

The subsequent application of an unique condition in amplitude, this is

considering that the events with $amp_0 > amp_2$ belongs to target 0 while the events with $amp_0 < amp_2$ comes from target 1 would not be in this case completely effective as it can be seen in Fig. 1.28 where the figure on the top is the two-dimensional histogram after imposing the condition $amp_0 > amp_2$ and the figure on the bottom is the same histogram after imposing the opposite condition.

When a fission occurs in the target 0, the FF emitted backward (in the opposite direction of the neutron beam) is detected by the detector 0 and the FF emitted forward is detected by the detector 1, after traversing the target 0 backing, and by the detector 2, after traversing the target 0 and target 1 backings and the detector 1. The FF emitted forward has to traverse a lot of material while the FF emitted backward goes directly to the detector, this is the reason why the amplitude of the signals produced in the detector by both FF have values well differenced and the amplitude condition works in this case. When a fission occurs in the target 1, however, the case is different, the FF emitted backward has to traverse the detector 1 and the target 0 backing to be detected by the detector 0 and the FF emitted forward has to traverse just the target 2 backing. In this case, the difference of the material traversed by the FFs is lower and as the HFF and LFF can be emitted in both directions it can happen that the amplitude of the signal in the detector 0 could be higher than the amplitude of the signal in the detector 2 and in the other way around, as it is shown respectively in the upper and lower panels of Fig. 1.28 which makes the amplitude condition ineffective in this case.

A more strict condition in time is then required to separate events coming from both targets in the cases in which those events are inside both time windows, this is in the center of the two-dimensional histogram. The histogram is then divided in four triangles limited by the lines given by the equations $t_0 = t_2$ and $t_0 - t_1 = t_1 - t_2$ (see Fig. 1.29) and the appropriate conditions are applied in each case.

The majority of the fission events accumulated in the left and top triangles around the time differences equal to zero correspond, as it was explained before, to the cases in which a fission of one target is detected in coincidence with another particle and, as it was shown in Fig. 1.28 the application of the amplitude condition is valid in this case to separate FF coming from target 0 and target 1. As such condition is not applicable to the bottom and right triangles, in both cases the limits in time defined by the triangles are sufficient to separate events from target 0 (bottom triangle) and from target 1 (right triangle).

After the application of these conditions in time and amplitude, the events coming from the target 0 and 1 are successfully separated and the type-3 is

reduced to type-2, this is to a coincidence between two detectors.

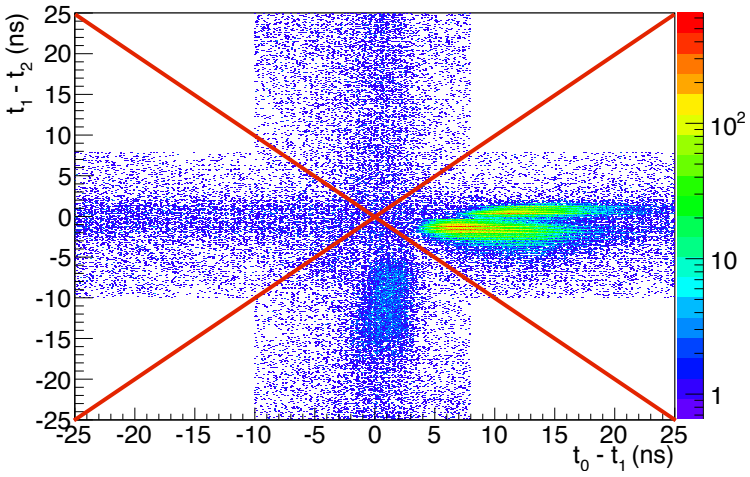

Figure 1.29: Two-dimensional histogram of (t_0-t_1,t_1-t_2). The red lines represent the division in four zones where more strict conditions in time and amplitude have been studied to separate the events coming from each of the two targets.

Type-2 events

The search of signals in coincidence between two detectors allows to discriminate the most of the random coincidences produced by the alphas which are emitted by the radioactive targets or signals induced by charged particles produced in other type of reactions. However this background is not totally eliminated, as it is shown in the two-dimensional histogram of Fig. 1.30, where the amplitudes of the signals in coincidence from two detectors are represented. A more detailed study of the type-2 events is required to remove this remaining background.

In order to apply the appropriate cuts in amplitude to optimise the background suppression, the evolution of the background with the incident neutron energy has been studied. The two-dimensional plot with the sum of both anode amplitudes as a function of the incident neutron energy (see Fig. 1.31) shows an accumulation of events with low amplitude at high energies. This background may be produced by random coincidences of signals produced by light particles and spallation residuals from neutron induced reactions in the detector and target layers. In addition, for the ^{234}U samples, there is also a presence of alpha background at low energies coming from the radioactivity of the target.

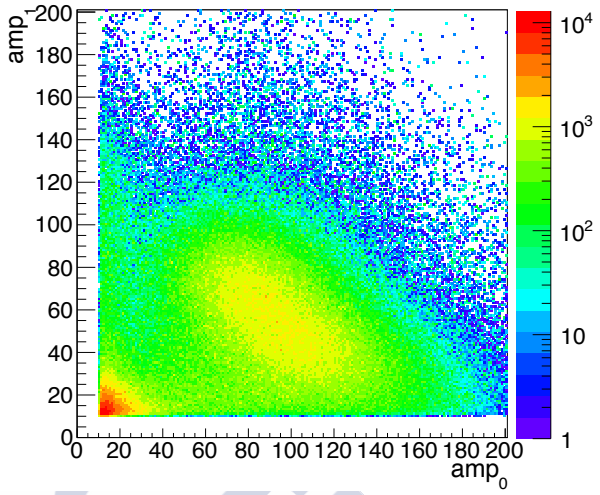

Figure 1.30: Two-dimensional plot, in the full energy range, of the amplitudes in the detectors 0 vs. 1 obtained for an ^{234}U target.

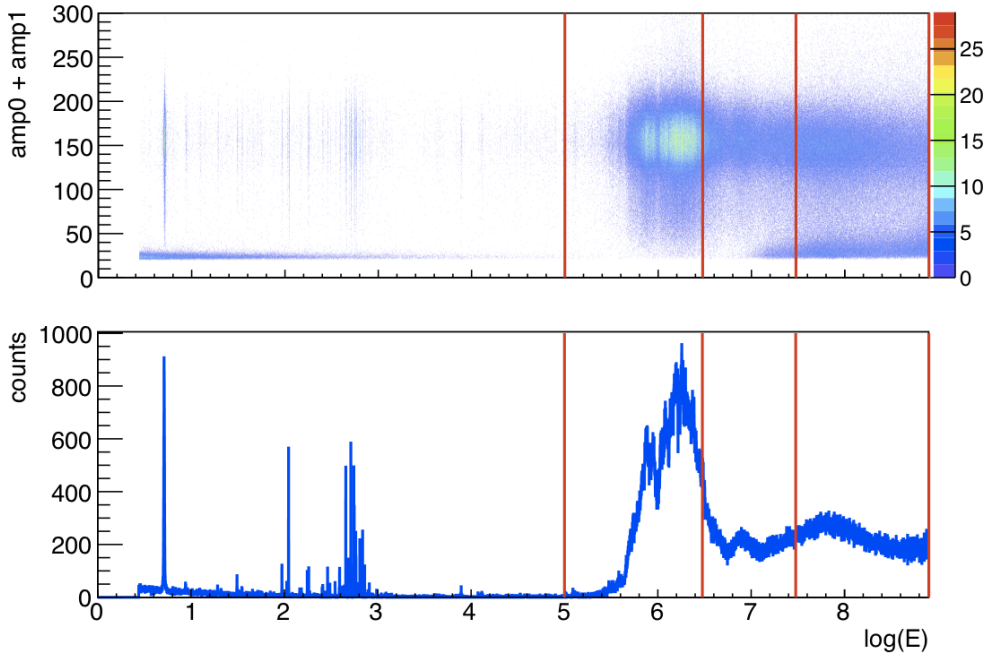

Figure 1.31: Two-dimensional plot of the sum of the amplitudes in two detectors vs. the incident neutron energy (upper panel) of an ^{234}U sample. The red lines limit the four energy regions. Histogram showing the counting rate obtained from the above plot (lower panel).

According to the different background behaviour, the spectrum is divided in four energy regions ("Region 1", "Region 2", "Region 3" and "Region 4") defined as a compromise between the background distribution shape and the statistics required to study it, whose limits (given in Table 1.3) are indicated by the vertical red lines in Fig. 1.31.

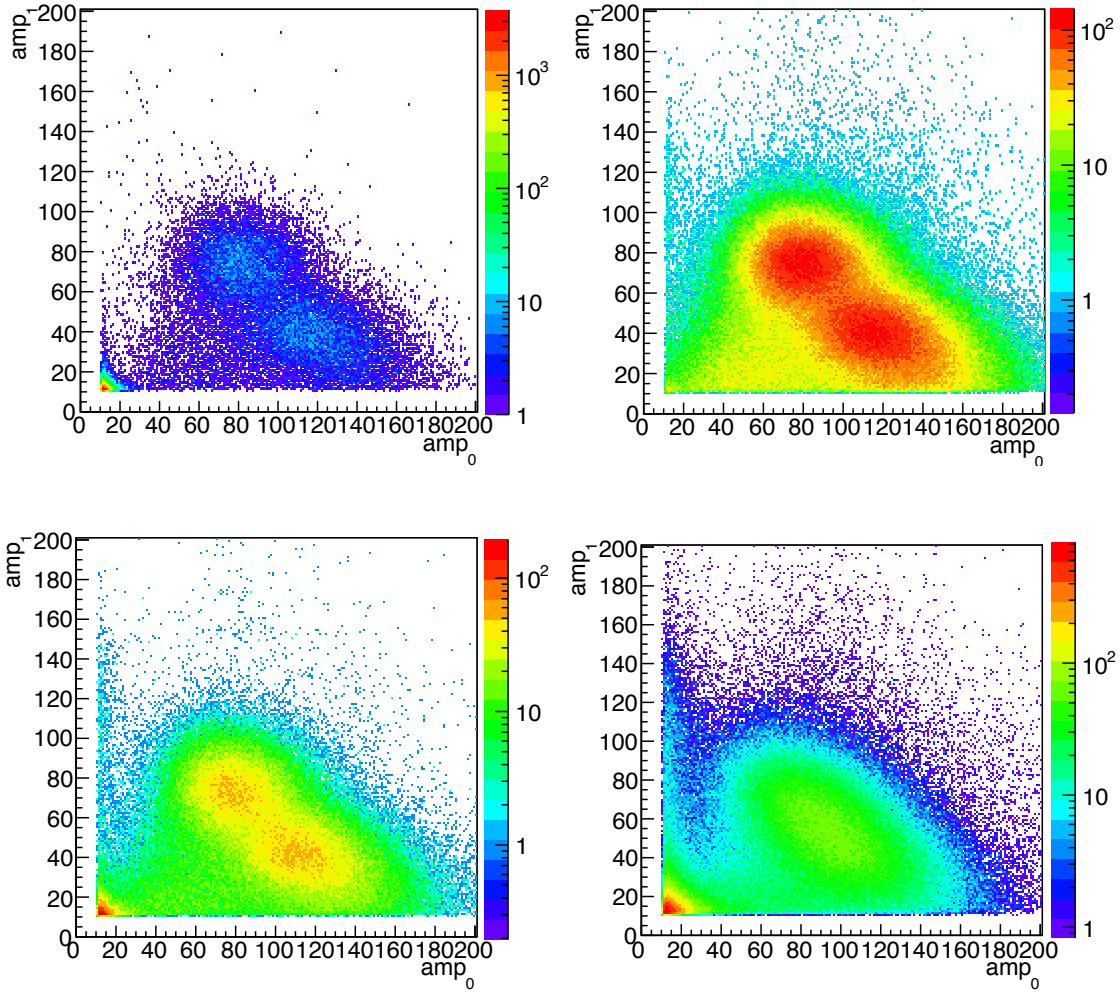

Figure 1.32: Two-dimensional histogram of the amplitude in the detector 0 vs. the amplitude in the detector 1 obtained for every energy region. The asymmetric fission mode dominates in Region 1 and 2, the symmetric mode dominates in Region 4 and Region 3 correspond to the transition.

The amplitude plot of Fig. 1.30 is shown in Fig. 1.32 for each energy region defined in Fig. 1.31. As it can be observed in this figure, dividing the

spectrum in energy regions, the background discrimination becomes more clean. This division in energy permits to distinguish in the figure FF signature corresponding to the asymmetric fission mode dominant in Region 1 and 2, and that of symmetric fission dominant at Region 4, being Region 3 the transition.

Energy region	E_n
Region 1	3 eV to 100 keV
Region 2	100 keV to 3 MeV
Region 3	3 MeV to 30 MeV
Region 4	30 MeV to 1 GeV

Table 1.3: Limits of the incident neutron energy regions in which the spectrum has been divided.

The low amplitude background has been separated from the FF events and removed applying a threshold in the sum of the anode amplitudes for every target at each energy region. This threshold is not applied in the minimum of the distribution, because the objective is to minimise the percentage of background events passing the threshold, which may affect to the angular distributions, specially at high energies, as it is shown in Fig. 1.33 corresponding to one ^{234}U target.

The peak centered in the sum of amplitudes around 150 is the FFs peak, with a tail towards low amplitudes, while the accumulated events observed at low amplitudes corresponds to the background. In order to separate the contribution of one in the other, a simple method has been used. It consisted in fitting the background peak to an exponential function which is extrapolated to reproduce the shape of the background curve tail. The area below the curve has been subtracted from the initial histogram to recover the tail of the FFs peak. To avoid statistical fluctuations in the shape of the FFs peak tail, this has been fitted to a linear function. After the application of a threshold in the sum of the anode amplitudes, the signals below the threshold are removed from the analysis. The percentage of background signals passing the threshold and FFs signals removed have been calculated, respectively, from the areas below the background and FFs tails above and below the threshold.

The factors including these percentages are applied to the counting rate at each energy range to consider, in the cross sections calculation, the possible

lost of fission events produced by the application of the threshold to remove the background.

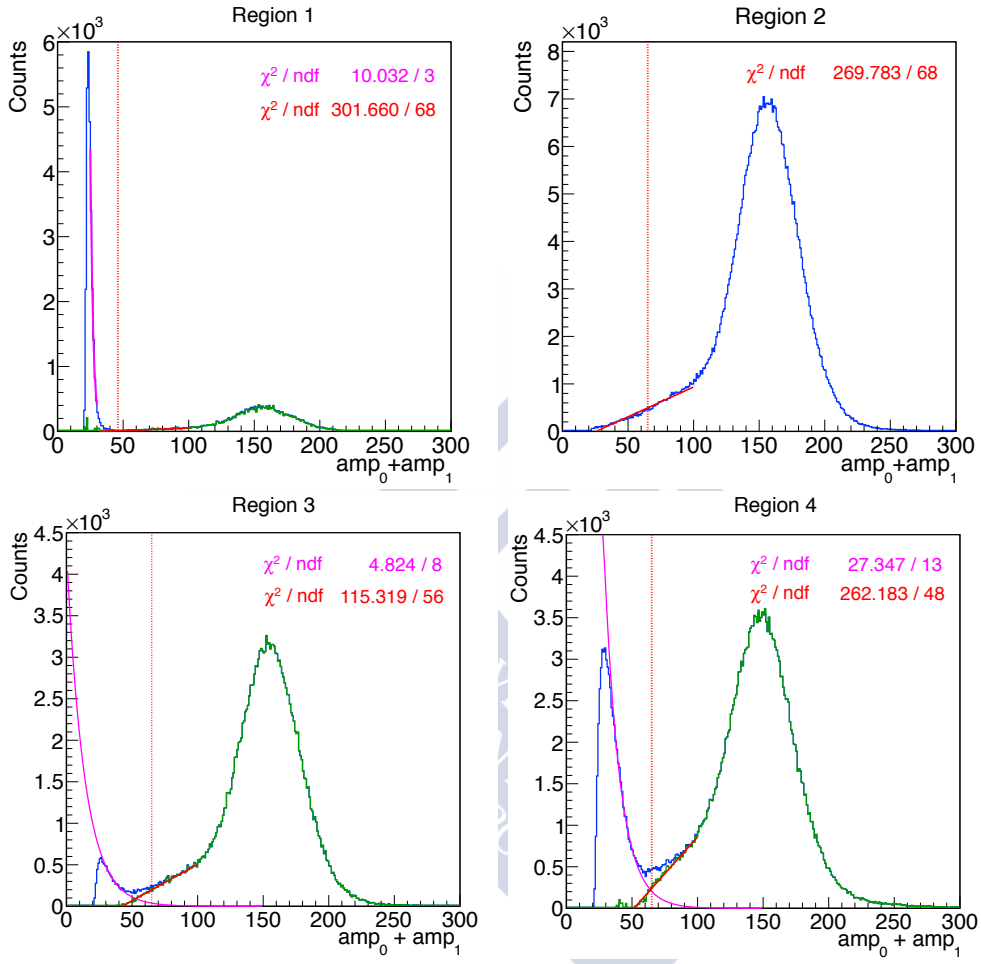

Figure 1.33: Sum of the anode amplitudes obtained at each energy region (blue solid line). The pink and red solid lines represent the extrapolation of the exponential fit and the linear fit of the peaks tails respectively. The green solid line is the histogram after the subtraction of the background curve. The red dashed line indicates the threshold applied to remove the low amplitude background.

1.8.2 Neutron energy

The incident neutron kinetic energy E_n has been calculated using the relativistic equation (Eq. 1.1) which can be expressed as:

$$E_n = mc^2 \left(\frac{1}{\sqrt{1 - \left(\frac{v}{c}\right)^2}} - 1 \right) \quad \text{with} \quad v = L/T \tag{1.5}$$

The velocity of the neutron (v) has been obtained from the time-of-flight (T) that takes the neutron to traverse the path length (L) from the spallation source to the reaction target. The time-of-flight is calculated considering the initial time as the time given by the g-flash signal and the arrival time to the reaction sample as the time measured in the anode.

The effective path length is composed by the effective moderation length of the neutrons inside the spallation source and the moderator, and by the geometrical distance. It is expressed therefore as the sum of two components, one dependent on the energy ($\lambda(E_n)$), due to the moderation length, and one independent on it which has into account the energy-independent term of the moderation length and the geometrical distance (L_0).

The value of $\lambda(E_n)$ was calculated by FLUKA simulations for the whole energy range as explained in [27], see Fig. 1.34.

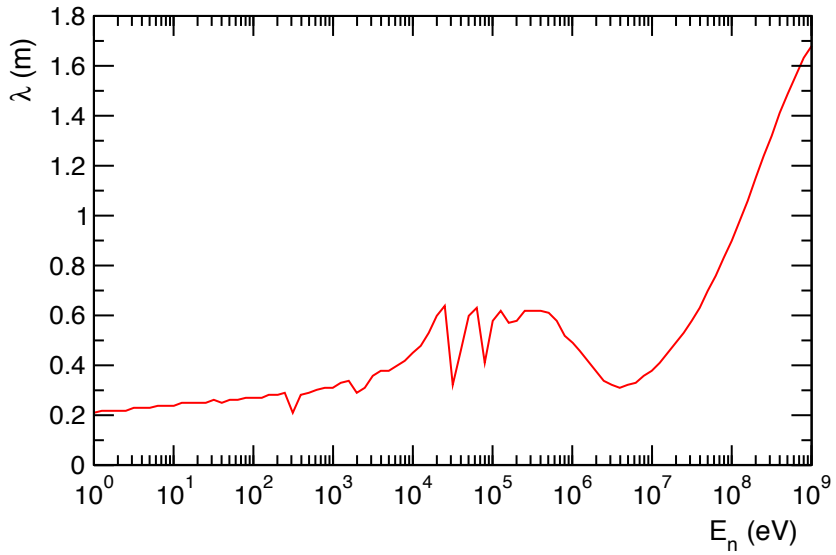

Figure 1.34: Energy dependent term of the moderation distance in the n_TOF facility.

The energy calibration is performed using the well-known ^{235}U(n,f) resonances as reference through an iterative process which is detailed as following. The process starts considering just the L_0 term of the effective path length with an initial value of approximately the geometrical distance from

the spallation source to the first ^{235}U sample to calculate an initial value of the incident neutron energy E_0 with Eq. 1.5. This E_0 is used to calculate $\lambda(E_0)$ and a new value of the incident neutron energy E_1 is obtained with the effective path length $L_0 + \lambda(E_0)$. This process is repeated until the result converges.

The ^{235}U(n,f) resonances given in the ENDF/B-VII.1 evaluation below 1 keV have been used to obtain the value of L_0 by fitting the energy of the resonances obtained in the first approximation E_0 to the evaluated below 1 keV. A value of L_0 = 183.282 m has been obtained for the first ^{235}U target. The value of L_0 for the rest of the targets has been obtained by adding to this value the distance between each target and the first ^{235}U sample. As the starting time is given by the γ-flash, it is required to take into account the time that takes it to travel along the flight path, therefore an offset of t_{offset} = L/c has been included in the energy calculation.

1.8.3 The position reconstruction

The fission fragment position in the detector is determined by using the PPAC cathodes information. As it was previously mentioned, each PPAC detector has one anode and two cathodes segmented with parallel aluminium strips which are connected to a delay line (DL). This cathodes are placed in perpendicular directions to provide the detection position in both directions, as it is represented in Fig. 1.35.

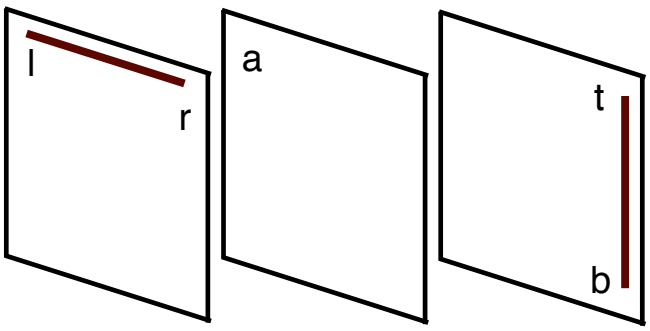

Figure 1.35: Picture showing the position of the cathodes in the PPAC. The cathode channels are named right (r), left (l), top (t) and bottom (b) while the anode is designed as (a).

The DL is read out at both ends and registered by the n_TOF DAQ. The channels corresponding to the same cathode are in the same DAQ module to improve the accuracy in the measurement of the DL and, therefore in

the position of the FF hit. The search of signals in the cathode considers the anode signal t_a as a reference looking for the corresponding signals in the cathode channels, within a time window of 400 ns after the anode signal. This time window is determined by the DL propagation time and the additional time introduced by the electronics.

The two-dimensional position of the fission fragment hit in the detector is obtained from both cathodes. The next paragraph is dedicated to the reconstruction of the horizontal position, the vertical position is determined in an analogous mode.

When the FF cross the detector, the signal produced travels along the cathode strips reaching the DL at a given point, labeled as x in Fig. 1.36. Then it propagates in both directions arriving to the ends at the times t_r and t_l.

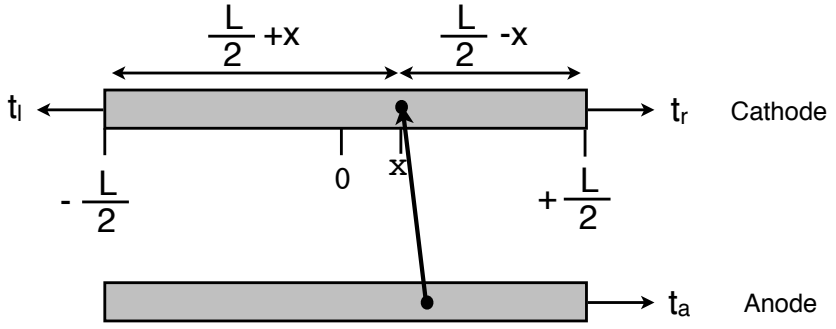

Figure 1.36: Signal propagation along the delay line of length L for the x-position cathode.

Using the anode signal, t_a, as a reference, the times t_r and t_l can be written as:

$$t_r = t_a + \frac{1}{v}\left(\frac{L}{2} - x\right) \tag{1.6}$$

$$t_l = t_a + \frac{1}{v}\left(\frac{L}{2} + x\right) \tag{1.7}$$

where v is the propagation velocity of the signal along the DL.

Considering that the propagation velocity v along the distance L is constant, the total DL propagation time (DLT) is given by the **sum of the times** that takes the signal in traveling from the signal position to both ends. Therefore, summing the times of Eq. 1.6 and Eq. 1.7:

$$t_r + t_l = 2t_a + \frac{L}{v} \tag{1.8}$$

where:

$$\frac{L}{v} = DLT \tag{1.9}$$

therefore:

$$DLT = t_r + t_l - 2t_a \tag{1.10}$$

This equation is known as "the diagonal condition" taken from the event distribution in the two-dimensional histogram of (t_t-t_a, t_b-t_a), see Fig. 1.37. The DLT for each cathode is obtained from the histogram of Eq. 1.10 as the mean value of the peak obtained from the fit to a gaussian function, however this value includes the propagation time of the signal along the delay line and also the additional time due to the preamplifiers.

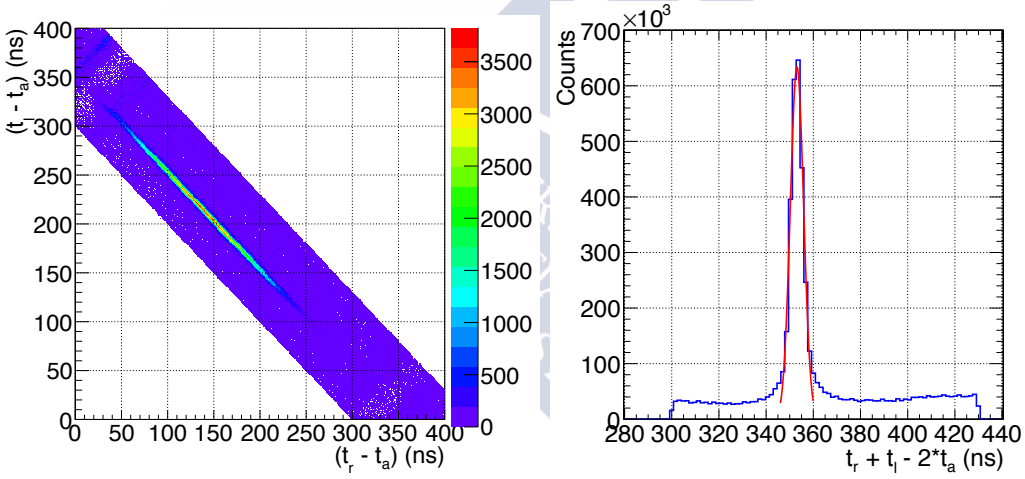

Figure 1.37: Two-dimensional plot showing the correlation between the propagation times along the DL for one x-cathode (left panel). Diagonal condition histogram where the mean of the peak is the DLT adding the time due to the preamplifiers (right panel).

The **time difference** between the two signals directly provides the FF hit position in the direction in which the strips are oriented. Extracting x from Eq. 1.6 and Eq. 1.7, and using the same procedure with the second cathode of the PPAC to obtain y, they are equal to:

$$x = \frac{v}{2}(t_l - t_r) \tag{1.11}$$

$$y = \frac{v}{2}\left(t_b - t_t\right) \tag{1.12}$$

Where the propagation velocity of the signal along the DL is equal to the traversed length divided by the spent time. Therefore the propagation time of the signal can be obtained from Eq. 1.11 (and likewise from Eq. 1.12) as:

$$t_{prop} = \frac{x}{v} = \frac{1}{2}\left(t_l - t_r\right) \tag{1.13}$$

The propagation time obtained for both cathodes is shown in Fig. 1.38, where the additional time due to the preamplifiers is easily identified at the extremes and the limits of the DL are the minima of the distribution located around (-160, 160) ns.

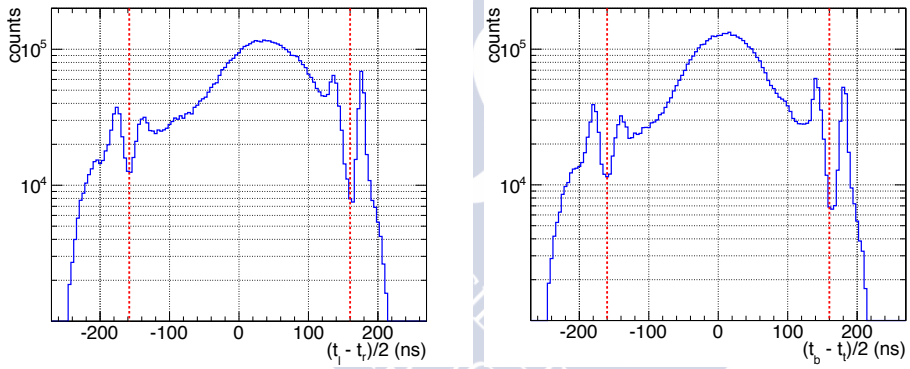

Figure 1.38: Histograms of the propagation time along the DL for the x (left panel) and the y (right panel) cathodes. The deviation of the distribution center from 0 in the x cathode is because the PPACs are tilted in the x direction. The values beyond the limits (red dashed lines) correspond to the reflections of the signals in the connections between the DL and the preamplifiers.

The real value of the propagation time along the whole DL has been calculated for each cathode from the respective DL limits, being around 320 ns. Thus the propagation velocity can be calculated as the total length of the DL (L), which is 200 mm, divided by the propagation time along the entire DL (DLT).

As the correlation between the times of the signals at both ends of the DL is given by the diagonal condition, its amplitudes are also correlated, due to the attenuation of the signal along the DL, as it is illustrated in Fig. 1.39.

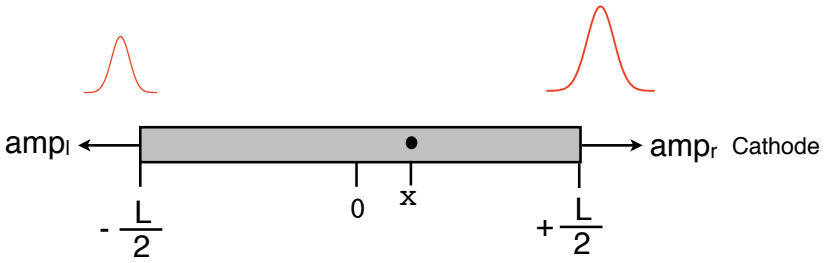

Figure 1.39: Picture of the signals attenuation along the DL.

This correlation is determined by the **ratio of both amplitudes**, see Fig. 1.40.

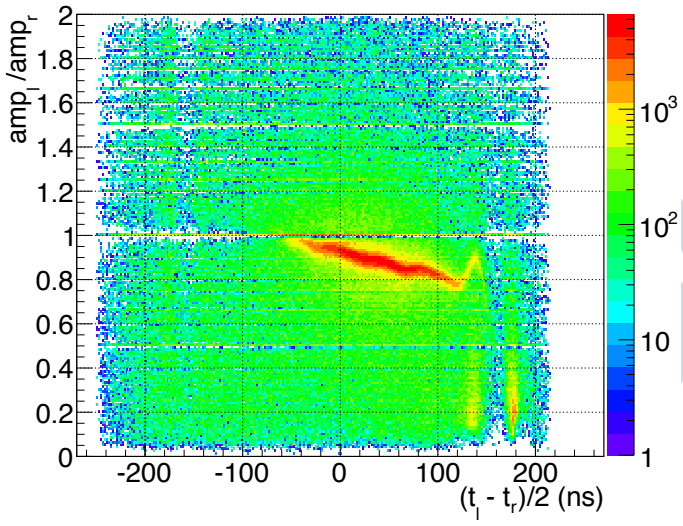

Figure 1.40: Two-dimensional histogram of the amplitudes dependency with the propagation time. FF events are accumulated in the figure.

Signals of the two cathode channels found inside the 400 ns time window with sum of times between the diagonal condition limits (300, 430) ns and with an amplitude ratio between (0, 2) are considered as a valid cathode event being saved for a further selection.

In case that multiple cathode signals combinations are found between the limits for an anode signal, the correct one is selected imposing strict limits in the diagonal condition, the signals out of these limits are discarded. The limits are placed at 40 ns at both sides of the mean value of the gaussian fit (see Fig. 1.41).

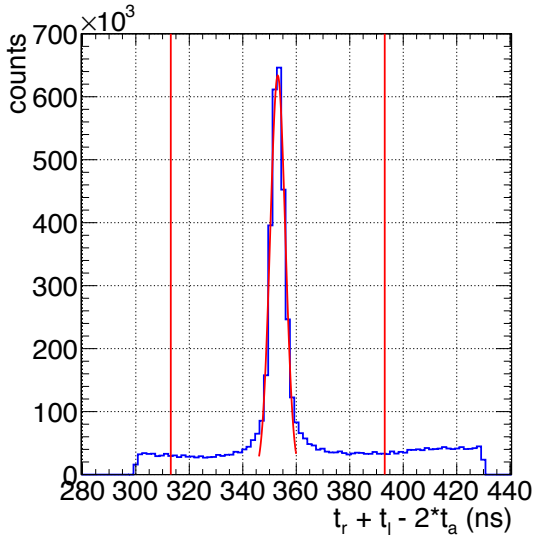

Figure 1.41: Diagonal condition limits (red lines) imposed at 40 ns at both sides of the mean value obtained from the gaussian fit to the peak.

If ambiguity persists for multiple possible combinations, strict limits on the amplitude ratio are also requested. The averaged value of the amplitude ratio given in Fig. 1.40 has been fitted to a linear function where the independent term of the fit equation is denoted as $P0$ and the slope as $P1$ (see Fig. 1.42).

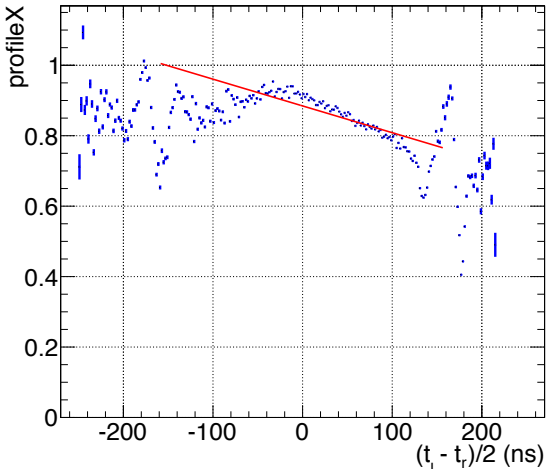

Figure 1.42: Averaged value of the amplitude ratio given the two-dimensional histogram of Fig. 1.40 fitted to a linear function.

The limits on the amplitude ratio have been calculated from the previous fit, being defined by two lines with slopes $P1$ and independent terms $P0 \pm 0.6$ (see Fig. 1.43).

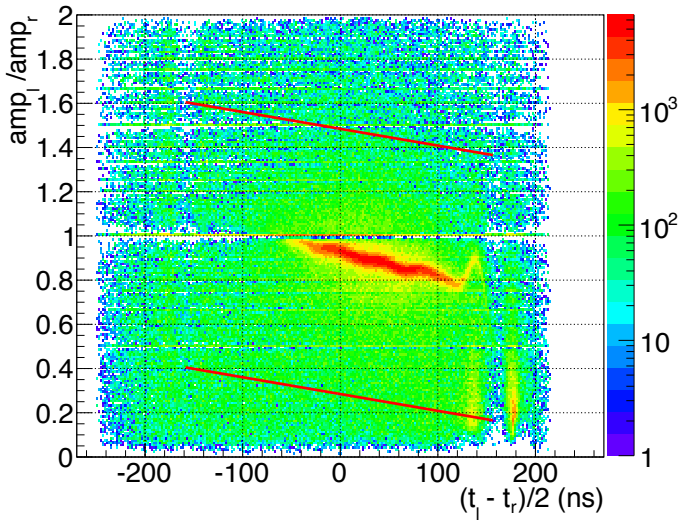

Figure 1.43: Limits (red lines) put in the two-dimensional histogram of the amplitudes dependence with the propagation time.

Finally, if multiple combinations are still remaining, then the combination of signals with DLT value closer to the peak in the distribution shown in Fig. 1.41 is saved, being the rest of the combinations discarded.

In the case that a detected particle do not produce signals in all the channels of the two PPAC cathodes, the position can not be reconstructed and, therefore it is not considered in the analysis of the cathodes.

1.8.4 Determination of the emission angle

The two-dimensional position of the detection in the PPAC is obtained from the position of the FF hit in both cathodes. Then, combining the information of two adjacent PPACs, each one providing the detection position of one of the two FFs, it is possible to reconstruct the fission fragment trajectory and thus, the emission angle, which is the relevant parameter for obtaining the FFAD, assuming that they are emitted from the target in opposite directions in the centre-of-mass frame. This is, considering that the nucleus fissions at rest. Simulations performed by D. Tarrío in his PhD. Thesis [3] using a momentum transfer of 350 MeV/c, which corresponds to

the maximum value achievable at 1 GeV show that the difference between the cosine of the measured angle and the cosine of the CM angle is less than 0.1%, which is lower than the angular resolution of the PPAC experimental setup which is determined by the 2 mm width of the cathode strips, being about 4% for the larger angles.

The fission fragment angular distribution is expressed as a function of the emission angle of the FF from the target with respect to the incident neutron beam. As the detectors and targets are tilted 45° with respect to the neutron beam, two reference frames have to be considered, both of them with origin in the center of the target. The first one is called the detector reference system with axis (x', y', z') in which the x and y axis are parallel to the detector surface and z axis is perpendicular to it and the second one, rotated 45° with respect to the first, is designed as the beam reference system with axis (x, y, z) in which the z axis is determined by the beam direction (see Fig. 1.44).

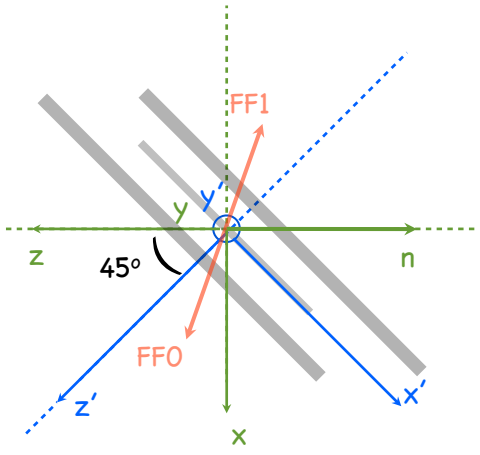

Figure 1.44: Detector (blue axis) and neutron beam (green axis) reference systems.

The polar angles between the FF trajectory and the respective z axis are θ' and θ while the azimuthal angle around the z axis are ϕ' and ϕ respectively. The variables of interest are the emission angle of the FF from the target with respect to the incident neutron beam (θ), which is required to calculate the fission fragment angular distribution, and the angle around the beam axis ϕ.

As the FF position on the detector has been calculated from the cathodes signals, which provided the (X,Y) information in the detector frame, then

the detection position of the FFs in the PPACs (labeled as 0 and 1) are, respectively P'$_0$ = (x'$_0$,y'$_0$,z'$_0$) and P'$_1$ = (x'$_1$,y'$_1$,z'$_1$) (see Fig. 1.45).

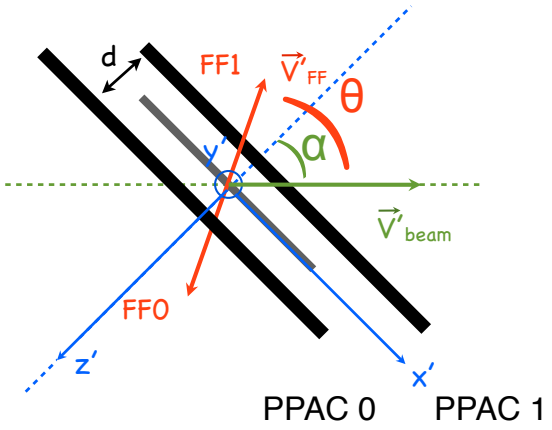

Figure 1.45: Variables represented in the detector reference frame.

The x' and y' coordinates are obtained from Eq. 1.11 and Eq. 1.12 taking into account in x' the inclination of the detectors and targets with respect to the neutron beam. The z' is obtained from the anode distance to the target. The FF0 and FF1 detection coordinates are given by the next equations:

$$\begin{aligned} x'_0 &= \frac{v}{2}(t_{l0} - t_{r0}) - \frac{d}{2} \cdot \tan\alpha \\ y'_0 &= \frac{v}{2}(t_{b0} - t_{t0}) \\ z'_0 &= \frac{d}{2} \end{aligned} \tag{1.14}$$

and

$$\begin{aligned} x'_1 &= \frac{v}{2}(t_{l1} - t_{r1}) + \frac{d}{2} \cdot \tan\alpha \\ y'_1 &= \frac{v}{2}(t_{b1} - t_{t1}) \\ z'_1 &= -\frac{d}{2} \end{aligned} \tag{1.15}$$

where d is the distance between the two anodes and α is the inclination angle (45°) of the PPACs and targets with respect to the neutron beam as it is indicated in the picture.

Being the neutron beam direction defined by the vector $\vec{V}'_{\text{beam}}$ and the FFs direction by the vector $\vec{V}'_{\text{FF}}$ in the detector reference frame as:

$$\vec{V'}_{beam} = (1, 0, -1) \tag{1.16}$$

and

$$\vec{V'}_{FF} = P'_1 - P'_0 = (x'_1 - x'_0, y'_1 - y'_0, z'_1 - z'_0) \tag{1.17}$$

the emission angle of the FFs with respect to the neutron beam (θ) is obtained as the scalar product of both vectors, with the equation:

$$cos\theta = \frac{\vec{V'}_{FF} \cdot \vec{V'}_{beam}}{|\vec{V'}_{FF}| \cdot |\vec{V'}_{beam}|} \tag{1.18}$$

The other variable of interest is the azimuthal angle of the FFs around the beam direction (ϕ). To calculate it, the neutron beam reference frame has to be considered, which coordinates are:

$$\begin{aligned} x &= x' \cdot cos\alpha + z' \cdot sen\alpha \\ y &= y' \\ z &= -x' \cdot cos\alpha + z' \cdot sen\alpha \end{aligned} \tag{1.19}$$

As the FFs direction is given in the neutron beam reference frame by the vector $\vec{V}_{\text{FF}}$:

$$\vec{V}_{FF} = P_1 - P_0 = (x_1 - x_0, y_1 - y_0, z_1 - z_0) \tag{1.20}$$

the azimuthal angle around the beam axis which is the z axis is equal to:

$$\phi = arctan\left(\frac{y_1 - y_0}{x_1 - x_0}\right) \tag{1.21}$$

The position on target where the fission event was produced can be obtained from the FFs hits position on the detectors using equivalent triangles as shown in Fig. 1.46 for the x coordinate. The y coordinate is obtained by the equivalent calculation.

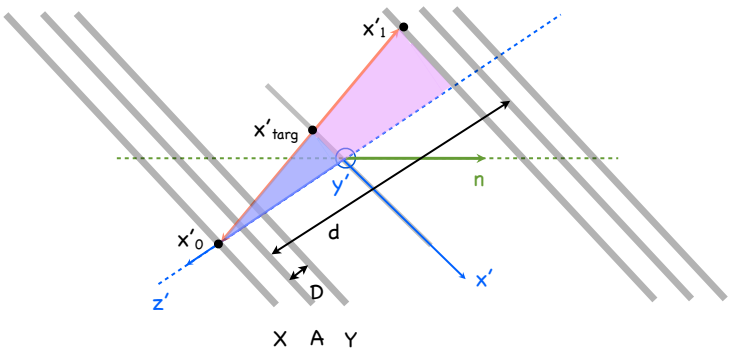

Figure 1.46: Scheme of the x position on target calculation. The cathodes are named X and Y while the anode is designated by A. The distance between the cathode and the anode is identified by D and the distance between anodes by d.

Hence, the position on target coordinates are:

$$\begin{aligned} x'_{targ} &= x'_0 + \frac{x'_1 - x'_0}{d} \cdot \left(\frac{d}{2} + D\right) \\ y'_{targ} &= y'_0 + \frac{y'_1 - y'_0}{d} \cdot \left(\frac{d}{2} - D\right) \end{aligned} \tag{1.22}$$

Some of the selected events coordinates (x'$_{targ}$, y'$_{targ}$) are out of the real sample deposit, therefore they do not correspond to fission events on such sample and they are removed from the analysis.

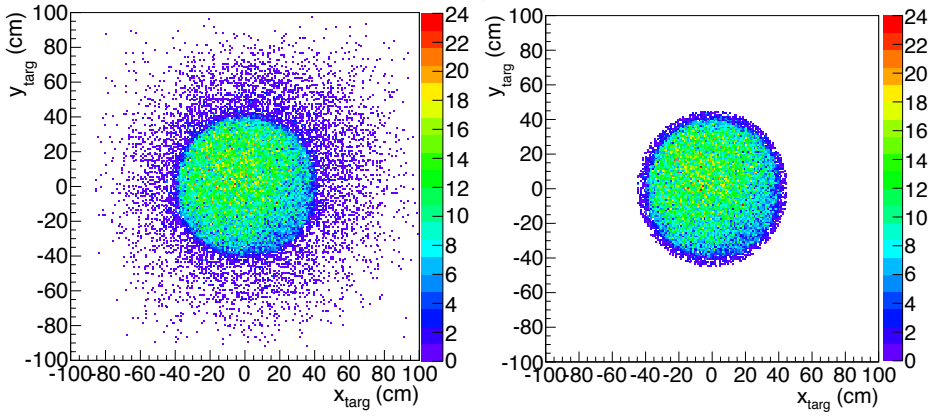

Figure 1.47: Fission position on target before the geometrical cut (left panel) and after it (right panel) for a group of events.

This is performed by means of a circular cut on the target position coordinates with radius of the order of the sample deposit (see Fig. 1.47). The cut perimeter has been defined using a radius slightly higher than the 40 cm of the deposit considering its possible deviation from the center and shape deformation.

USC
UNIVERSIDADE
DE SANTIAGO
DE COMPOSTELA

Chapter 2

Fission Fragment Angular Distributions

In this chapter, after a brief introduction of the FFAD fundamentals, the method used to obtain the FFAD will be described and the results obtained for the ^{234}U(n,f) and ^{235}U(n,f) reactions, calculated experimentally from the cathodes up to 300 MeV, will be presented and compared with the experimental data available in the literature.

The EXFOR database provides angular distribution experimental data of the ^{234}U(n,f) reaction up to 15 MeV and of the ^{235}U(n,f) up to 200 MeV. The present data will be compared with them and discussed, extending the ^{234}U and ^{235}U angular distributions up to 300 MeV and providing new information.

Above ∼300 MeV the pile-up and noise effects in the cathode signals affects highly to the reconstruction of the FFs trajectories and therefore, the angular distributions above such energy could not be obtained experimentally and had to be calculated using a different procedure.

The geometrical efficiency obtained in this chapter will be used in the next chapters to calculate the ^{234}U(n,f) cross section up to 100 keV, where the FFAD is isotropic, and from 100 keV up to 1 GeV, where the FF are not emitted isotropically and the detection efficiency depends on the FFAD.

2.1 Fission fragment angular distribution

As it was previously mentioned in the Introduction of this memory, the fission dynamics can be interpreted as the result of a compound nucleus having an evolving potential energy because of it is changing from its initial drop shape to the twofold drop which will produce the final FFs. This can be understood considering potential-energy surfaces (see Fig. 7 in the In-

troduction) where different fission paths are associated with a first fission barrier, followed by potential ridges defining different saddle points going to different valleys with its corresponding excited states, that are defined by a set of quantum numbers.

A. Bohr suggested in 1956 that a fissioning nucleus ends having low excitation energies in the outer well (for example after having surpassed the last saddle point) because in the transition process from the initial excited state to the last saddle point, most of the excitation energy has been used to get the nucleus deformed and it becomes thermodynamically cold with a spectrum of excited states similar to that found near the ground state of a normal nucleus. In other words, it should be in one of the few levels with well defined quantum numbers, as it do after capture of a low energy neutron. This idea is supported by the photofission studies (see [60]), where the dipole gamma absorption necessarily produces well defined quantum numbers. Some calculations showed that the first barrier is equal for the different fission modes [61], being found the bifurcation point in the second minimum and so different modes exhibit different outer barriers.

It is worth to recall that in the (n,f) reaction, below the second chance energy threshold, an odd-nucleus (as ^{235}U) becomes an even-nucleus after neutron capturing and, conversely happen for the even ones (as ^{234}U). Also, the compound nucleus remains in an excited state, being able to emit gammas changing the angular momentum. Therefore, the FFAD will depend on the fate of the compound nucleus. This dynamics becomes more complex above some 2 to 7 MeV, where the excess of excitation energy is enough to emit a neutron and, this second chance fission is then ruled by the quantum constraints of the new compound nucleus.

It can be concluded, from what it is exposed in the Appendix C, that different FFAD are obtained for different transition states, characterised by a set of quantum numbers, as well as by its barrier energy heights and a characteristic energy defining the barrier curvature. Therefore, for excitation energies near the fission barrier, only one or a few fission channels are found with well defined quantum numbers, and, this condition changes for each fission chance. This is the reason why huge changes of the FFAD anisotropy are found close to these fission chances, being the more clearly observed n the even-even isotopes at its first chance threshold. The anisotropy of the FFAD at higher energies (beyond the spallation region) remains a controversial question. Some theoretical models indicate that, fission at these energies should be isotropic and equal for both proton and neutron-induced reactions. However, an anisotropic behaviour was firstly found for ^{232}Th and ^{238}U up to 100 MeV by Ryzhov et al. [63] and, is definitively confirmed for both, ^{234}U and ^{235}U by the results of this thesis work.

The accurate measurement of the FFAD is required for a very precise calculation of the (n,f) cross sections, correcting for the efficiency of the experimental setups having a limited angular acceptance in the FFs detection. Furthermore, simultaneous reproduction of both: fission cross sections and FFAD is important for the determination of the fission barrier parameters [17,64].

2.2 Experimental results

The number of emitted fission fragments in function of the emission angle, considering it as the angle between the direction of the emitted fragments and one of the beam, is given by:

$$W_{emitted}(E_n, \theta)_x = \Phi(E_n) \cdot N_x \cdot \frac{d\sigma(E_n, \theta)_x}{d\Omega} \tag{2.1}$$

where $\Phi(\mathrm{E}_n)$ is the time-integrated neutron flux, N is the areal density of the target x and $\mathrm{d}\sigma(\mathrm{E_n},\theta)/\mathrm{d}\Omega$ is the differential cross section of the FF emitted with an angle θ.

Not all the emitted fragments can be detected because they may be stopped before reaching the detector by the traversed material. The quantity of traversed material depends on the distance that the fragment has to go through from its emission until reaching the detector. This distance is a function of the emission angle with respect to the beam (θ) and, because of the inclination of the detectors and targets, also of the azimuthal angle of the emitted fragments around the beam direction (ϕ). Hence, in order to calculate the number of detected fragments, Eq. 2.1 has to be multiplied by an efficiency factor in function of θ and ϕ. Therefore, the number of detected fragments in function of the emission angle is given by:

$$W_{detected}(E, \theta)_x = \Phi(E_n) \cdot N_x \cdot \frac{d\sigma(E_n, \theta)_x}{d\Omega} \cdot \epsilon(\theta, \phi)_x \tag{2.2}$$

Consequently, from Eq. 2.1 and Eq. 2.2, the number of emitted fragments is given by:

$$W_{emitted}(E_n, \theta)_x = \frac{W_{detected}(E_n, \theta)_x}{\epsilon(\theta, \phi)_x} \tag{2.3}$$

The number of detected fission fragments in function the emission angle has been obtained as it was explained in the previous chapter. In order to obtain the angular distribution of the emitted fission fragments it is necessary to divide the cosine distributions of the detected fragments by the detection efficiency of the tilted setup as given in Eq. 2.3.

2.2.1 Geometrical efficiency

The ^{235}U(n,f) and ^{234}U(n,f) angular distributions are isotropic below 1 keV, hence, the detection efficiency can be obtained from cosine distribution of the emitted angle in such energy range. As the angular distribution is known to be flat at these energies, then the shape of the cosine distribution in that energy region is fully due to the detection efficiency [3]. Considering that the detection efficiency is independent of the incident neutron energy, the efficiency distribution obtained at low energy can be used to calculate the angular distribution in the overall energy range.

During the experiment, one of the preamplifiers connected to the delay line in the cathode X of the PPAC 4 did not work. This detector was located between the ^{237}Np and one of the ^{234}U targets and, therefore, the fission fragment trajectories could not be reconstructed for these two targets. For this reason, both targets have been discarded from the analysis of the cathodes and only two of the three ^{234}U targets have been used to study the ^{234}U(n,f) FFAD. In the case of the ^{235}U all the samples have been used.

The cosine distributions below 1 keV obtained for the ^{234}U samples, both with thick backing, and for the ^{235}U targets, with thick and thin backings, are shown in the left and right panels of Fig. 2.1 respectively.

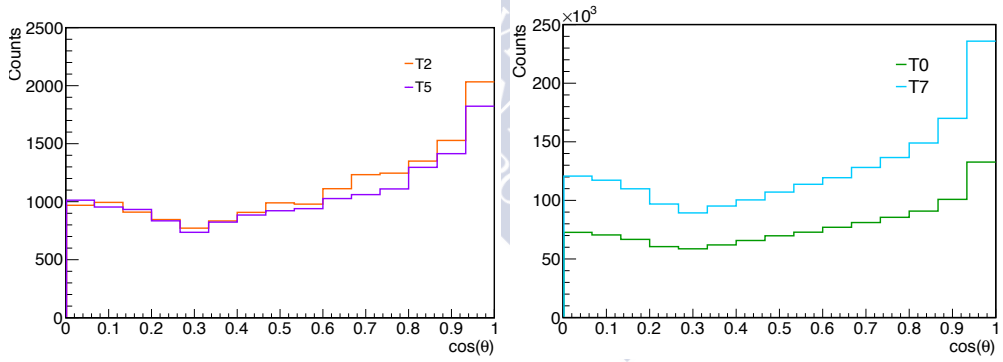

Figure 2.1: Cosine distribution below 1 keV for the first (orange line) and the second (violet line) ^{234}U(n,f) thick backing targets (left panel) and for the thick (green line) and the thin backing (cyan line) ^{235}U(n,f) targets (right panel).

The higher number of detected events for the target 7 compared with the target 0 is due to the different backing thickness, because in the thick backing sample, the FF have to traverse more material and it may be stopped before reaching the detector.

In order to obtain the geometrical efficiency distribution in function of the cosine of the emitted angle in the reference system defined by the neutron

beam, the efficiency shape obtained at low energies has to be properly normalized. For this purpose one can turn to the reference frame perpendicular to the detector (primed coordinates) and calculate the distribution below 1 keV in function of the cosine of the emitted angle ($\cos\theta'$). The normalisation procedure is the same for all the targets, taking as an example the ^{235}U(n,f) thick backing target, the $\cos\theta'$ distribution up to 1 keV is shown in Fig.2.2.

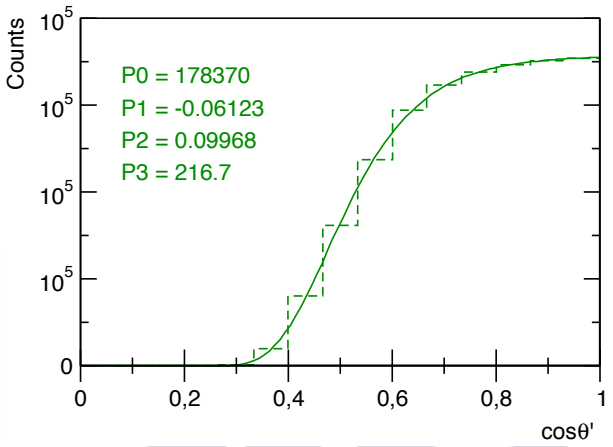

Figure 2.2: Distribution below 1 keV in function of the cosine of the emission angle in the reference system perpendicular to the detectors obtained for the ^{235}U thick backing sample (dashed line) fitted to a Fermi-like functional form (solid line).

In the detector reference frame, the maximum efficiency (ϵ=1), this is when all the FF are detected, is obtained at angle 0°, hence such distribution can be normalised to 1 at $\cos\theta' = 1$. In order to avoid statistical fluctuations, the $\cos\theta'$ distribution has been previously fitted to a Fermi-like functional form given by Eq. 2.4, which reproduces accurately the shape of the distribution [31].

$$\epsilon(cos\theta') = \frac{P_0}{[1 + exp((P_1 - cos\theta')/P_2)]^{P_3}} \tag{2.4}$$

Knowing the normalisation factor of the $\cos\theta'$ distribution and performing a change of coordinates to the beam reference frame one can obtain the normalisation factor that should be applied to the efficiency curve in function of $\cos\theta$. The efficiency distribution obtained for the ^{235}U(n,f) thick backing target is shown in Fig. 2.3.

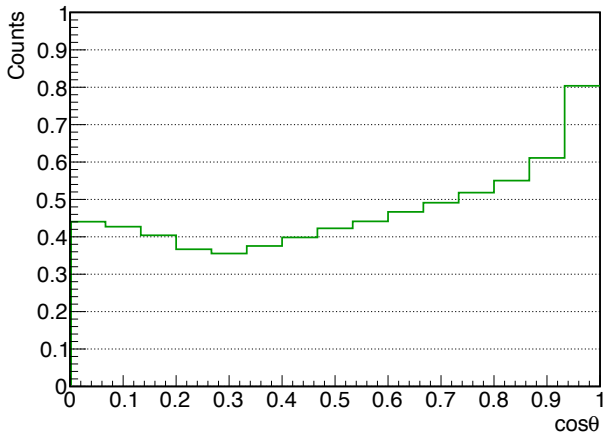

Figure 2.3: Geometrical efficiency obtained in function of cosθ for the ^{235}U(n,f) thick backing target.

2.2.2 Experimental angular distribution

The angular distribution has been calculated, for each energy interval up to 300 MeV dividing the cosine distributions of the detected fragments by the geometrical efficiency. Each energy interval has been determined by having a minimum of about 2000 counts compensating the number of counts per energy bin and the number of bins in the cosine distribution, which has been divided in 15 bins. A logarithmic energy binning have been used for each isotope in which each decade has a different binning according to the minimum number of counts required.

The angular distribution obtained for each energy range has been normalized to the first bin in the cosine distribution, this is to the value at cosθ equal to zero in order to facilitate the comparison between them.

The FFAD obtained for the ^{234}U and ^{235}U have been calculated as the mean value of the targets with the same isotope. The error bars indicate the statistical uncertainties.

^{234}U(n,f) FFAD

The ^{234}U(n,f) FFAD have been calculated using two of the three ^{234}U targets, as it was previously mentioned. The results obtained with both targets have been compared, an example is shown in Fig. 2.4 where the ratios between each sample and the mean value show differences lower than a 11%.

At the moment, the available experimental data provided in the EXFOR database have a maximum neutron energy of 15 MeV. The data presented

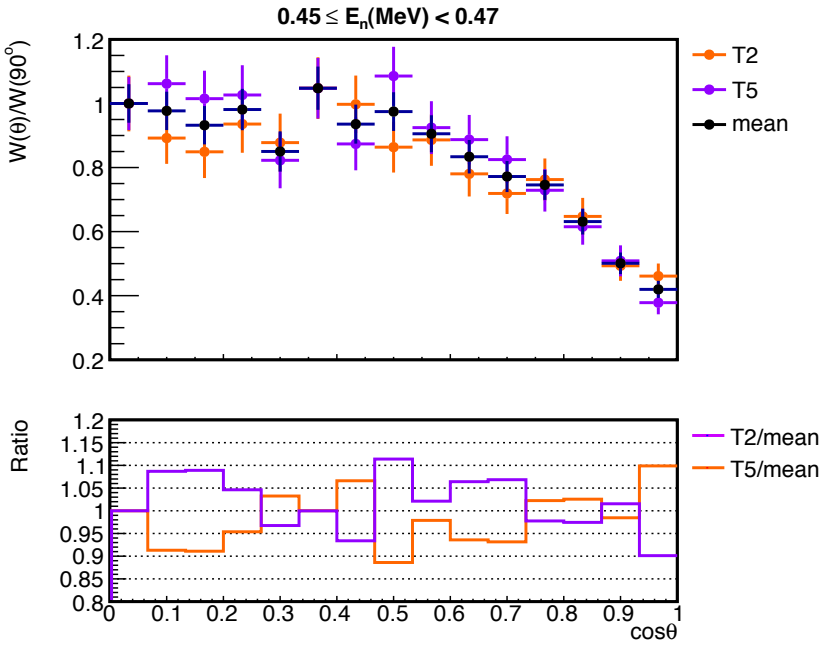

Figure 2.4: The ^{234}U(n,f) angular distribution obtained, in the energy range from 0.45 MeV to 0.47 MeV, with both thick backing samples (orange and violet marks), together with the mean value of both targets (black marks) are shown in the upper panel. The ratios of both samples results and the mean value are shown in the lower panel.

in this work will extend this energy region up to 300 MeV.

The ^{234}U(n,f) angular distributions have been compared with the most compeherensive sets of data provided in EXFOR. Those are the values measured in the threshold by Bekhami [32] 1968, which provides angular distributions between 0.20 MeV and 1.184 MeV, the data obtained by Simmons [33] in 1960 between 0.60 MeV to 8.50 MeV and the angular distributions measured by Lamphere [34] in 1962 between 0.843 MeV and 3.74 MeV. Above 9 MeV and up to 14.95 MeV, the present data have been compared with the angular distributions provided by Leachman [35] in 1965.

Some examples are shown in Fig. 2.5 for different energy ranges. In order to compare the angular distributions obtained by Bekhami with the rest of datasets, they have been normalised to the lower value of the cosine. The full energy range figures are given in the Appendix B.

In the threshold region, so-called **First Chance**, the angular distribution varies highly in a brief energy range from *side − peaked*, this is when the maximum value of the distribution is obtained at 90°, to *forward − peaked*,

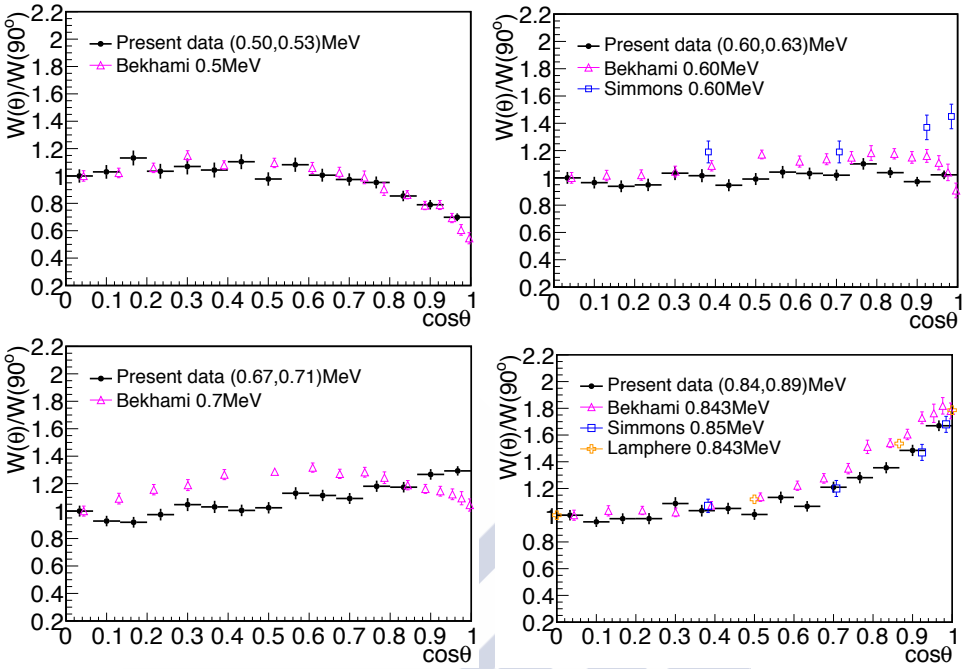

Figure 2.5: Present data (black filled circles) compared with the experimental data obtained by Bekhami (magenta empty triangles), Simmons (blue empty squares) and Lamphere (yellow empty crosses) in the threshold energy range.

when the maximum is obtained at 0°.

As it is shown in Fig. 2.5, between 0.50 MeV and 0.53 MeV, the present data are in a very good agreement with Bekhami, both showing a side-peaked distribution. Between 0.60 MeV and 0.63 MeV, there is a discrepancy between the side-peaked distribution obtained by Bekhami and the forward-peaked distribution obtained by Simmons, while the present data exhibit a flat distribution in such energy range. In the energy interval from 0.67 MeV and 0.71 MeV, Bekhami continues showing a side-peaked distribution, while the present data show a forward-peaked distribution, which is more prominent in the higher energy range, from 0.84 MeV to 0.89 MeV, where the three experimental data agree. These data indicate that the angular distributions of Bekhami change rapidly from side-peaked to forward-peaked between 0.71 MeV and 0.84 MeV while Simmons remains showing a constant forward-peaked behaviour. The present data, however, display a slower transition from side-peaked to forward-peaked in a wider energy range.

In the **Second Chance** the excitation energy of the compound nucleus is higher than the maximum of the fission barrier plus the neutron binding energy, therefore one neutron may be emitted from the compound nucleus

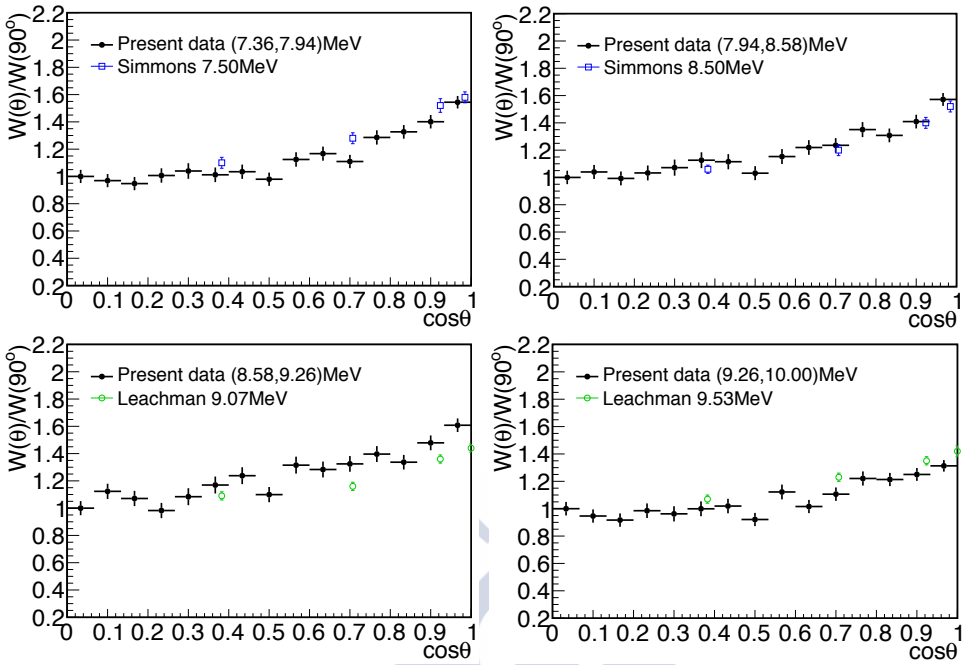

Figure 2.6: Present data (black filled circles) compared with the experimental data obtained by Simmons (blue empty squares) and Leachman (green empty circles) in the Second Chance energy range.

before it undergo fission. In this region, the anisotropies observed on the angular distributions are significative, being, however, lower than in the First Chance. In this energy region, the present data have been compared with Simmons and Leachman, as it is shown in Fig. 2.6, presenting a forward-peaked behaviour in all the datasets. Between 7.36 MeV and 8.38 MeV, the present data are in very good agreement with Simmons and, in the energy region from 8.58 MeV to 10.0 MeV with Leachman, being slightly above them between 8.58 MeV and 9.26 MeV.

^{235}U(n,f) FFAD

The ^{235}U(n,f) FFAD have been calculated for the two ^{235}U samples, which had different backing thickness. The data obtained using both targets and its mean value are compared in Fig. 2.7 in the neutron energy range from 12.59 MeV to 15.85 MeV. The ratios between each sample and the mean value show differences below the 11%.

The mean value of the ^{235}U(n,f) angular distributions has been compared with the most complete angular distribution data provided in EXFOR, which were measured by Simmons in 1960 between 0.52 MeV to 20 MeV and by

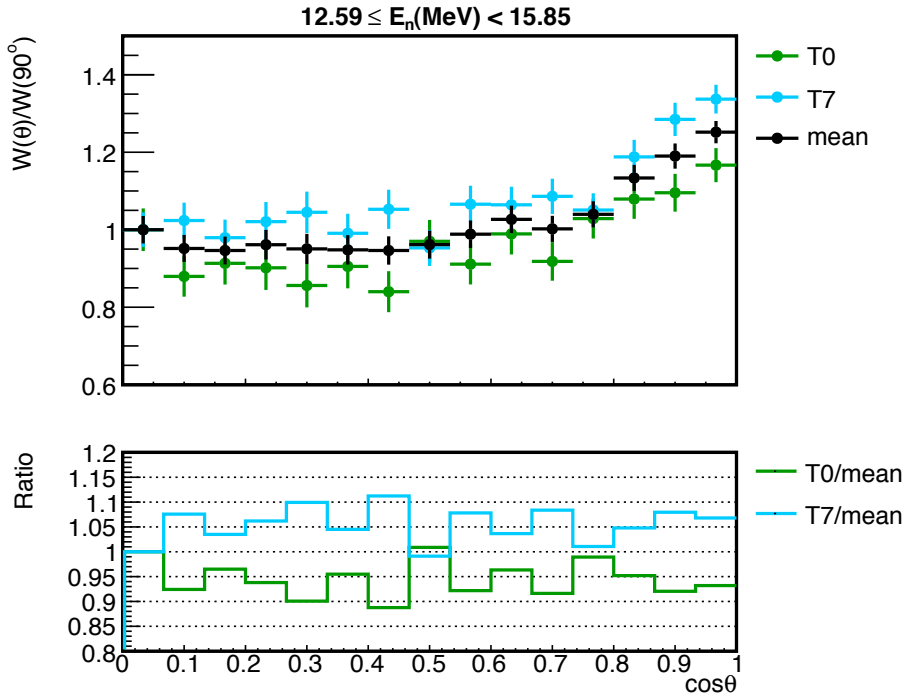

Figure 2.7: The ^{235}U(n,f) angular distribution obtained, in the energy interval from 12.59 MeV to 15.85 MeV, with the thick (green marks) and the thin backing (cyan marks) samples, together with the mean value of both targets (black marks) are shown in the upper panel. The ratios of both samples results and the mean value are shown in the lower panel.

Leachman in 1965 in the energy region from 0.70 MeV to 13.40 MeV. The figures in the full energy range are provided in the Appendix B.

The present data are in good agreement with Simmons and Leachman in the Second Chance energy region, showing all of them a forward-peaked distribution, see Fig. 2.8.

The anisotropy increases in the **Third Chance**, when the incident neutron energy is enough to lead to the emission of two neutrons from the compound nucleus before it fissions, as it is shown in Fig. 2.9, where the angular distributions have been compared with Simmons and Leachman, following, in all the data sets, a forward-peaked distribution.

Between 12.59 MeV and 15.85 MeV, this data are in good agreement with both experimental data and, from 15.85 MeV to 19.95 MeV they are systematically below Simmons.

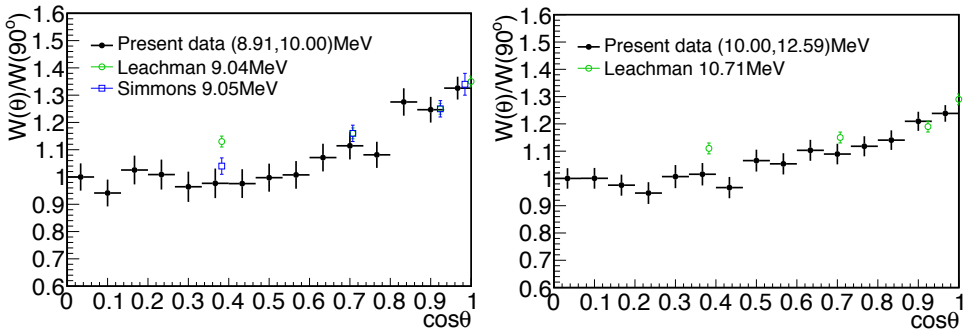

Figure 2.8: Present data (black filled circles) compared with the experimental data obtained by Simmons (blue empty squares) and Leachman (green empty circles) in the Second Chance.

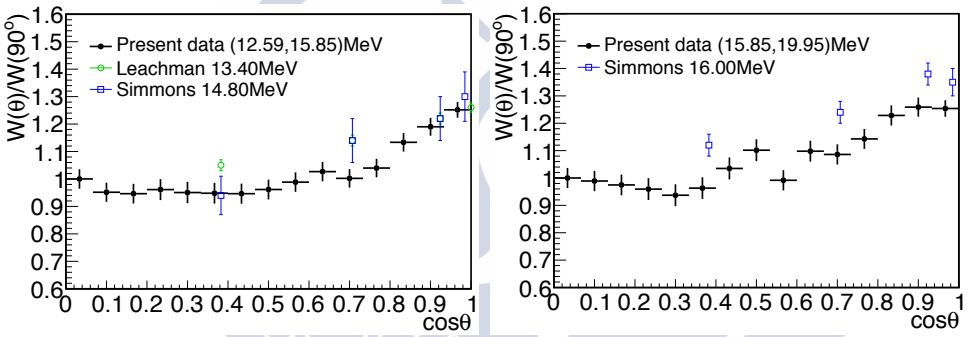

Figure 2.9: Present data (black filled circles) compared with the experimental data obtained by Simmons (blue empty squares) and Leachman (green empty circles) in the Third Chance.

2.2.3 Legendre polynomials

The angular distribution of the emitted fission fragments can be expressed as a series of Legendre polynomials in function of the cosine of the emission angle given by:

$$W(cos\theta) = A_0 \left(1 + \sum_{L=2}^{L_{max}} A_L P_L(cos\theta) \right) \tag{2.5}$$

Only even terms of the polynomials have been used due to the backward-forward symmetry of the emitted fission fragments. The angular distributions are usually fitted up to the second order, which is the simplest case, when the energy region under study is not characterized by rapid variations of the angular distributions, for example in the case [36], where the interested region was the high energies and the second order was enough to fit the

angular distributions. However, at energies where the angular distributions suffer significative variations in short energy ranges, as in the fission chances, fits up to the fourth order Legendre polynomials are required in order to reproduce better the angular distributions. The fourth order fits produce small differences with respect to the second order in the cases in which the second order is applicable, for this reason, the angular distributions obtained in this work for the ^{234}U(n,f) and the ^{235}U(n,f), have been fitted to the fourth order Legendre polynomials in the whole energy range, see the figures in Appendix B. The values of the parameters obtained from the fits are given in the tables of Appendix B. Note that the sixth order fit, used in other works [3,37], was also tested in the present data, however it was dominated by the statistical fluctuations being discarded in this analysis.

^{234}U(n,f) FFAD

The ^{234}U(n,f) angular distributions calculated in the previous subsection were fitted to the 2^{th} and 4^{th} order polynomials and the results of both fits were compared to select which was the maximum order required.

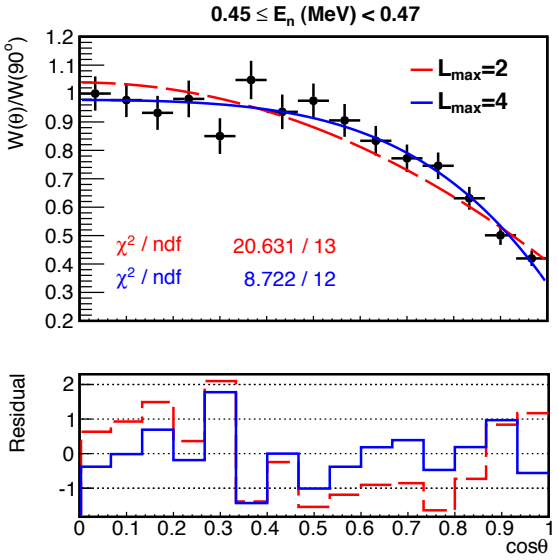

Figure 2.10: ^{234}U(n,f) angular distribution obtained, in the energy range from 0.45 MeV to 0.47 MeV fitted to the 2^{th} and 4^{th} order Legendre polynomials (upper panel) and the residuals obtained with both fits (lower panel).

An example of both fits to the angular distribution obtained in neutron energy range between 0.45 MeV and 0.47 MeV is shown in Fig. 2.10, where the better fit to the experimental data is achieved using the fourth order.

The fits up to the 4^{th} order Legendre polynomials of the experimental ^{234}U(n,f) angular distributions in the energy range from 0.1 MeV to 300 MeV are shown Fig. 2.12. The angular distributions in the figure have been normalised to the value obtained at cosθ equal to zero so that the anisotropy parameter, which is the ratio between the distributions obtained at 0° and 90°, is observed in the front projection.

^{235}U(n,f) FFAD

The ^{235}U angular distributions have been also fitted to the 2^{th} and 4^{th} order polynomials.

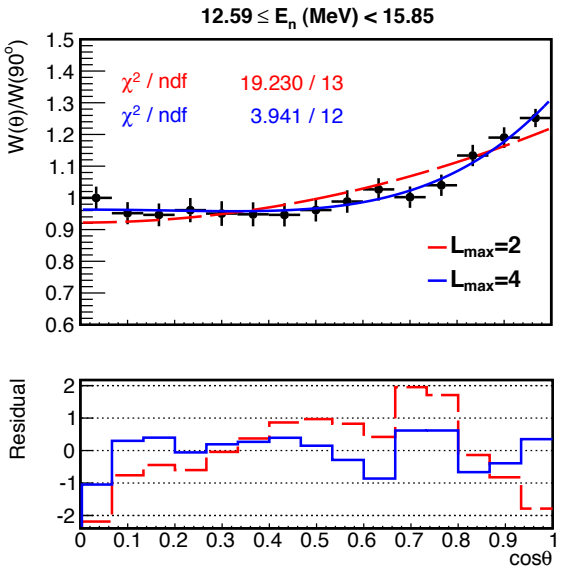

Figure 2.11: ^{235}U(n,f) angular distribution obtained, in the energy range from 12.59 MeV to 15.85 MeV fitted to the 2^{th} and 4^{th} order Legendre polynomials (upper panel) and their residuals (lower panel).

The values obtained in the energy interval from 12.59 MeV to 15.85 MeV are represented in Fig. 2.11, showing that the best fit is obtained with the 4^{th} order polynomial. As in the case of the ^{234}U, the ^{235}U(n,f) angular distributions fits up to the 4^{th} order Legendre polynomials are shown, in the energy range from 0.1 MeV to 300 MeV, in Fig. 2.13.

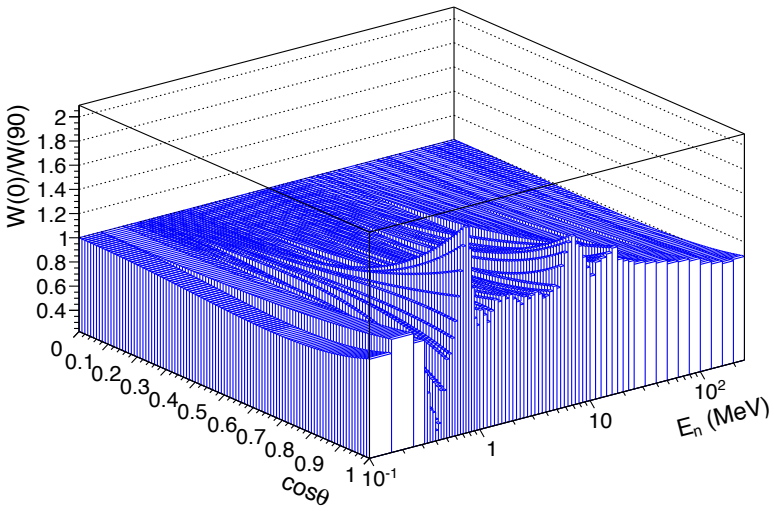

Figure 2.12: ^{234}U(n,f) angular distributions in function of the incident neutron energy.

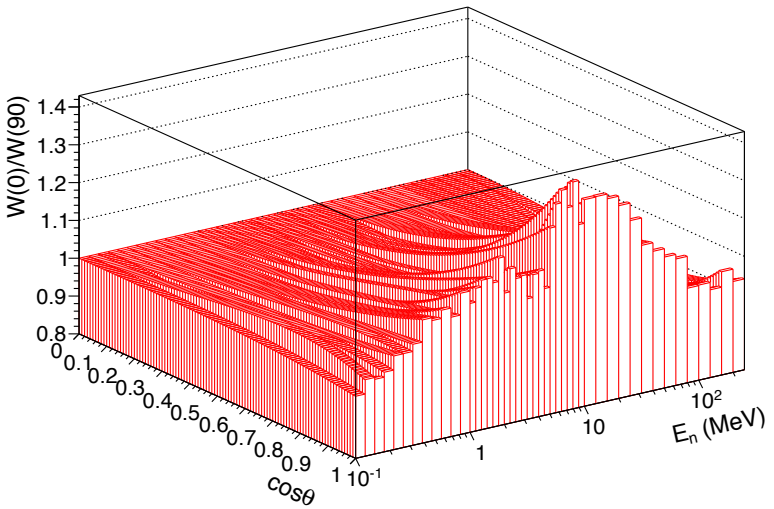

Figure 2.13: ^{235}U(n,f) angular distributions in function of the incident neutron energy.

2.2.4 Anisotropy parameter

The anisotropy parameter is the ratio between the angular distributions obtained at 0° and 90° and is commonly used to study the angular distributions in function of the incident-neutron energy. This parameter is useful to identify at which energies the angular distribution is not isotropic and also if the preferred emission angle is 0° or 90°. However, it is not enough to describe the angular distributions in the cases in which the FF preferred emission angle is not 0° neither 90°, this is when the distribution is not peaked at the edges but at intermediate angles.

The anisotropy parameter has been calculated through the values of the coefficients obtained from the fit of the angular distributions to the 4^{th} order Legendre polynomials with Eq. 2.6 which is obtained from Eq. 2.5,

$$\frac{W(0°)}{W(90°)} = \frac{1 + A_2 + A_4}{1 - \frac{1}{2} \cdot A_2 + \frac{3}{8} \cdot A_4} \tag{2.6}$$

where the coefficient A_0 cancels in the quotient. The error bars indicate the propagation of the uncertainties of the coefficients obtained from the fits to the 4^{th} order Legendre polynomials.

^{234}U(n,f) anisotropy parameter

The EXFOR library supplies experimental data of the anisotropy parameter up to an incident neutron energy of 15 MeV providing information, from different sets of data, of the threshold and the second chance. The anisotropy parameter has been obtained in this work up to 300 MeV, providing enough statistics to reproduce accurately the threshold and resolving for first time the third chance located at ∼12 MeV.

The present anisotropy parameter is compared with the experimental data provided in EXFOR in Fig. 2.14 from 100 keV up to ∼300 MeV.

These data were measured using a continuous neutron beam which present some advantages with respect to other measurements performed with monoenergetic beams [33,32,35], as a better resolution in energy and the possibility of providing anisotropy data in a wide energy range. Another advantage is the high energy achieved by the incident neutrons, 1 GeV, which allows to extend the experimental angular distribution data above the 15 MeV provided in the literature, however the pile-up effects in the signals of the cathodes at high energies limit the accuracy of the measurements to ∼300 MeV.

The good statistics achieved in this work permits to provide enough bins in the cosine distribution to provide a good description of the angular dis-

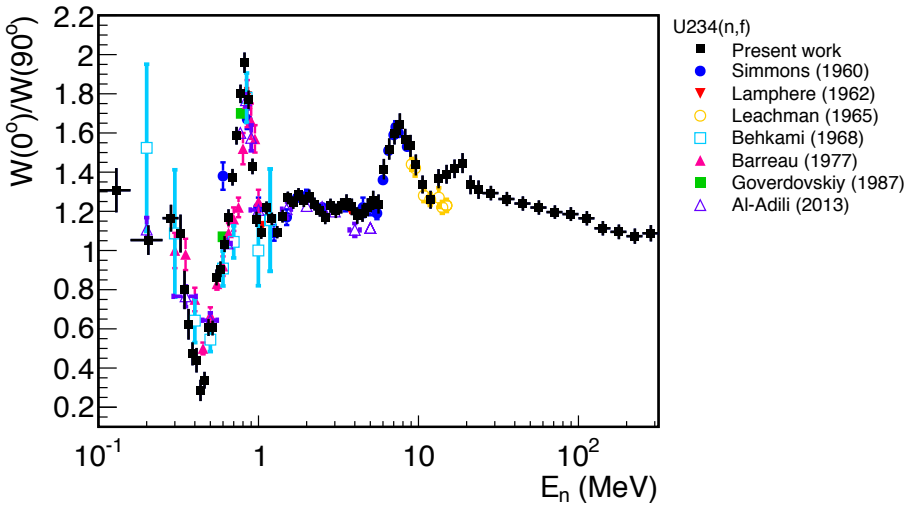

Figure 2.14: ^{234}U(n,f) anisotropy parameter compared with the EXFOR experimental data.

tributions, contrary to previous measurements as in the case of Simmons or Leachman which provided four points. The number of bins used in the present angular distributions is fifteen, close to the sixteen values of the cosine given by Bekhami.

Another feature of the present measurement is that the 45° tilted setup permits to detect the FF emitted at angles from 0° to 90° degrees, extending the angular range achieved, in the previous n_TOF experiment, with the non-tilted setup whose maximum detected angle was 60° and, therefore the anisotropy parameter had to be calculated extrapolating to 90° the angular distributions, diminishing its accuracy [29].

In this work, the angular distributions have been calculated experimentally up to ∼300 MeV. In the fission sub-threshold, the statistics were poor to provide anisotropy parameter data in narrow energy intervals. The previous experimental data provided in this region are scarce, both, Al-Adili [38] and Bekhami, give one point below the threshold with different values of the anisotropy parameter inside the error bars, which are very high for the last one. The present data are in better agreement at this energy with the value provided by Al-Adili.

In the threshold the situation changes and it is possible to reproduce a detailed structure of the anisotropy parameter. When comparing with previous experimental data [32,38] the present data are in good agreement in the maximum, however a deeper minimum around 450 keV has been observed in this experimental data with respect to them.

At higher energies, after the threshold, some structures are found in the anisotropy parameter, corresponding to vibrational resonances, which were already observed by Simmons, being reproduced in more detail in this work. Other works [38] found a smooth behaviour in this energy region, in which the anisotropy parameter was calculated relative to the isotropic ^{235}U distribution obtained at thermal neutron energies.

The second chance structure is well reproduced combining two sets of previous experimental data. The rising structure is given by Simmons and the tail is reconstructed by Leachman, however there is not a unique set of experimental data in the literature providing the full anisotropy parameter shape in the vicinity of the second chance. The present data provides information of the anisotropy parameter in the full energy range, providing a complete reconstruction of the anisotropy structure found around the second chance. Furthermore, this data provides information, for first time, of the third chance where there are not previous experimental data in the literature. Large anisotropies have been found in the present data near the third chance, showing a well-defined structure.

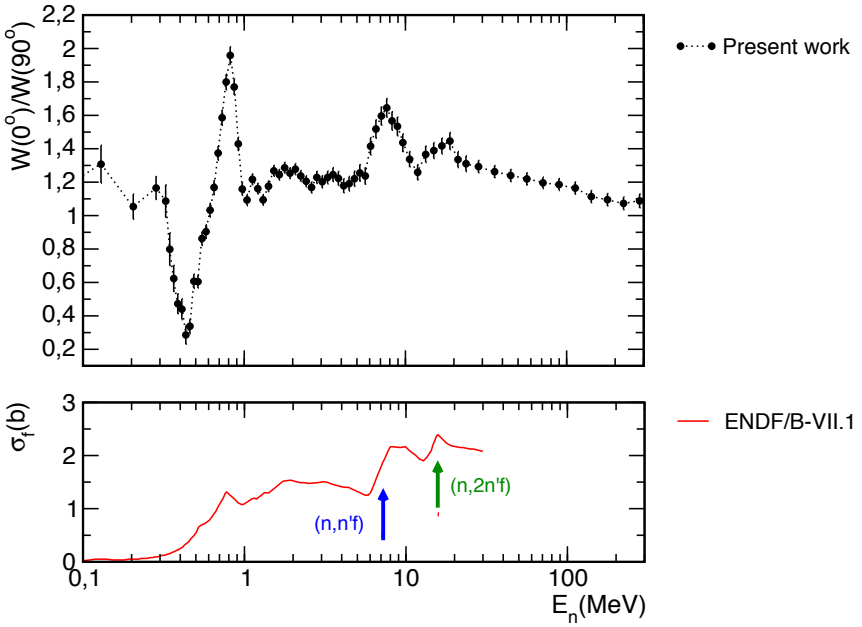

Figure 2.15: ^{234}U(n,f) anisotropy parameter (upper panel) compared with the ENDF/B-VII.1 ^{234}U(n,f) cross section.

After the third chance, the present data are the only available measurement showing a decreasing smooth tendency of the anisotropy parameter to the isotropic case.

The anisotropy parameter is compared with the ^{234}U(n,f) cross section given in the ENDF/B-VII.1 database in Fig. 2.15, showing that large variations of both, the anisotropies and the fission cross sections are observed near the fission chances.

In the fission threshold, the ^{234}U target anisotropy increases highly, having a similar behaviour than the ^{232}Th target isotope. As it was pointed out in previous works [3], it is considered to be due to the fact that both isotopes are even-even nuclei with 0 spin in the ground state, as the neutron spin is 1/2, the compound nucleus can undergo fission only through a few states with their defined angular momentums and the FFs are emitted at certain angles, anisotropically. In the case of the second chance, if a neutron is emitted before fission, the excitation energy of compound nucleus diminishes, dealing to a similar situation than in the threshold, however, at this energy there are more opened channels than in the threshold, minimising the anisotropies with respect to it. A similar behaviour is given in the third chance and so on.

^{235}U(n,f) anisotropy parameter

In the case of the ^{235}U(n,f) the most complete set of data provided in the EXFOR database, covering the full energy range up to 200 MeV are those of Vorobyev [36], together with recent studies performed in the n_TOF [31] and the LANSCE facilities [39].

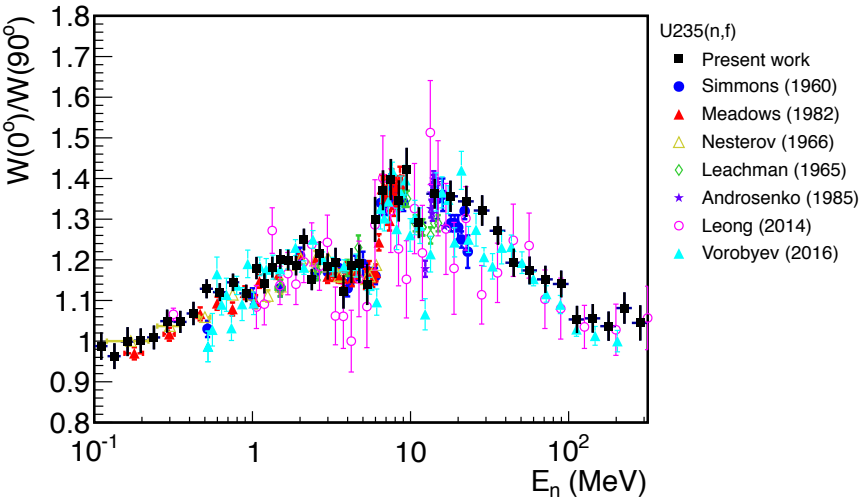

Figure 2.16: ^{235}U(n,f) anisotropy parameter compared with the available experimental data.

The present data are compared in the energy region from 100 keV up to 300 MeV with the experimental data available in EXFOR, in Fig. 2.16.

The ^{235}U target isotope is fissile, this is, the binding energy of the neutron is higher than the maximum of the fission barrier of the compound nucleus ^{236}U and, therefore it fissions at low incident neutron energies. This is the reason why no threshold is observed in the anisotropy parameter neither in the cross sections for this isotope. Instead of this, some structures are found below ∼2 MeV with an increasing tendency of the anisotropy with the energy. In this energy region, the present data are in good agreement with Meadows and Nesterov. The data provided by Vorobyev and Leong show some fluctuations in this energy range, however they are in general agreement with previous data and this work inside the error bars.

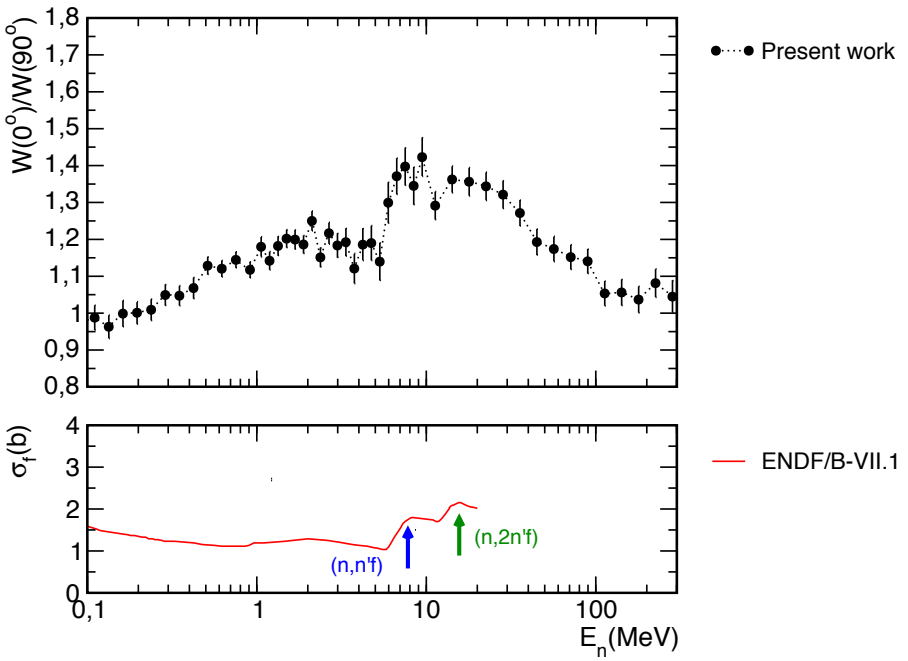

Figure 2.17: ^{235}U(n,f) anisotropy parameter (upper panel) compared with the ENDF/B-VII cross section (lower panel).

A fast increasing of the anisotropies is found in all the datasets in a thight energy range near the second chance, which hinder a detailed reconstruction of the anisotropy parameter structure. At higher energies the anisotropy varies rapidly showing a minimum in the anisotropy parameter around 11 MeV where the third chance is opened. In the vicinities of the third chance an structure is again observed in the experimental data, however the situation in this region is confused between the different datasets which exhibit high

discrepancies in the anisotropy parameter, making difficult to define a clear structure. The present data show a bump structure in this region with a tail that decreases at high energies in agreement with the available experimental data.

The anisotropy parameter tendency with the increasing energy is compared in Fig. 2.17. with the ^{235}U(n,f) cross section given in the ENDF/B-VII.1 database, showing, like in the case of the ^{234}U(n,f) that large variations of the anisotropies and the fission cross sections are observed in the vicinities of the fission chances.

2.2.5 Extrapolated angular distribution

As it was previously mentioned in the introduction of this chapter, above ∼300 MeV the pile-up and noise effects in the cathode signals prevent from a good reconstruction of the FFs trajectories. For this reason, an alternative procedure had to be applied to reproduce the angular distributions above such energy not involving the cathodes.

The anisotropy parameter can be approximated to one at the incident neutron energy of 1 GeV, therefore it has been linearly extrapolated from the value obtained experimentally at 316.23 MeV to 1 GeV. The extrapolation to 1 GeV obtained for the ^{234}U(n,f) and the ^{235}U(n,f) is shown in Fig. 2.18.

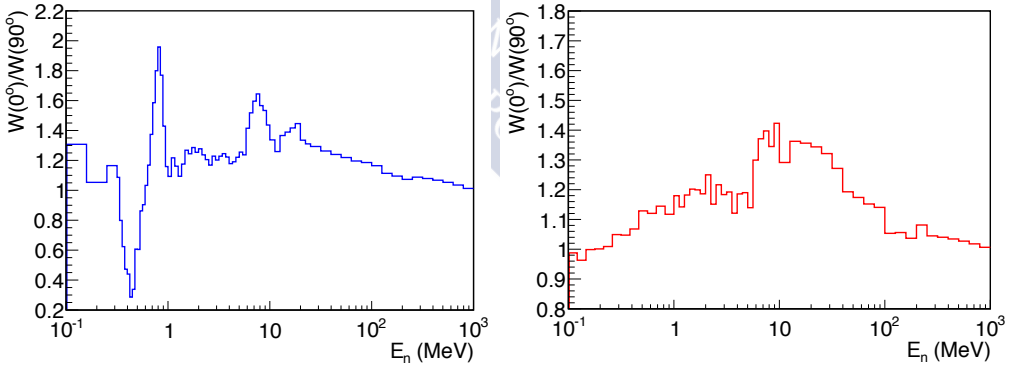

Figure 2.18: Anisotropy parameter extrapolated up to 1 GeV for the ^{234}U(n,f) (left panel) and the ^{235}U(n,f) (right panel).

The angular distributions can be reconstructed using the Legendre polynomials up to order 2 from Eq. 2.5, which is reduced to Eq. 2.7:

$$W(cos\theta) = A_0 \left[1 + \frac{A_2}{2}(3cos\theta^2 - 1)\right] \tag{2.7}$$

Using the last equation, the anisotropy parameter is calculated as:

$$\frac{W(0°)}{W(90°)} = \frac{1 + A_2}{1 - \frac{1}{2}A_2} \tag{2.8}$$

where the parameter A_0 cancels in the quotient.

Once that the anisotropy parameter is known, extracting the value of the parameter A_2 from the previous equation, and substituting it in Eq. 2.7 one can obtain the angular distributions up to 1 GeV.

The ^{234}U(n,f) and ^{235}U(n,f) angular distributions, normalised to the cosine at the angle of 90°, are shown in Fig. 2.19 in the neutron energy range from 316.23 MeV to 398.11 MeV, where the coefficient A_0 cancels in the quotient.

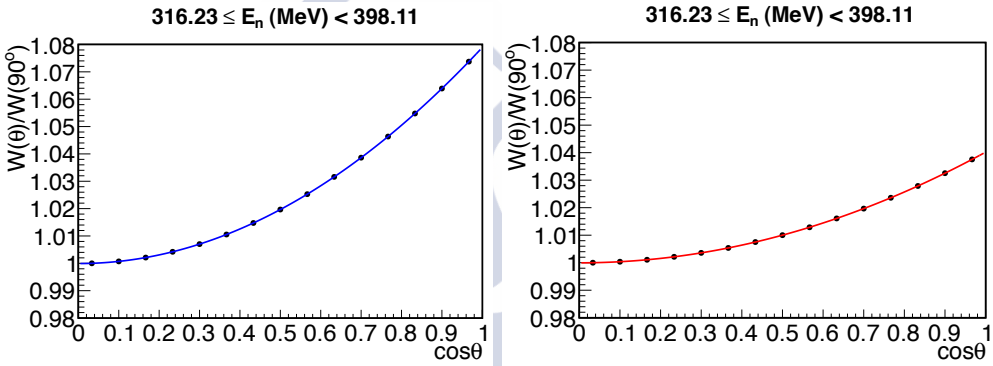

Figure 2.19: ^{234}U(n,f) (left panel) and ^{235}U(n,f) (right panel) FFAD in the neutron energy range from 316.23 MeV to 398.11 MeV.

The angular distributions obtained using both procedures: the cathodes signals up to ∼300 MeV and the extrapolations up to 1 GeV, will be included in the calculation of the detection efficiency required to obtain the ^{234}U(n,f) cross section, as it is explained in the next section.

2.3 Efficiency

An accurate measurement of the fission cross sections requires a precise calculation of the detection efficiency. The detection efficiency depends on different factors: the backing thickness, the thresholds applied in the routines and the mass distributions of the deposits in the samples.

Another factor contributing to the efficiency is the limited angular acceptance of the PPAC setup, which depends on the fragment emission angle. All these factors are included in the intrinsic efficiency calculated in this chapter for each target considering the isotropic FFAD case. However, the FFs are

emitted isotropically up to a certain energy above which, the anisotropies, which vary between isotopes, have to be included in the efficiency calculation.

The detection efficiency factor (f_θ) is therefore, given by Eq. 2.9:

$$f_\theta = \frac{\int_0^1 W(\theta) \cdot \epsilon(\theta) \cdot d(cos\theta)}{\int_0^1 W(\theta) \cdot d(cos\theta)} \tag{2.9}$$

where $\epsilon(\theta)$ is the geometrical efficiency of the detection.

Below 100 keV, the fission fragment angular distribution is isotropic ($W(\theta)$ = constant) and Eq. 2.9 is simplified to Eq. 2.10:

$$f_\theta = \frac{\int_0^1 \epsilon(\theta) \cdot d(cos\theta)}{\int_0^1 d(cos\theta)} \tag{2.10}$$

Above 100 keV, the FFAD is anisotropic ($W(\theta) \neq$ constant) and depends on the incident neutron energy. The ^{234}U and ^{235}U FFAD have been calculated in the previous section in the energy range from 100 keV to 1 GeV. Hence, using Eq. 2.9 one can calculate the efficiency factor at the different incident neutron energies for each individual target. It is worth to mention that the FFAD of the fourth target, as it was already mentioned, could not be reconstructed due to problems with one cathode. The intrinsic efficiency, in this case has been calculated as the mean value of the efficiency curves obtained for the other two ^{234}U samples.

The efficiency factors obtained for the thick backing ^{235}U and ^{234}U targets are given in Fig. 2.20.

At high energies, the neutron flux has not been accurately measured and, the ^{234}U(n,f) cross section is calculated relative to the ^{235}U. Hence, the efficiency quantity of interest is the ratio between the efficiency factors $f_\theta(^{235}U)/f_\theta(^{234}U)$.

In order to minimise uncertainties in the efficiency factor due to different backing thickness, samples with the same backing thickness have been used to calculate the cross sections.

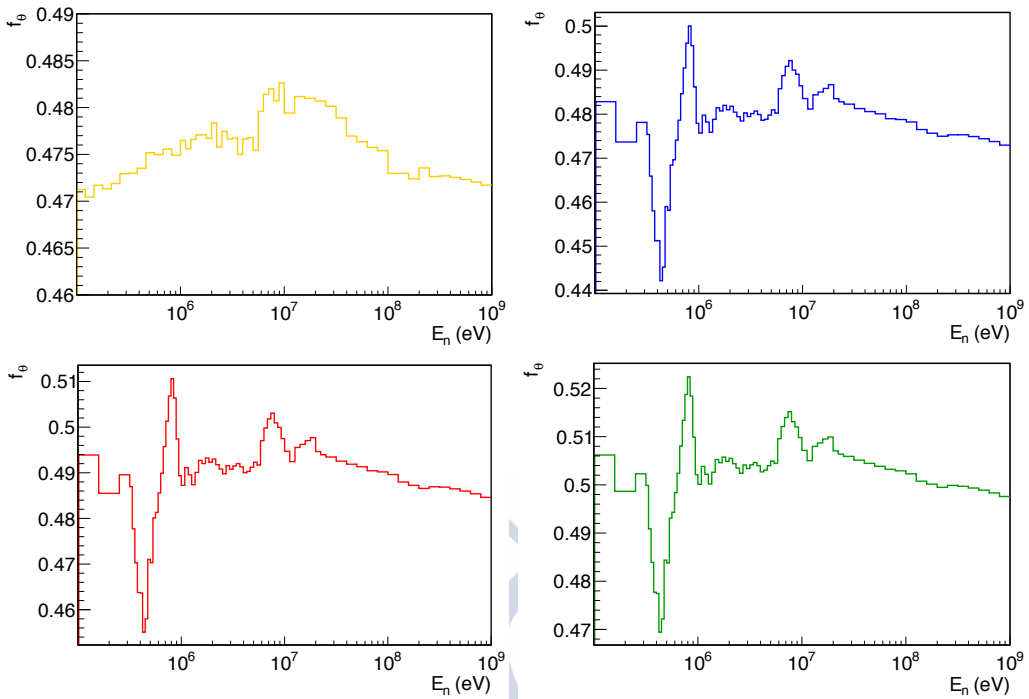

Figure 2.20: Angular efficiency factor obtained for the ^{235}U and ^{234}U samples between 100 keV and 1 GeV. The figures correspond to the ^{235}U target T0 (upper left panel) and the ^{234}U targets T2 (upper right panel), T4 (lower left panel) and T5 (lower right panel).

USC
UNIVERSIDADE
DE SANTIAGO
DE COMPOSTELA

Chapter 3

Cross section at energies below 100 keV

In this chapter, the neutron-induced fission cross section analysis and the obtained results are presented for the ^{235}U and the ^{234}U isotopes at energies below 100 keV.

The neutron flux shape obtained from the measurement of the ^{10}B(n,α) reaction with MGAS [40] has been used in this work to calculate both: the ^{235}U(n,f) and ^{234}U(n,f) cross sections from 2.75 eV up to 100 keV. In addition, the neutron flux shape obtained in this work though the PPAC measurement of the ^{235}U(n,f) reaction has been used to calculate the ^{234}U(n,f) cross section up to 10 keV.

During the experiment, in order to reduce the big size of data records, the lower energy limit was defined in this work by a time-of-flight of 8 ms, the ToF corresponding to a buffer size of 8 MB with a sampling frequency of 1 GHz (1ns time binning). This range is enough to cover completely the resonance region (RR) for the ^{234}U, because the lowest resonance reported in the evaluations is located at 5 eV. In the energy region up to 100 keV, the angular distribution of the FFs is assumed isotropic, so that no anisotropic correction has been performed to the detection efficiency.

3.1 Cross section measurement

The quantity of interest when measuring the cross section is the reaction yield per unit of energy, $Y(E_n)_{r,x}$, which is defined as the fraction of the neutron beam inducing a reaction in a sample. For a neutron-induced reaction (n,r) in a sample with N atoms per unit of area (areal density) of an isotope x, the reaction yield may be approximated, for thin samples or small cross

sections [23], to:

$$Y(E_n)_{r,x} = \sigma(E_n)_{r,x} \cdot N_x \tag{3.1}$$

where $\sigma(E_n)_{r,x}$ is the Doppler broadened cross section due to the thermal motion of the atoms in the sample, and N_x is the areal density of a target with radius R_x obtained as:

$$N_x = \frac{m_x \cdot N_A}{\pi \cdot R_x^2 \cdot M_x} \tag{3.2}$$

being m_x the mass of the sample, N_A the Avogadro Number, and M_x the atomic mass of the isotope x.

In an experiment, the measured quantity is the number of detected events per unit of energy, also denoted as total count rate, $C(E_n)_{tot,x}$. The total count rate is different from the reaction count rate, $C(E_n)_{r,x}$, which is the number of events from a reaction produced in the sample, because some of the detected events may come from a reaction on other material surrounding the sample from other reaction channels on or from the sample itself.

The reaction count rate must be corrected from this background contribution as:

$$C(E_n)_{r,x} = C(E_n)_{tot,x} - B_r \tag{3.3}$$

It is related to the reaction yield by:

$$C(E_n)_{r,x} = Y(E_n)_{r,x} \cdot f_r \cdot \Phi(E_n) \tag{3.4}$$

being $\Phi(E_n)$ the neutron flux and f_r the effective efficiency.

Combining Eq. 3.1 and Eq. 3.4:

$$C(E_n)_{r,x} = \sigma(E_n)_{r,x} \cdot N_x \cdot f_r \cdot \Phi(E_n) \tag{3.5}$$

For obtaining an accurate value of the cross section, high enough statistics are required, as well as a precise determination of both, the areal density and the effective efficiency.

3.1.1 Effective efficiency

The effective efficiency, f_r, depends on a combination of parameters and can be expressed as:

$$f(\theta)_r = A_r \cdot P(\theta)_r \cdot \Omega(\theta)_r \tag{3.6}$$

where A_r is the effective area of the sample, Ω_r is the solid angle between the target and the detector and ϵ_r is the intrinsic detection efficiency.

3.1.2 Neutron flux

The absolute or relative neutron flux expressed as a function of the neutron energy is required to calculate the cross section. It may be obtained using neutron-induced reactions, whose cross sections are well known, through Eq. 3.5 as:

$$\Phi(E_n) = \frac{C(E_n)_{r,x}}{\sigma(E_n)_{r,x} \cdot N_x \cdot f_r} \tag{3.7}$$

The preferred reactions for this purpose are those whose cross section is considered as a standard in a particular energy range. The Neutron Cross Section Standards [24] are given in Table 3.1:

Reaction	Neutron energy range
H(n,n)	1 keV to 20 MeV
^{3}He(n,p)	0.0253 eV to 50 keV
^{6}Li(n,t)	0.0253 eV to 1 MeV
^{10}B(n,α)	0.0253 eV to 1 MeV
^{10}B(n,$\alpha_1\gamma$)	0.0253 eV to 1 MeV
C(n,n)	up to 1.8 MeV
Au(n,γ)	0.0253 eV and 0.2 MeV to 2.5 MeV
^{235}U(n,f)	0.0235 eV and 0.15 MeV to 200 MeV
^{238}U(n,f)	2 MeV to 200 MeV

Table 3.1: Neutron Cross Section Standards and their energy ranges. From [24].

Standard reactions with a smooth cross section as a function of the energy are desirable in order to avoid artificial structures in the neutron flux,

although the evaluated libraries may be used instead of the standard files, i.e. the ENDF/B-VII.1 which was used in [25].

The standard reactions most commonly used for flux measurements are discussed in Appendix A. To calculate the neutron flux in a wide energy range, it may be suitable to use a combination of different reactions [25].

3.2 Samples contamination

The fission count rate indicating the number of detected fissions per neutron energy for each target has been obtained as it was explained in the previous chapter. However, as it was previously mentioned, there was a very little contamination of the samples which may contribute to the resulting counting rate, so it has to be subtracted. This is particularly important above hundreds of keV in the ^{235}U samples contaminated with ^{234}U, ^{236}U and ^{238}U, corresponding to the energies where the first chance threshold is found in the three cases, and also, in the RR in the case of the ^{234}U samples which are contaminated with ^{235}U.

As it was previously mentioned, in the fissile isotope ^{235}U, the binding energy after absorbing a neutron is higher than the maximum of the fission barrier, which is the energy required for fission and, hence, the compound nucleus can undergo fission with high probability after capturing a neutron, even for thermal energies. However, for the fertile ^{234}U, the neutron binding energy is lower than the maximum of the fission barrier and, when a neutron is captured with an incident energy below the maximum of the barrier, the probability for fission is much lower than for the fissile isotope. Therefore, due to the much higher cross section, a small contamination of ^{235}U produces a significant contribution of fission counts in the ^{234}U resonance region.

In the case of the ^{235}U targets, the presence of a 6.28 % of ^{238}U, a 0.74 % of ^{234}U and a 0.27 % of ^{236}U was rated by multiplying the percentage factor by the evaluated cross section of each isotope. The final contamination spectrum including the contribution of every isotope was subtracted from the initial one.

The contribution to the counting rate due to the isotopic contamination on the ^{234}U targets, was calculated through the quantification of a strong resonance in the spectrum produced by the contaminant isotope. Once the flight path has been conveniently applied to each target to calculate the energy from the tof, all the targets spectrums are calibrated in energy and, the counting rate obtained with the ^{235}U target may be normalised to the one of the ^{234}U in such resonance and subtracted to remove the isotopic

contamination.

The counting rate after and before the contamination subtraction for one of the ^{234}U samples is shown in Fig. 3.1.

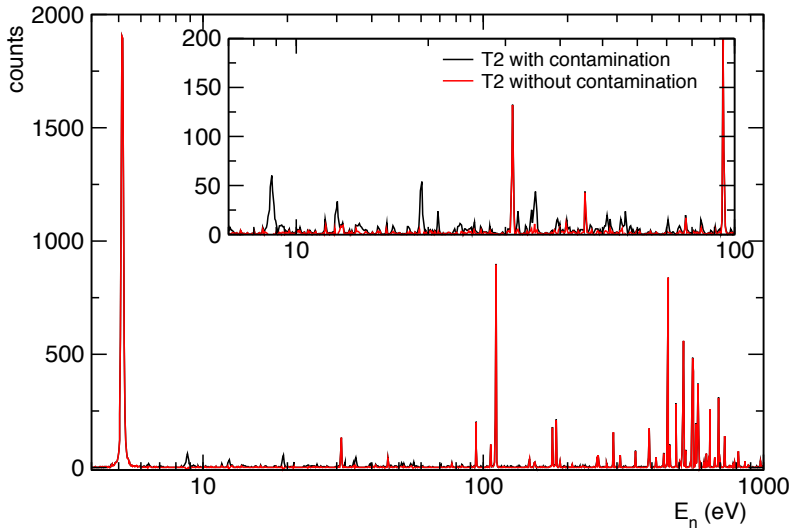

Figure 3.1: Counting rate of one of the ^{234}U samples before (black line) and after (red line) the contamination subtraction.

3.3 Neutron flux shape

During the fission 2012 campaign, with the fission collimator, the neutron flux was measured through the ^{10}B(n,α) reaction using a MGAS chamber [40] running in parallel during the PPAC experiment. As the flux is not enough accurately known, only the neutron flux shape is required. As it was mentioned in Chapter 1, below hundreds of eV (∼500 eV) the neutron flux depends on the ^{10}B concentration in the water used as moderator which changes for every campaign (when the water container is refilled) and also during the same campaign because the ^{10}B crystallises diminishing its concentration on the moderator water. Above this energy, the neutron flux is independent on it.

The official neutron flux measured in 2011 is compared in Fig. 3.2 with the flux obtained in 2012 with the MGAS up to 100 keV. This last one has been normalized to the official neutron flux in the energy range from 750 eV to 850 eV where no structure is observed in the flux shape.

The difference observed at low energies between both measurements in Fig. 3.2 indicates that the ^{10}B concentration on the moderator water was

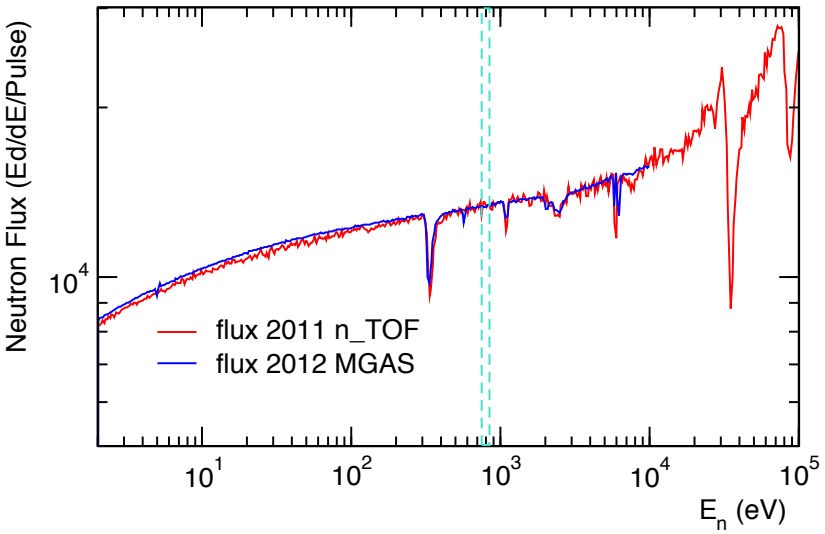

Figure 3.2: Comparison between the official neutron flux measured in 2011 during the capture campaing (red line) and the MGAS neutron flux measured in 2012 (blue line) normalized to it in the energy range from 750 eV to 850 eV (cyan dashed lines).

higher in 2011 than in 2012.

As the neutron flux measured with the MGAS in 2012 is reliable up to 10 keV, above this energy we have used the shape of the n_TOF official neutron flux measured in 2011 [25].

3.4 Fission cross section

The cross section calculations have been performed using the Analysis of Geel Spectrum (AGS) code, developed at the European Commission, Joint Research Centre, Institute for Reference Materials and Measurements (EC-JRC-IRMM) [41]. The AGS code was developed for the data reduction of neutron time-of-flight measurements although it can be used for other analysis involving spectra. It includes a full propagation of uncertainties accounting for the correlated and uncorrelated uncertainty components and providing the full covariance information.

The cross section has been calculated by means of two methods, which are described in detail in the next subsections. In the PPAC chamber, the targets are placed in the beam direction one besides the other separated by a few centimeters, hence one can assume that all the targets receive the same neutron flux. The absolute neutron flux received by the targets during the

experiment is known by using, a sample reference with an isotope which cross section is accurately known in a particular energy range.

First method (n_TOF$_1$)

In this work, ^{235}U is used as reference because the cross section area is considered a secondary standard in the energy region from 7.8 eV to 11 eV, with a value given by the IAEA of 246.4 ± 1.2 b · eV [24].

The ^{235}U(n,f) cross section has ben obtained with Eq. 3.8 (obtained from Eq. 3.5) using the normalised neutron flux shape measured through the ^{10}B(n,α) reaction with the MGAS.

$$\sigma(E_n) = \frac{C(E_n)}{\Phi(E_n) \cdot N \cdot \epsilon} \tag{3.8}$$

Then, as the normalization factor obtained for the ^{235}U is inversely proportional to ($N_5 \cdot \epsilon_5$), knowing the detection efficiency for each target and also the areal densities of the samples, one can obtain the value of the product ($N_4 \cdot \epsilon_4$) required to calculate the ^{234}U(n,f) cross section using Eq. 3.9.

The relation between the areal densities of the samples is obtained from Eq. 3.2, where the radius is the same for all the targets and cancels in the quotient.

$$N_4 = N_5 \cdot \frac{m_4 \cdot M_5}{m_5 \cdot M_4} \tag{3.9}$$

Both, the ^{235}U(n,f) and ^{234}U(n,f) cross sections have been calculated with this method below 100 keV, where the shape of the considered neutron flux is well-known.

Second method (n_TOF$_2$)

As it was previously mentioned, in the present setup all the samples receive the same neutron flux. Then, the ^{235}U reference target can be used to calculate the neutron flux using an accurate evaluation of the ^{235}U(n,f) cross sections in the resonance region through Eq. 3.7 as:

$$\Phi(E_n) = \frac{C(E_n)_5}{\sigma(E_n)_5 \cdot N_5 \cdot \epsilon_5} \tag{3.10}$$

At low energies, below 10 keV, some discrepancies have been recently found between the current evaluations and the n_TOF ^{235}U(n,f) cross section data measured by Paradela et al. [42]. These discrepancies have motivated a new evaluation of the Resonance Region, which has been performed by L. C.

Leal [43] including the n_TOF experimental data. This evaluation has been used in the present work to calculate the neutron flux in the energy region from eV to 10 keV. This neutron flux has been used to calculate the ^{234}U(n,f) cross section using Eq. 3.8.

The cross section has been calculated for each isotope as the mean value of the result obtained with each individual target.

3.4.1 ^{235}U(n,f) cross section

Two regions are found in the resonance region: the Resolved Resonance Region (RRR), which in the case of the ^{235}U(n,f) reaction is limited to 2.25 keV above which energy extends the Unresolved Resonance Region (URR).

According to the energy resolution, which is $\Delta E_n/E_n = 5.4{\cdot}10^{-4}$ at 1 keV, the ^{235}U and ^{234}U a binning of 2000 bins/decade which corresponds to a binwidth of $5{\cdot}10^{-4}$ in logarithmic scale has been used in the resonance region below 10 keV.

The cross section obtained in this work in the resonance region has been compared with the ENDF/B-VII.1 database and with the recent evaluation performed by L. C. Leal, see Fig. 3.3.

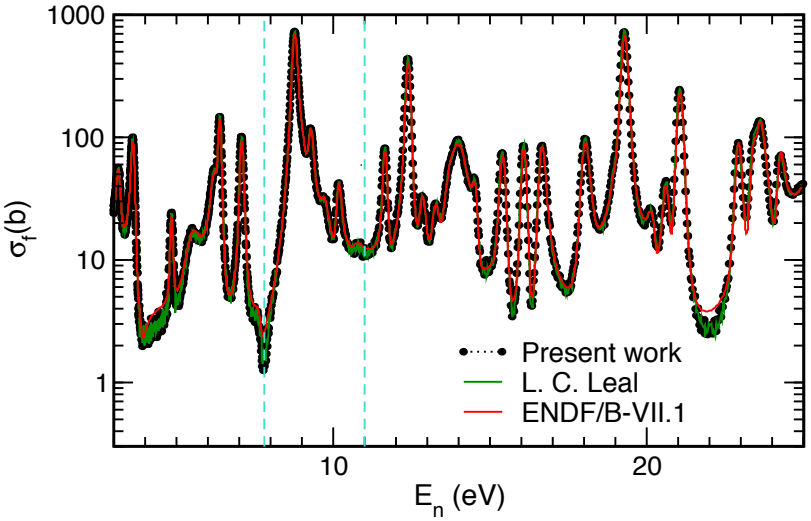

Figure 3.3: ^{235}U(n,f) cross section obtained in this work as the average of the targets (black marks) compared with the new evaluation of L. C. Leal (green line) and the ENDF/B-VII.1 evaluation (red line). The limits of the IAEA secondary standard interval are denoted by the cyan dashed lines.

The CERN-n_TOF facility is characterized by a low background, partially achieved due to the long flight path, which reduces the time-independent neutron background, and partially because the proton pulses are very well separated on time avoiding the overlap of neutrons from previous pulses. This low background minimise the counts in the valleys between resonances as it is observed in Fig. 3.3 when comparing with the ENDF/B-VII evaluation.

IAEA provide averaged data above 100 eV. Therefore, in Table 3.2 these reference values have been compared with the averaged cross sections obtained in this work, with the values obtained with the experimental data of Paradela, with the evaluation of L. C. Leal and with the ENDF/B-VII.1 library. The ratios of the present experimental data to each column of Table 3.2 are given in parentheses and shown in Fig. 3.4.

E_n	n_TOF	Paradela	Leal	IAEA	ENDF/B-VII.1
100-200	21.13	21.31(0.99)	21.02(1.01)	21.17(1.00)	20.32(1.04)
200-300	20.70	20.82(1.00)	20.77(1.00)	20.69(1.00)	20.60(1.01)
300-400	13.02	12.90(1.01)	13.22(0.99)	13.14(0.99)	12.81(1.02)
400-500	13.66	13.68(1.00)	13.49(1.01)	13.78(0.99)	13.29(1.03)
500-600	15.51	15.30(1.01)	15.20(1.02)	15.17(1.02)	14.87(1.04)
600-700	11.50	11.56(1.00)	11.53(1.00)	11.51(1.00)	11.24(1.02)
700-800	11.12	10.05(1.01)	11.10(1.00)	11.10(1.00)	10.88(1.02)
800-900	8.236	8.305(0.99)	8.150(1.01)	8.213(1.00)	7.977(1.03)
900-1000	7.440	7.259(0.99)	7.370(1.01)	7.502(0.99)	7.240(1.03)
1000-2000	7.359	7.318(1.01)	7.290(1.01)	7.303(1.01)	7.138(1.03)
2000-3000	5.390	5.237(1.03)	5.330(1.01)	5.386(1.00)	5.290(1.02)
3000-4000	4.758	4.740(1.00)	4.790(0.99)	4.784(0.99)	4.778(1.00)
4000-5000	4.250	4.216(1.01)	4.270(1.00)	4.261(1.00)	4.207(1.01)
5000-6000	3.745	3.808(0.98)	3.820(0.98)	3.838(0.98)	3.905(0.96)
6000-7000	3.374	3.214(1.05)	3.350(1.01)	3.291(1.03)	3.287(1.03)
7000-8000	3.203	3.140(1.02)	3.210(1.00)	3.236(0.99)	3.158(1.01)

8000-9000	2.916	2.934(0.99)	3.090(0.94)	3.009(0.97)	2.940(0.99)
9000-10000	3.072	3.071(1.00)	3.060(1.00)	3.120(0.98)	3.043(1.01)

Table 3.2: ^{235}U(n,f) averaged integral cross sections. The energy unit is [eV] and the cross section unit is for all the datasets [b].

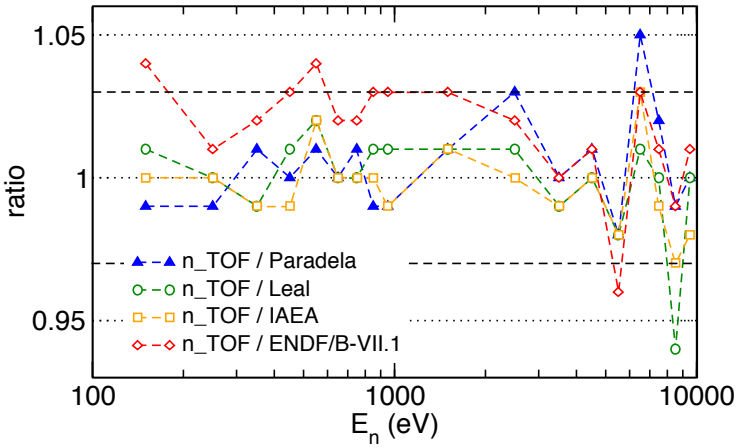

Figure 3.4: ^{235}U(n,f) integral cross section ratios of the experimental data and the sets of data of Table 3.2 for different energy ranges between 100 eV and 10 keV.

In the energy range from 10 keV to 100 keV the n_TOF neutron flux shape is less accurately known, which has motivated the new flux measurement discussed in [25]. The present data have been compared, in such energy region, with the experimental data measured by Gwin and Weston, both measured in the ORNL and retrieved from the EXFOR database. The neutron capture and fission data obtained by Gwin were measured in 1979 using a liquid scintillator detector and a fission chamber respectively. A subsequent measurement was performed by Weston using a Parallel Plate Fission Chamber in 1984. Comparing the present work with both experimental data, an energy offset is observed in the cross sections obtained by Gwin with respect to Weston and this work, as it is shown in Fig. 3.5.

The present data are compared with the experimental data of Weston and with the IAEA averaged values in Fig. 3.6 in the energy range from 10 keV to 100 keV.

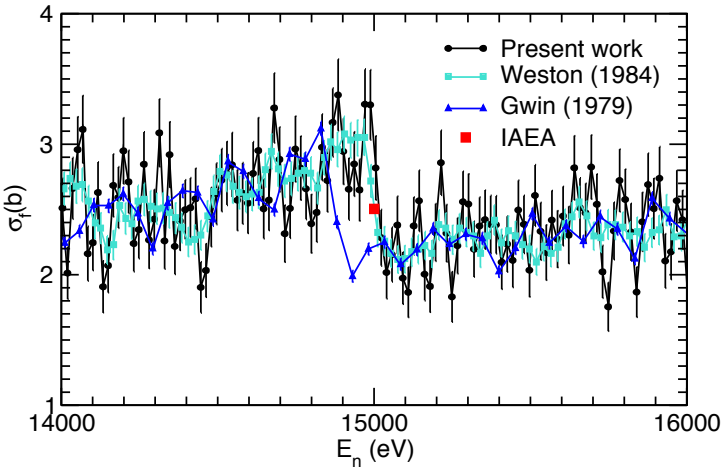

Figure 3.5: ^{235}U(n,f) cross section obtained in this work compared with the experimental data provided in the EXFOR database.

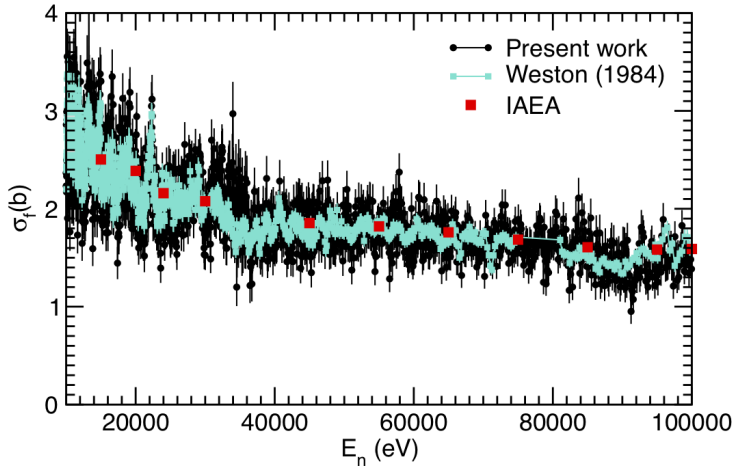

Figure 3.6: ^{235}U(n,f) experimental cross section in the energy range from 10 keV to 100 keV.

3.4.2 ^{234}U(n,f) cross section

The resolved resonance region, in the case of the ^{234}U(n,f) cross section extends up to 1.5 keV, at which energy starts the URR.

The ^{234}U(n,f) cross section results have been compared with the experimental data available and with the ENDF/B-VII.1 and JENDL-4.0 evaluations. In these two evaluations, the resonance energies are not in agreement,

neither the number of evaluated resonances.

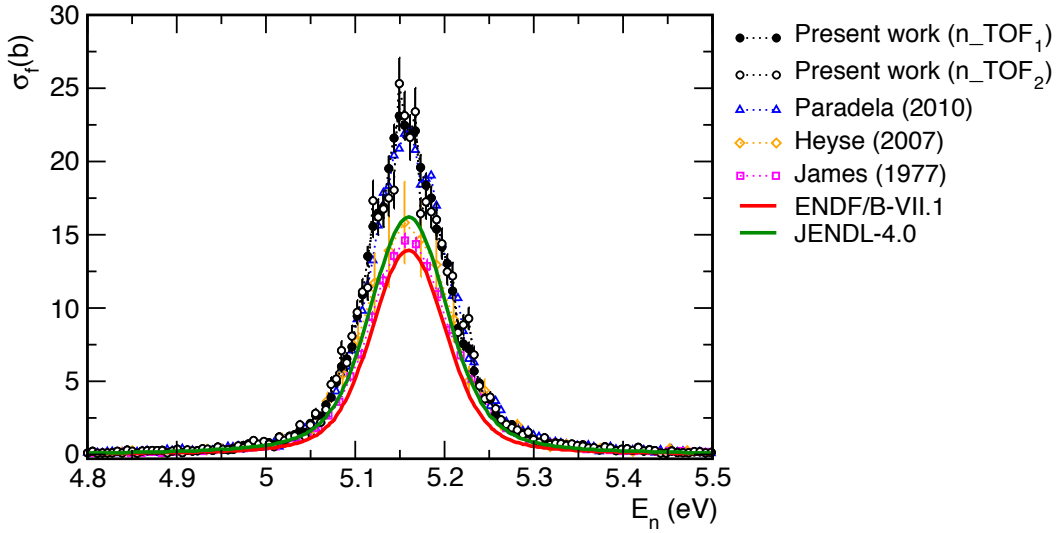

Figure 3.7: Comparison between the present data, the EXFOR experimental data and the ENDF/B-VII.1 and JENDL-4.0 evaluations at the first resonance energy region.

The largest fission cross section resonance, is placed around 5 eV, being also the first ^{234}U(n,f) resonance, see Fig. 3.7. The present cross sections are in close agreement in this energy region with the previous n_TOF experimental data obtained by Paradela [1]. However, significant discrepancies have been found with the ENDF/B-VII.1 and JENDL-4.0 evaluations, both in fair agreement with the experimental data of James et al. in which they are based and also with the data set of Heyse et al., which cross section in this resonance is used in JENDL-4.0.

The most prominent resolved resonances are found in the energy region around 500 eV. This work has been compared in this energy region with the experimental data available in EXFOR, see Fig. 3.8. The present cross sections have better resolution than the data measured by James [7] and Heyse [9] as it can be seen in the upper panel of the figure. The cross sections obtained by James were measured in the ORNL in 1977 using a multiplate ionization chamber from a few eV to 8.9 MeV. In 2007 a new measurement was performed by Heyse at the GELINA neutron time-of-flight facility of the Institute of Reference Materials and Measurements (IRMM) from 0.5 eV to 100 keV using a double Frisch-gridded ionization chamber. The previous n_TOF measurement was performed by Paradela, using a PPAC chamber with the perpendicular setup, this is, in which the targets and detectors were

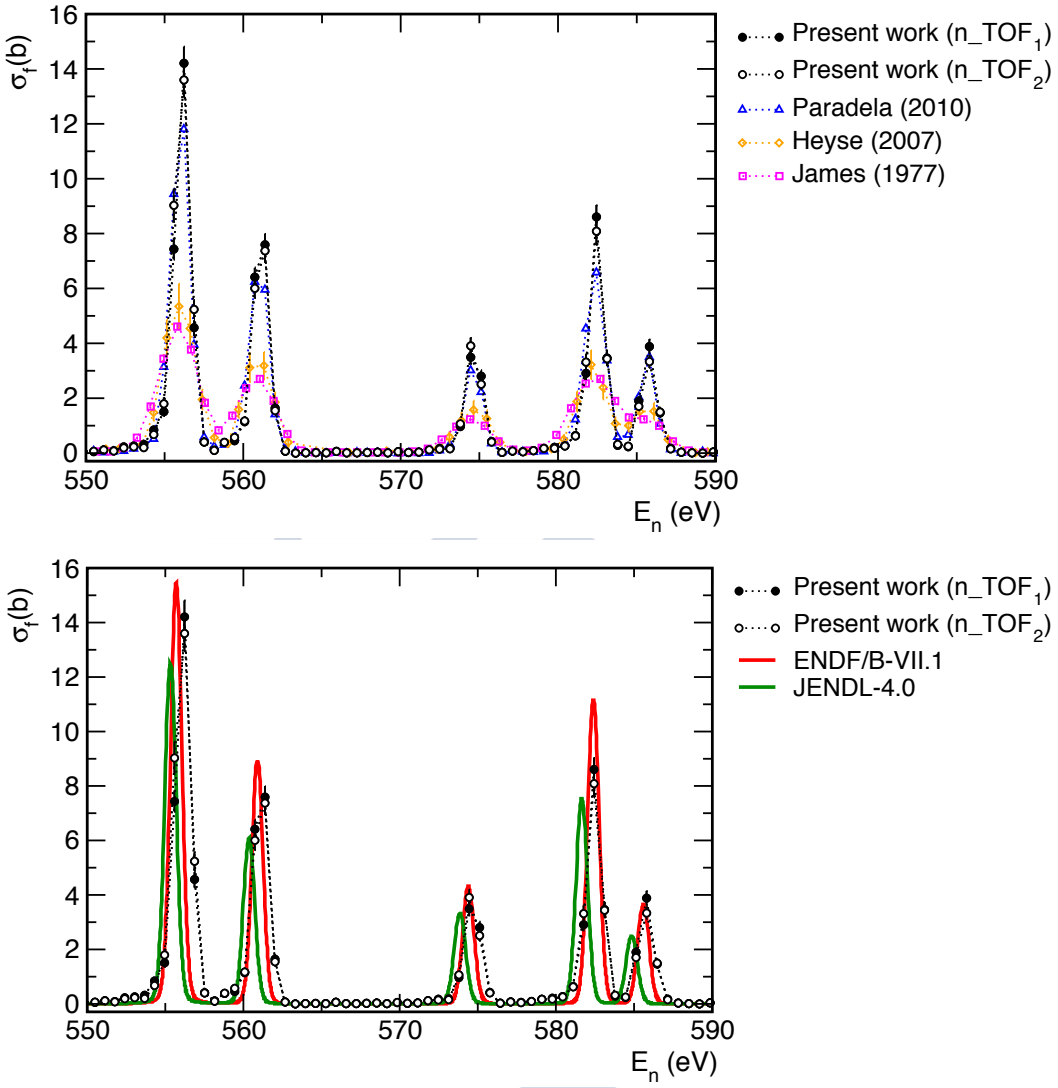

Figure 3.8: Comparison between the ^{234}U(n,f) experimental cross section obtained in this work with the EXFOR data (upper panel) and with the ENDF/B-VII.1 and JENDL-4.0 evaluations (lower panel) in the 550 eV energy region.

placed perpendicular to the neutron beam. Comparing with the EXFOR data sets, the present data are closer to this last one.

The shift in energy between the ENDF/B-VII.1 and JENDL-4.0 evaluations is also observed between the evaluations and the present experimental data being more pronounced in the case of the JENDL-4.0 evaluation, see Fig. 3.8 (lower panel) and Fig. 3.9 in which one of the resonances is com-

pletely allocated in JENDL-4.0.

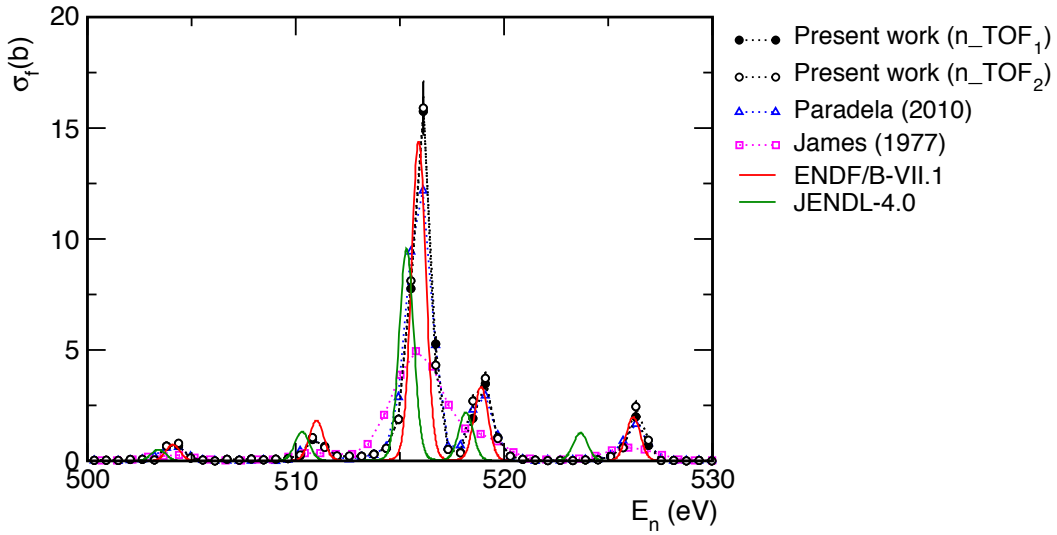

Figure 3.9: Comparison between the ^{234}U(n,f) experimental cross section obtained in this work with the EXFOR data, ENDF/B-VII.1 and JENDL-4.0 evaluations in the 500 eV energy region.

In the energy region from 1 keV to 1.5 keV, two resonances have found in the present data which are evaluated in ENDF/B-VII.1 but do not appear in JENDL-4.0, see Fig. 3.10.

Above 1.5 keV, in the beginning of the URR, the resonances become closer and the cross sections lower. Nevertheless, some resonant structures are well defined in the present data which were also reported in previous works not being observed in the evaluations, which provide an average value of the cross section in that energy region.

This is the case of the resonance located around 7.8 keV shown in Fig. 3.11 that corresponds to a Class-II level. These resonances are formed by bands of mixed pure vibrational resonances which are formed in the secondary well region.

The averaged cross sections for different energy ranges are given in Table 3.3.

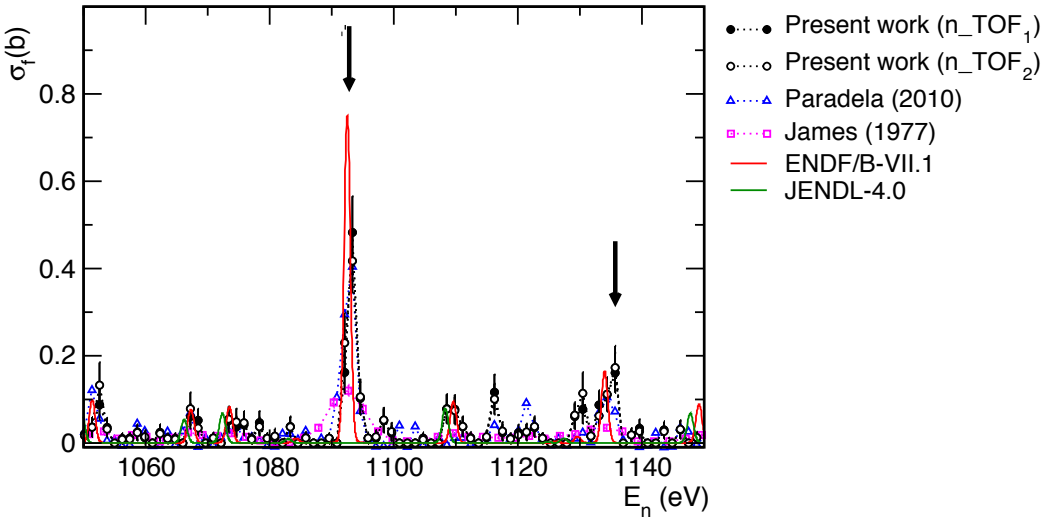

Figure 3.10: ^{234}U(n,f) cross section in the 1 keV energy region. The two resonances missing in JENDL-4.0 are indicated by an arrow.

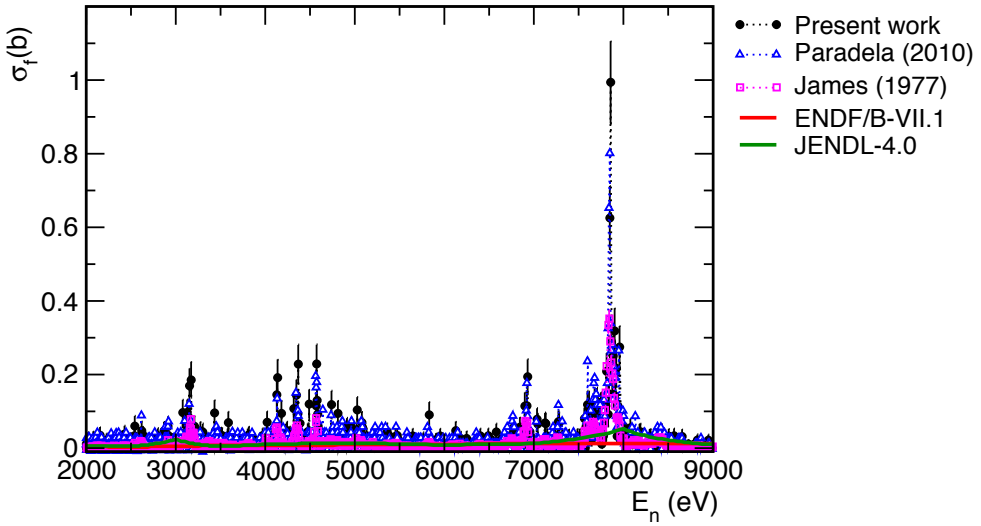

Figure 3.11: ^{234}U(n,f) cross section in the URR energy region.

E_n	n_TOF$_1$	n_TOF$_2$	Paradela	ENDF/B-VII.1	JENDL-4.0
100-120	353.9	332.8(1.06)	344.2(1.03)	255.0(1.39)	243.1(1.46)
120-160	25.97	25.80(1.01)	20.08(1.29)	12.81(2.03)	12.34(2.10)
160-220	78.22	76.81(1.02)	74.80(1.05)	55.08(1.42)	52.80(1.48)
220-300	59.76	58.12(1.03)	46.08(1.30)	35.98(1.66)	27.01(2.21)
300-400	81.71	75.29(1.09)	76.33(1.07)	55.92(1.46)	41.95(1.95)

400-520	470.5	474.8(0.99)	458.2(1.03)	338.5(1.39)	244.7(1.92)
520-660	482.9	491.0(0.98)	473.9(1.02)	367.2(1.32)	268.1(1.80)
660-820	148.3	158.9(0.93)	142.6(1.04)	103.5(1.43)	74.14(2.00)
820-1000	31.87	33.18(0.96)	26.26(1.21)	19.98(1.59)	15.63(2.04)
1000-1200	27.79	28.99(0.96)	22.11(1.26)	13.23(2.10)	5.858(4.74)
1200-1600	21.62	22.23(0.97)	17.01(1.27)	11.57(1.87)	9.282(2.33)
1600-2200	7.862	7.841(1.00)	5.996(1.31)	5.597(1.40)	5.486(1.43)
2200-3000	7.642	7.460(1.02)	5.201(1.47)	3.873(1.97)	9.862(0.77)
3000-4000	12.04	12.05(1.00)	9.068(1.33)	6.887(1.75)	9.757(1.23)
4000-5200	24.74	25.74(0.96)	21.02(1.18)	8.661(2.86)	12.78(1.94)
5200-6600	8.105	8.908(0.91)	8.335(0.97)	10.63(0.76)	10.56(0.77)
6600-8200	52.29	53.28(0.98)	57.33(0.91)	12.83(4.07)	25.54(2.05)
8200-10000	5.927	6.206(0.96)	7.013(0.85)	13.23(0.45)	11.99(0.49)

Table 3.3: ^{234}U(n,f) averaged cross sections. The incident neutron energy is given in [eV] units and the averaged integral fission cross section in [mb].

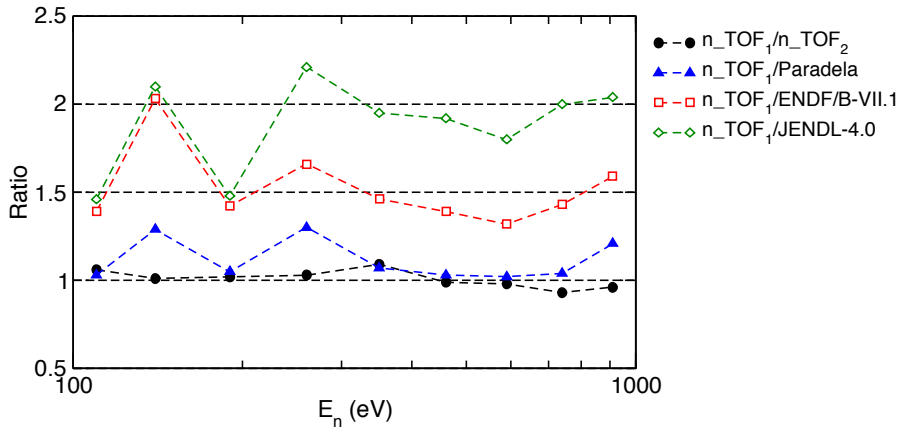

Figure 3.12: Ratios of the integral cross section experimental data given in parentheses in Table 3.3 in the RRR up to 1 keV.

The values in parentheses are the ratios of the experimental data obtained

with the first method to each column, which are shown in Fig. 3.12.

The energy resolution at 10 keV is $\Delta E_n/E_n = 1.1{\cdot}10^{-3}$, and accordingly, the cross section has been calculated in this energy regionusing a binning of 1000 bins/decade, which corresponds to a binwidth of $1{\cdot}10^{-3}$ in logarithmic scale.

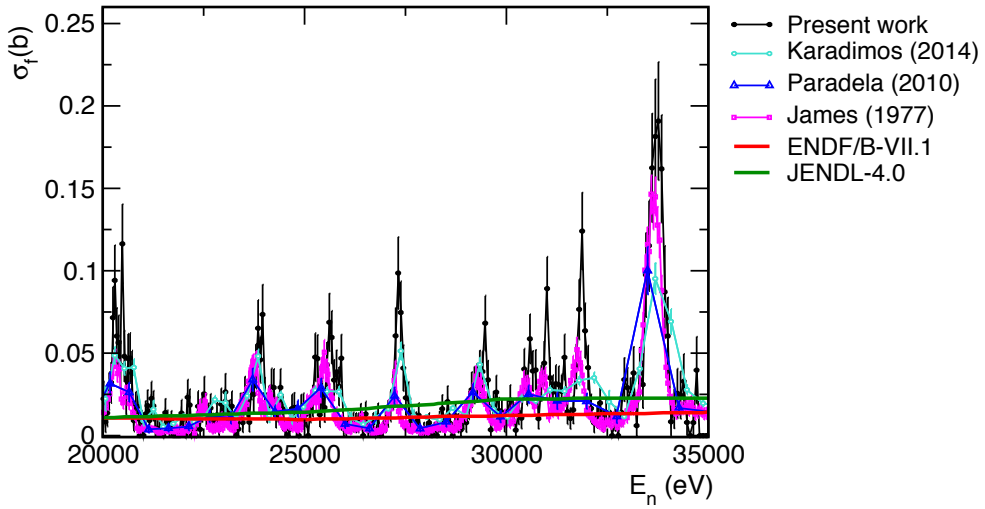

Figure 3.13: ^{234}U(n,f) cross section in the energy interval from 20 keV to 35 keV.

The ^{234}U(n,f) cross section has been compared in this energy range with the experimental data available in EXFOR. Two of the experimental datasets were measured in n_TOF: those of Paradela (2010) and Karadimos (2014) [44]. Paradela provided cross section data in such energy region using a binning of 100bins/decade and Karadimos used a different binning for each energy range limited by the statistics of the reference sample: below 1.4 MeV, the ^{234}U(n,f) cross section was measured relative to the ^{235}U and the energy range was divided in 200 bins/decade below 900 keV, and 20 bins/decade up to 1.4 MeV.

The narrower binning used in this work allows to resolve the resonances structure with higher resolution than the previous n_TOF data as it is shown in Fig. 3.13. In that figure, the present data have been also compared with the ENDF/B-VII.1 and JENDL-4.0 evaluations which provide an average value in that energy region.

The ^{234}U(n,f) averaged integral cross sections from 10 keV to 100 keV are given in Table 3.4 in comparison with the ENDF/B-VII.1 and JENDL-4.0 evaluations.

E_n	n_TOF$_1$	ENDF/B-VII.1	JENDL-4.0
10-12	13.12	12.62(1.06)	10.26(1.31)
12-16	31.96	11.92(2.73)	21.51(1.52)
16-22	18.47	10.85(1.74)	11.17(1.69)
22-30	18.71	10.68(1.79)	16.39(1.17)
30-40	36.56	14.10(2.65)	22.63(1.65)
40-52	19.07	14.21(1.37)	16.37(1.19)
52-66	18.92	12.19(1.58)	13.34(1.45)
66-82	23.94	15.36(1.59)	13.11(1.86)
82-100	17.53	18.84(0.95)	21.45(0.84)

Table 3.4: ^{234}U(n,f) averaged integral cross sections from 10 keV to 100 keV. The incident neutron energy is given in [keV] units and the averaged fission cross section in [mb].

Chapter 4

Cross section at energies above 100 keV

This chapter deals with the analysis of the ^{234}U(n,f) cross section at neutron energies from 100 keV up to 1 GeV. At these energies, the ^{234}U(n,f) cross section has been calculated from the ratio with the ^{235}U reference sample, and hence, the status of the evaluations of the ^{235}U(n,f) cross section is previously discussed.

The detection efficiency, used to calculate the cross section in this energy region, has been corrected for the anisotropies in the angular distribution of the FFs. The cross section results are discussed and compared with previous experimental data and with the evaluations.

4.1 ^{235}U(n,f) reference cross section

Above 100 keV, the ^{234}U(n,f) cross section has been calculated in this work relative to the ^{235}U(n,f) cross section through the fission cross section ratio ^{234}U/^{235}U using Eq. 3.8, where the neutron flux cancels, as:

$$\sigma(E_n)_4 = \sigma(E_n)_5 \frac{C(E_n)_4 \cdot N_5 \cdot \epsilon_5}{C(E_n)_5 \cdot N_4 \cdot \epsilon_4} \tag{4.1}$$

The ^{235}U(n,f) reaction is considered by the IAEA as a standard cross section from 0.15 MeV up to 200 MeV and the correspondent dataset can be retrieved from its Nuclear Standards [24]. A general good agreement is found between the main evaluated libraries and the IAEA standard in this energy range (see Fig. 4.1).

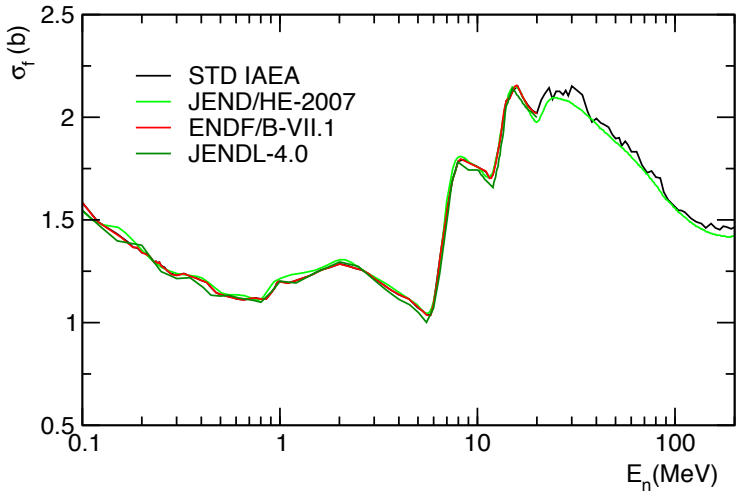

Figure 4.1: Comparison between the ^{235}U(n,f) cross section given by the IAEA standard (black line), JENDL/HE-2007 (dark green line), JENDL-4.0 (light green line) and ENDF/B-VII.1 (red line) in the energy range from 100 keV to 200 MeV.

Above 200 MeV the lack of a good reference for the (n,f) reactions is discussed in [45]. As it is there stated, the only references up to 1 GeV come from JENDL/HE-2007. For this reason, in previous PPAC measurements, such evaluation was used above 30 MeV [1] and above 200 MeV [3]. However, some inconsistences were recently found in this evaluation, which are discussed in the work of Lo Meo et al. [46]. In such work, the (n,f) cross sections were reproduced using Monte Carlo calculations to adjust fission model parameters to experimental (p,f) cross sections in the energy range from 100 MeV to 1 GeV. Above the fission barrier, neutrons and protons are expected to have a similar behaviour with the energy, therefore, the proton-induced cross sections measured in [47] from 200 MeV up to 1 GeV, were used to calculate the fission model parameters required to predict the neutron-induced cross sections.

The fission reactions induced by nucleons were described in the work of Lo Meo et al. as a two step process consisting in a intranuclear cascade originated by the incident nucleon, which leaves the compound nucleus in an excited state, and a subsequent decay by fission or other types of reactions. The first step was reproduced using a C++ version of the Liège Intranuclear Cascade Model (INCL++) [48] and the second step by a C++ version of GEMINI (GEMINI++) [49,50] or a Fortran version of ABLA07 [51]. This work pointed out that JENDL/HE-2007 reproduced the (p,f) cross sections

very well up to 200 MeV, showing a decreasing trend above 500 MeV which was inconsistent with the experimental data. In the case of the ^{234}U, as there were not (p,f) experimental data above 30 MeV, the model parameters of the ^{235}U were used in the GEMINI++ calculations.

More recently, the IAEA published a new document with the reference cross sections of the ^{235}U, ^{238}U, ^{209}Bi and ^{nat}Pb isotopes [52], in the intermediate energy region, recommended for nuclear-fission applications. In the ^{235}U(n,f) reference cross section, evaluated up to 1 GeV, the scaled down high energy (p,f) cross section data from Kotov above 200 MeV were included to reduce the uncertainties of the reference cross section. The two points provided by the IAEA in the energy interval from 200 MeV to 500 MeV, are in disagreement with the neutron-induced cross section data reproduced by Lo Meo et al. with the codes INCL++/GEMINI++ and INCL++/ABLA07.

In the work of Durán et al. [45], a new analysis that combines the n_TOF cross section ratios [2,53] with the calculations done by Lo Meo et al. was performed. The comparison between the ^{235}U(n,f) cross section provided by JENDL/HE-2007, the IAEA reference and the work of Durán et al. is shown in Fig. 4.2.

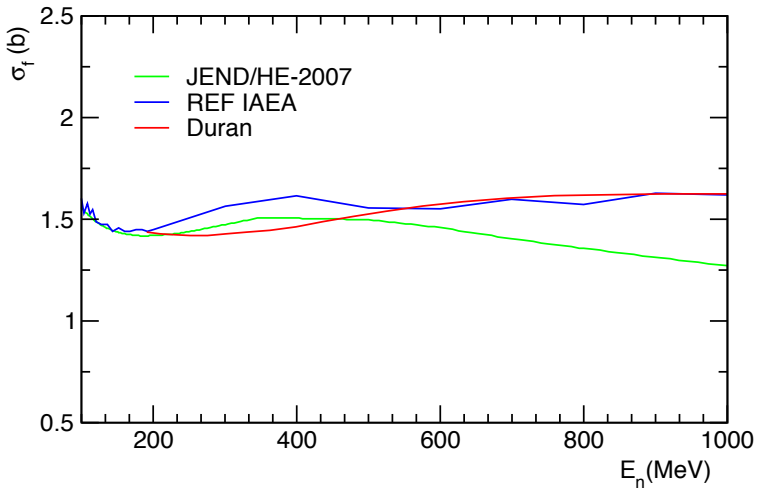

Figure 4.2: Comparison between the ^{235}U(n,f) cross section given by the IAEA reference (blue line), JENDL/HE-2007 (green line) and Durán et al. (red line) in the energy range from 100 MeV to 1 GeV.

JENDL/HE-2007 and the IAEA reference show a bump in the cross section in the energy interval from 200 MeV to 500 MeV, produced by the (n,p)

experimental data measured by Kotov, which were used in both evaluations. Above 500 MeV, JENDL/HE-2007 shows a decreasing trend while the IAEA reference maintains a constant behaviour up to 1 GeV. The cross section data provided by Durán et al. show a behaviour contrary to JENDL/HE-2007, with a lower cross section below 500 MeV which increases above it.

4.2 ^{234}U/^{235}U cross section ratio

The cross section ratio ^{234}U/^{235}U has been compared with the ENDF/B-VII.1 and JENDL-4.0 evaluations up to 20 MeV, which is the higher energy reached by the evaluations (see upper panel of Fig. 4.3).

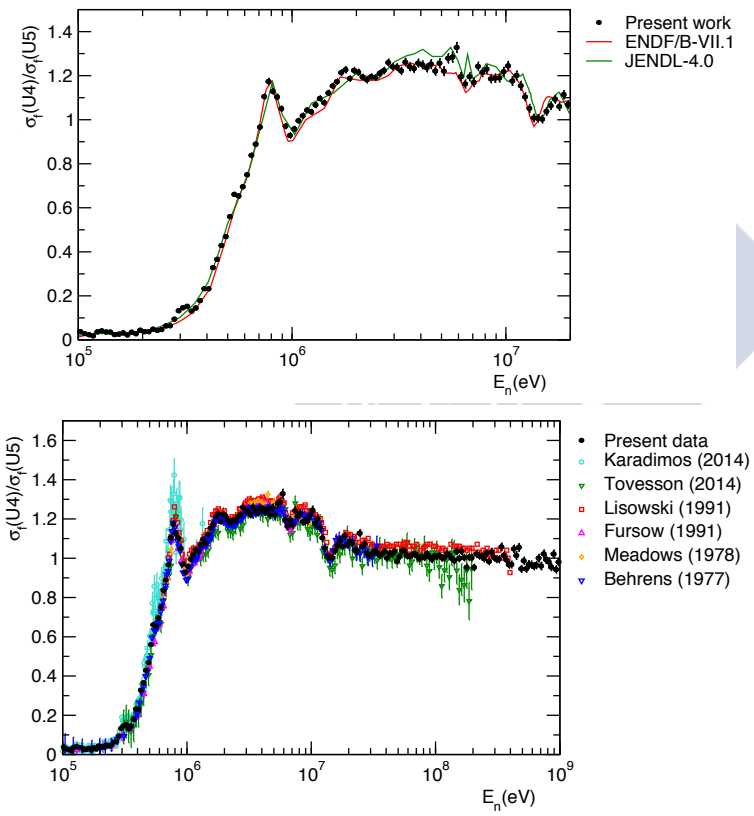

Figure 4.3: ^{234}U/^{235}U cross section ratio (black marks) compared with the ENDF/B-VII.1 (red line) and the JENDL/4.0 (green line) evaluations in the energy region from 100 keV up to 20 MeV (upper panel). ^{234}U/^{235}U cross section ratio (black marks) compared with the EXFOR experimental data up to 1 GeV (lower panel).

The data extended up to 1 GeV are shown in the lower panel of Fig. 4.3 in comparison with the experimental data provided in the EXFOR library.

The discussion between the different sets of experimental data and the evaluations will be presented in the next section, where the ^{234}U(n,f) cross sections are obtained.

4.3 ^{234}U(n,f) cross section

The ^{234}U(n,f) cross section has been obtained from the ^{234}U/^{235}U cross section ratio using the ^{235}U(n,f) cross section given by the IAEA Reference from 0.15 MeV up to 200 MeV and the data of Durán et al. above it up to 1 GeV. The results obtained for each energy region are exposed and discussed as follows in different energy ranges.

4.3.1 Threshold Region

At 100 keV, the energy resolution is $\Delta E_n/E_n = 2.9{\cdot}10^{-3}$, hence according to it, in the energy region from 100 keV to 1 MeV the ^{234}U(n,f) cross section has been calculated using a binning of 400 bins/decade, corresponding to a binwidth of $2.5{\cdot}10^{-3}$ in logarithmic scale.

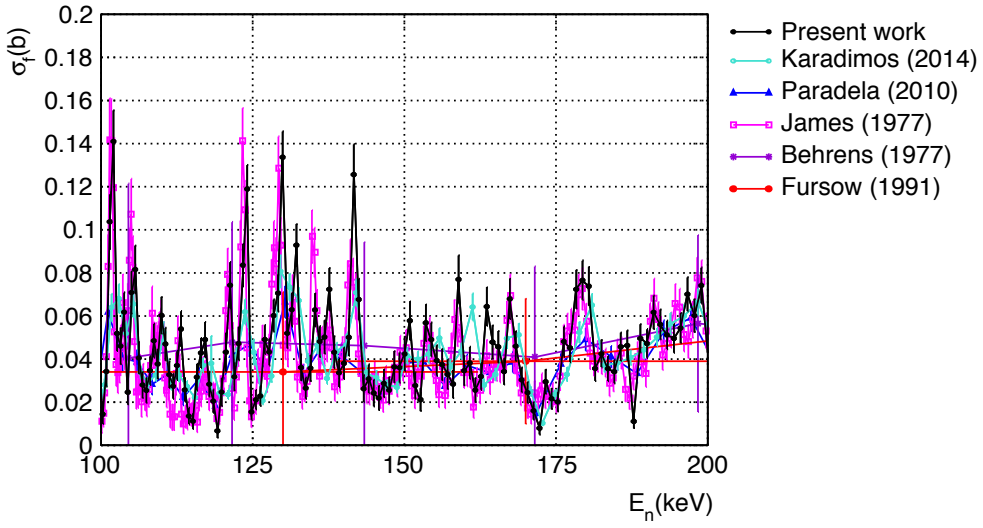

Figure 4.4: ^{234}U(n,f) cross section in the 125 keV energy region.

Below the threshold, a structure has been observed around 125 keV. The present cross section allows to resolve this structure in quite good agreement

with the higher resolution experimental data sets provided in EXFOR [7,1,44] (see Fig. 4.4).

In addition, three resonant structures reported in previous works [7,1,44] have been found in the present data in the energy regions around 310 keV, 550 keV and 770 keV (see Fig. 4.5). These structures were claimed to correspond to β-vibrational levels in [7] and in the last n_TOF work [44] the first two mentioned structures were identified as class-II states and the third one as class-III resonant states in the third well which corresponds to the second isomer.

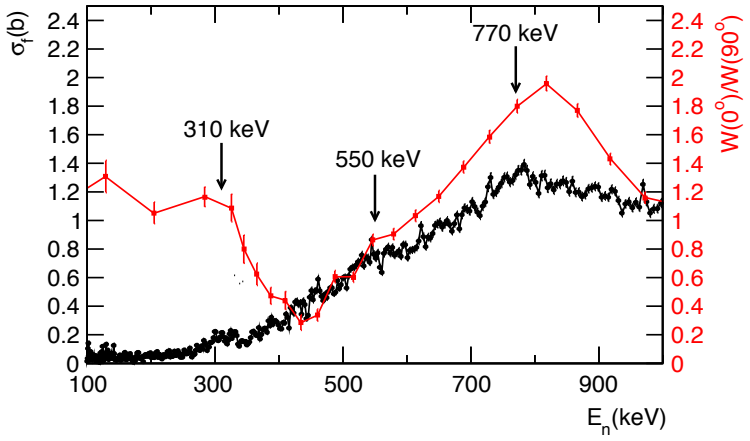

Figure 4.5: ^{234}U(n,f) cross section in the energy region from 100 keV to 1 MeV (black marks) and anisotropy parameter (red marks) obtained in this work.

As it is observed in Fig. 4.5, large variations are found in the anisotropy parameter at energies immediately after these structures are found, especially at 310 keV and 770 keV where the anisotropy parameter starts to decrease. A similar behaviour is found in the fission cross section, which may indicate that the output channels opened in the peaks start to compete after such energies reducing the fission cross section.

The ^{234}U(n,f) cross section has been compared in such energy region with the experimental data available in EXFOR, see Fig. 4.6. The ^{234}U/^{235}U cross section ratios provided by Lisowski [54], Fursow [55] and Behrens [56], have been multiplied by the ^{235}U(n,f) IAEA reference cross section in order to extract the ^{234}U(n,f) cross section required to compare them with the present data.

The structures observed around 310 keV were attributed to β-vibrational levels in the second well of the fission potential barrier [7]. In this energy

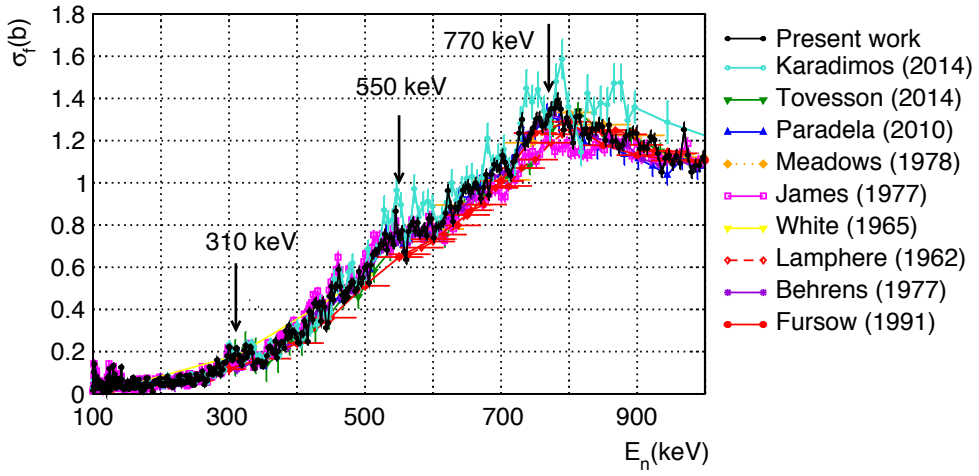

Figure 4.6: ^{234}U(n,f) cross section obtained in this work in the energy region from 100 keV to 1 MeV compared with the EXFOR experimental data.

region, the binning used by Paradela does not allow to distinguish fine details in the resonance-like structure although it is enough to confirm its existence. Above 300 keV it is also confirmed by Tovesson [57]. However, in the measurements of Behrens and Fursow it is not observed due to the thick binning used in both cases, being both cross sections in agreement in that energy region.

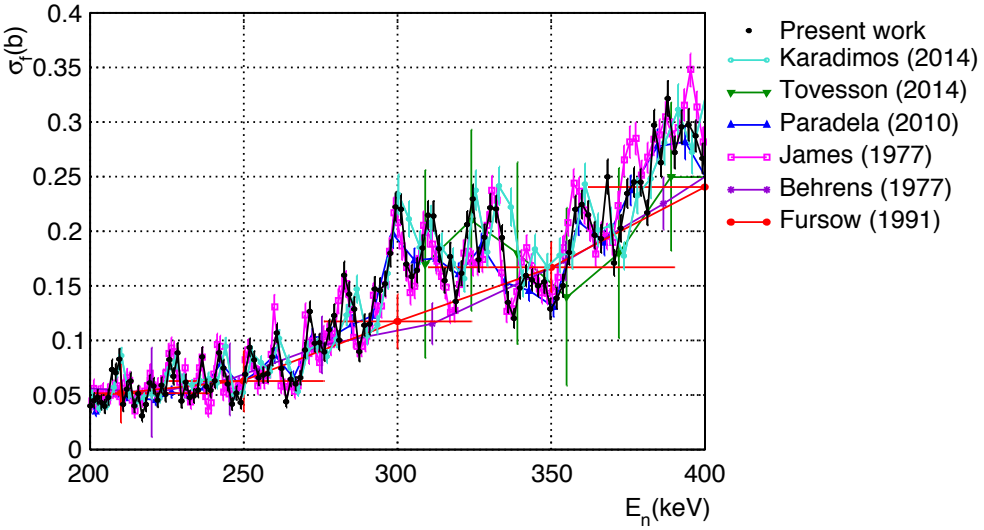

Figure 4.7: ^{234}U(n,f) cross section in the 310 keV energy region.

The present high resolution data allow to distinguish in very fine detail

the resonances found around 310 keV which are in quite good agreement with James and Karadimos (see Fig. 4.7). In the second structure found around 550 keV which is shown in Fig. 4.8, the present data are in quite good agreement with James although this last cross section remains above them in the energy interval from 400 keV to 530 keV.

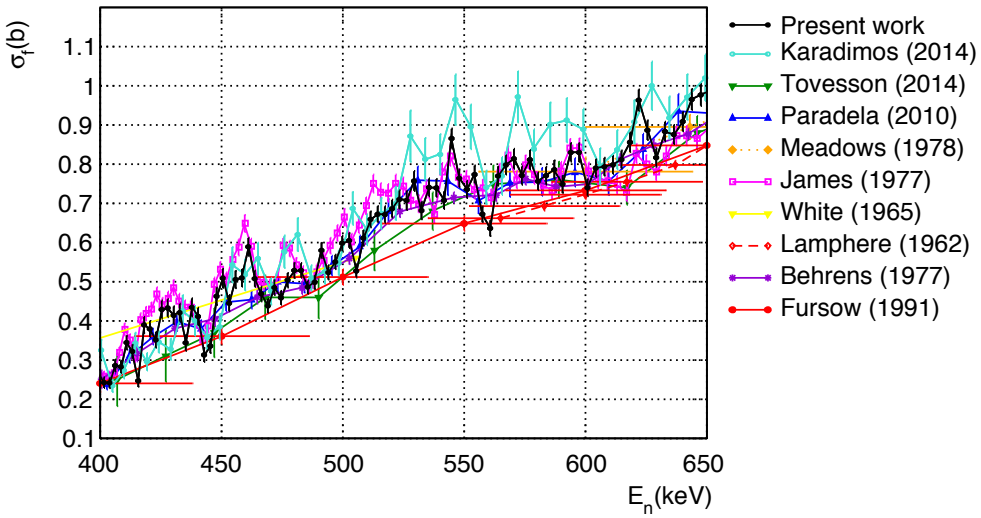

Figure 4.8: ^{234}U(n,f) cross section around 550 keV.

Huge discrepancies are found in the measurement of Karadimos respect to the rest of data sets in the peak around 550 keV. Although the resonance shape agrees with the finer experimental data in that energy, its cross section is a 10% higher than the present data and James. Although the binning is not enough thin to resolve in detail the resonances in the cross sections provided by Paradela, Behrens and Tovesson, the structure is confirmed in the three data sets. Fursow and Lamphere cross sections show a linear increasing behaviour in that energy region.

In the third structure observed around 770 keV, the present data has enough resolution to resolve the resonance structure in very fine detail not provided by other measurements like Paradela, Behrens, Meadows [58] and Fursow, with which this data are in quite good agreement (see Fig. 4.9). Discrepancies have been found when comparing with the experimental data of Karadimos, which are significantly higher than the rest of data sets and with those of James, which are systematically lower than other measurements.

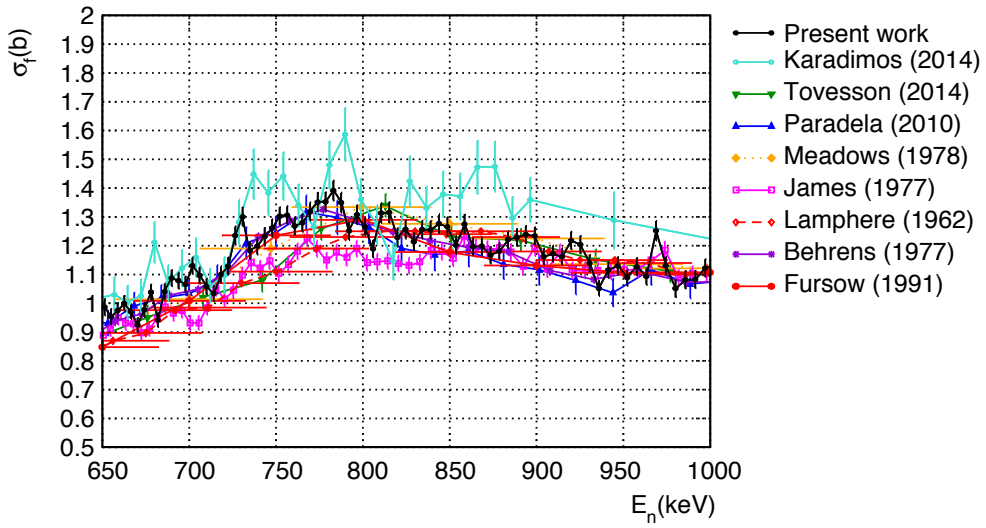

Figure 4.9: ^{234}U(n,f) cross section in the energy region around 770 keV.

4.3.2 Higher energy fission chances

In the energy region above the threshold and up to 100 MeV large variations are observed in the cross section in the proximities of the second and third chance.

Two energy binnings have been used in this region defined by the statistics and according to the energy resolution. At 1 MeV, the energy resolution is $\Delta E_n/E_n = 5.3{\cdot}10^{-3}$, hence in the energy region from 1 MeV to 10 MeV the ^{234}U cross section has been calculated using a binning of 200 bins/decade, corresponding to a binwidth of $5{\cdot}10^{-3}$ in logarithmic scale. From 10 MeV to 100 MeV the binning has been reduced, due to the lower neutron flux, to 100 bin/decade, this is, to a binwidth of $1{\cdot}10^{-2}$ in logarithmic scale.

The second chance is found below 10 MeV, when the incident neutron energy is enough so that one neutron may be emitted before fission occurs. In this case, the fissioning nucleus is the ^{234}U instead of the ^{235}U. The opening of a new channel (n,nf) in the second chance, produces a plateau in the cross section, where the (n,f) and (n,nf) channels starts to compete, see Fig. 4.10.

The cross section obtained in the energy range from 1 MeV to 10 MeV, is shown in Fig. 4.11 in comparison with the experimental data available in EXFOR.

Huge discrepancies have been found when comparing the present data with James; some peaks and dips are found in its cross section not appearing in the rest of data sets. This is the case of the two dips found at 3 MeV and 4.5 MeV which are not explained in [7]. Above 100 keV James calculated the

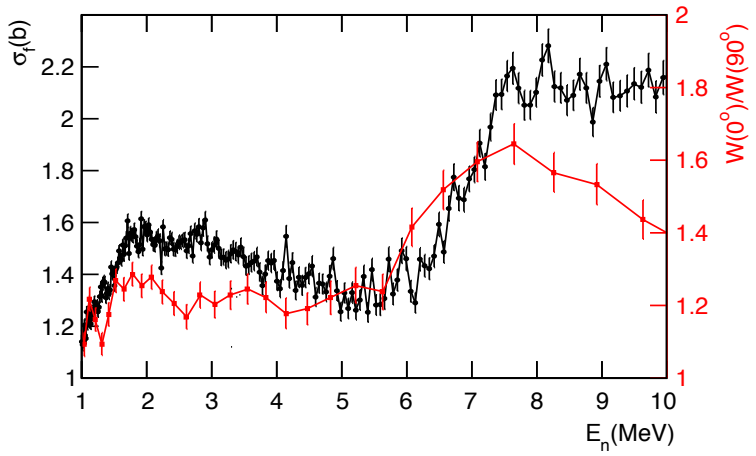

Figure 4.10: ^{234}U(n,f) cross section (black marks) and anisotropy parameter (red marks) obtained in this work in the energy region from 1 MeV to 10 MeV.

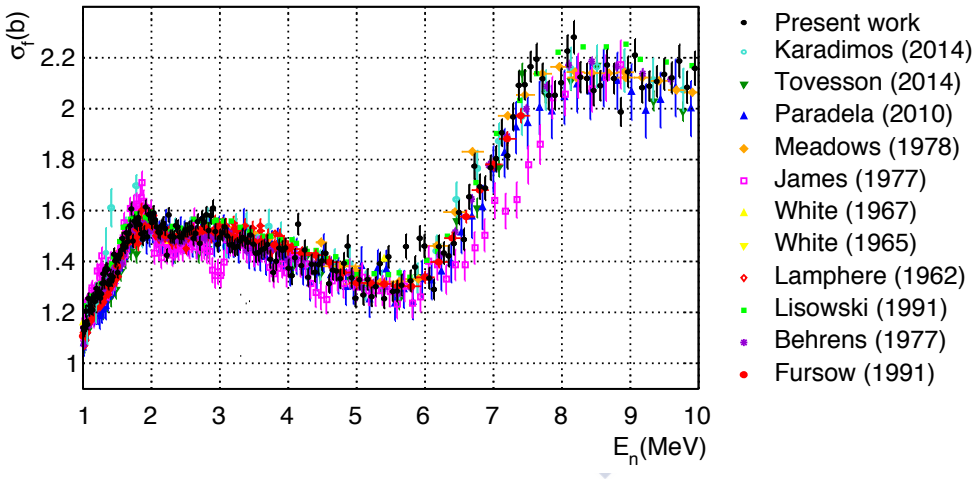

Figure 4.11: ^{234}U(n,f) cross section in the energy region from 1 MeV to 10 MeV compared with the EXFOR data.

^{234}U(n,f) cross section multiplying the ^{234}U/^{235}U ratio by a parametric fit to the evaluated ^{235}U(n,f) cross section. The parametric fit, correct the possible structures coming from the ^{235}U(n,f) cross section. Another discrepancy is an energy shift observed in the data of James with respect to the rest of data sets in the rising cross section in the proximity of the second chance. Above 1.4 MeV, Karadimos calculated the ^{234}U(n,f) cross section relative to the ^{238}U, the first point is completely allocated, despite of this, the rest of

cross section values are in good agreement with this work.

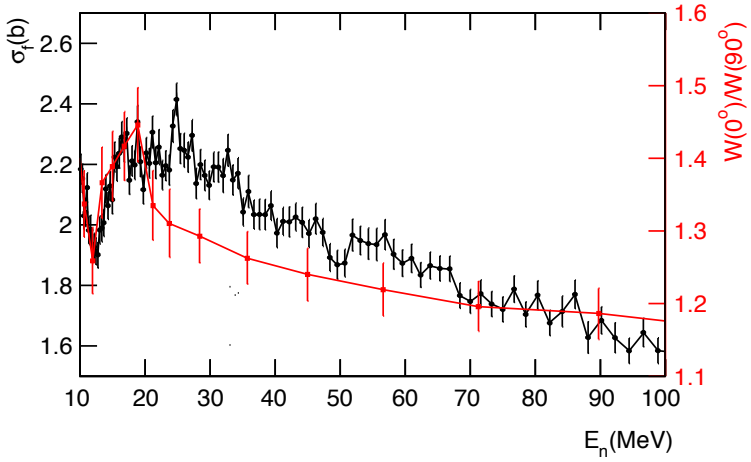

Figure 4.12: ^{234}U(n,f) cross section (black marks) and anisotropy parameter (red marks) obtained in this work in the energy region between 10 MeV and 100 MeV.

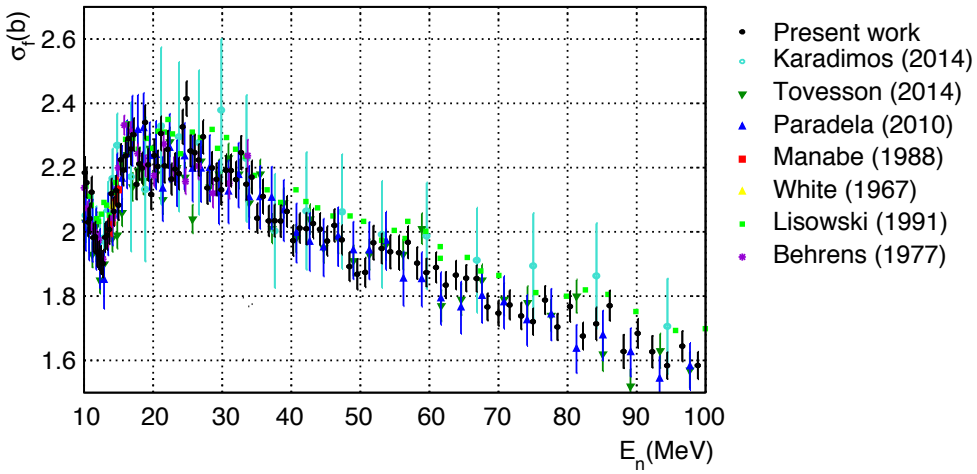

Figure 4.13: ^{234}U(n,f) cross section in the energy region between 10 MeV and 100 MeV obtained in this work compared with the EXFOR data.

This work is in good agreement with Meadows, Behrens, Fursow, Lamphere, White, Lisowski and Paradela. The agreement with Tovesson is good except at energies below 3 MeV, where its cross section is underestimated with respect to the present data and other measurements. The differences in its cross section when comparing with Paradela in this energy region were already mentioned in [57].

In the third chance, below 20 MeV, the incident neutron energy is sufficient so that two neutrons may be emitted from the compound nucleus before it fissions, being the fissioning nucleus in this case the ^{233}U. The opening of the (n,2nf) channel produces a plateau in the cross section due to the competition between the (n,f), (n,nf) and (n,2nf) channels (see Fig. 4.12 and Fig. 4.13). The cross section results are compared with the anisotropy parameter obtained in Chapter 2 in Fig. 4.13, both showing a decreasing trend with the energy. The present data are provided using 100 bins/decade in this region, as it was previously mentioned. In this region, Karadimos used a binning of 20 bins/decade due to the low intensity of the neutron beam with large error bars. A fair agreement is found with Karadimos within its error bars, however its cross section presents considerable fluctuations in all the energy range, remaining on top of the present data at energies above 40 MeV. A very good agreement is found with Paradela, and with the four points provided by Manabe [59] and the point provided by White. Discrepancies have been observed when comparing with the cross section measured by Lisowski, which is above the present data in the overall energy interval. A general good agreement is found with Behrens and Tovesson despite some discrepancies observed near the third chance.

4.3.3 Intermediate energy region

Only a few measurements are provided in EXFOR above 100 MeV, showing huge discrepancies between them and, from those, only the data of Paradela reach 1 GeV, however above 500 MeV these data are not reliable as it will be discussed in this section.

In this work, the binning has been reduced to 50 bin/decade from 100 MeV to 1 GeV, this is, to a binwidth of $2{\cdot}10^{-2}$ in logarithmic scale appropriate to the statistics.

In this energy region, Karadimos and Tovesson provide data up to 200 MeV, showing high statistical fluctuations and large discrepancies with respect to this work. The data of Karadimos and Tovesson are systematically higher and lower than the present data in the entire energy interval (see Fig. 4.15).

Lisowski provided data of the ^{234}U/^{235}U fission cross section ratio up to 400 MeV which are above the present cross section in the whole energy range. The only measurement above this energy is the one of Paradela which extends up to 1GeV, however the ^{234}U(n,f) cross section was calculated in his work using the ^{235}U(n,f) cross section provided by the JENDL/HE-2007 evaluation which is not correct above 500 MeV. As it was mentioned at the beginning of this section, the ^{234}U(n,f) cross section was obtained in this work using

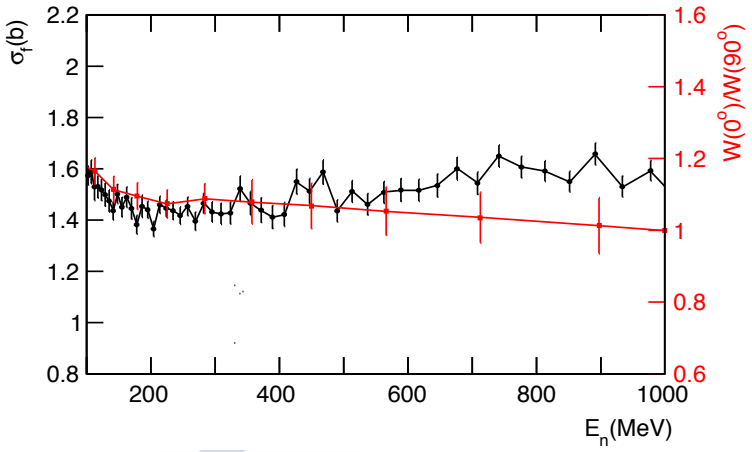

Figure 4.14: ^{234}U(n,f) cross section (black marks) and anisotropy parameter (red marks) obtained in this work in the energy region between 100 MeV and 1 GeV.

the recent ^{235}U(n,f) cross section evaluated in [45] above 200 MeV, therefore, when comparing the experimental data of Paradela, with the present data at high energies both cross sections have a completely different behaviour, while this data show a slight increase with the energy, the cross section measured by Paradela present a decreasing trend (see Fig. 4.15).

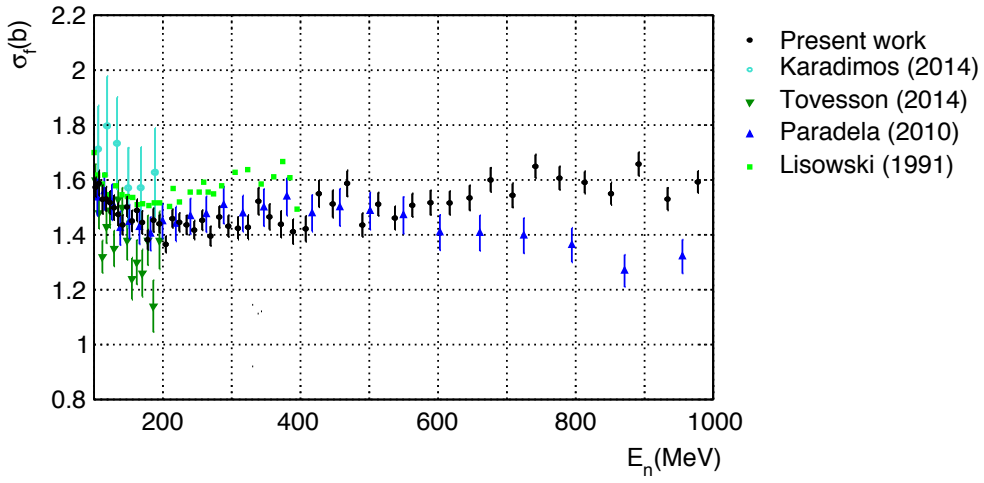

Figure 4.15: ^{234}U(n,f) cross section in the energy region between 100 MeV and 1 GeV obtained in this work compared with the EXFOR data.

In order to make a more exact comparison with the data measured by Paradela, a new calculation of its ^{234}U(n,f) cross section has been performed

in this work using as reference the ^{235}U(n,f) cross section provided by the IAEA Reference up to 200 MeV and the cross section obtained by Durán et al. up to 1 GeV (see Fig. 4.16). As it can be observed in the figure, the differences found between the present data and the data of Paradela above 200 MeV are clearly due to the ^{235}U(n,f) cross section used as a reference in each case.

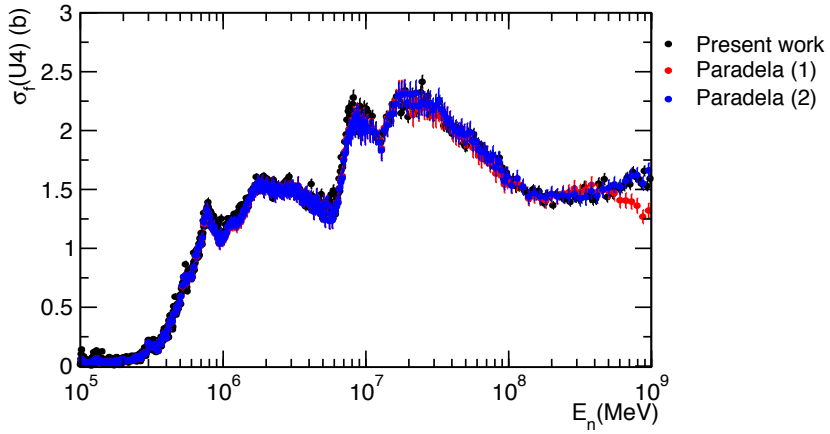

Figure 4.16: ^{234}U(n,f) cross section obtained in this work (black marks) compared with the results obtained by Paradela using the ENDF/B-VI evaluation below 30 MeV and JENDL/HE-2007 up to 1 GeV (red marks) and with the results obtained using the IAEA Reference up to 200 MeV and the data of Durán et al. up to 1 GeV (blue marks).

4.4 Evaluated cross section

The ^{234}U(n,f) cross section is compared in Fig. 4.17 with the ENDF/B-VII.1 and the JENDL-4.0 evaluations in the energy range from 100 keV to 20 MeV.

Large discrepancies are observed between both evaluations and the present experimental data below the fission threshold. Those are of a ∼60% with ENDF/B-VII.1 and a ∼30% with JENDL-4.0 around 310 keV where non evaluated structures, previously discussed, are found in the experimental cross section. In the energy region from 800 keV up to 2 MeV the present data are closer to JENDL-4.0 being underestimated in ENDF/B-VII.1 by a factor lower than the 5%. Above this energy the better agreement is found with ENDF/B-VII.1 and JENDL-4.0 data are in general above our results. Although slight discrepancies are observed, the peak at ∼800 keV is better

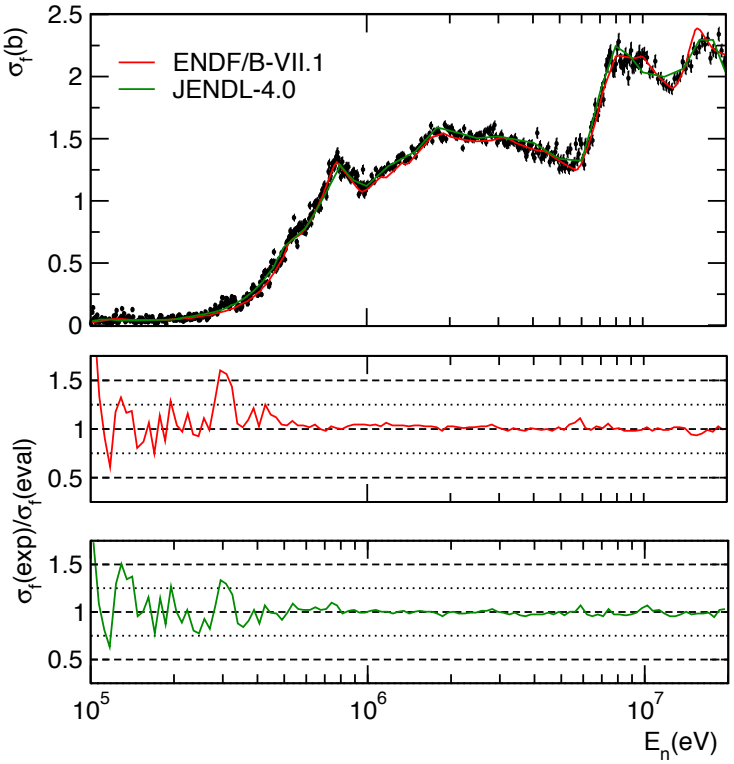

Figure 4.17: ^{234}U(n,f) cross section (black marks) compared with the ENDF/B-VII.1 (red line) and the JENDL-4.0 (green line) evaluations in the energy interval from 100 keV to 1 GeV (upper panel). Average ratio to the evaluations (lower panel).

reproduced by ENDF/B-VII.1 and the peak around 15 MeV by JENDL-4.0 while the elbows around 5 MeV and 12 MeV are closer to JENDL-4.0 and ENDF/B-VII.1 respectively.

USC
UNIVERSIDADE
DE SANTIAGO
DE COMPOSTELA

Summary and conclusions

Summary

This thesis work is framed into the study of the neutron-induced fission reaction in actinides carried out in the CERN-n_TOF facility using Parallel Plate Avalanche Counter (PPAC) detectors. This facility is characterized by a wide energy neutron beam, produced by proton-induced spallation reactions on a lead target, with unique energy resolution due to the high path length (185 m) to the experimental area (EAR-1).

After the thorium measurement this was the second time that the tilted setup was used. This setup permits to measure targets alternated with detectors, allowing to perform measurements of one target relative to other. Nine targets of ^{234,235,238}U and ^{237}Np were used in the experiment. This thesis focuses on the experiment and subsequent data analysis of the FFAD and fission cross section of the ^{235}U and ^{234}U targets.

As the setup efficiency is reduced, the angular distribution of the FFs must be included to correct the cross sections when it is anisotropic. The FFAD is considered to be isotropic below 100 keV and anisotropic above such energy. In previous n_TOF measurements of the ^{234}U(n,f) cross section with PPACs, the setup configuration was perpendicular to the beam and, therefore the higher emission angles could not be measured. The tilted setup used in this experiment allows to cover all the angles obtaining the ^{234}U(n,f) and ^{235}U(n,f) FFAD up to 300 MeV. The limit at high energy is due to pile-up effects in the cathode signals which may affect to the reconstruction of the fragment position in the detectors.

An innovative contribution performed in this analysis with respect to previous measurements reside in the detailed study of the cuts required for an improved discrimination of the background from the FFs. The background is different for each energy region because it comes from random coincidences

of signals produced by light particles and spallation residuals from neutron-induced reactions in the detector and target layers. In addition, for the detectors close to ^{234}U targets, there is also a larger contribution of the alpha background at low energies. For this reason the background has been studied specifically at each energy range for each individual target. This study has been performed through the amplitudes of the signals at the two detectors flanking the target, the sum of both amplitudes allow to distinguish the background particles, accumulated at lower amplitude, from the usually higher amplitude signals corresponding to FFs events. A threshold has been then applied in this distribution to remove the low amplitude background events, calculating after that, the percentage of background events passing the threshold and the percentage of rejected FFs respectively from the areas below the tails of both distributions. These correction factors have been applied to obtain the cross sections for each target.

The ^{235}U(n,f) cross section has been obtained below 100 keV using the neutron flux shape normalised to the IAEA secondary reference between 7.8 eV and 11 eV. The PPAC detectors were running in parallel with a MGAS detector during the data taking of this experiment, which was used to measure the neutron flux through the ^{10}B(n,α) reaction accurately up to 10 keV [40], above this energy it was feasible to use the neutron flux shape obtained in a previous campaign because the n_TOF neutron flux shape above 100 eV is independent of the type of moderator water/borated water used and on the ^{10}B concentration.

The ^{234}U(n,f) cross section has been calculated, separately in two energy ranges, up to 1 GeV using as reference the ^{235}U(n,f) cross section which, besides being considered a secondary reference is a IAEA standard in the neutron energy range from 0.15 MeV to 200 MeV. Both results have been compared, obtaining a very good agreement between them with better resolution than the experimental data provided in the EXFOR database [4].

Above 100 keV the ^{234}U(n,f) cross section has been calculated relative to the ^{235}U(n,f) cross section provided by the IAEA Reference [52] up to 200 MeV and to the recent evaluation of Durán et al. up to 1 GeV.

Conclusions

The main conclusions of this thesis work are summarised as follows:

- Successful cross section and FFAD results have been obtained for the ^{234}U(n,f) and ^{235}U(n,f) reactions measured with PPAC detectors at CERN-n_TOF.

- The detailed study of the amplitude cuts during the data analysis improved the background discrimination at different energy ranges allowing to correct the cross section by the percentage of lost fission events.

- Results of the ^{234}U(n,f) FFAD are provided in this work for first time above 15 MeV covering the third chance region, where no experimental data are available in EXFOR. In addition, this is the first experimental measurement in the full energy range from 100 keV up to 300 MeV. Some discrepancies have been observed in the FFAD and in the anisotropy parameter with respect to previous experimental data in the threshold region, where the angular distributions of the FFs varies rapidly.

- The ^{235}U(n,f) FFAD and the anisotropy parameter have been compared in the wide energy region up to 300 MeV with the EXFOR data showing a general good agreement within the errors with them despite the discrepancies shown by the different experimental data sets in the second and third chance regions.

- High energy resolution ^{235}U(n,f) cross sections have been calculated up to 100 keV using the n_TOF flux shape based on the measurement of the ^{10}B(n,α) reaction with MGAS normalised to the IAEA secondary reference between 7.8 eV and 11 eV. The present data are in very good agreement with the recent evaluation performed by L. C. Leal up to 10 keV, based on the previous n_TOF data measured by Paradela, confirming the discrepancies with the ENDF/B-VII.1 database due to the low background achieved in the n_TOF facility. Above this energy these data contribute to clarify some discrepancies existing between the available sets of experimental data.

- The ^{234}U(n,f) cross section results obtained below 100 keV using the neutron flux shape obtained through two different reactions (^{10}B(n,α) and ^{235}U(n,f)) are in very close agreement between them. The present data have better resolution than EXFOR experimental data being closer to the previous n_TOF PPAC measurement of Paradela. The

existence of two resonances in the resolved resonance region (RRR) which are evaluated in ENDF/B-V.II but not in JENDL-4.0 is confirmed by the present data. In the unresolved resonance region (URR) some Class-II resonances are clearly identified in this work and in previous data where an averaged cross section is provided by the evaluated databases.

- The ^{234}U(n,f) cross section has been calculated relative to the ^{235}U(n,f) cross section above 100 keV. The high energy resolution achieved allows to distinguish in very fine detail the structures found in the subthreshold region around 215 keV, 310 keV, 550 keV and 770 keV, corresponding to Class-II and Class-III levels in the fission barrier wells. The study of these structures was one of the main objectives of this experiment, where the angular distribution of the FFs varies rapidly and, therefore, an accurate measurement of the ^{234}U(n,f) cross section depends, to a great extend, on a precise value of the FFAD. The cross section has been compared with the EXFOR data in the fission chances region, where some discrepancies are found between the available experimental data in the thresholds, probably due to the large anisotropies which have been successfully included in the efficiency calculation in this work. Above 100 MeV and up to 1 GeV, the present results are in very good agreement with the only experimental dataset available in EXFOR (Paradela) when these are recalculated using the ^{235}U(n,f) cross section provided by the IAEA Reference and the recent evaluation of Durán et al. instead of the JENDL/HE-2007 evaluation originally used, which has been recently seriously question.

Resumen en castellano

Este trabajo de tesis está enmarcado en la medida de la reacción de fisión inducida por neutrones en actínidos llevada a cabo en la instalación n_TOF del CERN utilizando detectores de tipo gaseoso PPAC (Parallel Plate Avalanche Counter). Esta instalación se caracteriza por un haz de neutrones continuo en energía que abarca desde neutrones térmicos hasta 1 GeV, producido por reacciones de espalación inducida por un haz de protones en un blanco de plomo, con una resolución única en energía ($5.3 \cdot 10^{-3}$ a 1 MeV) debido a la larga distancia (185 m) entre el blanco de espalación y la sala experimental (EAR-1), donde se encuentran los blancos y los detectores.

El dispositivo experimental utilizado contiene blancos alternados entre detectores, permitiendo realizar medidas de un blanco relativo a otro. En este experimento se han utilizado nueve blancos, de ^{234,235,238}U y ^{237}Np, de los cuales han sido medidos y analizados en esta tesis los de ^{234}U y ^{235}U para obtener la distribución angular de los fragmentos de fisión y la sección eficaz de fisión de ambos isótopos.

En este trabajo se ha realizado un estudio detallado de los cortes requeridos para mejorar la separación del fondo de los fragmentos de fisión que no se había llevado a cabo en anteriores medidas. El fondo es diferente para cada región de energía, esto es debido a que proviene de coincidencias aleatorias de señales que son producidas por partículas ligeras y residuos de espalación de reacciones inducidas por neutrones en el detector y en las láminas de los blancos. Además, en los detectores cercanos a los blancos de ^{234}U hay también una gran contribución del fondo de radiación alfa a bajas energías. Por este motivo, para cada blanco individual se ha estudiado específicamente el fondo en cada rango de energía. Este estudio ha sido realizado a través de las amplitudes de las señales en los dos detectores a los lados del blanco, la suma de ambas amplitudes permite distinguir las partículas del fondo, acumuladas a menor amplitud, de las amplitudes normalmente mayores correspondientes a los fragmentos de fisión. Los eventos del fondo de baja amplitud han sido eliminados aplicando un umbral en dicha distribución de amplitudes, tras lo cual se ha calculado el porcentaje de eventos del fondo que pasan el umbral y

el porcentaje de fragmentos de fisión eliminados, respectivamente, a través de las áreas bajo las colas de ambas distribuciones. Estos factores de corrección han sido aplicados para obtener las secciones eficaces de cada blanco.

Como la eficiencia del dispositivo experimental es reducida, la distribución angular de los fragmentos de fisión debe ser incluida, cuando es anisótropa, para corregir la sección eficaz. La distribución angular de los fragmentos de fisión se considera isótropa por debajo de 100 keV y anisótropa por encima de dicha energía. En la anterior medida de la sección eficaz de la reacción ^{234}U(n,f) realizada con PPACs en n_TOF, el dispositivo experimental se dispuso perpendicular al haz y, por lo tanto, los ángulos mayores de emisión de los fragmentos no podían ser medidos. El dispositivo inclinado 45° respecto al haz de neutrones, utilizado en este experimento, permite cubrir todos los ángulos. En este trabajo se han medido las distribuciones angulares de los fragmentos de fisión de las reacciones ^{234}U(n,f) y ^{235}U(n,f) hasta 300 MeV. El límite en energía es debido a efectos de acumulación en las señales de los cátodos que pueden afectar a la reconstrucción de la posición de detección de los fragmentos en los detectores.

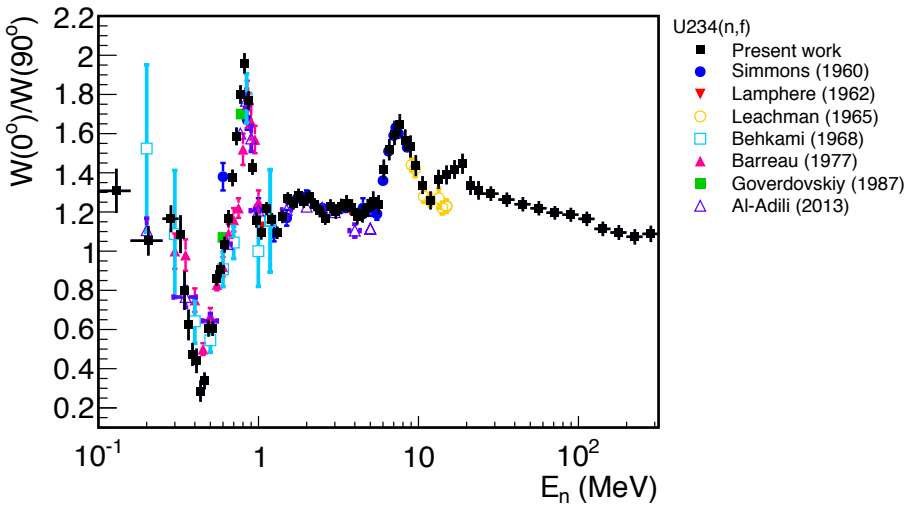

Figure 4.18: Resultado del parámetro de anisotropía de la reacción ^{234}U(n,f) comparado con los datos experimentales de EXFOR.

En esta tesis, se proporcionan por primera vez resultados de la distribución angular de los fragmentos de fisión de la reacción ^{234}U(n,f) por encima de 15 MeV, cubriendo la región del third chance (n,2nf), de la que no hay datos experimentales disponibles en EXFOR [4]. Además, esta es la primera medida experimental en el rango completo de energía entre 100 keV y 300 MeV (ver Fig. 4.18). Se han observado algunas discrepancias en las

distribuciones angulares y en el parámetro de anisotropía (W(0°)/W(90°)) con respecto a medidas experimentales anteriores en la zona del umbral (n,f), donde las distribuciones angulares de los fragmentos de fisión varían rápidamente.

Los resultados de la distribución angular de los fragmentos de fisión y el parámetro de anisotropía de la reacción ^{235}U(n,f) han sido comparados en el rango de energía entre 100 keV y 300 MeV con los datos experimentales proporcionados por EXFOR, mostrando en general un buen acuerdo dentro de los errores a pesar de las discrepancias existentes entre los distintos conjuntos de datos experimentales en las regiones del second (n,nf) y third chances (ver Fig. 4.19).

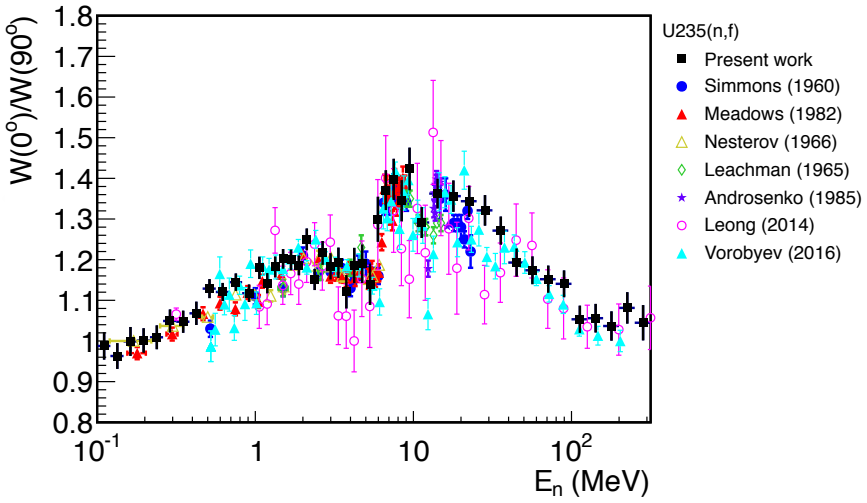

Figure 4.19: Resultado del parámetro de anisotropía de la reacción ^{235}U(n,f) comparado con anteriores datos experimentales.

La sección eficaz de la reacción ^{235}U(n,f) ha sido obtenida por debajo de 100 keV utilizando la forma del flujo de neutrones, normalizada al valor de la sección eficaz proporcionado por la referencia secundaria de la IAEA, entre 7.8 eV y 11 eV. Durante este experimento, los detectores PPAC midieron en paralelo con detectores MGAS, que fueron usados para medir el flujo de neutrones con precisión hasta 10 keV a través de la reacción ^{10}B(n,α) [40], por encima de dicha energía se utilizó el flujo de neutrones de n_TOF obtenido en una campaña previa, ya que por encima de unos cientos de eV es independiente del tipo de moderador (agua/agua borada) utilizado y de la concentración de ^{10}B en el agua. Los resultados obtenidos están en muy buen acuerdo con la reciente evaluación de L. C. Leal [43], basada en los datos experimentales medidos por Paradela en n_TOF hasta 10 keV, confirmando las

discrepancias encontradas con la evaluación ENDF/B-VII.1debidas al bajo fondo obtenido en la instalación n_TOF (ver Fig. 4.20). Por encima de esta energía, estos datos contribuyen a clarificar algunas discrepancias observadas entre los datos experimentales obtenidos en medidas previas.

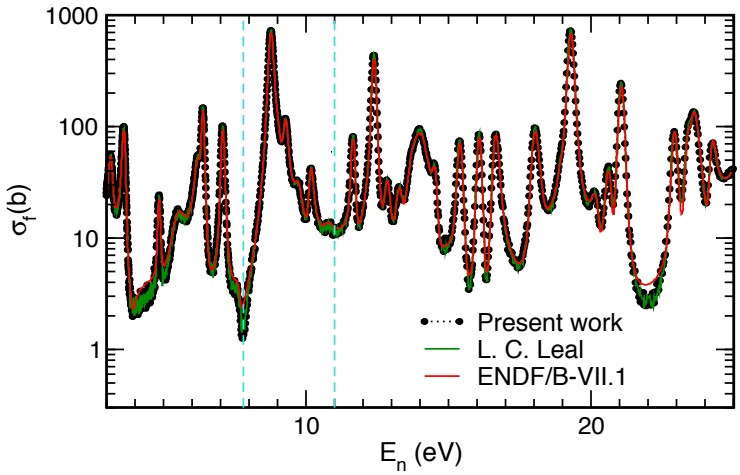

Figure 4.20: Sección eficaz de la reacción ^{235}U(n,f) obtenida en este trabajo comparada con la nueva evaluación de L. C. Leal y la evaluación ENDF/B-VII.1. Los límites de la referencia secundaria de la IAEA están indicados con líneas punteadas azules.

La sección eficaz de la reacción ^{234}U(n,f) ha sido calculada, de manera independiente en dos rangos de energía hasta 1 GeV usando como referencia la sección eficaz de la reacción ^{235}U(n,f) que, además de ser considerada una referencia secundaria, es un estándar de la IAEA en el rango de energía entre 0.15 MeV y 200 MeV. Los resultados obtenidos por debajo de 100 keV usando la forma del flujo de neutrones obtenida a través de dos reacciones diferentes (^{10}B(n,α) y ^{235}U(n,f)) están en muy buen acuerdo entre sí y tienen mejor resolución que los datos experimentales de EXFOR, siendo próximos a los resultados obtenidos en la anterior medida realizada con PPACs en n_TOF por Paradela [1] (ver Fig. 4.21).

En este trabajo se confirma la existencia de dos resonancias observadas en la zona de resonancias resueltas que han sido evaluadas en ENDF/B-V.II pero no en JENDL-4.0 (ver Fig. 4.22). En la zona de resonancias no resueltas, se identifican con claridad algunas resonancias de Clase-II en este trabajo y en anteriores medidas, en una región en la que las bases de datos evaluadas proporcionan un valor promediado de la sección eficaz.

Por encima de 100 keV, la sección eficaz de la reacción ^{234}U(n,f) ha sido calculada relativa a la del ^{235}U utilizando la sección eficaz proporcionada por

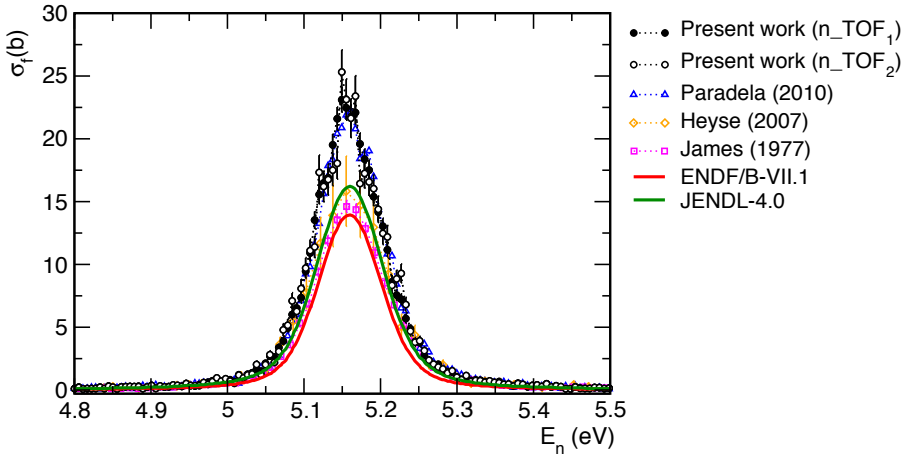

Figure 4.21: Comparación entre los resultados de este trabajo, los datos experimentales de EXFOR y las evaluaciones ENDF/B-VII.1 y JENDL-4.0 en la primera resonancia de la reacción ^{234}U(n,f).

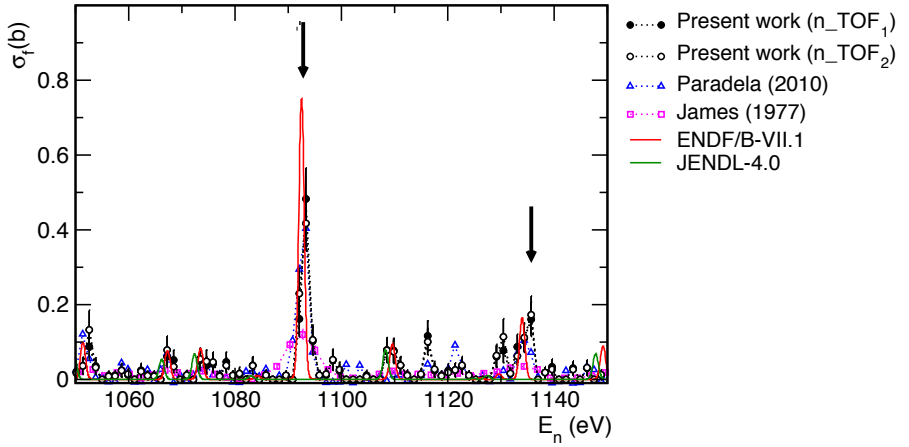

Figure 4.22: Sección eficaz de la reacción ^{234}U(n,f) en torno a 1 keV. Las dos resonancias que no aparecen en JENDL-4.0 están indicadas con una flecha.

la Referencia de la IAEA [52] hasta 200 MeV y la reciente evaluación de Durán et al. [45] hasta 1 GeV. La alta resolución de estos datos permite distinguir en detalle las estructuras encontradas en la región del umbral en 215 keV, 310 keV, 550 keV y 770 keV, atribuidas a niveles de Clase-II y Clase-III en los pozos de la barrera de fisión (ver Fig. 4.23). El estudio de estas estructuras era uno de los principales objetivos de este trabajo, en una zona en la que la distribución angular de los fragmentos de fisión varía rápidamente y, por lo tanto, una medida precisa de la sección eficaz

de la reacción ^{234}U(n,f) depende, en gran medida, de un valor preciso de la distribución angular.

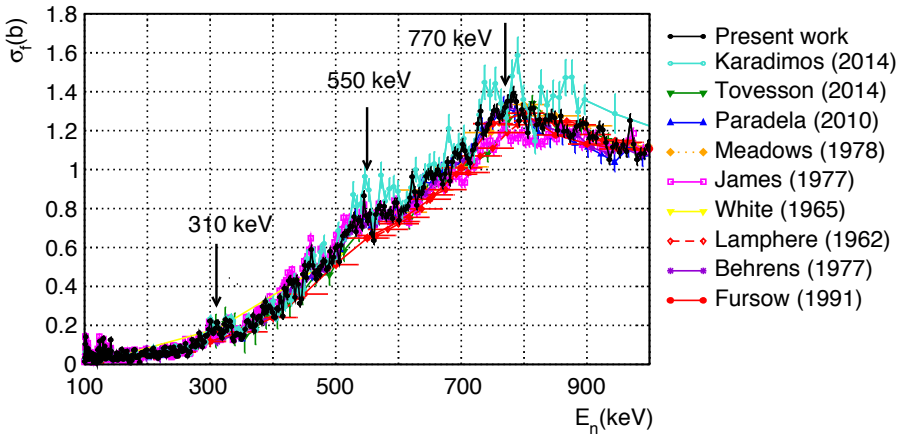

Figure 4.23: Sección eficaz de la reacción ^{234}U(n,f) en el rango de energía entre 100 keV y 1 MeV comparado con los datos experimentales de EXFOR.

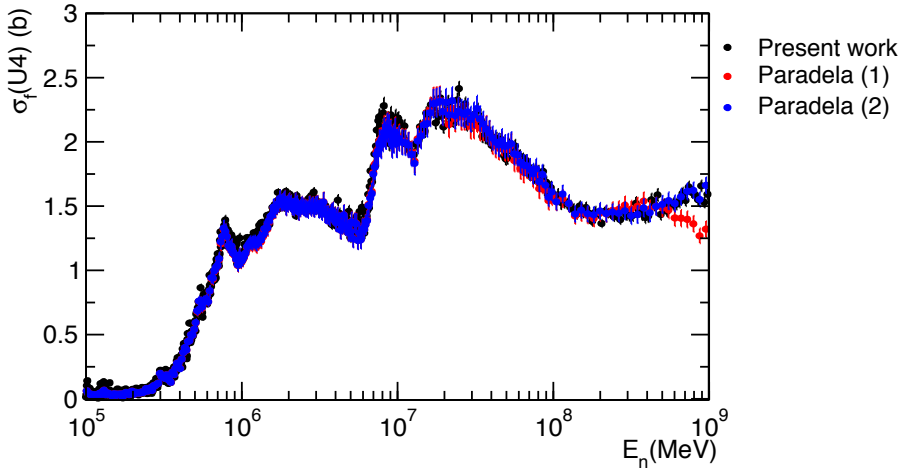

Figure 4.24: Sección eficaz de la reacción ^{234}U(n,f) obtenida en este trabajo comparada con los resultados de Paradela usando la evaluación ENDF/B-VI hasta 30 MeV y JENDL/HE-2007 hasta 1 GeV y con sus resultados recalculados usando la Referencia de la IAEA hasta 200 MeV y la evaluación de Durán et al. hasta 1 GeV.

La sección eficaz ha sido comparada con los datos experimentales disponibles en EXFOR en la zona de los fission chances, donde se han observado algunas discrepancias respecto a anteriores medidas en los umbrales, probablemente

debido a las grandes anisotropías, que han sido eficazmente incluídas en el cálculo de la eficiencia en este trabajo.

En la región de energía entre 100 MeV y 1 GeV, la sección eficaz obtenida en este trabajo está en muy buen acuerdo con la única medida experimental proporcionada en EXFOR por Paradela tras recalcular su sección eficaz usando sección eficaz de la reacción ^{235}U(n,f) proporcionada por la Referencia de la IAEA y la evaluación de Durán et al. en lugar de la evaluación JENDL/HE-2007 utilizada en los datos originales, la cual ha sido seriamente cuestionada recientemente [46] (ver Fig. 4.24).

USC
UNIVERSIDADE
DE SANTIAGO
DE COMPOSTELA

Appendix A

Standard cross section

A.1 ^{6}Li(n,α)t

The ^{6}Li(n,α)t cross section has a smooth trend inversely proportional to the velocity of the neutron, presenting one resonance around 240 keV (see Fig. A.1).

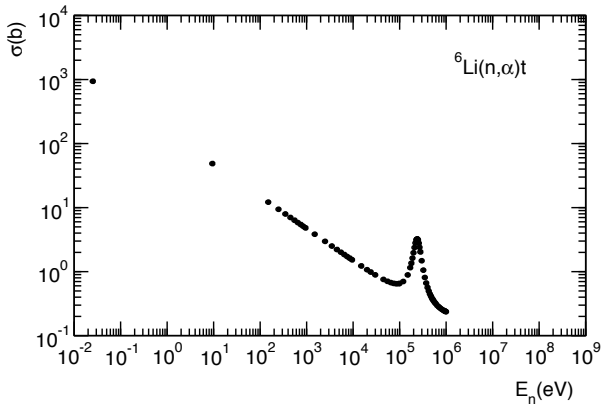

Figure A.1: ^{6}Li(n,α)t standard cross section.

Li-glass scintillator detectors or Si monitors are commonly used to measure this reaction at low neutron energies.

A.2 ^{10}B(n,α)^{7}Li

There are two exit channels for the ^{10}B(n,α)^{7}Li reaction: in the first case, the product is in the ground state. The ^{10}B(n,α)^{7}Li cross section has quite a smooth shape (see Fig. A.2).

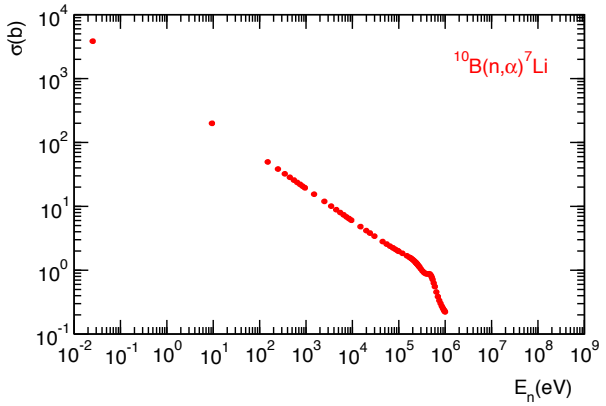

Figure A.2: ^{10}B(n,α)^{7}Li standard cross section.

Proportional counters or ionization chambers are commonly used to measure this reaction in the mentioned energy range.

In the second exit channel of the ^{10}B(n,α)^{7}Li reaction, the product is in the first excited state and decay to the ground state emitting a characteristic 478 keV γ-ray. The α particle is emitted with a kinetic energy of 1.47 MeV and the ^{7}Li with 0.84 MeV. The ^{10}B(n,$\alpha\gamma$)^{7}Li standard cross section is shown in Fig. A.3.

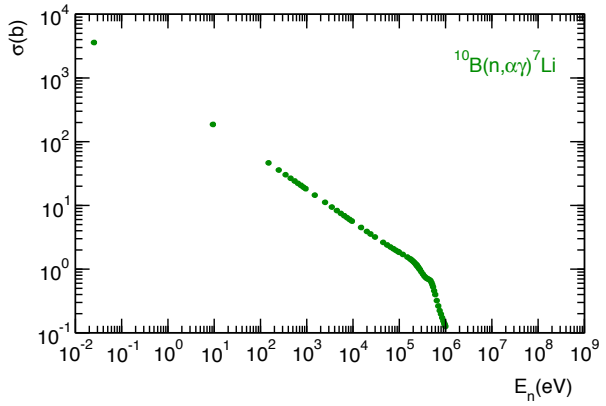

Figure A.3: ^{10}B(n,$\alpha\gamma$)^{7}Li standard cross section.

The flux may be determined trough this reaction measuring the 478 keV γ-ray peak with γ-ray detectors such as Ge-spectrometers. Other possibility is to detect both the α particles and the γ-ray peak, for example, using a MicroMegas (MGAS) detector as in n_TOF [25]. The backward/forward anisotropy of the emitted α particles has to be considered in the detection efficiency when measuring this reaction above a few keV.

A.3 ^{235}U(n,f)

The determination of the neutron flux using the ^{235}U(n,f) relies in the detection of one or the two fission fragments (FF). The n_TOF facility the MGAS detector and the PTB fission chamber were used to detect one FF and the PPACs to detect both of them. Although this reaction is considered a standard from 0.15 MeV to 200 MeV, it is worth to mention the fact that in the IAEA nuclear standards database there are some files termed as "recommended" which are not accurate enough to be included as standard, being, nevertheless, very trustworthy (see Fig. A.4).

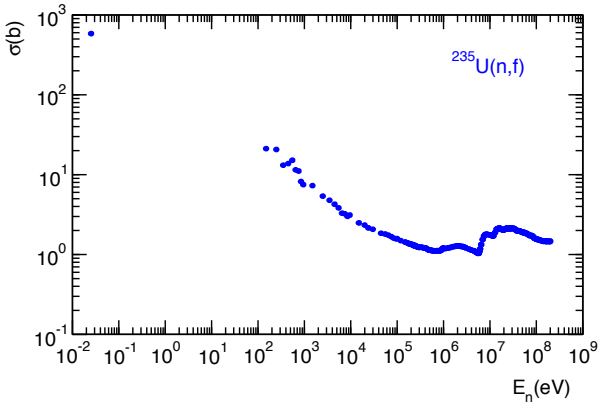

Figure A.4: ^{235}U(n,f) standard cross section.

USC
UNIVERSIDADE
DE SANTIAGO
DE COMPOSTELA

Appendix B

Numerical results

B.1 ^{234}U(n,f) angular distributions compared with EXFOR

Figure B.1: ^{234}U(n,f) angular distributions compared with EXFOR data.

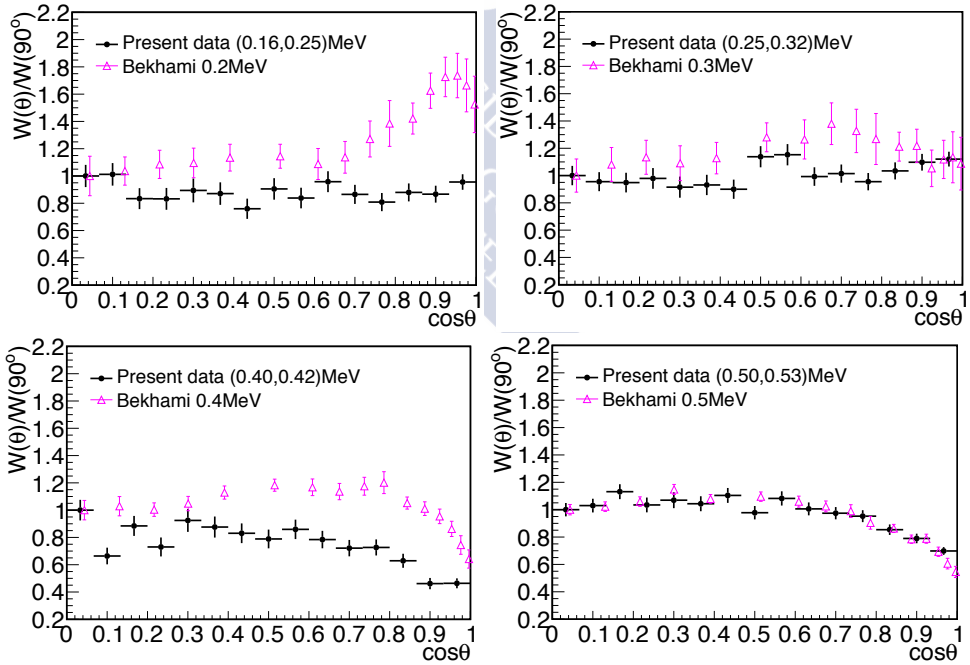

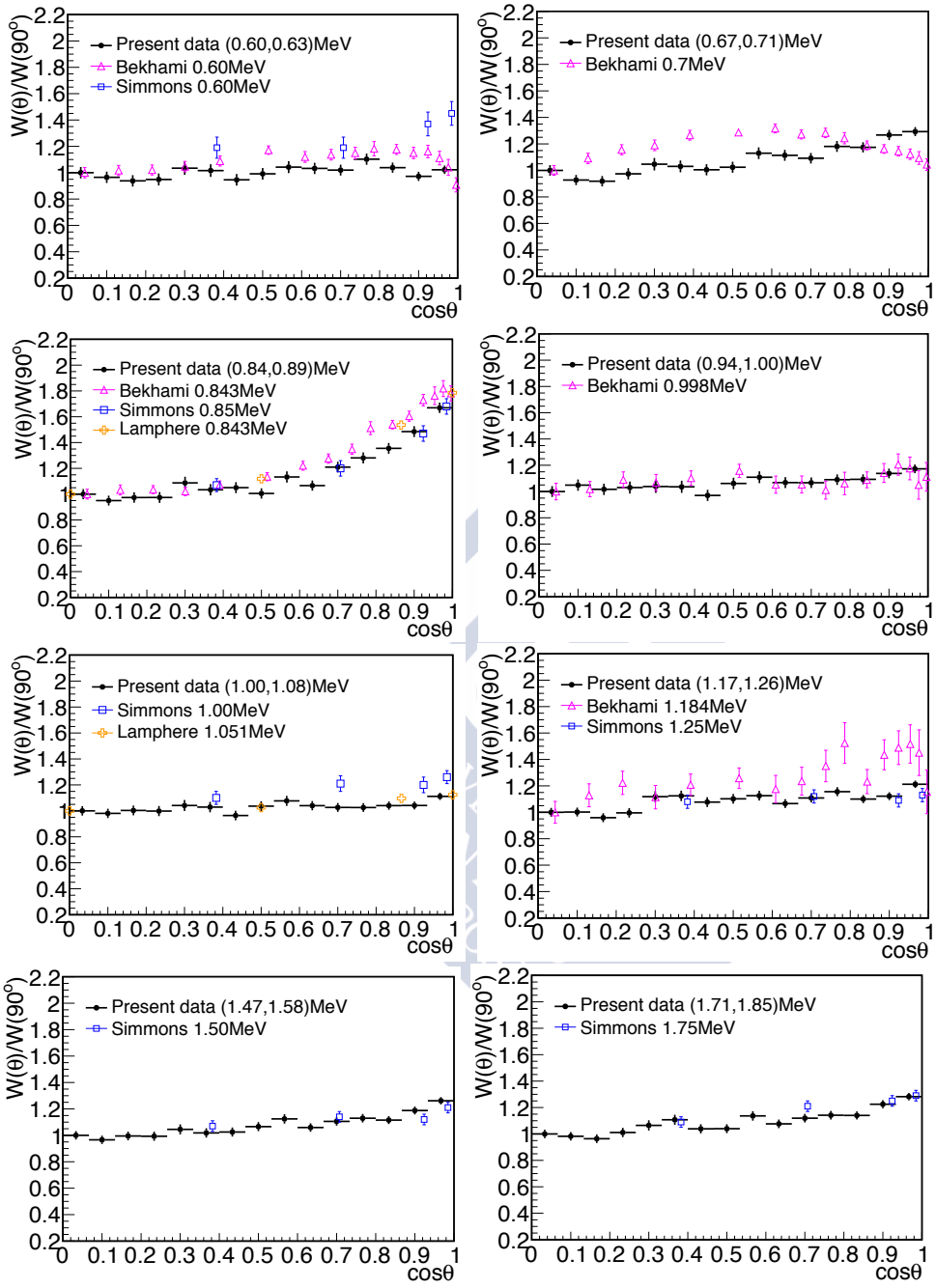
W(θ)/W(90°)
cosθ
Present data (0.60,0.63)MeV
Bekhami 0.60MeV
Simmons 0.60MeV
Present data (0.67,0.71)MeV
Bekhami 0.7MeV
Present data (0.84,0.89)MeV
Bekhami 0.843MeV
Simmons 0.85MeV
Lamphere 0.843MeV
Present data (0.94,1.00)MeV
Bekhami 0.998MeV
Present data (1.00,1.08)MeV
Simmons 1.00MeV
Lamphere 1.051MeV
Present data (1.17,1.26)MeV
Bekhami 1.184MeV
Simmons 1.25MeV
Present data (1.47,1.58)MeV
Simmons 1.50MeV
Present data (1.71,1.85)MeV
Simmons 1.75MeV

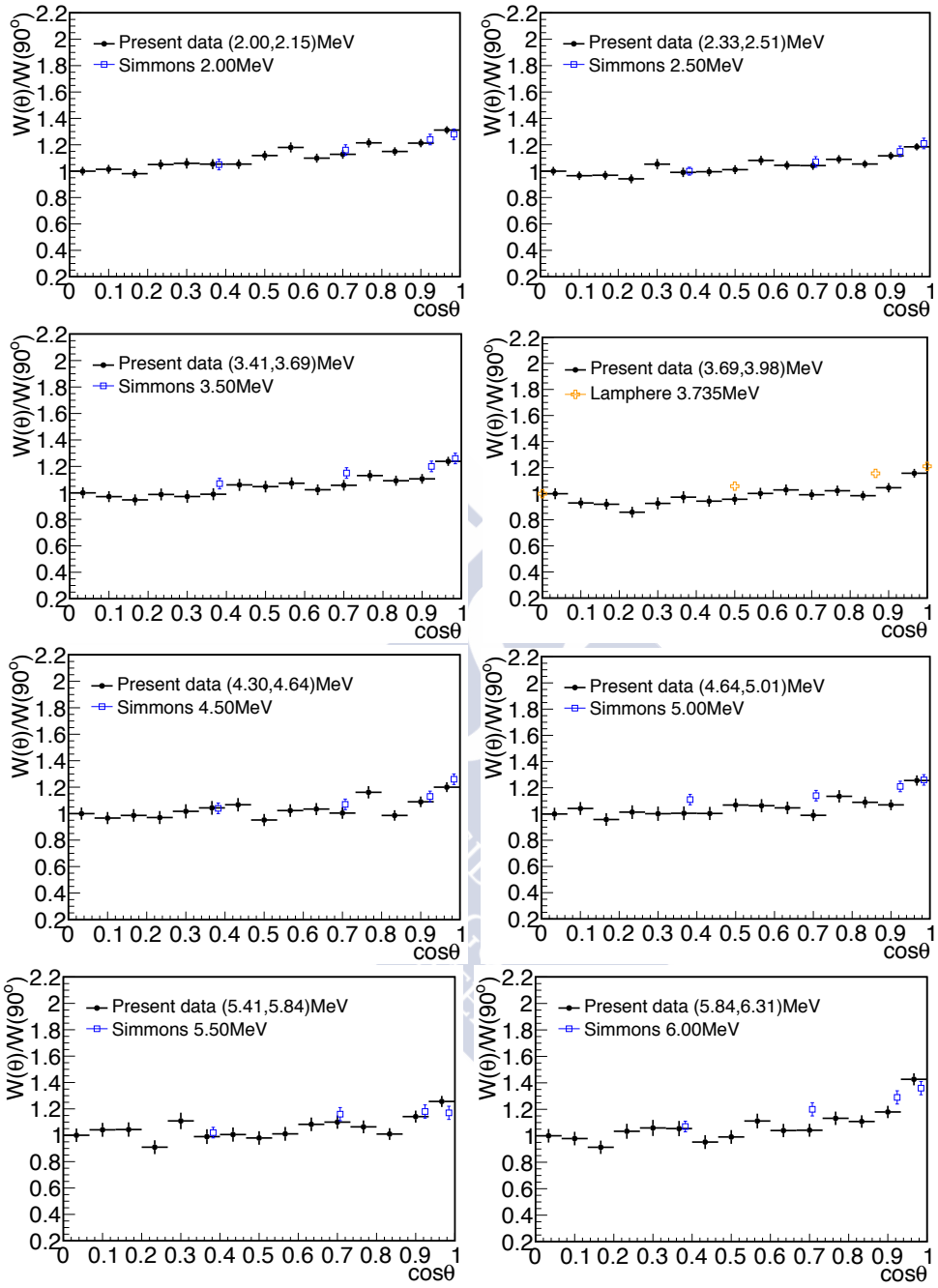
Present data (2.00,2.15)MeV
Simmons 2.00MeV
Present data (2.33,2.51)MeV
Simmons 2.50MeV
Present data (3.41,3.69)MeV
Simmons 3.50MeV
Present data (3.69,3.98)MeV
Lamphere 3.735MeV
Present data (4.30,4.64)MeV
Simmons 4.50MeV
Present data (4.64,5.01)MeV
Simmons 5.00MeV
Present data (5.41,5.84)MeV
Simmons 5.50MeV
Present data (5.84,6.31)MeV
Simmons 6.00MeV
W(θ)/W(90°)
cosθ

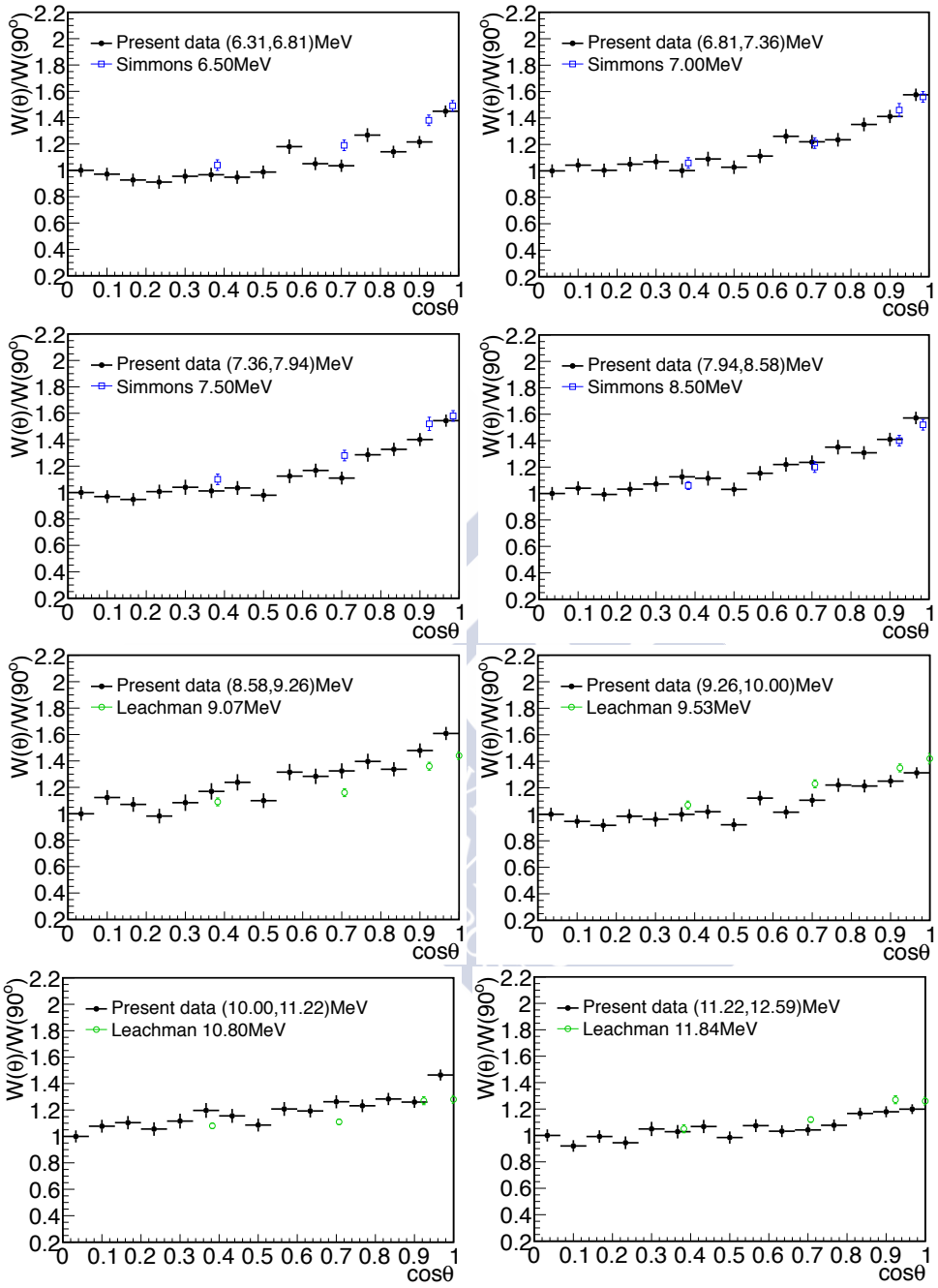
Present data (6.31,6.81)MeV
Simmons 6.50MeV
Present data (6.81,7.36)MeV
Simmons 7.00MeV
Present data (7.36,7.94)MeV
Simmons 7.50MeV
Present data (7.94,8.58)MeV
Simmons 8.50MeV
Present data (8.58,9.26)MeV
Leachman 9.07MeV
Present data (9.26,10.00)MeV
Leachman 9.53MeV
Present data (10.00,11.22)MeV
Leachman 10.80MeV
Present data (11.22,12.59)MeV
Leachman 11.84MeV
W(θ)/W(90°)
cosθ

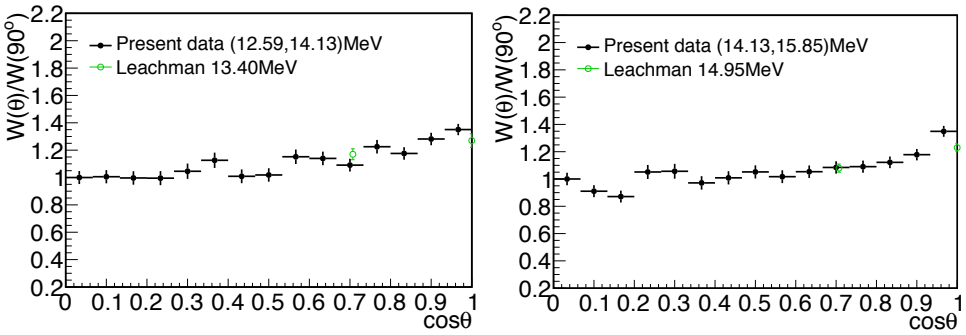

B.2 ^{235}U(n,f) angular distributions compared with EXFOR

Figure B.2: ^{235}U(n,f) angular distributions compared with EXFOR data.

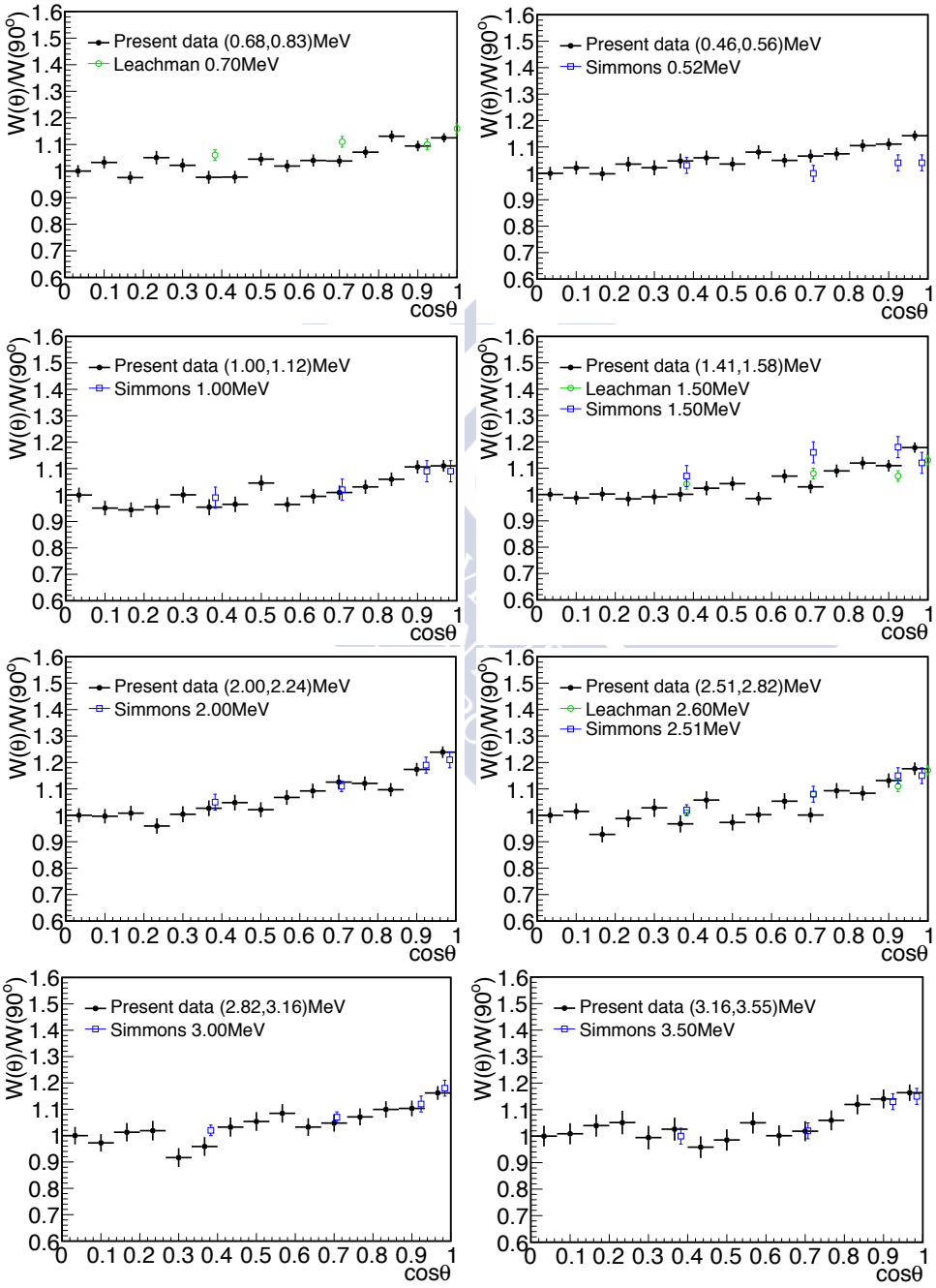

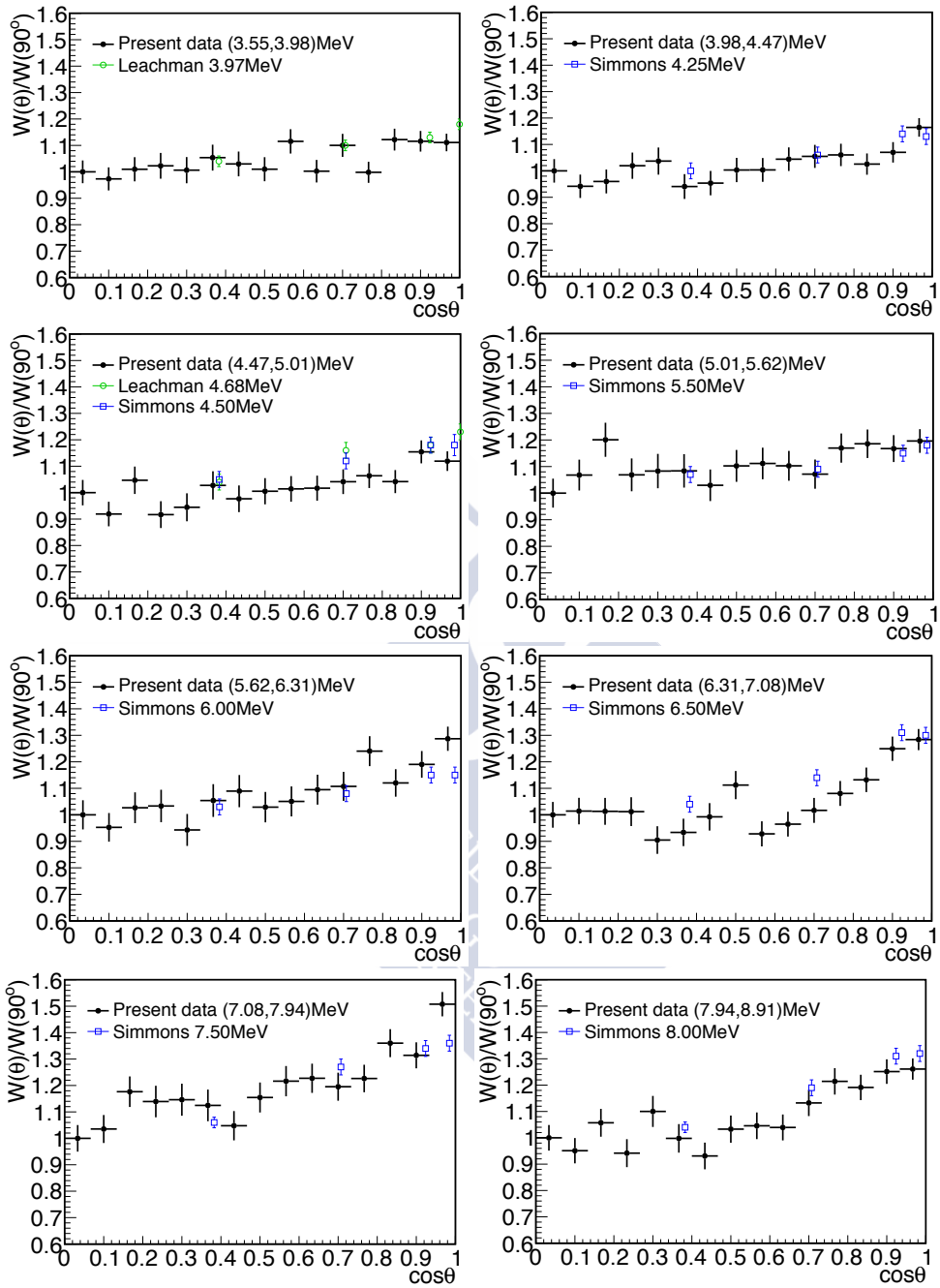
Present data (3.55,3.98)MeV
Leachman 3.97MeV
Present data (3.98,4.47)MeV
Simmons 4.25MeV
Present data (4.47,5.01)MeV
Leachman 4.68MeV
Simmons 4.50MeV
Present data (5.01,5.62)MeV
Simmons 5.50MeV
Present data (5.62,6.31)MeV
Simmons 6.00MeV
Present data (6.31,7.08)MeV
Simmons 6.50MeV
Present data (7.08,7.94)MeV
Simmons 7.50MeV
Present data (7.94,8.91)MeV
Simmons 8.00MeV
W(θ)/W(90°)
cosθ

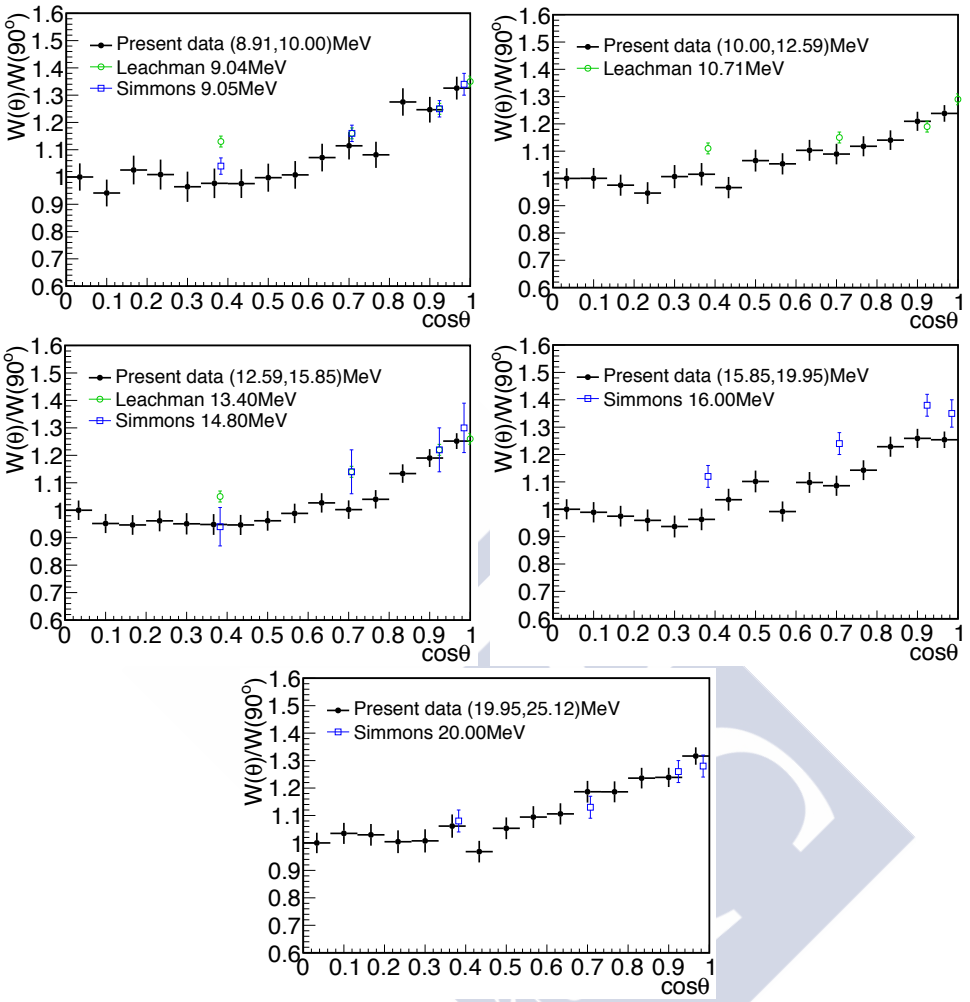
W(θ)/W(90°)
cosθ
Present data (8.91,10.00)MeV
Leachman 9.04MeV
Simmons 9.05MeV
Present data (10.00,12.59)MeV
Leachman 10.71MeV
Present data (12.59,15.85)MeV
Leachman 13.40MeV
Simmons 14.80MeV
Present data (15.85,19.95)MeV
Simmons 16.00MeV
Present data (19.95,25.12)MeV
Simmons 20.00MeV

B.3 ^{234}U(n,f) angular distributions

Figure B.3: ^{234}U(n,f) angular distributions.

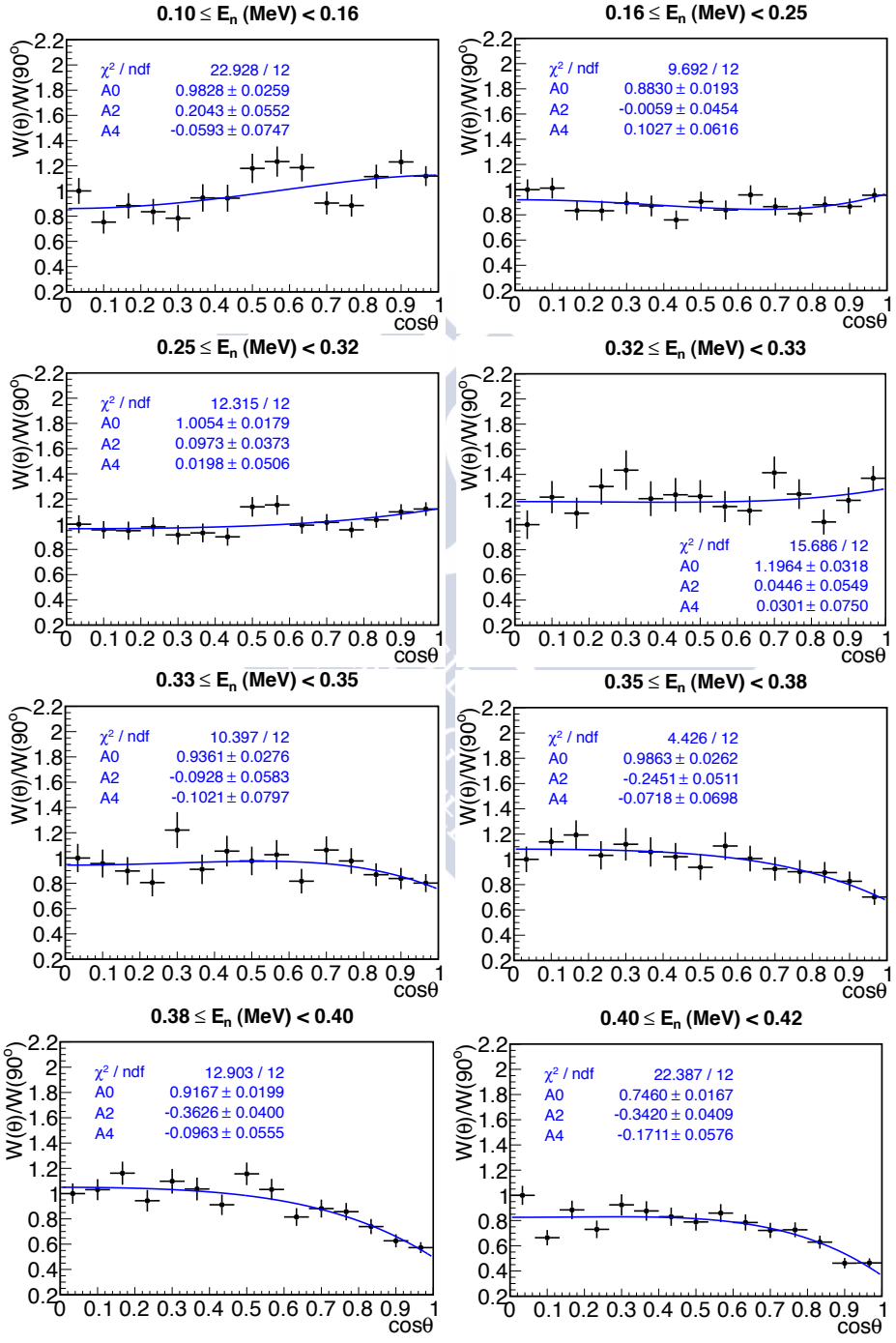

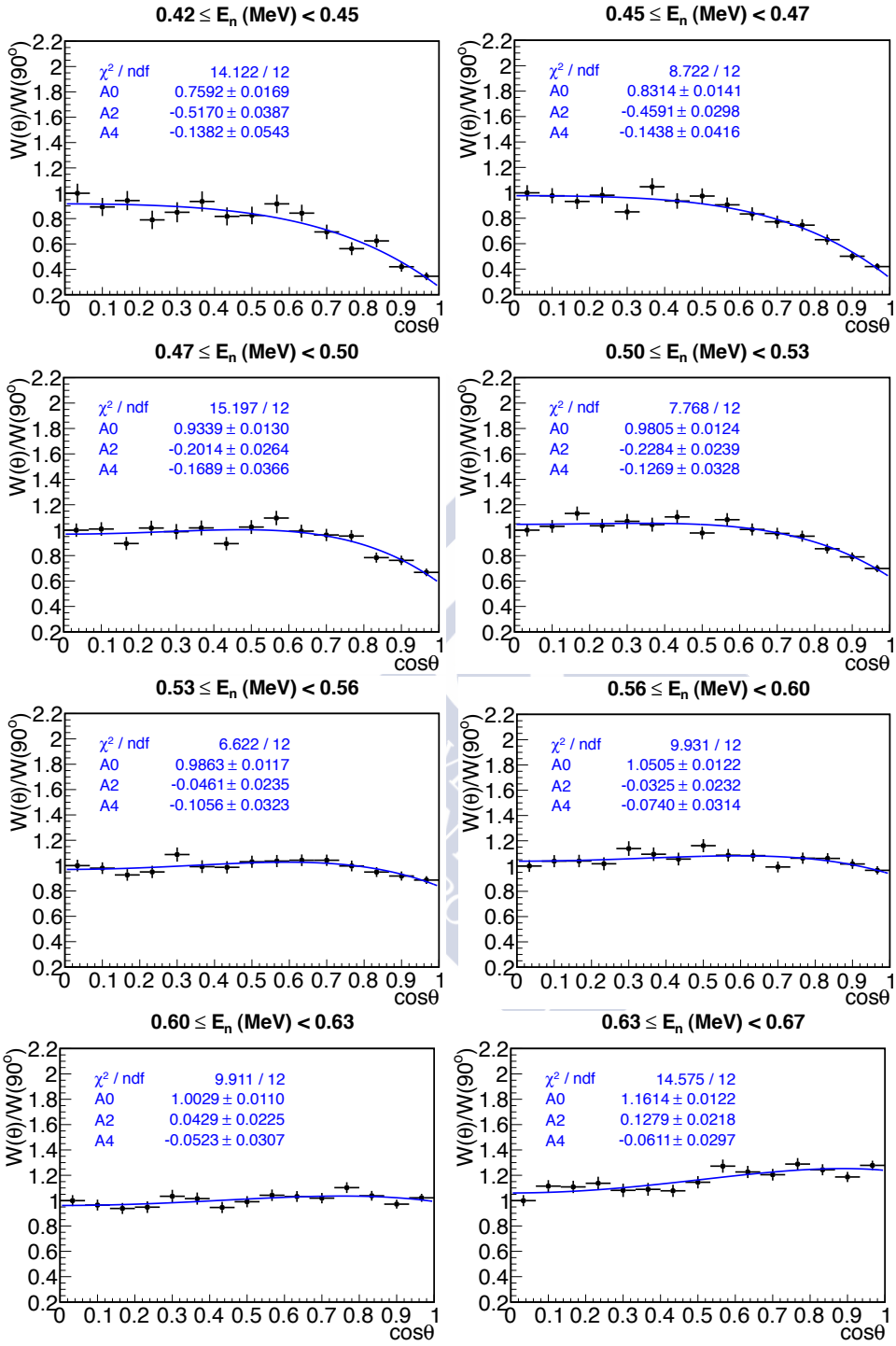
0.42 ≤ E_n (MeV) < 0.45
χ² / ndf 14.122 / 12
A0 0.7592 ± 0.0169
A2 -0.5170 ± 0.0387
A4 -0.1382 ± 0.0543
0.45 ≤ E_n (MeV) < 0.47
χ² / ndf 8.722 / 12
A0 0.8314 ± 0.0141
A2 -0.4591 ± 0.0298
A4 -0.1438 ± 0.0416
0.47 ≤ E_n (MeV) < 0.50
χ² / ndf 15.197 / 12
A0 0.9339 ± 0.0130
A2 -0.2014 ± 0.0264
A4 -0.1689 ± 0.0366
0.50 ≤ E_n (MeV) < 0.53
χ² / ndf 7.768 / 12
A0 0.9805 ± 0.0124
A2 -0.2284 ± 0.0239
A4 -0.1269 ± 0.0328
0.53 ≤ E_n (MeV) < 0.56
χ² / ndf 6.622 / 12
A0 0.9863 ± 0.0117
A2 -0.0461 ± 0.0235
A4 -0.1056 ± 0.0323
0.56 ≤ E_n (MeV) < 0.60
χ² / ndf 9.931 / 12
A0 1.0505 ± 0.0122
A2 -0.0325 ± 0.0232
A4 -0.0740 ± 0.0314
0.60 ≤ E_n (MeV) < 0.63
χ² / ndf 9.911 / 12
A0 1.0029 ± 0.0110
A2 0.0429 ± 0.0225
A4 -0.0523 ± 0.0307
0.63 ≤ E_n (MeV) < 0.67
χ² / ndf 14.575 / 12
A0 1.1614 ± 0.0122
A2 0.1279 ± 0.0218
A4 -0.0611 ± 0.0297
W(θ)/W(90°)
cosθ

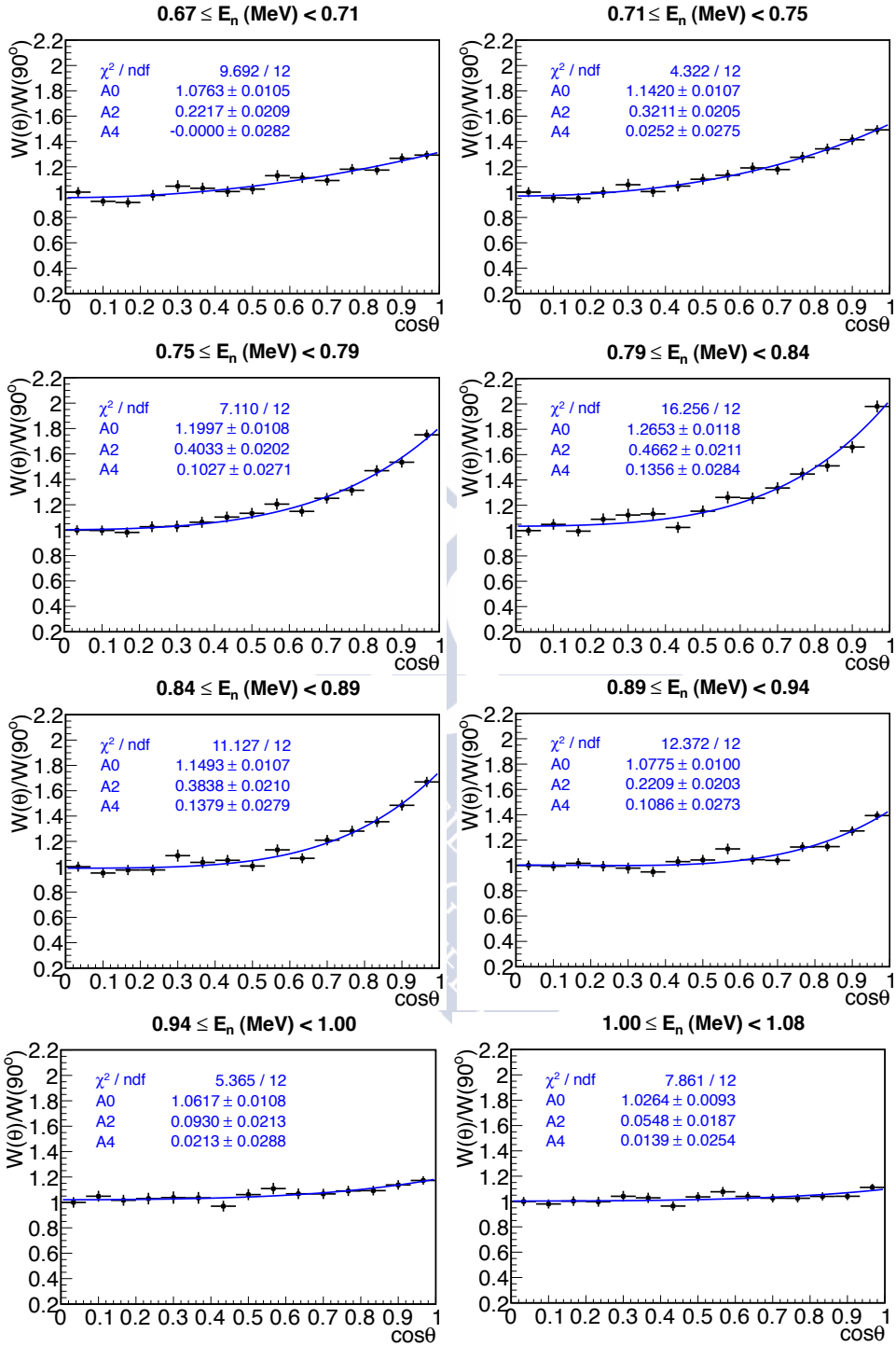
0.67 ≤ E_n (MeV) < 0.71
χ² / ndf 9.692 / 12
A0 1.0763 ± 0.0105
A2 0.2217 ± 0.0209
A4 -0.0000 ± 0.0282
0.71 ≤ E_n (MeV) < 0.75
χ² / ndf 4.322 / 12
A0 1.1420 ± 0.0107
A2 0.3211 ± 0.0205
A4 0.0252 ± 0.0275
0.75 ≤ E_n (MeV) < 0.79
χ² / ndf 7.110 / 12
A0 1.1997 ± 0.0108
A2 0.4033 ± 0.0202
A4 0.1027 ± 0.0271
0.79 ≤ E_n (MeV) < 0.84
χ² / ndf 16.256 / 12
A0 1.2653 ± 0.0118
A2 0.4662 ± 0.0211
A4 0.1356 ± 0.0284
0.84 ≤ E_n (MeV) < 0.89
χ² / ndf 11.127 / 12
A0 1.1493 ± 0.0107
A2 0.3838 ± 0.0210
A4 0.1379 ± 0.0279
0.89 ≤ E_n (MeV) < 0.94
χ² / ndf 12.372 / 12
A0 1.0775 ± 0.0100
A2 0.2209 ± 0.0203
A4 0.1086 ± 0.0273
0.94 ≤ E_n (MeV) < 1.00
χ² / ndf 5.365 / 12
A0 1.0617 ± 0.0108
A2 0.0930 ± 0.0213
A4 0.0213 ± 0.0288
1.00 ≤ E_n (MeV) < 1.08
χ² / ndf 7.861 / 12
A0 1.0264 ± 0.0093
A2 0.0548 ± 0.0187
A4 0.0139 ± 0.0254
W(θ)/W(90°)
cosθ

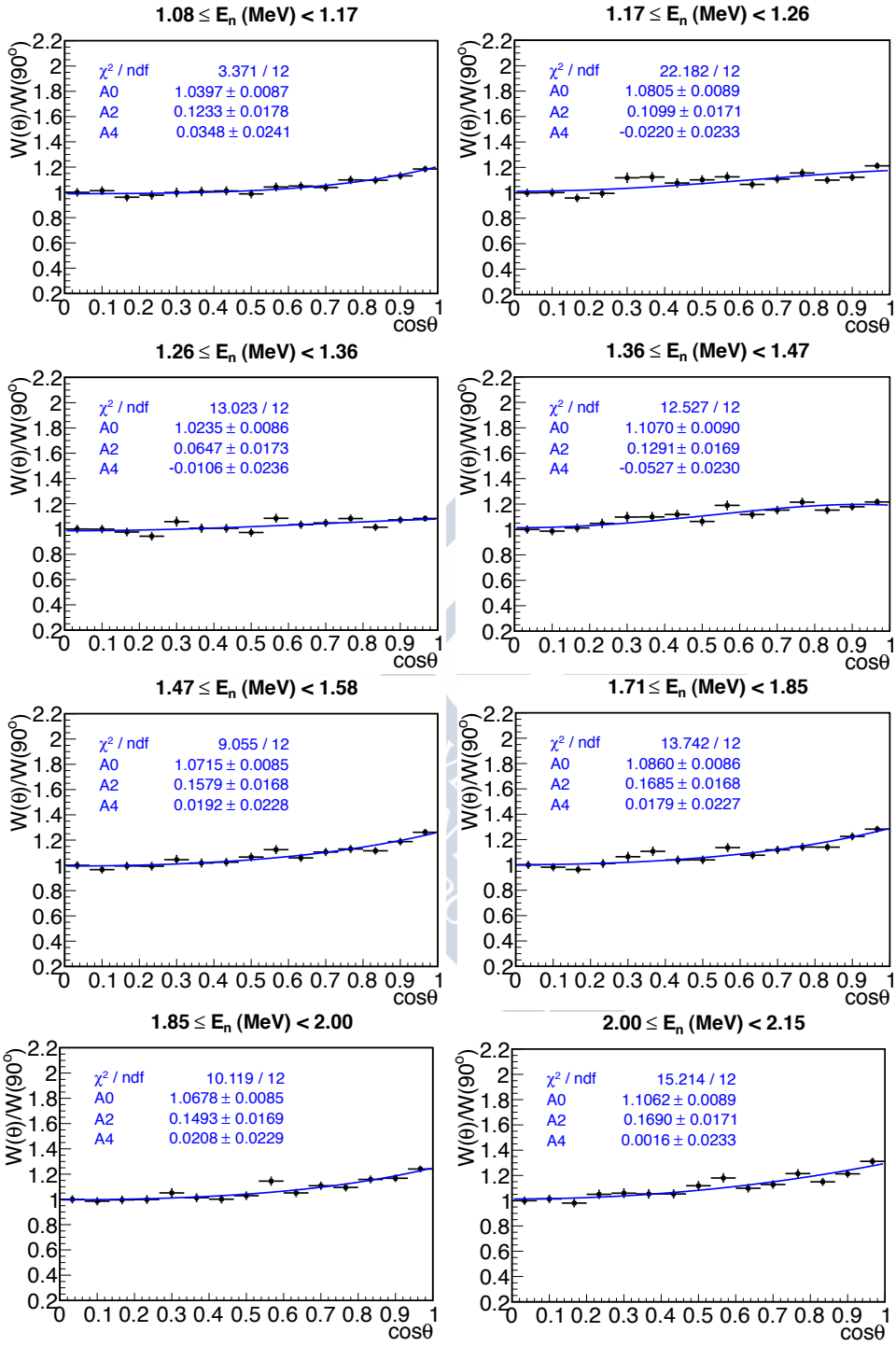
1.08 ≤ E_n (MeV) < 1.17
χ² / ndf 3.371 / 12
A0 1.0397 ± 0.0087
A2 0.1233 ± 0.0178
A4 0.0348 ± 0.0241
1.17 ≤ E_n (MeV) < 1.26
χ² / ndf 22.182 / 12
A0 1.0805 ± 0.0089
A2 0.1099 ± 0.0171
A4 -0.0220 ± 0.0233
1.26 ≤ E_n (MeV) < 1.36
χ² / ndf 13.023 / 12
A0 1.0235 ± 0.0086
A2 0.0647 ± 0.0173
A4 -0.0106 ± 0.0236
1.36 ≤ E_n (MeV) < 1.47
χ² / ndf 12.527 / 12
A0 1.1070 ± 0.0090
A2 0.1291 ± 0.0169
A4 -0.0527 ± 0.0230
1.47 ≤ E_n (MeV) < 1.58
χ² / ndf 9.055 / 12
A0 1.0715 ± 0.0085
A2 0.1579 ± 0.0168
A4 0.0192 ± 0.0228
1.71 ≤ E_n (MeV) < 1.85
χ² / ndf 13.742 / 12
A0 1.0860 ± 0.0086
A2 0.1685 ± 0.0168
A4 0.0179 ± 0.0227
1.85 ≤ E_n (MeV) < 2.00
χ² / ndf 10.119 / 12
A0 1.0678 ± 0.0085
A2 0.1493 ± 0.0169
A4 0.0208 ± 0.0229
2.00 ≤ E_n (MeV) < 2.15
χ² / ndf 15.214 / 12
A0 1.1062 ± 0.0089
A2 0.1690 ± 0.0171
A4 0.0016 ± 0.0233
W(θ)/W(90°)
cosθ

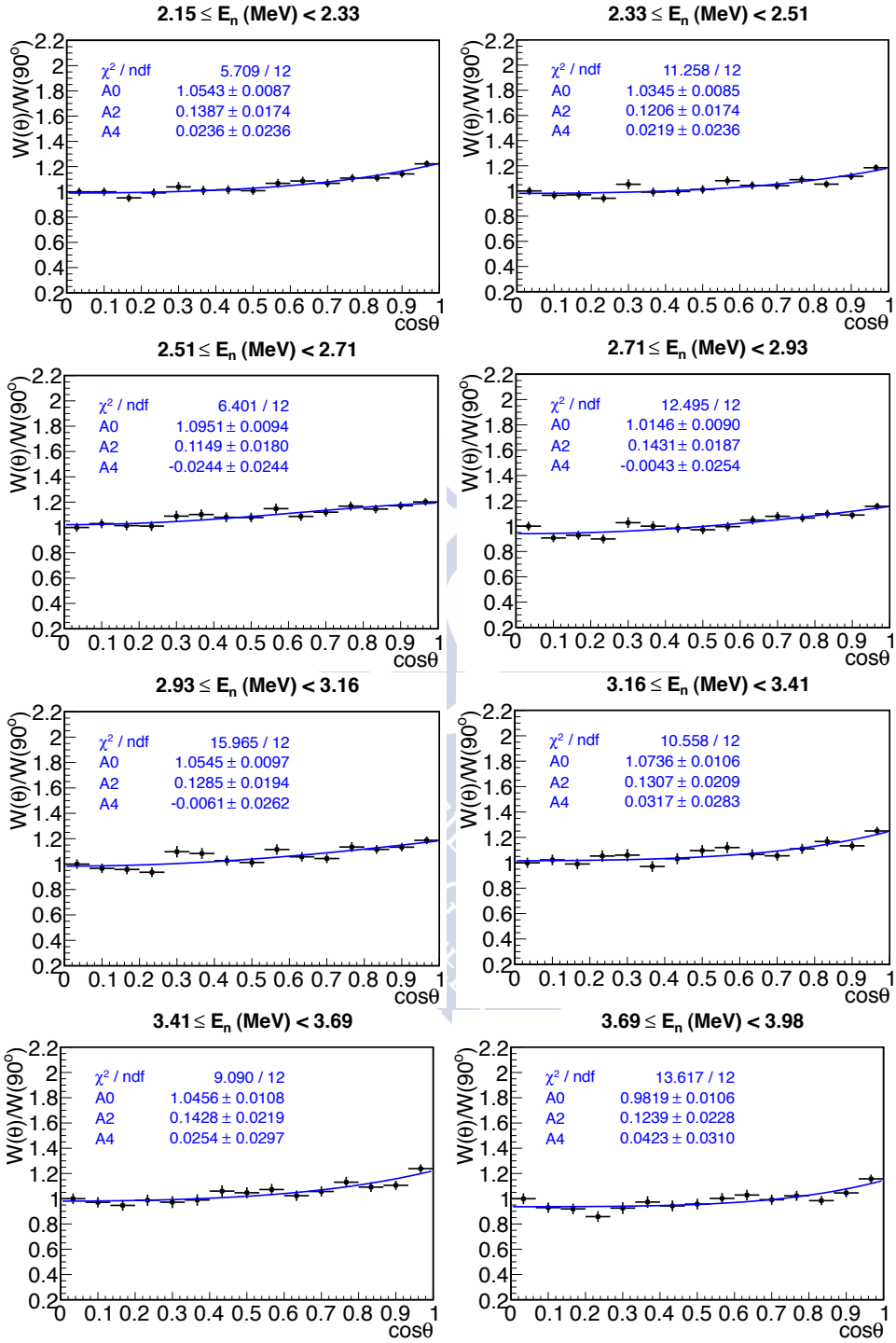
2.15 ≤ E_n (MeV) < 2.33
χ² / ndf 5.709 / 12
A0 1.0543 ± 0.0087
A2 0.1387 ± 0.0174
A4 0.0236 ± 0.0236
2.33 ≤ E_n (MeV) < 2.51
χ² / ndf 11.258 / 12
A0 1.0345 ± 0.0085
A2 0.1206 ± 0.0174
A4 0.0219 ± 0.0236
2.51 ≤ E_n (MeV) < 2.71
χ² / ndf 6.401 / 12
A0 1.0951 ± 0.0094
A2 0.1149 ± 0.0180
A4 -0.0244 ± 0.0244
2.71 ≤ E_n (MeV) < 2.93
χ² / ndf 12.495 / 12
A0 1.0146 ± 0.0090
A2 0.1431 ± 0.0187
A4 -0.0043 ± 0.0254
2.93 ≤ E_n (MeV) < 3.16
χ² / ndf 15.965 / 12
A0 1.0545 ± 0.0097
A2 0.1285 ± 0.0194
A4 -0.0061 ± 0.0262
3.16 ≤ E_n (MeV) < 3.41
χ² / ndf 10.558 / 12
A0 1.0736 ± 0.0106
A2 0.1307 ± 0.0209
A4 0.0317 ± 0.0283
3.41 ≤ E_n (MeV) < 3.69
χ² / ndf 9.090 / 12
A0 1.0456 ± 0.0108
A2 0.1428 ± 0.0219
A4 0.0254 ± 0.0297
3.69 ≤ E_n (MeV) < 3.98
χ² / ndf 13.617 / 12
A0 0.9819 ± 0.0106
A2 0.1239 ± 0.0228
A4 0.0423 ± 0.0310
W(θ)/W(90°)
cosθ

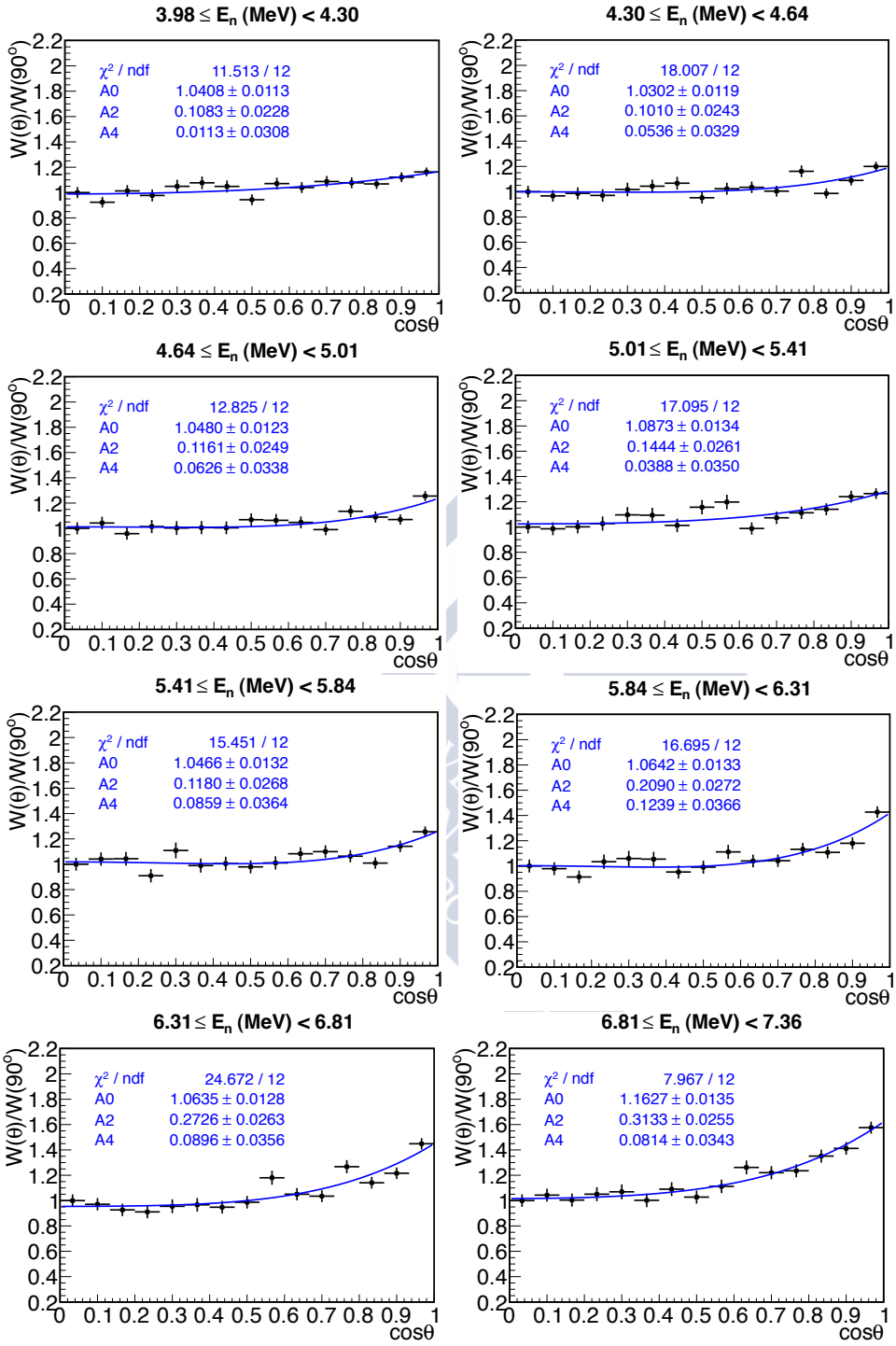
3.98 ≤ E_n (MeV) < 4.30
χ² / ndf 11.513 / 12
A0 1.0408 ± 0.0113
A2 0.1083 ± 0.0228
A4 0.0113 ± 0.0308
4.30 ≤ E_n (MeV) < 4.64
χ² / ndf 18.007 / 12
A0 1.0302 ± 0.0119
A2 0.1010 ± 0.0243
A4 0.0536 ± 0.0329
4.64 ≤ E_n (MeV) < 5.01
χ² / ndf 12.825 / 12
A0 1.0480 ± 0.0123
A2 0.1161 ± 0.0249
A4 0.0626 ± 0.0338
5.01 ≤ E_n (MeV) < 5.41
χ² / ndf 17.095 / 12
A0 1.0873 ± 0.0134
A2 0.1444 ± 0.0261
A4 0.0388 ± 0.0350
5.41 ≤ E_n (MeV) < 5.84
χ² / ndf 15.451 / 12
A0 1.0466 ± 0.0132
A2 0.1180 ± 0.0268
A4 0.0859 ± 0.0364
5.84 ≤ E_n (MeV) < 6.31
χ² / ndf 16.695 / 12
A0 1.0642 ± 0.0133
A2 0.2090 ± 0.0272
A4 0.1239 ± 0.0366
6.31 ≤ E_n (MeV) < 6.81
χ² / ndf 24.672 / 12
A0 1.0635 ± 0.0128
A2 0.2726 ± 0.0263
A4 0.0896 ± 0.0356
6.81 ≤ E_n (MeV) < 7.36
χ² / ndf 7.967 / 12
A0 1.1627 ± 0.0135
A2 0.3133 ± 0.0255
A4 0.0814 ± 0.0343
W(θ)/W(90°)
cosθ

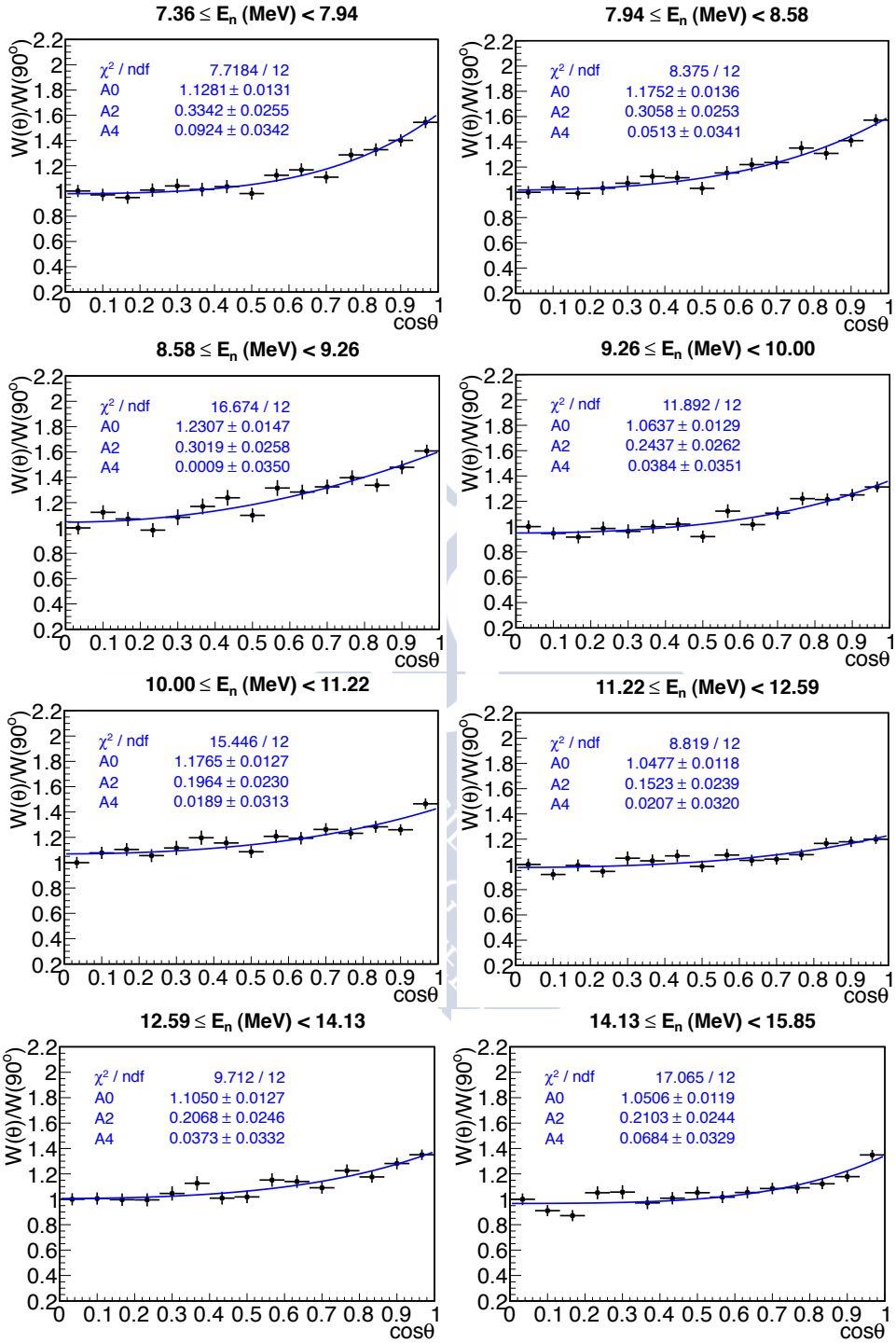
7.36 ≤ E_n (MeV) < 7.94
χ² / ndf 7.7184 / 12
A0 1.1281 ± 0.0131
A2 0.3342 ± 0.0255
A4 0.0924 ± 0.0342
7.94 ≤ E_n (MeV) < 8.58
χ² / ndf 8.375 / 12
A0 1.1752 ± 0.0136
A2 0.3058 ± 0.0253
A4 0.0513 ± 0.0341
8.58 ≤ E_n (MeV) < 9.26
χ² / ndf 16.674 / 12
A0 1.2307 ± 0.0147
A2 0.3019 ± 0.0258
A4 0.0009 ± 0.0350
9.26 ≤ E_n (MeV) < 10.00
χ² / ndf 11.892 / 12
A0 1.0637 ± 0.0129
A2 0.2437 ± 0.0262
A4 0.0384 ± 0.0351
10.00 ≤ E_n (MeV) < 11.22
χ² / ndf 15.446 / 12
A0 1.1765 ± 0.0127
A2 0.1964 ± 0.0230
A4 0.0189 ± 0.0313
11.22 ≤ E_n (MeV) < 12.59
χ² / ndf 8.819 / 12
A0 1.0477 ± 0.0118
A2 0.1523 ± 0.0239
A4 0.0207 ± 0.0320
12.59 ≤ E_n (MeV) < 14.13
χ² / ndf 9.712 / 12
A0 1.1050 ± 0.0127
A2 0.2068 ± 0.0246
A4 0.0373 ± 0.0332
14.13 ≤ E_n (MeV) < 15.85
χ² / ndf 17.065 / 12
A0 1.0506 ± 0.0119
A2 0.2103 ± 0.0244
A4 0.0684 ± 0.0329
W(θ)/W(90°)
cosθ

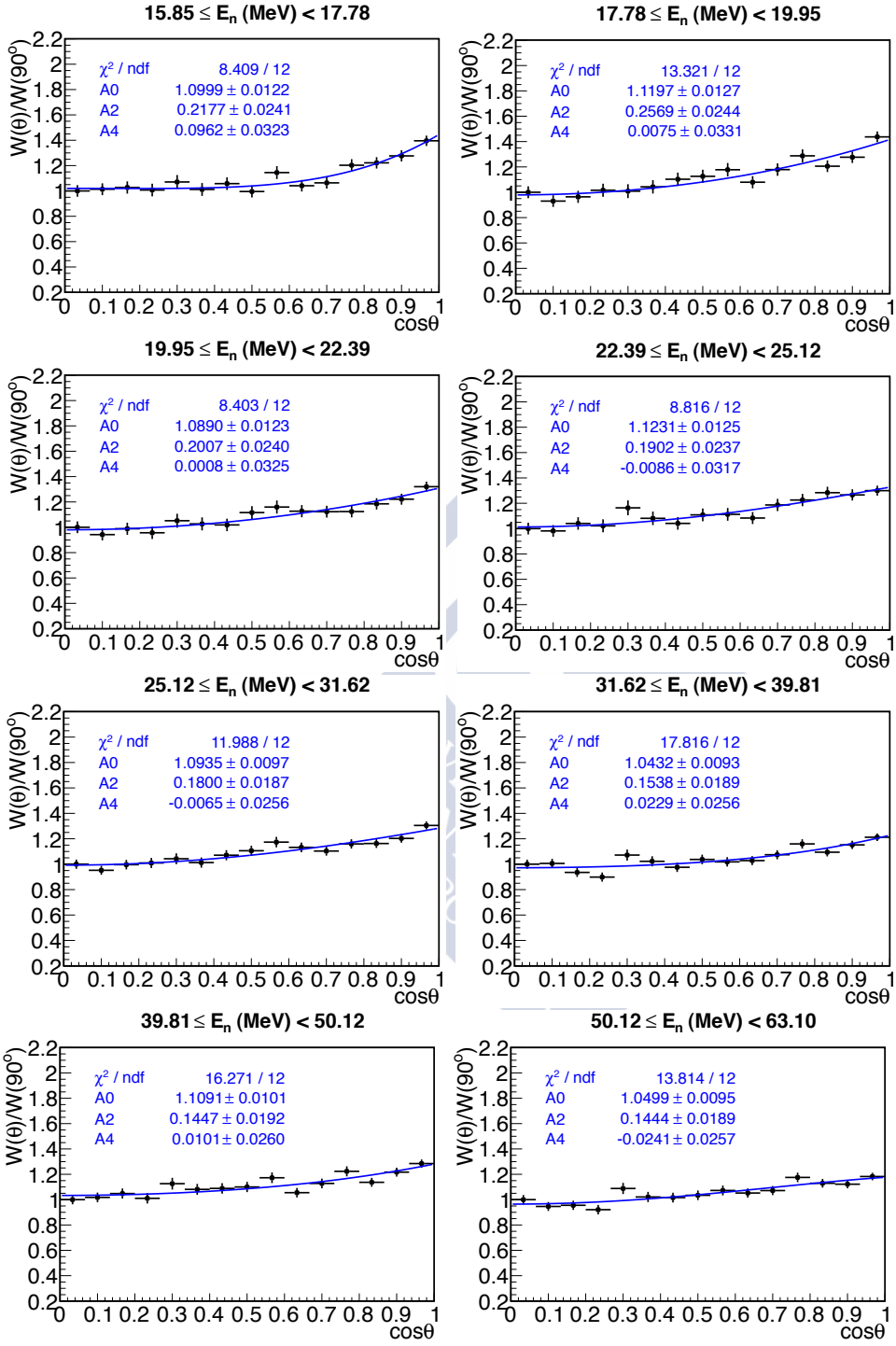
15.85 ≤ E_n (MeV) < 17.78
χ² / ndf 8.409 / 12
A0 1.0999 ± 0.0122
A2 0.2177 ± 0.0241
A4 0.0962 ± 0.0323
17.78 ≤ E_n (MeV) < 19.95
χ² / ndf 13.321 / 12
A0 1.1197 ± 0.0127
A2 0.2569 ± 0.0244
A4 0.0075 ± 0.0331
19.95 ≤ E_n (MeV) < 22.39
χ² / ndf 8.403 / 12
A0 1.0890 ± 0.0123
A2 0.2007 ± 0.0240
A4 0.0008 ± 0.0325
22.39 ≤ E_n (MeV) < 25.12
χ² / ndf 8.816 / 12
A0 1.1231 ± 0.0125
A2 0.1902 ± 0.0237
A4 -0.0086 ± 0.0317
25.12 ≤ E_n (MeV) < 31.62
χ² / ndf 11.988 / 12
A0 1.0935 ± 0.0097
A2 0.1800 ± 0.0187
A4 -0.0065 ± 0.0256
31.62 ≤ E_n (MeV) < 39.81
χ² / ndf 17.816 / 12
A0 1.0432 ± 0.0093
A2 0.1538 ± 0.0189
A4 0.0229 ± 0.0256
39.81 ≤ E_n (MeV) < 50.12
χ² / ndf 16.271 / 12
A0 1.1091 ± 0.0101
A2 0.1447 ± 0.0192
A4 0.0101 ± 0.0260
50.12 ≤ E_n (MeV) < 63.10
χ² / ndf 13.814 / 12
A0 1.0499 ± 0.0095
A2 0.1444 ± 0.0189
A4 -0.0241 ± 0.0257
W(θ)/W(90°)
cosθ

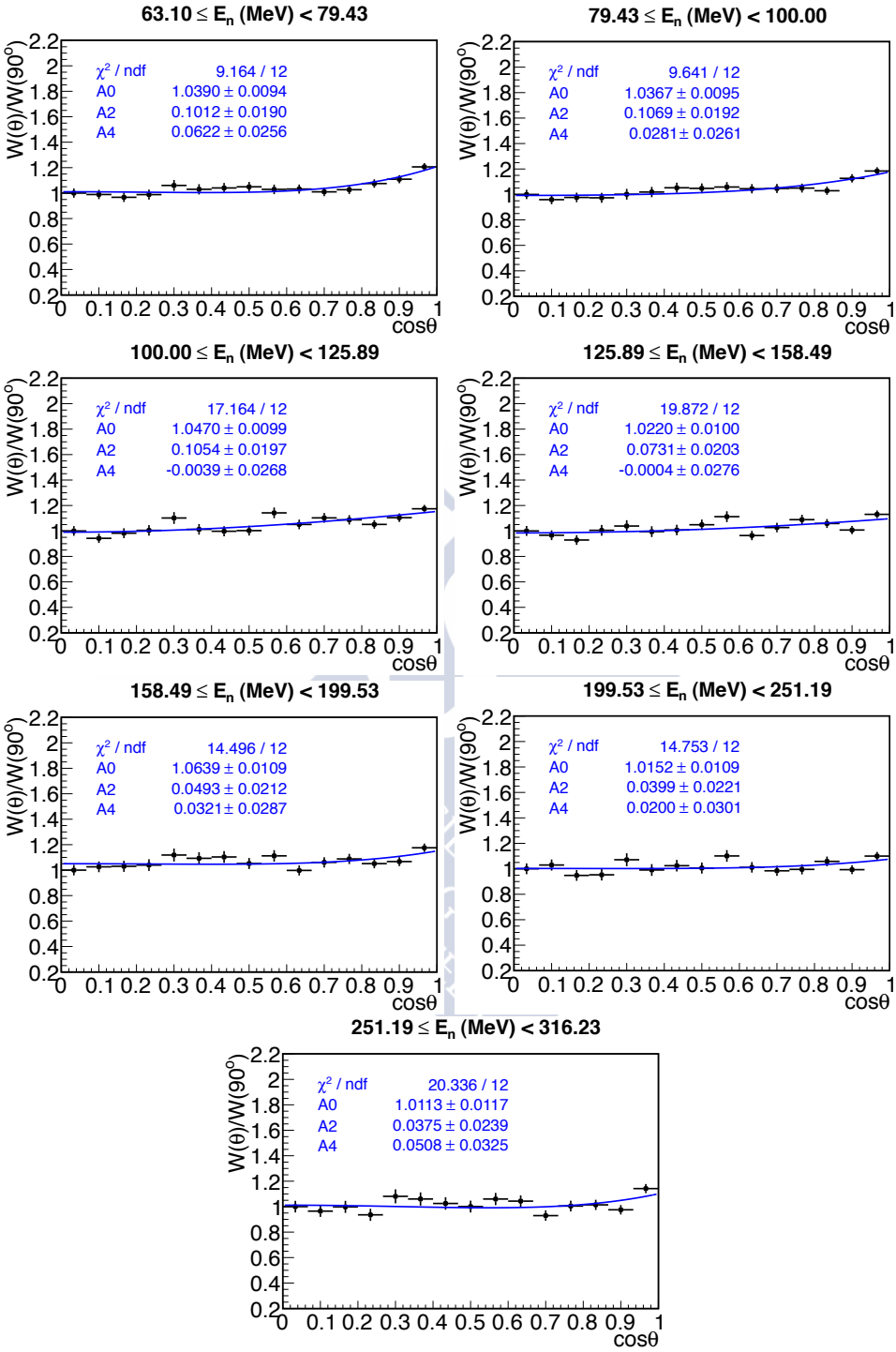
63.10 ≤ E_n (MeV) < 79.43
χ² / ndf 9.164 / 12
A0 1.0390 ± 0.0094
A2 0.1012 ± 0.0190
A4 0.0622 ± 0.0256
79.43 ≤ E_n (MeV) < 100.00
χ² / ndf 9.641 / 12
A0 1.0367 ± 0.0095
A2 0.1069 ± 0.0192
A4 0.0281 ± 0.0261
100.00 ≤ E_n (MeV) < 125.89
χ² / ndf 17.164 / 12
A0 1.0470 ± 0.0099
A2 0.1054 ± 0.0197
A4 -0.0039 ± 0.0268
125.89 ≤ E_n (MeV) < 158.49
χ² / ndf 19.872 / 12
A0 1.0220 ± 0.0100
A2 0.0731 ± 0.0203
A4 -0.0004 ± 0.0276
158.49 ≤ E_n (MeV) < 199.53
χ² / ndf 14.496 / 12
A0 1.0639 ± 0.0109
A2 0.0493 ± 0.0212
A4 0.0321 ± 0.0287
199.53 ≤ E_n (MeV) < 251.19
χ² / ndf 14.753 / 12
A0 1.0152 ± 0.0109
A2 0.0399 ± 0.0221
A4 0.0200 ± 0.0301
251.19 ≤ E_n (MeV) < 316.23
χ² / ndf 20.336 / 12
A0 1.0113 ± 0.0117
A2 0.0375 ± 0.0239
A4 0.0508 ± 0.0325
W(θ)/W(90°)
cosθ

Table B.1: Coefficients of the Legendre polynomials fits to the ^{234}U(n,f) angular distributions.

E_n (MeV)	A_0	A_2	A_4	A=W(0°)/W(90°)
0.10 - 0.16	0.98 ± 0.03	0.20 ± 0.06	-0.06 ± 0.07	1.31 ± 0.11
0.16 - 0.25	0.88 ± 0.02	-0.01 ± 0.05	0.10 ± 0.06	1.05 ± 0.08
0.25 - 0.32	1.01 ± 0.02	0.10 ± 0.04	0.02 ± 0.05	1.17 ± 0.07
0.32 - 0.33	1.20 ± 0.03	0.04 ± 0.05	0.03 ± 0.07	1.09 ± 0.10
0.33 - 0.35	0.94 ± 0.03	-0.09 ± 0.06	-0.10 ± 0.08	0.80 ± 0.10
0.35 - 0.38	0.99 ± 0.03	-0.25 ± 0.05	-0.07 ± 0.07	0.62 ± 0.08
0.38 - 0.40	0.92 ± 0.02	-0.36 ± 0.04	-0.10 ± 0.06	0.47 ± 0.06
0.40 - 0.42	0.75 ± 0.02	-0.34 ± 0.04	-0.17 ± 0.06	0.44 ± 0.06
0.42 - 0.45	0.76 ± 0.02	-0.52 ± 0.04	-0.14 ± 0.05	0.29 ± 0.05
0.45 - 0.47	0.83 ± 0.01	-0.46 ± 0.03	-0.14 ± 0.04	0.34 ± 0.04
0.47 - 0.50	0.93 ± 0.01	-0.20 ± 0.03	-0.17 ± 0.04	0.61 ± 0.04
0.50 - 0.53	0.98 ± 0.01	-0.23 ± 0.02	-0.13 ± 0.03	0.60 ± 0.04
0.53 - 0.56	0.99 ± 0.01	-0.05 ± 0.02	-0.11 ± 0.03	0.86 ± 0.04
0.56 - 0.60	1.05 ± 0.01	-0.03 ± 0.02	-0.07 ± 0.03	0.90 ± 0.04
0.60 - 0.63	1.00 ± 0.01	0.04 ± 0.02	-0.05 ± 0.03	1.03 ± 0.04
0.63 - 0.67	1.16 ± 0.01	0.13 ± 0.02	-0.06 ± 0.03	1.17 ± 0.04
0.67 - 0.71	1.08 ± 0.01	0.22 ± 0.02	-0.00 ± 0.03	1.37 ± 0.04
0.71 - 0.75	1.14 ± 0.01	0.32 ± 0.02	0.03 ± 0.03	1.59 ± 0.05
0.75 - 0.79	1.20 ± 0.01	0.40 ± 0.02	0.10 ± 0.03	1.80 ± 0.05
0.79 - 0.84	1.27 ± 0.01	0.47 ± 0.02	0.14 ± 0.03	1.96 ± 0.05
0.84 - 0.89	1.15 ± 0.01	0.38 ± 0.02	0.14 ± 0.03	1.77 ± 0.05
0.89 - 0.94	1.08 ± 0.01	0.22 ± 0.02	0.11 ± 0.03	1.43 ± 0.04
0.94 - 1.00	1.06 ± 0.01	0.09 ± 0.02	0.02 ± 0.03	1.16 ± 0.04
1.00 - 1.08	1.03 ± 0.01	0.05 ± 0.02	0.01 ± 0.03	1.09 ± 0.03

1.08 - 1.17	1.04 ± 0.01	0.12 ± 0.02	0.03 ± 0.02	1.22 ± 0.03
1.17 - 1.26	1.08 ± 0.01	0.11 ± 0.02	-0.02 ± 0.02	1.16 ± 0.03
1.26 - 1.36	1.02 ± 0.01	0.06 ± 0.02	-0.01 ± 0.02	1.09 ± 0.03
1.36 - 1.47	1.11 ± 0.01	0.13 ± 0.02	-0.05 ± 0.02	1.18 ± 0.03
1.47 - 1.58	1.07 ± 0.01	0.16 ± 0.02	0.02 ± 0.02	1.27 ± 0.03
1.58 - 1.71	1.07 ± 0.01	0.15 ± 0.02	0.01 ± 0.02	1.24 ± 0.03
1.71 - 1.85	1.09 ± 0.01	0.17 ± 0.02	0.02 ± 0.02	1.29 ± 0.03
1.85 - 2.00	1.07 ± 0.01	0.15 ± 0.02	0.02 ± 0.02	1.25 ± 0.03
2.00 - 2.15	1.11 ± 0.01	0.17 ± 0.02	0.00 ± 0.02	1.28 ± 0.03
2.15 - 2.33	1.05 ± 0.01	0.14 ± 0.02	0.02 ± 0.02	1.24 ± 0.03
2.33 - 2.51	1.03 ± 0.01	0.12 ± 0.02	0.02 ± 0.02	1.21 ± 0.03
2.51 - 2.71	1.10 ± 0.01	0.11 ± 0.02	-0.02 ± 0.02	1.17 ± 0.03
2.71 - 2.93	1.01 ± 0.01	0.14 ± 0.02	-0.00 ± 0.03	1.23 ± 0.04
2.93 - 3.16	1.05 ± 0.01	0.13 ± 0.02	-0.01 ± 0.03	1.20 ± 0.04
3.16 - 3.41	1.07 ± 0.01	0.13 ± 0.02	0.03 ± 0.03	1.23 ± 0.04
3.41 - 3.69	1.05 ± 0.01	0.14 ± 0.02	0.03 ± 0.03	1.25 ± 0.04
3.69 - 3.98	0.98 ± 0.01	0.12 ± 0.02	0.04 ± 0.03	1.22 ± 0.04
3.98 - 4.30	1.04 ± 0.01	0.11 ± 0.02	0.01 ± 0.03	1.18 ± 0.04
4.30 - 4.64	1.03 ± 0.01	0.10 ± 0.02	0.05 ± 0.03	1.19 ± 0.04
4.64 - 5.01	1.05 ± 0.01	0.12 ± 0.02	0.06 ± 0.03	1.22 ± 0.05
5.01 - 5.41	1.09 ± 0.01	0.14 ± 0.03	0.04 ± 0.03	1.26 ± 0.05
5.41 - 5.84	1.05 ± 0.01	0.12 ± 0.03	0.09 ± 0.04	1.24 ± 0.05
5.84 - 6.31	1.06 ± 0.01	0.21 ± 0.03	0.12 ± 0.04	1.42 ± 0.05
6.31 - 6.81	1.06 ± 0.01	0.27 ± 0.03	0.09 ± 0.04	1.52 ± 0.05
6.81 - 7.36	1.16 ± 0.01	0.31 ± 0.03	0.08 ± 0.03	1.60 ± 0.05
7.36 - 7.94	1.13 ± 0.01	0.33 ± 0.03	0.09 ± 0.03	1.64 ± 0.06
7.94 - 8.58	1.18 ± 0.01	0.31 ± 0.03	0.05 ± 0.03	1.57 ± 0.05

8.58 - 9.26	1.23 ± 0.01	0.30 ± 0.03	0.00 ± 0.04	1.53 ± 0.06
9.26 - 10.00	1.06 ± 0.01	0.24 ± 0.03	0.04 ± 0.04	1.44 ± 0.05
10.00 - 11.22	1.18 ± 0.01	0.20 ± 0.02	0.02 ± 0.03	1.34 ± 0.05
11.22 - 12.59	1.05 ± 0.01	0.15 ± 0.02	0.02 ± 0.03	1.26 ± 0.05
12.59 - 14.13	1.10 ± 0.01	0.21 ± 0.02	0.04 ± 0.03	1.37 ± 0.05
14.13 - 15.85	1.05 ± 0.01	0.21 ± 0.02	0.07 ± 0.03	1.39 ± 0.05
15.85 - 17.78	1.10 ± 0.01	0.22 ± 0.02	0.10 ± 0.03	1.42 ± 0.05
17.78 - 19.95	1.12 ± 0.01	0.26 ± 0.02	0.01 ± 0.03	1.45 ± 0.05
19.95 - 22.39	1.09 ± 0.01	0.20 ± 0.02	0.00 ± 0.03	1.34 ± 0.05
22.39 - 25.12	1.12 ± 0.01	0.19 ± 0.02	-0.01 ± 0.03	1.31 ± 0.05
25.12 - 31.62	1.09 ± 0.01	0.18 ± 0.02	-0.01 ± 0.03	1.29 ± 0.04
31.62 - 39.81	1.04 ± 0.01	0.15 ± 0.02	0.02 ± 0.03	1.26 ± 0.04
39.81 - 50.12	1.11 ± 0.01	0.14 ± 0.02	0.01 ± 0.03	1.24 ± 0.04
50.12 - 63.10	1.05 ± 0.01	0.14 ± 0.02	-0.02 ± 0.03	1.22 ± 0.04
63.10 - 79.43	1.04 ± 0.01	0.10 ± 0.02	0.06 ± 0.03	1.20 ± 0.03
79.43 - 100.00	1.04 ± 0.01	0.11 ± 0.02	0.03 ± 0.03	1.19 ± 0.04
100.00 - 125.89	1.05 ± 0.01	0.11 ± 0.02	-0.00 ± 0.03	1.16 ± 0.04
125.89 - 158.49	1.02 ± 0.01	0.07 ± 0.02	-0.00 ± 0.03	1.11 ± 0.04
158.49 - 199.53	1.06 ± 0.01	0.05 ± 0.02	0.03 ± 0.03	1.10 ± 0.04
199.53 - 251.19	1.02 ± 0.01	0.04 ± 0.02	0.02 ± 0.03	1.07 ± 0.04
251.19 - 316.23	1.01 ± 0.01	0.04 ± 0.02	0.05 ± 0.03	1.09 ± 0.04

B.4 ^{235}U(n,f) angular distributions

Figure B.4: ^{235}U(n,f) angular distributions.

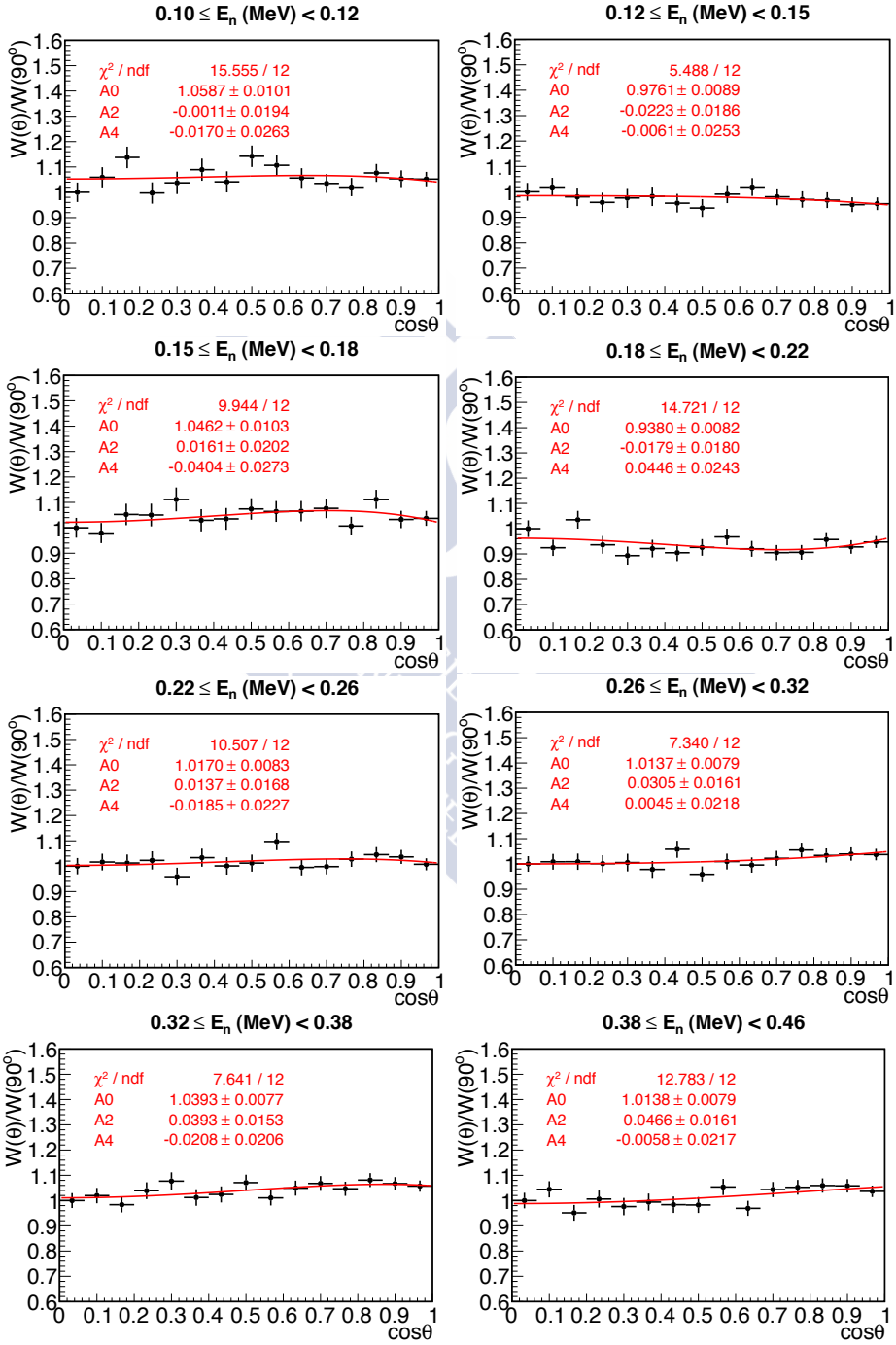

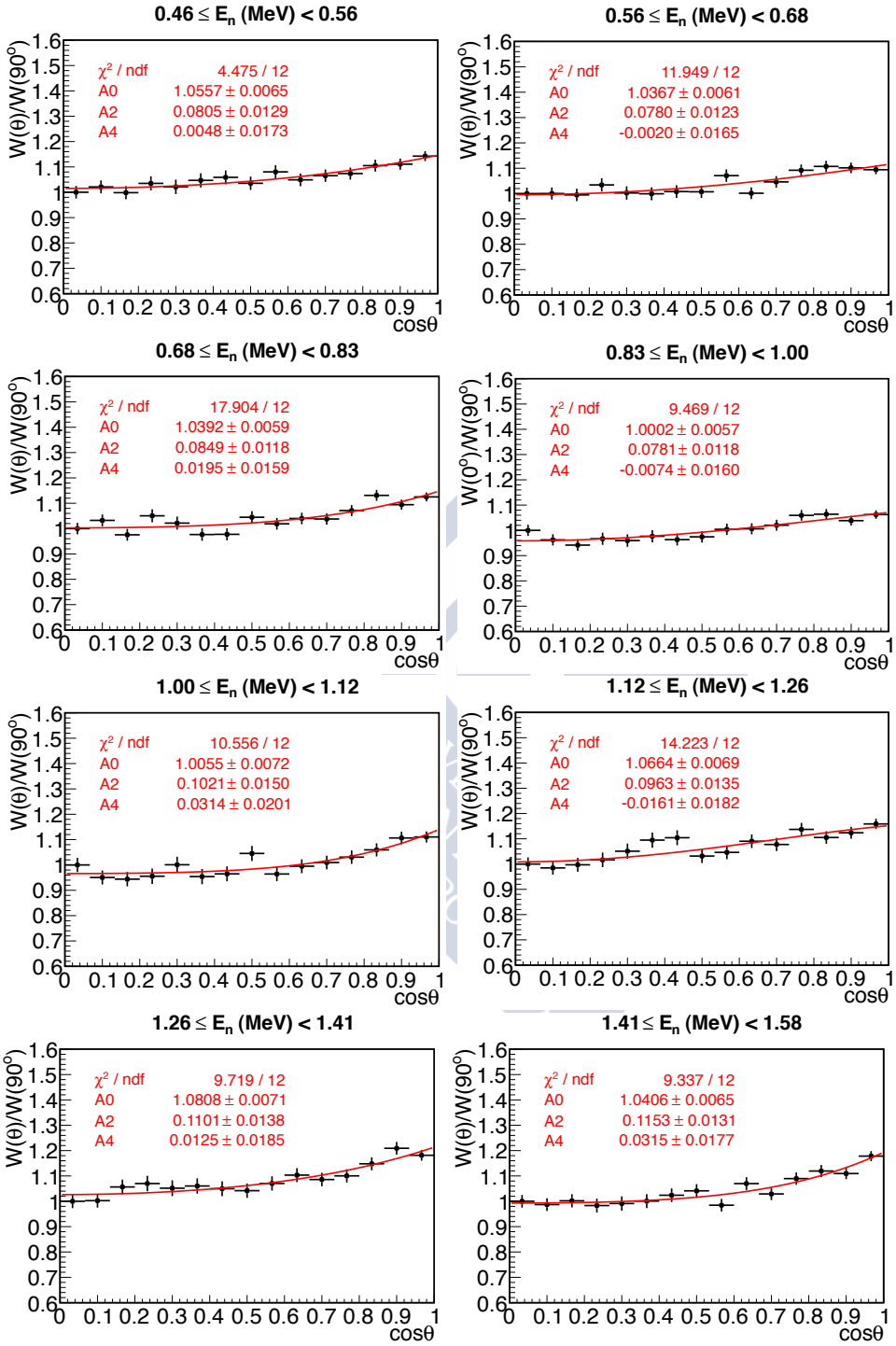
0.46 ≤ E_n (MeV) < 0.56
χ² / ndf 4.475 / 12
A0 1.0557 ± 0.0065
A2 0.0805 ± 0.0129
A4 0.0048 ± 0.0173
0.56 ≤ E_n (MeV) < 0.68
χ² / ndf 11.949 / 12
A0 1.0367 ± 0.0061
A2 0.0780 ± 0.0123
A4 -0.0020 ± 0.0165
0.68 ≤ E_n (MeV) < 0.83
χ² / ndf 17.904 / 12
A0 1.0392 ± 0.0059
A2 0.0849 ± 0.0118
A4 0.0195 ± 0.0159
0.83 ≤ E_n (MeV) < 1.00
χ² / ndf 9.469 / 12
A0 1.0002 ± 0.0057
A2 0.0781 ± 0.0118
A4 -0.0074 ± 0.0160
1.00 ≤ E_n (MeV) < 1.12
χ² / ndf 10.556 / 12
A0 1.0055 ± 0.0072
A2 0.1021 ± 0.0150
A4 0.0314 ± 0.0201
1.12 ≤ E_n (MeV) < 1.26
χ² / ndf 14.223 / 12
A0 1.0664 ± 0.0069
A2 0.0963 ± 0.0135
A4 -0.0161 ± 0.0182
1.26 ≤ E_n (MeV) < 1.41
χ² / ndf 9.719 / 12
A0 1.0808 ± 0.0071
A2 0.1101 ± 0.0138
A4 0.0125 ± 0.0185
1.41 ≤ E_n (MeV) < 1.58
χ² / ndf 9.337 / 12
A0 1.0406 ± 0.0065
A2 0.1153 ± 0.0131
A4 0.0315 ± 0.0177
W(θ)/W(90°)
cosθ

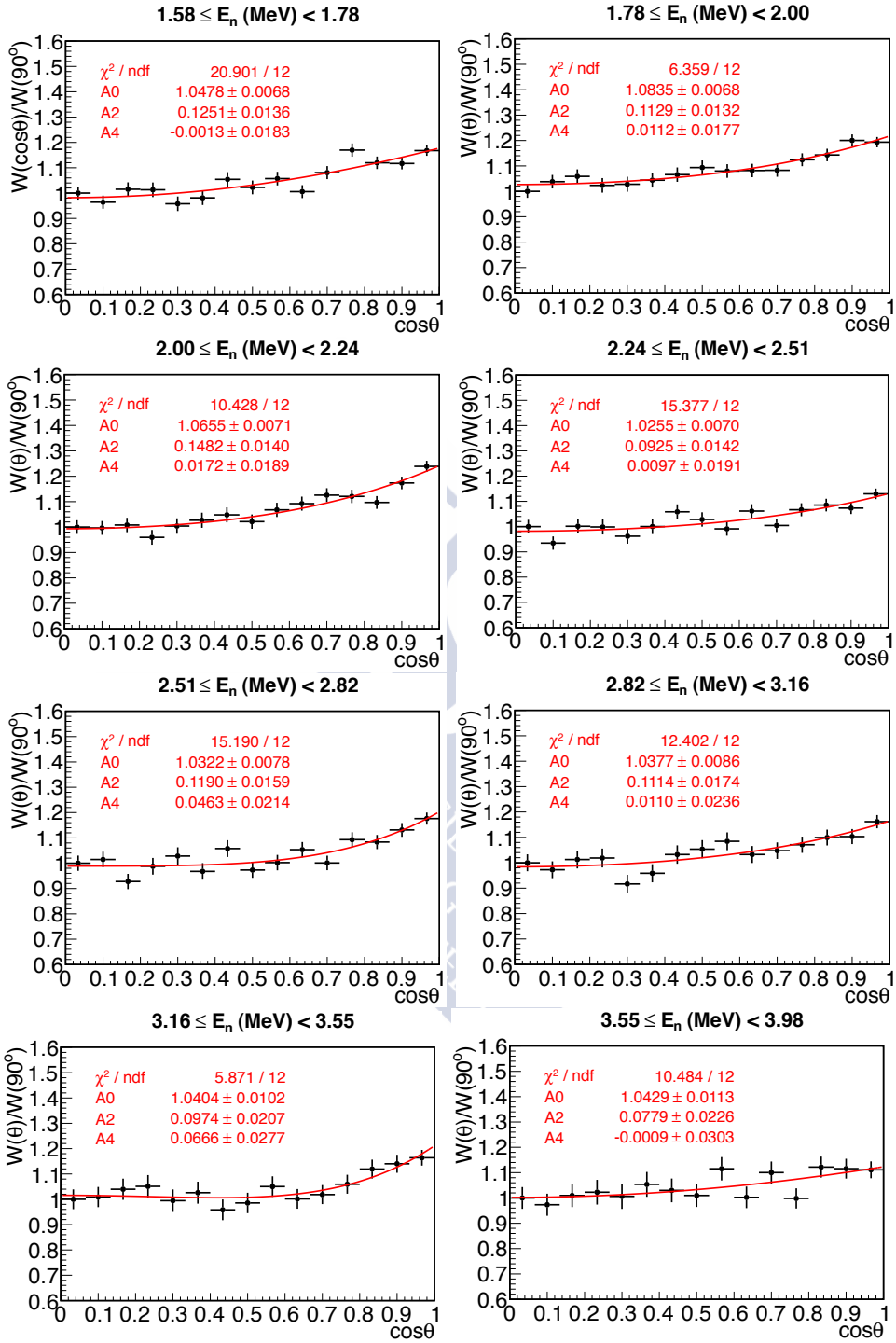
1.58 ≤ E_n (MeV) < 1.78
χ² / ndf 20.901 / 12
A0 1.0478 ± 0.0068
A2 0.1251 ± 0.0136
A4 -0.0013 ± 0.0183
W(cosθ)/W(90°)
cosθ
1.78 ≤ E_n (MeV) < 2.00
χ² / ndf 6.359 / 12
A0 1.0835 ± 0.0068
A2 0.1129 ± 0.0132
A4 0.0112 ± 0.0177
W(θ)/W(90°)
cosθ
2.00 ≤ E_n (MeV) < 2.24
χ² / ndf 10.428 / 12
A0 1.0655 ± 0.0071
A2 0.1482 ± 0.0140
A4 0.0172 ± 0.0189
W(θ)/W(90°)
cosθ
2.24 ≤ E_n (MeV) < 2.51
χ² / ndf 15.377 / 12
A0 1.0255 ± 0.0070
A2 0.0925 ± 0.0142
A4 0.0097 ± 0.0191
W(θ)/W(90°)
cosθ
2.51 ≤ E_n (MeV) < 2.82
χ² / ndf 15.190 / 12
A0 1.0322 ± 0.0078
A2 0.1190 ± 0.0159
A4 0.0463 ± 0.0214
W(θ)/W(90°)
cosθ
2.82 ≤ E_n (MeV) < 3.16
χ² / ndf 12.402 / 12
A0 1.0377 ± 0.0086
A2 0.1114 ± 0.0174
A4 0.0110 ± 0.0236
W(θ)/W(90°)
cosθ
3.16 ≤ E_n (MeV) < 3.55
χ² / ndf 5.871 / 12
A0 1.0404 ± 0.0102
A2 0.0974 ± 0.0207
A4 0.0666 ± 0.0277
W(θ)/W(90°)
cosθ
3.55 ≤ E_n (MeV) < 3.98
χ² / ndf 10.484 / 12
A0 1.0429 ± 0.0113
A2 0.0779 ± 0.0226
A4 -0.0009 ± 0.0303
W(θ)/W(90°)
cosθ

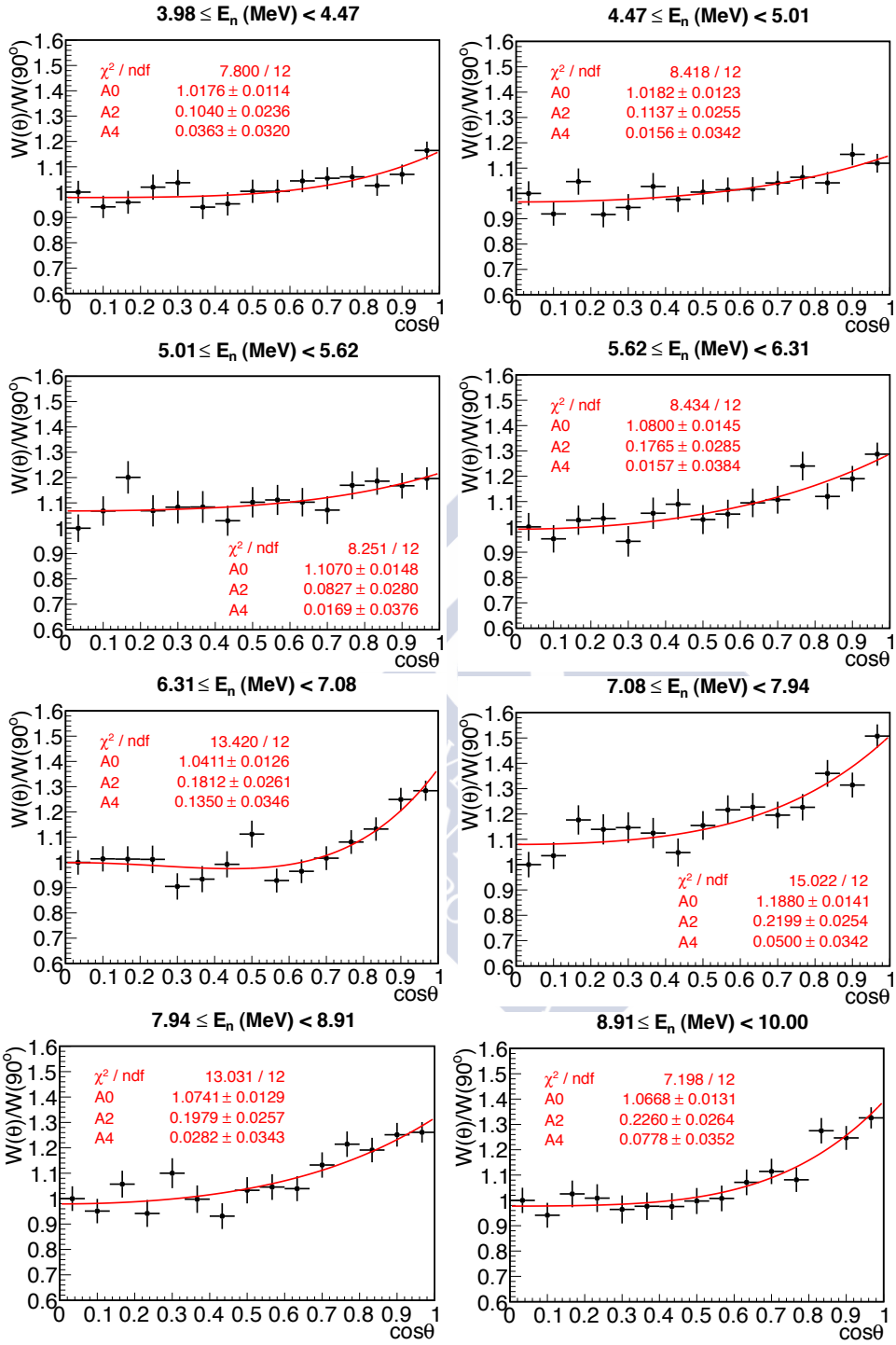
3.98 ≤ E_n (MeV) < 4.47
χ² / ndf 7.800 / 12
A0 1.0176 ± 0.0114
A2 0.1040 ± 0.0236
A4 0.0363 ± 0.0320
4.47 ≤ E_n (MeV) < 5.01
χ² / ndf 8.418 / 12
A0 1.0182 ± 0.0123
A2 0.1137 ± 0.0255
A4 0.0156 ± 0.0342
5.01 ≤ E_n (MeV) < 5.62
χ² / ndf 8.251 / 12
A0 1.1070 ± 0.0148
A2 0.0827 ± 0.0280
A4 0.0169 ± 0.0376
5.62 ≤ E_n (MeV) < 6.31
χ² / ndf 8.434 / 12
A0 1.0800 ± 0.0145
A2 0.1765 ± 0.0285
A4 0.0157 ± 0.0384
6.31 ≤ E_n (MeV) < 7.08
χ² / ndf 13.420 / 12
A0 1.0411 ± 0.0126
A2 0.1812 ± 0.0261
A4 0.1350 ± 0.0346
7.08 ≤ E_n (MeV) < 7.94
χ² / ndf 15.022 / 12
A0 1.1880 ± 0.0141
A2 0.2199 ± 0.0254
A4 0.0500 ± 0.0342
7.94 ≤ E_n (MeV) < 8.91
χ² / ndf 13.031 / 12
A0 1.0741 ± 0.0129
A2 0.1979 ± 0.0257
A4 0.0282 ± 0.0343
8.91 ≤ E_n (MeV) < 10.00
χ² / ndf 7.198 / 12
A0 1.0668 ± 0.0131
A2 0.2260 ± 0.0264
A4 0.0778 ± 0.0352
W(θ)/W(90°)
cosθ

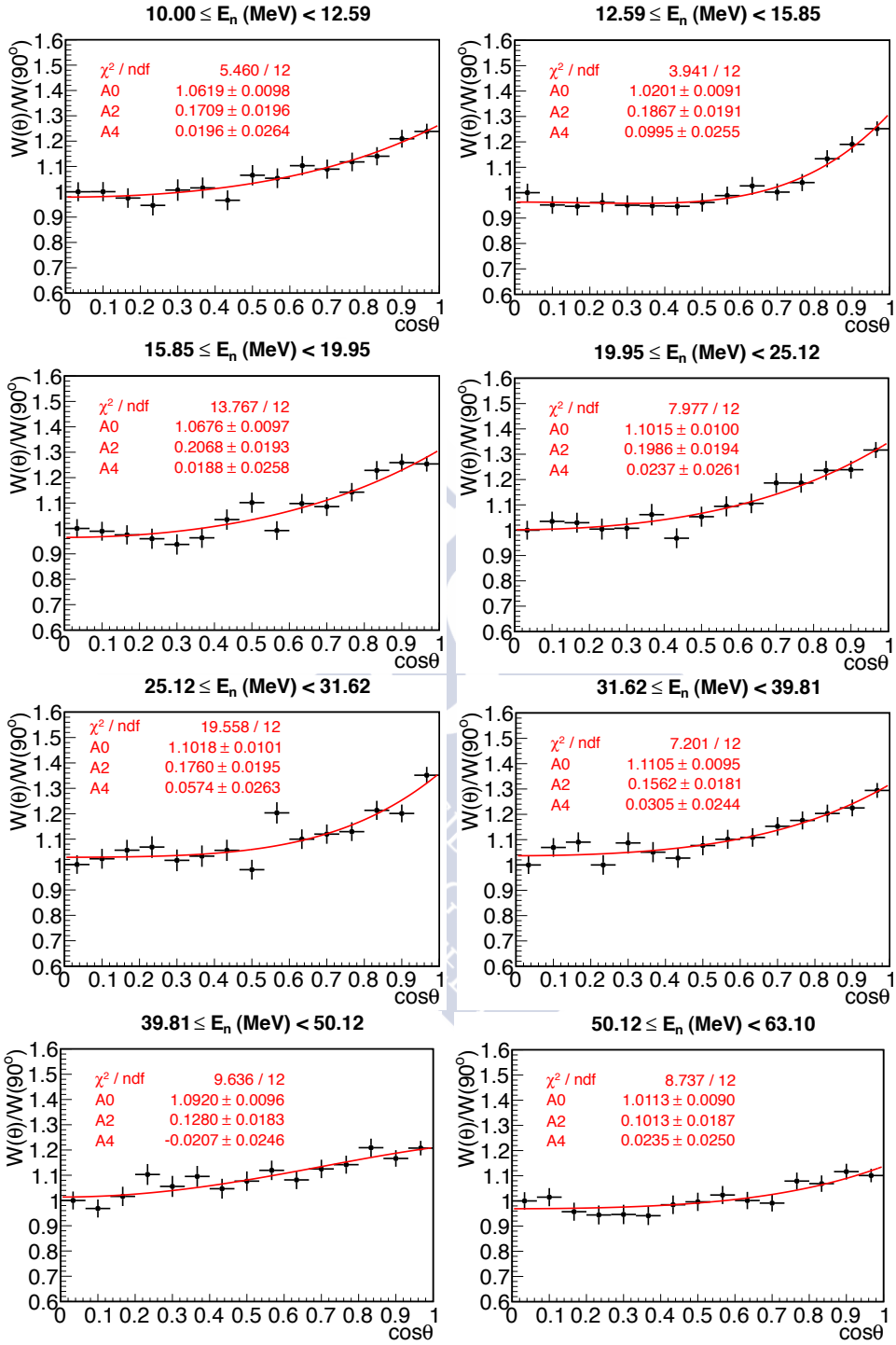
10.00 ≤ E_n (MeV) < 12.59
χ² / ndf 5.460 / 12
A0 1.0619 ± 0.0098
A2 0.1709 ± 0.0196
A4 0.0196 ± 0.0264
12.59 ≤ E_n (MeV) < 15.85
χ² / ndf 3.941 / 12
A0 1.0201 ± 0.0091
A2 0.1867 ± 0.0191
A4 0.0995 ± 0.0255
15.85 ≤ E_n (MeV) < 19.95
χ² / ndf 13.767 / 12
A0 1.0676 ± 0.0097
A2 0.2068 ± 0.0193
A4 0.0188 ± 0.0258
19.95 ≤ E_n (MeV) < 25.12
χ² / ndf 7.977 / 12
A0 1.1015 ± 0.0100
A2 0.1986 ± 0.0194
A4 0.0237 ± 0.0261
25.12 ≤ E_n (MeV) < 31.62
χ² / ndf 19.558 / 12
A0 1.1018 ± 0.0101
A2 0.1760 ± 0.0195
A4 0.0574 ± 0.0263
31.62 ≤ E_n (MeV) < 39.81
χ² / ndf 7.201 / 12
A0 1.1105 ± 0.0095
A2 0.1562 ± 0.0181
A4 0.0305 ± 0.0244
39.81 ≤ E_n (MeV) < 50.12
χ² / ndf 9.636 / 12
A0 1.0920 ± 0.0096
A2 0.1280 ± 0.0183
A4 -0.0207 ± 0.0246
50.12 ≤ E_n (MeV) < 63.10
χ² / ndf 8.737 / 12
A0 1.0113 ± 0.0090
A2 0.1013 ± 0.0187
A4 0.0235 ± 0.0250
W(θ)/W(90°)
cosθ

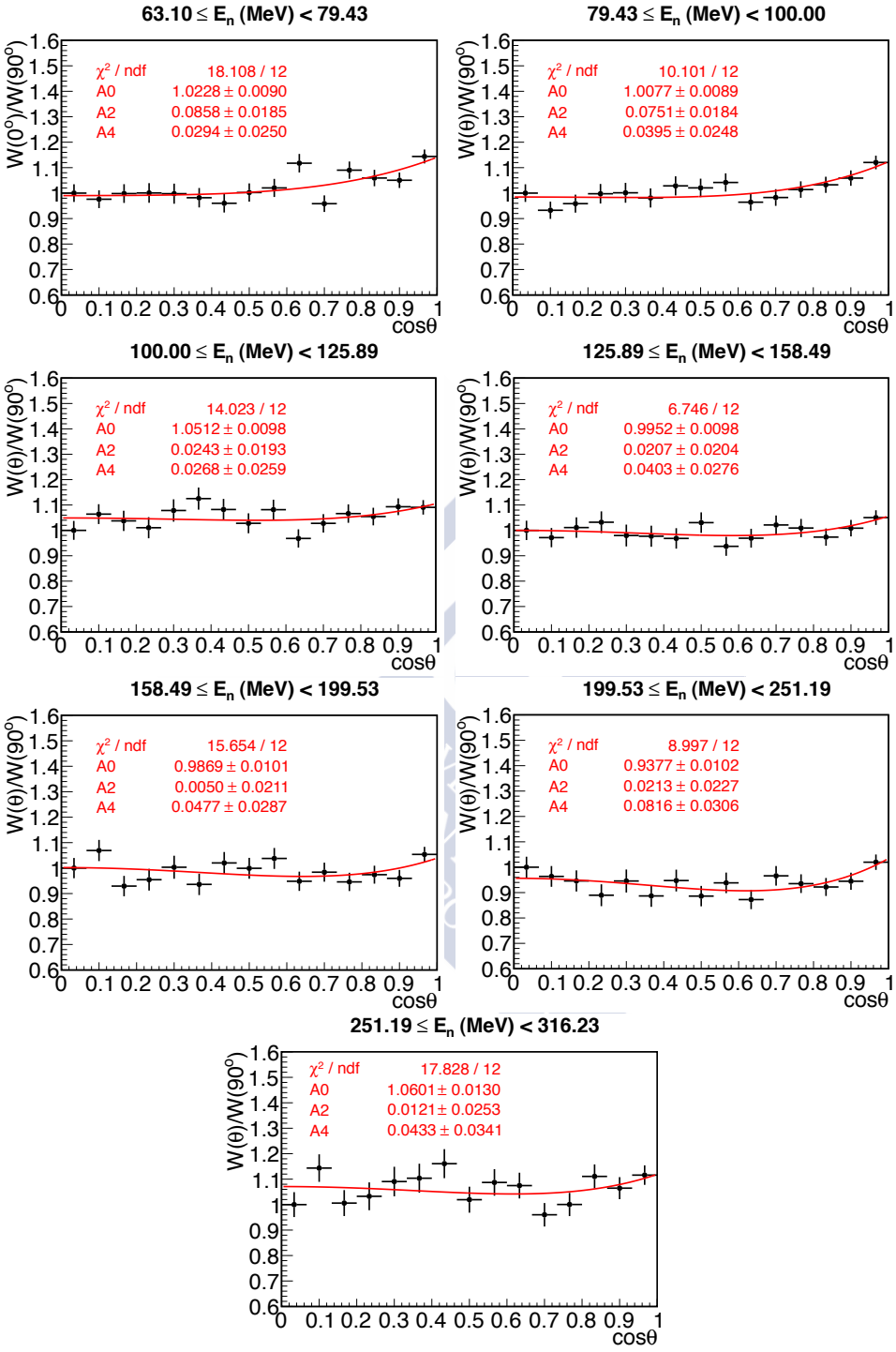
63.10 ≤ E_n (MeV) < 79.43
χ² / ndf 18.108 / 12
A0 1.0228 ± 0.0090
A2 0.0858 ± 0.0185
A4 0.0294 ± 0.0250
W(0°)/W(90°)
cosθ
79.43 ≤ E_n (MeV) < 100.00
χ² / ndf 10.101 / 12
A0 1.0077 ± 0.0089
A2 0.0751 ± 0.0184
A4 0.0395 ± 0.0248
W(θ)/W(90°)
cosθ
100.00 ≤ E_n (MeV) < 125.89
χ² / ndf 14.023 / 12
A0 1.0512 ± 0.0098
A2 0.0243 ± 0.0193
A4 0.0268 ± 0.0259
W(θ)/W(90°)
cosθ
125.89 ≤ E_n (MeV) < 158.49
χ² / ndf 6.746 / 12
A0 0.9952 ± 0.0098
A2 0.0207 ± 0.0204
A4 0.0403 ± 0.0276
W(θ)/W(90°)
cosθ
158.49 ≤ E_n (MeV) < 199.53
χ² / ndf 15.654 / 12
A0 0.9869 ± 0.0101
A2 0.0050 ± 0.0211
A4 0.0477 ± 0.0287
W(θ)/W(90°)
cosθ
199.53 ≤ E_n (MeV) < 251.19
χ² / ndf 8.997 / 12
A0 0.9377 ± 0.0102
A2 0.0213 ± 0.0227
A4 0.0816 ± 0.0306
W(θ)/W(90°)
cosθ
251.19 ≤ E_n (MeV) < 316.23
χ² / ndf 17.828 / 12
A0 1.0601 ± 0.0130
A2 0.0121 ± 0.0253
A4 0.0433 ± 0.0341
W(θ)/W(90°)
cosθ

Table B.2: Coefficients of the Legendre polynomials fits to the ^{235}U(n,f) angular distributions.

E_n (MeV)	A_0	A_2	A_4	A=W(0°)/W(90°)
0.10 - 0.12	1.06 ± 0.01	-0.00 ± 0.02	-0.02 ± 0.03	0.99 ± 0.03
0.12 - 0.15	0.98 ± 0.01	-0.02 ± 0.02	-0.01 ± 0.03	0.96 ± 0.03
0.15 - 0.18	1.05 ± 0.01	0.02 ± 0.02	-0.04 ± 0.03	1.00 ± 0.04
0.18 - 0.22	0.94 ± 0.01	-0.02 ± 0.02	0.04 ± 0.02	1.00 ± 0.03
0.22 - 0.26	1.02 ± 0.01	0.01 ± 0.02	-0.02 ± 0.02	1.01 ± 0.03
0.26 - 0.32	1.01 ± 0.01	0.03 ± 0.02	0.00 ± 0.02	1.05 ± 0.03
0.32 - 0.38	1.04 ± 0.01	0.04 ± 0.02	-0.02 ± 0.02	1.05 ± 0.03
0.38 - 0.46	1.01 ± 0.01	0.05 ± 0.02	-0.01 ± 0.02	1.07 ± 0.03
0.46 - 0.56	1.06 ± 0.01	0.08 ± 0.01	0.00 ± 0.02	1.13 ± 0.02
0.56 - 0.68	1.04 ± 0.01	0.08 ± 0.01	-0.00 ± 0.02	1.12 ± 0.02
0.68 - 0.83	1.04 ± 0.01	0.08 ± 0.01	0.02 ± 0.02	1.14 ± 0.02
0.83 - 1.00	1.00 ± 0.01	0.08 ± 0.01	-0.01 ± 0.02	1.12 ± 0.02
1.00 - 1.12	1.01 ± 0.01	0.10 ± 0.02	0.03 ± 0.02	1.18 ± 0.03
1.12 - 1.26	1.07 ± 0.01	0.10 ± 0.01	-0.02 ± 0.02	1.14 ± 0.02
1.26 - 1.41	1.08 ± 0.01	0.11 ± 0.01	0.01 ± 0.02	1.18 ± 0.03
1.41 - 1.58	1.04 ± 0.01	0.12 ± 0.01	0.03 ± 0.02	1.20 ± 0.02
1.58 - 1.78	1.05 ± 0.01	0.13 ± 0.01	-0.00 ± 0.02	1.20 ± 0.03
1.78 - 2.00	1.08 ± 0.01	0.11 ± 0.01	0.01 ± 0.02	1.19 ± 0.02
2.00 - 2.24	1.07 ± 0.01	0.15 ± 0.01	0.02 ± 0.02	1.25 ± 0.03
2.24 - 2.51	1.03 ± 0.01	0.09 ± 0.01	0.01 ± 0.02	1.15 ± 0.03
2.51 - 2.82	1.03 ± 0.01	0.12 ± 0.02	0.05 ± 0.02	1.22 ± 0.03
2.82 - 3.16	1.04 ± 0.01	0.11 ± 0.02	0.01 ± 0.02	1.18 ± 0.03
3.16 - 3.55	1.04 ± 0.01	0.10 ± 0.02	0.07 ± 0.03	1.19 ± 0.04
3.55 - 3.98	1.04 ± 0.01	0.08 ± 0.02	-0.00 ± 0.03	1.12 ± 0.04

3.98 - 4.47	1.02 ± 0.01	0.10 ± 0.02	0.04 ± 0.03	1.19 ± 0.04
4.47 - 5.01	1.02 ± 0.01	0.11 ± 0.03	0.02 ± 0.03	1.19 ± 0.05
5.01 - 5.62	1.11 ± 0.01	0.08 ± 0.03	0.02 ± 0.04	1.14 ± 0.05
5.62 - 6.31	1.08 ± 0.01	0.18 ± 0.03	0.02 ± 0.04	1.30 ± 0.06
6.31 - 7.08	1.04 ± 0.01	0.18 ± 0.03	0.13 ± 0.03	1.37 ± 0.05
7.08 - 7.94	1.19 ± 0.01	0.22 ± 0.03	0.05 ± 0.03	1.40 ± 0.05
7.94 - 8.91	1.07 ± 0.01	0.20 ± 0.03	0.03 ± 0.03	1.34 ± 0.05
8.91 - 10.00	1.07 ± 0.01	0.23 ± 0.03	0.08 ± 0.04	1.42 ± 0.05
10.00 - 12.59	1.06 ± 0.01	0.17 ± 0.02	0.02 ± 0.03	1.29 ± 0.04
12.59 - 15.85	1.02 ± 0.01	0.19 ± 0.02	0.10 ± 0.03	1.36 ± 0.04
15.85 - 19.95	1.07 ± 0.01	0.21 ± 0.02	0.02 ± 0.03	1.36 ± 0.04
19.95 - 25.12	1.10 ± 0.01	0.20 ± 0.02	0.02 ± 0.03	1.34 ± 0.04
25.12 - 31.62	1.10 ± 0.01	0.18 ± 0.02	0.06 ± 0.03	1.32 ± 0.04
31.62 - 39.81	1.11 ± 0.01	0.16 ± 0.02	0.03 ± 0.02	1.27 ± 0.03
39.81 - 50.12	1.09 ± 0.01	0.13 ± 0.02	-0.02 ± 0.02	1.19 ± 0.03
50.12 - 63.10	1.01 ± 0.01	0.10 ± 0.02	0.02 ± 0.03	1.17 ± 0.03
63.10 - 79.43	1.02 ± 0.01	0.09 ± 0.02	0.03 ± 0.02	1.15 ± 0.03
79.43 - 100.00	1.01 ± 0.01	0.08 ± 0.02	0.04 ± 0.02	1.14 ± 0.03
100.00 - 125.89	1.05 ± 0.01	0.02 ± 0.02	0.03 ± 0.03	1.05 ± 0.03
125.89 - 158.49	1.00 ± 0.01	0.02 ± 0.02	0.04 ± 0.03	1.06 ± 0.04
158.49 - 199.53	0.99 ± 0.01	0.01 ± 0.02	0.05 ± 0.03	1.04 ± 0.04
199.53 - 251.19	0.94 ± 0.01	0.02 ± 0.02	0.08 ± 0.03	1.08 ± 0.04
251.19 - 316.23	1.06 ± 0.01	0.01 ± 0.03	0.04 ± 0.03	1.04 ± 0.04

Appendix C

Fission fragment angular distributions

The standard theory of fission fragment angular distribution (FFAD) is based on the model of axially symmetric transition states at the saddle point of the fissioning nucleus, that is, on the assumption that it behaves as a symmetrical top, which is a rigid body in which two of the three moments of inertia are fixed. A general description of this process is developed in this section. A more detailed explanation can be found in [19,20].

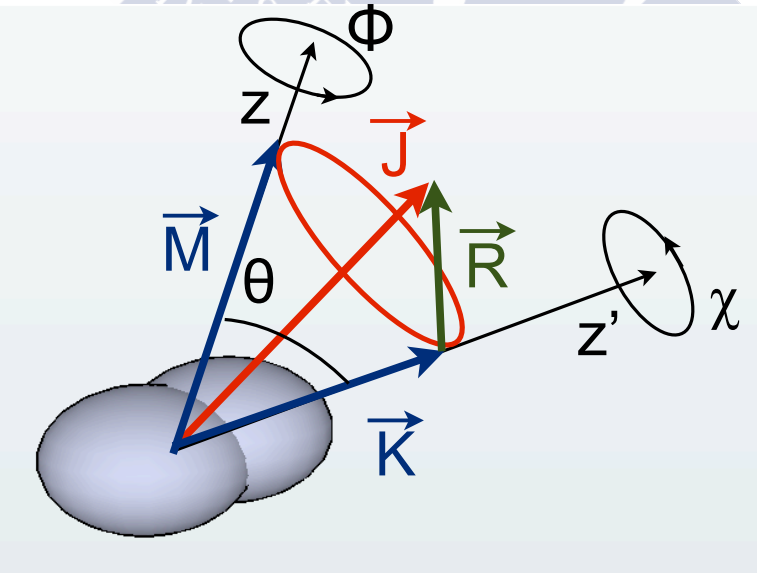

Figure C.1: Illustration of the fission process where the fissioning nucleus is considered as a symmetrical top.

The fission process is illustrated in Fig. C.1, where a neutron initially

moving in a direction determined by the space-fixed axis (z) impinges on the target nucleus. Then, an excited compound nucleus is formed with a total angular momentum $\overrightarrow{J}$. This compound nucleus is deformed along the nuclear symmetry axis (z'). The projections of $\overrightarrow{J}$ in the space-fixed axis and in the symmetry axis are respectively $\overrightarrow{M}$ and $\overrightarrow{K}$. The angles ϕ, χ, and θ correspond to the azimuthal angle around the space-fixed axis (z), the azimuthal angle around the symmetry axis (z'), and the angle between both axis.

During the passage from the initial compound nucleus to the saddle point or transition state, the J and M quantum numbers are constants of the motion due to the conservation of the angular momentum. It is not the case for the quantum number K, which, as a consequence of the vibrations and changes in shape of the compound nucleus, is not fixed during the entire process, however it may be assumed to be constant if we consider as the initial state the transition state deformation. With this assumption, the angular distribution at which the FFs are emitted from an initial transition state is uniquely determined by three quantum numbers: J, M and K.

The quantum mechanical wave equation of the symmetrical top, being $J_{||}$ and $J_{\perp}$ respectively the moments of inertia parallel and perpendicular to the symmetry axis, is given by:

$$\frac{\hbar^2}{2J_{\perp}}\left[\frac{1}{sin\theta}\cdot\frac{\partial}{\partial\theta}\left(sin\theta\cdot\frac{\partial\Psi}{\partial\theta}\right)+\frac{\left(cos\theta\frac{\partial}{\partial\chi}-\frac{\partial}{\partial\phi}\right)^2\Psi}{sin^2\theta}\right]+\frac{\hbar^2}{2J_{||}}\cdot\frac{\partial^2\Psi}{\partial\chi^2}+E\cdot\Psi=0 \tag{C.1}$$

The solution of this equation is obtained through the method of separation of variables as:

$$\Psi=\sqrt{\frac{2J+1}{8\pi^2}}\cdot e^{iM\phi}\cdot e^{iK\chi}\cdot d^J_{M,K}(\theta) \tag{C.2}$$

and the energies of the levels of the symmetric top are obtained from Eq. C.1 as:

$$E=\frac{\hbar^2\left[J\left(J+1\right)-K^2\right]}{2J_{\perp}}+\frac{\hbar^2K_2}{2J_{||}} \tag{C.3}$$

The $d^J_{M,K}(\theta)$ functions of the wave function are independent of ϕ and χ being given by:

$$d^J_{M,K}(\theta) = \sum_n (-)^n \frac{[(J+M)!\,(J-M)!\,(J+K)!\,(J-K)!]^{1/2}}{(J-M-n)!\,(J+K-n)!\,(M-K+n)!n!} \cdot \left(cos\frac{\theta}{2}\right)^{2J+K-M-2n} \cdot \left(sin\frac{\theta}{2}\right)^{2n+M-K} \tag{C.4}$$

The probability for the FFs to be emitted from a transition state in a determined space orientation is given by:

$$W^J_{M,K}(\theta) \cdot d\phi \cdot d\chi \cdot sin\theta \cdot d\theta = |\Psi|^2 \cdot d\phi \cdot d\chi \cdot sin\theta \cdot d\theta \tag{C.5}$$

where the angular distribution of the FFs is obtained substituting Eq. C.2 in Eq. C.5 as:

$$W^J_{M,K}(\theta) = \frac{2J+1}{2} |d^J_{K,M}(\theta)|^2 \tag{C.6}$$

For a particular channel defined by a set of quantum numbers, the angular distribution of the FFs is related to the differential fragment cross section through the next equation:

$$\frac{d\sigma_f(J,\pi,K,M,\theta)}{d\Omega} = \frac{W^J_{M,K}(\theta)}{2\pi} \cdot \sigma_f(J,\pi,K,M) \tag{C.7}$$

where dΩ is the differential solid angle.

FFAD on neutron-induced fission

The quantum numbers associated to a particular channel are jointly determined by the projectile and the target that interact to form the compound nucleus. When the projectile is a neutron, its spin quantum number is 1/2 with positive parity.

As it was discussed previously, for **even − even** targets, the neutron binding energy is usually lower than the fundamental fission barrier. This allows to resolve the level structure near the threshold through the calculation of the cross section and the angular distribution of the FFs in such energy region.

The first works providing an explanation for the anisotropies of the FFs in terms of a transition state with a particular K state were performed by Wilets and Chase [21] through the study of the ^{232}Th(n,f) reaction and, a few years later, by Lamphere [22] who studied the ^{234}U(n,f) reaction.

For an even-even target with zero spin, I =0, two values of M are allowed with the same probability, M = ±1/2, and the angular distribution of the FFs given in Eq. C.6 is reduced in this case to the next equation:

$$W^J_{\pm 1/2,\pm K}(\theta) = \frac{2J+1}{4}\left[|d^J_{1/2,K}(\theta)|^2 + |d^J_{-1/2,K}(\theta)|^2\right] \tag{C.8}$$

The theoretical FFAD for transitions states with different J and K quantum numbers obtained using Eq. C.8 are shown in Fig. C.2. The figures on the left panel show the angular distributions obtained for a fixed value of K and different values of J while the figures on the right panel correspond to the distributions calculated using a fixed J value and different values of K. It is worth to mention that in Fig. C.2, the angular distributions for the transition states in the K = 1/2 band peak around 0° (the neutron beam direction), however in bands with higher value of K, the angular distributions peak at higher values of θ.

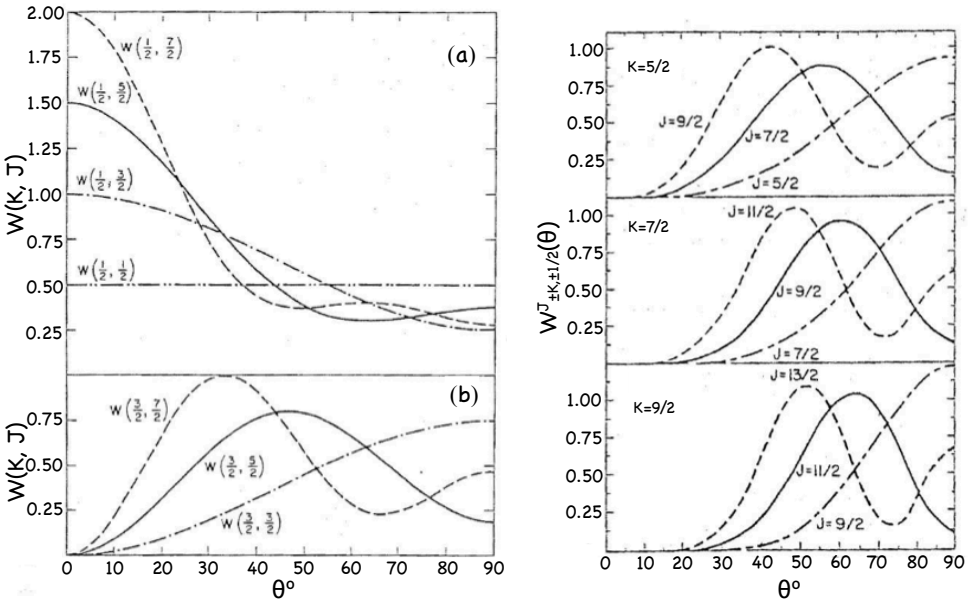

Figure C.2: Fission fragment angular distributions for neutron-induced fission of even-even targets obtained with Eq. C.8. Figure from [20].

It can be concluded from the figure that different FFAD are obtained for different transition states. A transition state is characterized by a set of quantum numbers (J, K, π) as well as by its barrier energy B(J, K, π) and a characteristic energy $\hbar\omega$(J, K, π) defining the barrier curvature. Near the fission barrier only one or a few fission channels are found with their correspondent FFAD. This is the reason why large anisotropies are found in the angular distributions of the FFs near the fission chance thresholds.

For **even − odd** target nuclei, as it was previously explained, the neutron binding energy is usually larger than the fundamental fission barrier and the

angular distribution data analysis are mostly based on the assumption of a Gaussian K distribution.

USC
UNIVERSIDADE
DE SANTIAGO
DE COMPOSTELA

Bibliography

[1] C. Paradela *et al.*, Phys. Rev. C, **82**, 034601 (2010).

[2] D. Tarrío *et al.*, Phys. Rev. C, **83**, 044620 (2011).

[3] D. Tarrío. PhD. thesis, Universidade de Santiago de Compostela (2012).

[4] EXFOR (Experimental Nuclear Reaction Data). http://www-nds.iaea.org/exfor/exfor.htm.

[5] https://www-nds.iaea.org/exfor/endf.htm

[6] The n_TOF Collaboration, *Nuclear data activities at the n_TOF facility at CERN*. Eur. Phys. J. Plus, **131**:371 (2016).

[7] G. D. James *et al.*, Phys. Rev. C, **15**, 2083 (1977).

[8] W. Dridi, PhD. Thesis, CEA/Saclay (2006).

[9] J. Heyse *et al.*, Nucl. Sci. Eng. **156**, 211 (2007).

[10] O. Hahn and F. Strassmann, Naturwissenschaften **26**:755 (1938).

[11] L. Meitner and O. R. Frisch. Nature **143**:239 (1939).

[12] N. Bohr and J. A. Wheeler. Phys. Rev., **56**:426 (1939).

[13] P. Möller and J. R. Nix, Proceedings of the Third IAEA Symposium on the Physics and Chemistry of fission, Rochester, New York, 1973, p. 103, 1974. INDC(NDS)-245.

[14] P. Möller, D. G. Madland, A. J. Sierk and A. Iwamoto. Nature **409**:785 (2001).

[15] T. Ichikawa, A. Iwamoto, P. Möller and A. J. Sierk, Phys. Rev. C, **86**, 024610 (2012).

[16] U. Brosa, S. Grossman and A. Müller, Phys. Rev., **197**:167, (1990).

[17] M. Sin, R. Capote, M. W. Herman and A. Trkov, Nuclear Data Sheets **139**, 138-170 (2017).

[18] T. Ichikawa, P. Möller and A. J. Siek, Phys. Rev. C, **87**, 054326 (2013).

[19] C. Wagemans. *The Nuclear Fission Process*. CRC Press (1991).

[20] R. Vandenbosch and J. R. Huizenga. *Nuclear Fission*. Academic Press (1973).

[21] L. Wilets and D. M. Chase. Phys. Rev, **103**:1296 (1956).

[22] R. W. Lamphere. Nucl. Phys., **38**:561 (1962).

[23] P. Schillebeeckx *et al.*, Nuclear Data Sheets **113**, 3054-3100 (2012).

[24] International Atomic Energy Agency, *International Evaluation of Neutron Cross − Section Standards*, Vienna, (2007).

[25] M. Barbagallo *et al.*, Eur. Phys. J. A **49**:156 (2013).

[26] C. Paradela. Master thesis, Universidade de Santiago de Compostela (2003).

[27] C. Guerrero *et al.*, Eur. Phys. J. A **49**: 27 (2013).

[28] C. Borcea *et al.*, Nucl. Instr. and Meth. A, 513:524-537 (2003).

[29] C. Paradela. PhD. thesis, Universidade de Santiago de Compostela (2005).

[30] U. Abbondanno *et al.*, (The n_TOF Collaboration). Status Report. CERN/INTC 2001-021, (2002).

[31] L. S. Leong. PhD. thesis, Universitè Paris Sud (2013).

[32] A. N. Behkami *et al.*, Phys. Rev. **171**, 1267 (1968).

[33] J. E. Simmons and R. L. Henkel, Phys. Rev. **120**, 198 (1960).

[34] R. W. Lamphere *et al.*, Nucl. Phys. **38**, 561-589 (1962).

[35] R. B. Leachman and L. Blumberg, Phys. Rev. **137**, B814 (1965).

[36] A. S. Vorobyev *et al.*, JETP Letters **102**, 231 (2015).

[37] D. Tarrío *et al.*, Nucl. Instrum. Meth. A **743**, 79 (2014).

[38] A. Adili *et al.*, Phys. Rev. C **93**, 034603 (2016).

[39] V. Kleinrath. PhD. thesis, Technische Universität Wien (2015).

[40] n_TOF internal communication.

[41] B. Becker et al., Data reduction and uncertainty propagation of time-of-flight spectra with AGS J. of Instrumentation, 7 P11002-19 (2012).

[42] C. Paradela *et al.*, The European Physical Journal Conferences 111, 02003 (2016).

[43] L. Leal *et al.*, Submitted to EPJ.

[44] D. Karadimos *et al.*, Phys. Rev. C **89**, 044606 (2014).

[45] I. Durán *et al.*, Submitted to EPJ.

[46] S. Lo Meo *et al.*, Journal of Physics: Conference Series **527** 012007 (2014).

[47] A.A. Kotov, L.A. Vaishnene, V.G. Vovchenko, Y.A. Gavrikov, V.V. Poliakov, M.G. Tverskoy, O.Y., Fedorov, Y.A. Chestnov, A.I. Shchetkovskiy, A.V. Shvedchikov, A.Y. Doroshenko and T. Fukahori, ÒEnergy dependence of proton induced fission cross sections for heavy nuclei in the energy range 200-1000 MeVÓ, Phys. Rev. C 74, 34605, 2006.

[48] A. Boudard, J. Cugnon, J-C David, S. Leray and D. Mancusi, Phys. Rev C, **87**, 014606 (2013).

[49] R. J. Charity, Proceedings of the Joint ICTP-IAEA Advanced Workshop on Model Codes for Spallation Reactions, ICTP Trieste, Italy, 4-8 February 2008, Eds Filges D et al., IAEA report INDC(NDS)-530, Vienna, 2008, p. 139.

[50] D. Mancusi, R. J. Charity and J. Cugnon, Phys. Rev. C, **82**, 044610 (2010).

[51] A. Kelić, M. V. Ricciardi and K-H Schmidt, Proceedings of the Joint ICTP-IAEA Advanced Workshop on Model Codes for Spallation Reactions, ICTP Trieste, Italy, 4-8 February 2008, Eds Filges D et al., IAEA report INDC(NDS)-530, Vienna, 2008, p. 181.

[52] 45 B. Marcinkevicius *et al.*, IAEA report INDC(NDS)-0681 (2015).

[53] C. Paradela *et al.*, Phys. Rev. C **91**, 024602 (2015).

[54] P. Lisowski, A. Gavron, W. Parker, S. Balestrini, A. Carlson, O. Wasson, and N. Hill, *Conference on Nuclear Data for Science Technology*, Juelich (American Institute of Physics, College Park, MD, 1991), p. 732.

[55] B. Fursow *et al.*, At. Energy. **71**, 827 (1992).

[56] J. Behrens and G. Carlson, Nucl. Sci. Eng. **63**, 250 (1977).

[57] F. Tovesson and T. Hill, Phys. Rev. C **75**, 034610 (2007).

[58] J. Meadows, Nucl. Sci. Eng. **65**, 171 (1978).

[59] F. Manabe *et al.*, Tohoku Univ. Tech. Rep. **52**, 97 (1988).

[60] L. P. Gerardo, J. Phys. G: Nucl. Phys. 12 (1986) 1423-1431.

[61] E. Birgersson, A. Oberstedt, S. Oberstedt, and F.-J. Hambsch, Nucl. Phys. A 817 (2009) 1-34.

[62] A. A. Goverdovski. In Proceedings of the Workshop on Nuclear Reaction Data and Nuclear Reactors: Physics, Design and Safety, Trieste, Italy (2002).

[63] I. V. Ryzhov et al. Nucl. Phys. A, **760**:19 (2005).

[64] M. Sin, R. Capote, A. Ventura, M. Herman, and P. ObloŽinskÝ, Phys. Rev. C **74**, 014608 (2006).

[65] E. J. Winhold, P. T. Demos, and I. Halpern. Minutes of the Meeting at Chicago, October 24-27, 1951. Phys. Rev., **85**:728 (1952).

[66] E. J. Winhold, P. T. Demos, and I. Halpern. Phys. Rev., **87**:1139 (1952).

[67] J. E. Brolley and W. C. Dickinson. Phys. Rev., **94**:640 (1954).

[68] J. E. Brolley, W. C. Dickinson, and R. L. Henkel. Phys. Rev., **99**:159 (1955).

[69] R. L. Henkel and J. E. Brolley Jr. Phys. Rev., **103**:1292 (1956).

[70] www.oecd-nea.org/science/wpec/sg40-cielo/.

[71] S. F. Mughabghab, *Atlas of Neutron Resonances* 5^{th} Edition, Elsevier Science (2006).

[72] C. Guerrero *et al.*, J. Korean Phys. Soc., **59** No. 2:1624-1627 (2011).